DISSERTATION

DESIGN AND SYNTHESIS OF METAL-ORGANIC FRAMEWORKS FOR APPLICATIONS IN CATALYZING ORGANIC CHEMICAL REACTIONS

Submitted by

Jonathan E. Thai

Department of Chemistry

In partial fulfillment of the requirements

For the Degree of Doctor of Philosophy

Colorado State University

Fort Collins, Colorado

Fall 2022

Doctoral Committee:

Advisor: Melissa M. Reynolds

Charles S. Henry
Delphine K. Farmer
Mark D. Zabel

ABSTRACT

DESIGN AND SYNTHESIS OF METAL-ORGANIC FRAMEWORKS FOR APPLICATIONS IN CATALYZING ORGANIC CHEMICAL REACTIONS

Metal-organic frameworks (MOFs) are versatile materials that possess a lot of potential for use as heterogeneous catalysts. Their crystalline structure creates a uniform, well-defined, highly porous framework that has a high density of active sites. Furthermore, their unprecedented tunability has allowed scientists to create several thousands of unique MOF structures. This has made MOFs a prominent area of research as they provide a clear path to move from homogeneous catalysis into heterogeneous catalysis. Heterogeneous catalysts are of utmost importance in the modern chemicals industry, playing key roles in the production of both organic and inorganic compounds. Heterogeneous catalysts help create lower energy pathways that allow for the catalysts to be more easily recovered and recycled (relative to homogeneous catalysts) and can enable more efficient production on large scale chemical production. However, MOFs have yet to be seen in widespread use for this purpose despite the many advantages they possess and the large variety of available MOFs due to their limitations, typically their lack of stability at high temperatures (most MOFs are typically only stable up to temperatures around 350-400°C).

This dissertation works towards improving current MOFs for heterogeneous catalysis and using MOFs as heterogeneous catalysis in a continuous flow reactor. Chapter 1 of this dissertation provides a discussion on the background of MOFs, how they are made, their limitations as heterogeneous catalysts, the advantages they bring to the field of heterogeneous catalysis, and some of the key techniques used to characterize MOFs.

Chapters 2 and 3 focus on the synthesis and development of CuBDTri (where H_2BDTri = 1,4-1*H*-1,2,3-triazol-5-yl)benzene), the first Cu-based MOF nanosheet (MOFN) that is water stable and shown to be more catalytically active for the release of nitric oxide from *S*-nitrosoglutathione relative to CuBTTri (where H_3BTTri = 1,3,5-tris(1*H*-1,2,3-triazol-5-yl)benzene). Chapter 2 focuses on how CuBDTri was originally designed, synthesized, and confirmed to be a newly created MOF. Chapter 3 then focuses on the work done to optimize the synthetic process used to make CuBDTri so that the resulting MOFN particles are as thin as possible, maximizing their efficiency as heterogeneous catalysts on a per-total-Cu-atom basis.

Chapter 4 originally aimed to develop a continuous flow process using the MOF CuBTC (where BTC = benzene-1,3,5-tricarboxylate) to catalyze the Friedländer synthesis. However, over the course of this work, it was found that the conditions being used to perform the Friedländer synthesis resulted in the breakdown of the CuBTC and so efforts were redirected to determine what caused this breakdown and the identity of the active catalyst in this reaction system. The data provided in this chapter track the breakdown of CuBTC by the Friedländer synthesis and provide evidence towards what the catalyst identity is.

Chapter 5 takes what was learned from Chapter 4 to transfer a condensation reaction to produce xanthene derivatives under continuous flow conditions, catalyzed by CuBTC. The results from the work completed here suggest that the reaction is being successfully performed under continuous flow conditions and is producing the desired xanthene. Furthermore, the success of this system provides further insight and understanding towards why CuBTC breaks down in the conditions used for the Friedländer synthesis in Chapter 4 but is stable under the conditions used to perform the condensation reaction in this chapter.

ACKNOWLEDGMENTS

I would like to thank Dr. Melissa M. Reynolds for being an amazing advisor and giving me the opportunity to learn and grow so much while in her group here at CSU. Her support and guidance throughout the past years have helped develop me into the scientist I am proud to be today. I also wish to thank the members of my committee, Dr. Delphine Farmer, Dr. Chuck Henry, Dr. Mark Zabel, and Dr. Yian Shi for being a part of my committee and for their time, support, and advice during my journey to earning a Ph. D. I am also thankful for Dr. Brian Newell and Dr. Roy Geiss for their time, hard work, and advice to help support my research. I also want to thank the wonderful professors I had at Western New England University that supported me and inspired me to pursue my Ph.D., Dr. Suzanna Milheiro, Dr. Isaac Stayton, Dr. Sean McClintock, Dr. Keri Lee, Dr. Francis Gerberich, Dr. Anne Poirot, and Dr. William Macanka whom without their dedication to be excellent educators and mentors, I would not be where I am today.

Thank you to my family, Vinh, Phuong, and Ryan for their support in very long, very difficult journey. Thank you to the current and previous members of the Reynolds group with whom I have worked, collaborated, and have shared many great (and tough) times with. Special thanks to Dr. Alec Lutzke, Dr. Jesus Tapia, Dr. Chris Allison, Dr. Hailey Hibbard, Dr. Rob Tuttle, Dr. Alyssa Galvin, Jamie Cuchiaro, Jacob DeRoo and Maddie Roach, for all of their help, guidance, and camaraderie throughout this journey we have been on together, for being wonderful people to work and share my time with. Thank you to Adam Pianka, Amanda Rose, Sally Wong, Mohamed Mire, Joanna Torres, Michelle Barnes, Nicholas Michelangelo, and Tyler Maffei for helping me stay sane in some of the hardest of times and for being such great friends, regardless of the distance and time between us. Lastly, thank you Stetson for being the best little pupper.

TABLE OF CONTENTS

ABSTRACT ii

ACKNOWLEDGEMENTS iv

CHAPTER 1 – INTRODUCTION 1

1.1 Metal-Organic Frameworks 1

1.1.1 The Synthesis of Metal-Organic Frameworks 2

1.1.2 Considering the Limitations of Metal-Organic Frameworks as Heterogeneous Catalysts 3

1.1.3 Why Use Metal-Organic Frameworks as Heterogeneous Catalysts 4

1.2 Key Characterization Methods Used to Analyze Metal-Organic Frameworks 5

1.2.1 Scanning Electron Microscopy (SEM) 8

1.2.2 Powder X-ray Diffraction (pXRD) 10

1.3 Dissertation Overview 11

1.3.1 Chapter 2 11

1.3.2 Chapter 3 13

1.3.3 Chapter 4 14

1.3.4 Chapter 5 16

1.4.5 Chapter 6 18

CHAPTER 1 – REFERENCES 19

CHAPTER 2 – DESIGNING AND SYNTHESIZING Cu-BASED METAL-ORGANIC FRAMEWORK NANOSHEETS FOR GREATER CATALYTIC EFFICIENCY 39

2.1 Overview 39

2.2 Introduction 41
2.3 Experimental 44
2.3.1 Materials 44
2.3.2 Synthesis of CuBTTri MOFNs via Three-Layer Bottom-Up Synthesis 45
2.3.3 Synthesis of H_2BDTri Ligand 45
2.3.4 Synthesis of CuBDTri MOFs via Solvothermal Synthesis 46
2.3.5 Synthesis of CuBDTri MOFNs via Three-Layer Bottom-Up Synthesis 46
2.3.6 Characterization by Scanning Electron Microscopy (SEM) and Energy-Dispersive X-ray Spectroscopy (EDS) 47
2.3.7 Characterization by Transmission Electron Microscopy (TEM) 48
2.3.8 Characterization by Powdered X-Ray Diffraction (pXRD) 48
2.3.9 Determination of CuBDTri Stability in Water 48
2.3.10 Elemental Analysis of CuBDTri MOFNs 49
2.3.11 Acid Digestion and Time of Flight Mass Spectrometry (TOF-MS) of CuBDTri MOFNs 49
2.3.12 Synthesis of S-Nitrosoglutathione (GSNO) 50
2.3.13 Preliminary Catalytic Studies – Conversion of GSNO to NO Catalyzed by CuBDTri MOFNs 50
2.3.14 Data Analysis 51
2.4 Results and Discussion 52
2.4.1 Synthesis of Cu-Based metal-Organic Framework Nanosheets Using Three-Later Method and Initial Analysis of Particle Morphologies Using Scanning Electron Microscopy and Transition Electron Microscopy 52

2.4.2 Characterization to Ascertain CuBDTri as a MOF 56
2.4.3 Determining Stability of CuBDTri MOFNs in Water 63
2.4.4 Preliminary Catalytic Performance of CuBDTri MOFNs in Reaction to Convert GSNO to NO 64
2.5 Conclusions 67
CHAPTER 2 – REFERENCES 69
CHAPTER 3 – OPTIMIZING OF THE THREE-LAYER BOTTOM-UP SYNTHETIC METHOD FOR MAKING CuBDTri METAL-ORGANIC FRAMEWORK NANOSHEETS .. 79
3.1 Overview 79
3.2 Introduction 81
3.3 Experimental 84
3.3.1 Materials 84
3.3.2 Synthesis of H_2BDTri Ligand 84
3.3.3 Synthesis of CuBDTri MOFNs via Bottom-Up Three-Layer Synthesis 85
3.3.4 Characterization by Scanning Electron Microscopy (SEM) 87
3.3.5 Characterization by Powder X-ray Diffraction (pXRD) 87
3.3.6 Chatacterization by Atomic Force Microscopy (AFM) 87
3.3.7 Data Analysis 88
3.4 Results and Discussion 88
3.4.1 Determining the Synthetic Conditions for CuBDTri MOFNs to Optimize . 91
3.4.2 Towards the Understanding of the Formation of the CuBDTri MOF Nanosheets Based on the Synthetic Conditions Used 93
3.4.3 Development of AFM Methods 99

3.5 Conclusions 107
3.6 Future Directions 108
CHAPTER 3 - REFERENCES 109
CHAPTER 4 – TOWARDS THE UNDERSTANDING OF THE BREAKDOWN OF CuBTC METAL-ORGANIC FRAMEWORKS BY FRIEDLÄNDER SYNTHESIS AND REIDENTIFICATION OF THE CATALYST 117
4.1 Overview 117
4.2 Introduction 118
4.2.1 Quinolines and the Friedländer Synthesis 118
4.2.2 Reported Use of CuBTC as a Catalyst for the Friedländer Synthesis 119
4.2.3 Developing a Continuous Flow Reactor for the Friedländer Synthesis Using CuBTC as the Catalyst 120
4.2.4 Towards a Better Understanding of the Role of CuBTC in the Friedländer Synthesis 121
4.3 Experimental 124
4.3.1 Materials 124
4.3.2 Synthesis of CuBTC MOF 124
4.3.3 Using CuBTC to Catalyze the Friedländer Synthesis Between 2-Aminobenzophenone and Acetylacetone Under Batch Conditions 125
4.3.4 Using CuBTC to Cataylze the Friedländer Synthesis Between 2-Aminobenzophenone and Acetylacetone under Continuous Flow Conditions .. 126
4.3.5 Characterization by Scanning Electron Microscopy (SEM) 126
4.3.6 Characterization by Powder X-ray Diffraction (pXRD) 127

4.3.7 Characterization by Time of Flight-Mass Speectrometry (TOF-MS) 127
4.3.8 Data Analysis 127
4.4 Results and Discussion 128
4.4.1 Proof of Concept for the Friedländer Synthesis Catalyzed by CuBTC Between 2-Aminobenzophenone and Acetylacetone & Determining Parameters for Performing the Reaction Under Continuous Flow 128
4.4.2 The Breakdown of CuBTC in the Friedländer System 130
4.4.3 Investigations into the Blue Solids ("Unidentified Crystal") Collected in the Eluent After Undergoing Friedländer Synthesis Under Continuous Flow 151
4.4.4 Towards Reidneitifying the Catalyst in the System for the Friedländer Synthesis 156
5.5 Conclusions 161
CHAPTER 4 - REFERENCES 164
CHAPTER 5 – USING CuBTC METAL-ORGANIC FRAMEWORKS TO CATALYZE CONDENSATIONS BETWEEN DIMEDONE AND BENZALDEHYDE TO FORM A XANTHENE DERIVATIVE UNDER CONTINUOUS FLOW CONDITIONS 172
5.1 Overview 172
5.2 Introduction 173
5.3 Experimental 179
5.3.1 Materials 179
5.3.2 Synthesis of CuBTC MOF 180
5.3.3 Using CuBTC to Catalyze the Condensation Between Dimedone and Benzaldehyde Under Batch Conditions 180

5.3.4 Using CuBTC to Cataylze the Condensation Between Dimedone and Benzaldehyde Under Continuous Flow Conditions 181
5.3.5 Characterization by Scanning Electron Microscopy (SEM) 182
5.3.6 Characterization by Powder X-ray Diffraction (pXRD) 182
5.3.7 Characterization by Time of Flight-Mass Spectrometry (TOF-MS) 183
5.3.8 Data Analysis 183
5.4 Results and Discussion 183
5.4.1 Analysis of Products Obtained After Performing the Xanthene Condensation Under Batch Conditions 183
5.4.2 Analysis of Products Obtained After Performing the Xanthene Condensation Under Continuous Flow Conditions 185
5.4.3 Analysis of the CuBTC MOF Used to Catalyze the Xanthene Condensation to Ensure it is Still Intact 187
5.5 Conclusions 194
CHAPTER 5 – REFERENCES 199
CHAPTER 6 – SUMMARY OF CONCLUSIONS AND FUTURE DIRECTIONS 208
6.1 Summary of Conclusions 208
6.2 Future Directions 211
6.2.1 Future Directions for Designing and Synthesizing Cu-Based Metal-Organic Framework Nanosheets for Greater Catalytic Efficiency 211
6.2.2 Future Directions in Optimizing the Three-Layer Bottom-Up Synthetic Method for Making CuBDTri MOFNs 212

6.2.3 Future Directions to Better the Understanding of the Breakdown of CuBTC MOF by Friedländer Synthesis and to Reidntify the Catalyst 213

6.2.4 Future Directions for Developing CuBTC MOFs to Catalyze the Condensation Between Dimedone and Benzaldehyde to Form 3,3,6,6-Tetramethyl-9-phenyl-3,4,5,6,7,9-hexahydro-1*H*-xanthene-1,8(2*H*)-dione Under Continuous Flow Conditions 215

6.3 Impacts on Future Research 217

6.3.1 Impacts of Chapter 2 218

6.3.2 Impacts of Chapter 3 219

6.3.3 Impacts of Chapter 4 220

6.3.4 Impacts of Chapter 5 221

APPENDIX A 222

CHAPTER 1

INTRODUCTION

1.1 Metal-Organic Frameworks

Metal-organic frameworks (MOFs), refer to a class of self-assembling, crystalline materials composed of metal ions (or clusters of metal ions) linked to each other by organic ligands, forming porous particles with one-, two-, or three-dimensional morphologies.[1–11] MOFs became a focus in materials research in the late 1990s, and have since garnered increased interest due to several factors.[12–17]

I. MOFs possess unprecedented tunability, both physically and chemically relative to other similar materials (there have been over 90,000 different MOF structures that have been reported and over 500,000 predicted computationally compared to zeolites, which have been around for significantly longer, but only have about 250 unique reported structures).[18–23]

II. The crystallinity of MOFs provides a uniform, well-defined structural geometry, allowing us to get a clearer understanding of the active site allowing for more targeted design of the active catalytic sites.

III. MOFs form highly porous structures that can allow for molecules to diffuse through and interact with the internal surface of the particle. This results in an extremely high surface area, ranging from hundreds to tens of thousands of square meters per gram of material.

Due to these key properties of MOFs, scientists have been able to use them for a large variety of applications, including gas separation, gas storage, luminescence in materials, thermal conduction, electrical conduction, hydrogen energy, energy storage, sensors, water treatment, biomedicines, drug delivery vehicles, medical devices, coatings, and catalysis.[17,24–36] The focus of my research and this dissertation is the design, synthesis, and application of MOFs as solid-state heterogeneous catalysts for use in organic transformations. To do so, the work in this dissertation aims to improve the catalytic efficiency of MOF particles by modifying the particle morphology of the MOFs, provide an understanding of the stability and how breakdown occurs in a catalytic MOF system, and using a MOF to catalyze an organic reaction in a continuous flow reactor.

1.1.1 The Synthesis of Metal-Organic Frameworks

MOFs are commonly synthesized using a solvothermal method, which is performed by dissolving or suspending the desired metal (as a salt) and ligand into a solvent or mixture of solvents and heating over a period of time.[37,38] Formation of the crystalline MOF then occurs via self-assembly as the metal and ligand form an ordered network of metal organic coordination bonds.

A large variety of metals with stable oxidation states have been used to create MOFs from each of the metal-containing groups on the periodic table such as alkali metals, alkaline earth metals, rare-earth elements, main group metals, and transition metals.[38–41] The organic ligands used are typically rigid molecules (commonly using conjugated aromatic systems) rather than more flexible molecules as they can form crystalline, porous MOFs more easily.[42–45] Furthermore, the choice of solvent or the presence of other compounds can drastically affect the crystal structure of the MOF created, allowing for a given metal-ligand combination to result in polymorphism, where the crystal structure of the product varies.[46–48]

1.1.2 Considering the Limitations of Metal-Organic Frameworks as Heterogeneous Catalysts

While MOFs are most commonly used for gas-storage applications, the use of MOFs as heterogeneous catalysts has been increasing in recent years due to their well-defined, porous structure, high active site density, and tunability.[18–22,49] However, there are certain limitations that must be considered when trying to use MOFs as heterogeneous catalysts:

I. Due to the inclusion of organic components, MOFs have limited thermal stability (many MOFs are typically only stable up to temperatures of 350-400°C)[7,50]
II. Some MOFs can be broken down in the presence of specific reactants, products, and/or solvents, so MOFs catalysts be carefully selected for their stability to compounds that may be present at any stage of a given reaction.[32,51–53]
III. MOFs can be hard to regenerate under the reaction conditions used, resulting in them breaking down and participating in homogeneous catalysis rather than heterogeneous catalysis.[54–56]

These limitations have hindered the use of MOFs in large-scale catalytic processes such as fuel processing, emissions abatement, petrochemical synthesis, and commodity chemical synthesis. Thus, the proper use of MOFs in heterogeneous catalytic systems require scientists to find ways to either mitigate these potential drawbacks in the design of the MOFs or to limit their use to conditions which the selected MOF is stable.

In designing MOFs for heterogeneous catalysis, one key design principle is to permit access to the metal centers. One way to do this is to use labile ligands (typically a solvent that can act as a ligand) that can be reversibly removed to introduce free coordination positions during an "activation stage", where the MOF crystals are heated under reduced pressure for a period of

time.[57–59] These unsaturated metal sites are key for adsorption and catalysis in MOFs as they allow for direct interaction between the metal centers of the MOF and the substrates. Ultimately, it is of key importance to understand the current limitations of MOFs in heterogeneous catalysis to be able to properly address these limitations in the design and synthesis of new MOFs, and in doing so, help push them into more practical applications.

1.1.3 Advantages of MOFs as Heterogeneous Catalysts

While it is important to understand the limitations of MOF catalysts, there are also many advantages to using MOFs as heterogeneous catalysts, which has resulted in growing interest in the field. These advantages include, but are not limited to:

I. As mentioned previously, MOFs are highly porous materials that possess large internal surface areas (with a record reaching up to 10,400 m^2 per gram of material) and high active site densities, allowing them to reach high catalytic reaction rates per unit volume.[60–63]

II. Also stated previously, MOFs are extremely tunable, allowing for various different metals and ligands to be used in their construction. This allows for MOFs to be designed for more specific reactions and applications than zeolites with some examples including:

    a. MOFs can be modified to create larger pore sizes to accommodate larger substrates and products.[64,65]

    b. MOFs can also be modified to perform shape-selective catalysis.[66]

    c. MOFs can provide confined environments that can stabilize substrates, catalytic species, or products as well as better mass transfer between substrates in reactions.[67,68]

III. Post-synthetic modification of MOFs with complementary catalytic groups can allow for catalysis by multiple functional groups at once or even allow for tandem catalysis.[69–71]

IV. MOFs can be synthesized to catalyze reactions based on their ligands as well as their metals, so can also be used in heterogeneous organocatalysis.[72,73]

Furthermore, the inherent Lewis acid and base characteristics found in many MOFs have shown to allow MOFs to be used for a large scope of applications within heterogeneous catalysis that provide more environmentally friendly alternatives to current reaction conditions.[74–77] These advantages, as well as others are helping push MOFs into focus in the field of heterogeneous catalysis as they have become ideal supports for many transition metal catalysts that have been previously limited as homogeneous catalysts.

1.2 Key Characterization Methods Used to Analyze Metal-Organic Frameworks

There are several key types of analysis used for MOFs to confirm MOF identity and other key characteristics of MOFs, including, but not limited to:

I. Powder x-ray diffraction (pXRD) – Used to confirm the crystallinity of MOFs. By comparing the diffraction patterns of MOFs, one can confirm the consistency of crystal structures between different batches of MOF synthesized. Furthermore, by comparing the diffraction patterns of MOFs before and after being used as a catalyst, pXRD can be used to help determine the integrity of the MOF.[37,78,79]

II. Scanning electron microscopy (SEM) and transmission electron microscopy (TEM) – Used to show the morphology and sizes of the MOF particles. Can be used to analyze MOFs before and after catalysis to help determine the integrity of

the MOF. In some cases, these techniques can even be used to determine the crystallinity and porosity of the MOF.[79]

III. Thermogravimetric analysis (TGA) – Used to determine the thermal stability of MOFs.[7,40]

IV. Gas absorption analyzer – Can be used to test the Brunnauer-Emmett-Teller (BET) surface area of MOFs based on adsorption and desorption isotherms of gasses or vapors.[14,17,80]

V. Energy-dispersive x-ray spectroscopy (EDX or EDS) – Can be used to determine elements present in MOFs. Can also be used to provide evidence of whether substrate/products are adsorbed to the surface of the MOF particle after being used for catalysis.[40,79]

VI. Inductively coupled plasma optical emission spectroscopy (ICP-OES), atomic absorption spectroscopy (AES) – Used to detect and quantitatively determine the presence of metals and to test for metal leaching from the catalyst to the solution. It should be noted that this technique is not typically done on the MOF itself, but performed on the reaction solution or supernatant that MOF was in.[79]

VII. Ultraviolet-visible spectroscopy (UV-Vis) – Can provide information on the coordination environment of the metal before and after catalysis.[79]

VIII. Infrared spectroscopy (IR) – Can also provide information on the coordination environment of the metal before and after catalysis. Can also help determine if there is substrate/product adsorbed on the MOF after catalysis.[79]

IX. Mass spectrometry (MS) – By digesting the MOF, one can obtain the individual ligand and metal centers contained in the MOF. By analyzing the resulting solution

used to digest the MOF using MS, one can determine the presence of the ligand from the MOF structure.

While several of these techniques are used throughout this dissertation, SEM and pXRD are used as key characterization techniques in all of the work included in this dissertation and so will be discussed here in further detail.

1.2.1 Scanning Electron Microscopy (SEM)

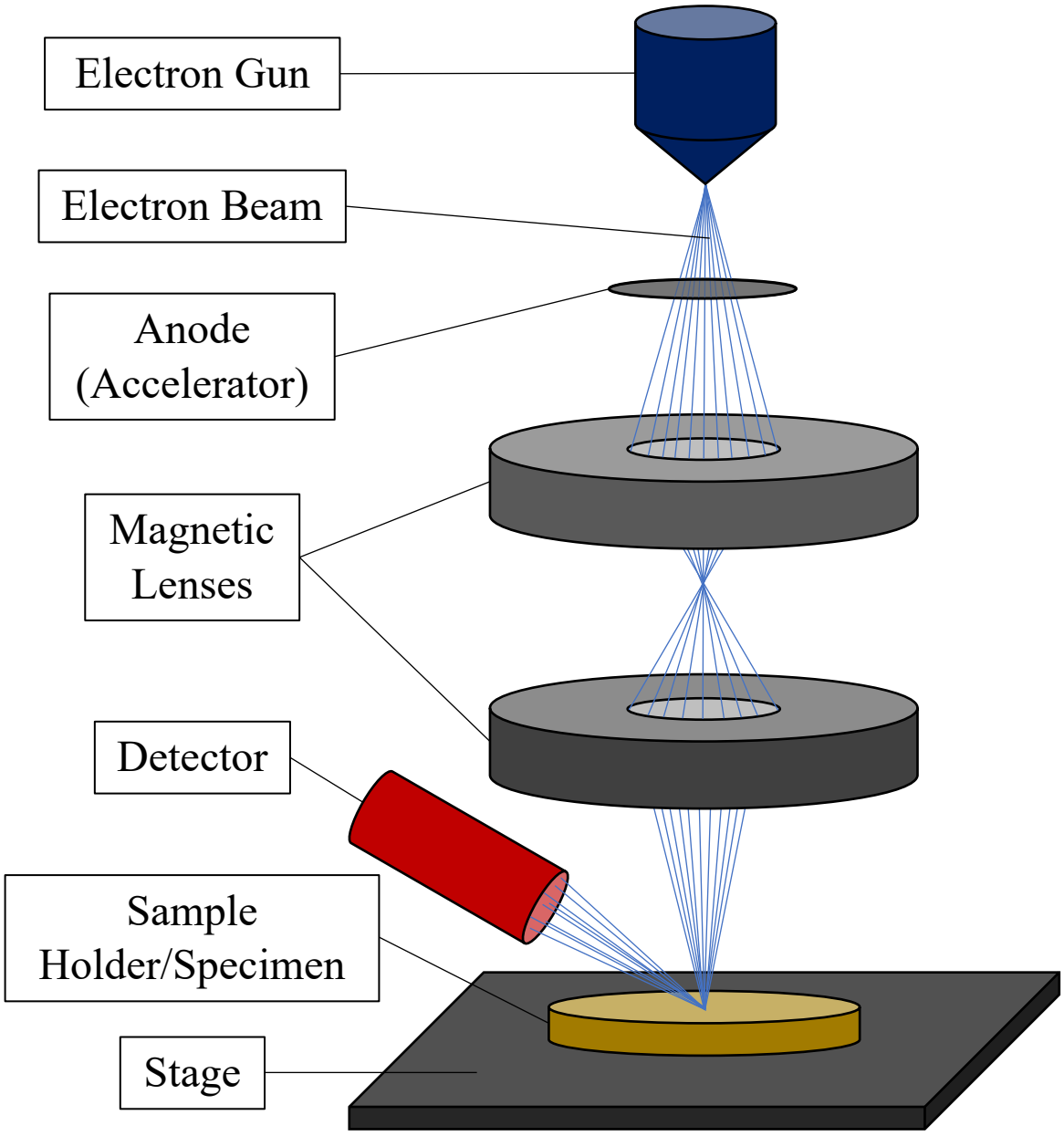

Figure 1.1. General schematic of a scanning electron microscope.

SEM can be used to generate high-resolution images of MOF particles, allowing one to determine the size and morphology of the MOF particle. It is also highly important to analyze MOFs using SEM before and after catalysis to ensure the MOF has not broken down due to the catalytic conditions used. An SEM uses electrons instead of light to produce drastically magnified

images (Figure 1.1). In brief, an electron gun produces a beam of electrons inside a vacuum. The electrons then accelerate down the microscope, passing through a series of lenses and apertures, focusing the beam onto the sample. When the electron beam hits the sample, the x-rays and electrons are ejected from the sample. Detectors then collect the x-rays and electrons, converting them into a signal that is then seen as an image (Figure 1.2).

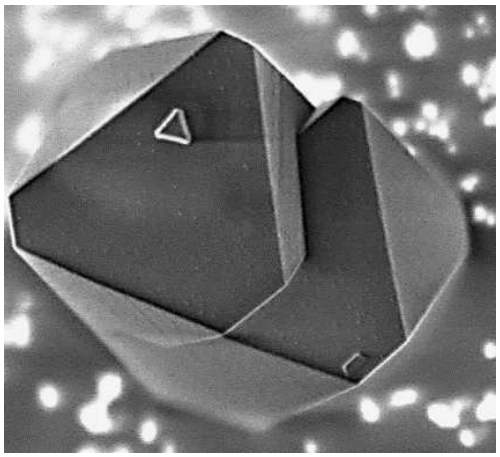

Figure 1.2. An SEM image of a CuBTC MOF particle.

1.2.2 Powder X-ray Diffraction (pXRD)

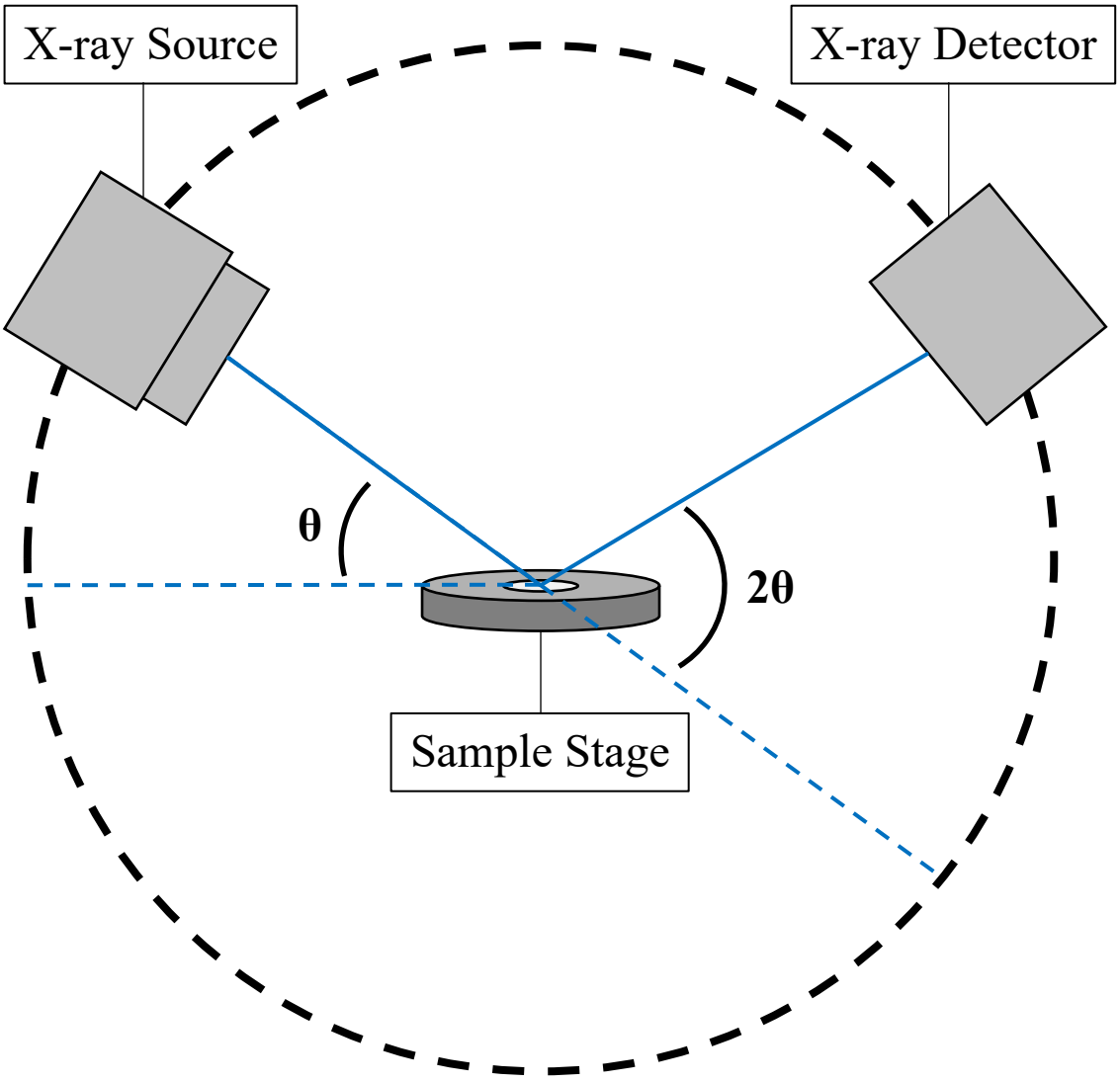

Figure 1.3. General schematic of a powder x-ray diffractometer

To determine the crystallinity of MOFs, pXRD is one of the main techniques used (Figure 1.3). In short, x-rays are generated by an x-ray source (typically a cathode ray tube that is filtered to produce monochromatic radiation) toward the sample. These interaction of the incident x-rays with a crystalline sample then produces constructive interference when the x-rays are in alignment, amplifying and deflecting the x-ray or producing destructive interference when the x-rays are not in alignment, destroying the signal. The diffracted x-rays from constructive interference are then

detected by a detector, processed, and then counted to determine how frequently that signal is generated by the sample. By moving the x-ray source and detector around in a circle in a synchronized motion, x-rays diffracting at specific angles can by measured in this way. The repeated structure of atoms in crystalline materials form distinct planes that can be defined be specific distances (d). When exposed to x-rays, the x-rays can then be scatted by the atoms, producing constructive interference at specific angles and the angle between the incident x-ray and scattered x-ray is defined as 2θ. The relationship between the diffraction angle and the spacing between the atoms in crystalline material can be described using Bragg's Law (Eq. 1).[78]

$$n\lambda = 2dsin\theta \qquad \text{Eq. 1}$$

In Bragg's Law, n = the diffraction order, λ = the wavelength, d = the distance between the atoms in the crystal lattice, and θ = half of the angle between the incident and scattered x-ray beams.

1.3 Dissertation Overview

The research in this dissertation aims to improve the catalytic efficiency of MOFs and apply MOFs as heterogeneous catalysts under continuous flow. Though a relatively new (with the first reports of MOFs being used in heterogeneous catalysis coming from the late 1990's to the early 2000's), the use of MOFs as heterogeneous catalysis has garnered a large amount of interest. The work done and discussed in this dissertation aims to help provide some of the foundation to facilitate the transition of MOFs being studied in academic research settings to practical applications and use as heterogeneous catalysts.

1.3.1 Chapter 2

Chapter 2 of this dissertation discusses the first steps made to develop, design, and synthesize the first known water-stable, copper-based MOF nanosheet (MOFN), CuBDTri (where

H_2BDTri = 1,4-1*H*-1,2,3-triazol-5-yl)benzene). In the 1990s, it was found that solvated Cu^{2+} is capable of catalyzing the generation of nitric oxide (NO) from a class of molecules known as *S*-nitrosothiols.[81–83] Furthermore, the *S*-nitrosothiol, *S*-nitrosoglutathione (GSNO) is a NO containing tripeptide endogenous to the human body.[84–87] This has led to the study towards the application of Cu^{2+}-containing materials to generate NO from GSNO *in vivo*.[88,89] However, copper ions have been shown to be acutely toxic and can result in cellular toxicity, liver damage, and neurodegenerative diseases (such as Alzheimer's disease).[90–92]

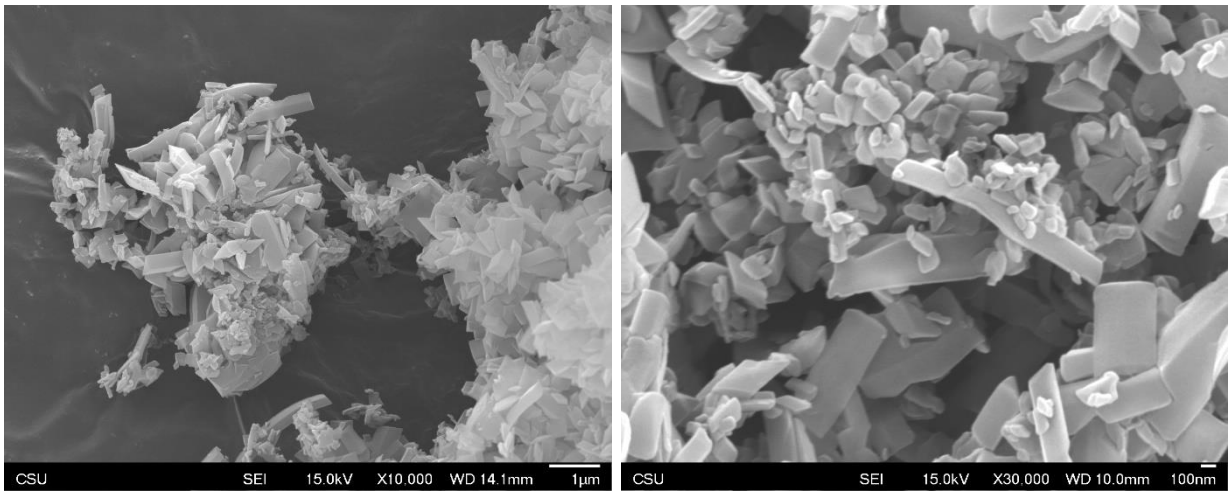

Figure 1.4. SEM images of some CuBDTri MOFNs

Most copper-based MOFs are known to be unstable in water as they typically contain Cu-oxo linkages which can interact readily with water, resulting in the breaking of the bond between the metal and ligand in these MOFs.[93,94] However, copper MOFs like CuBTTri (where H_3BTTri = 1,3,5-tris(1*H*-1,2,3-triazol-5-yl)benzene) are known to be stable in water and biological systems, allowing for them to be safely used in the human body.[95,96] However, in 2020, it was reported by Tuttle *et. al.* that only about 1.3% of the Cu sites in a CuBTTri MOF particle were actually available for catalysis as substrates like GSNO are too large to fit and diffuse through the pores of the MOF, restricting them to the external sites of the MOF particle.[97]

Thus, the project discussed in Chapter 2 of this dissertation aimed to develop, design, and synthesize a water-stable, Cu-based MOFN that was capable of catalyzing the generation of NO from GNSO, but reshape the MOF particle into a sheet so that internal volume is minimized, and external surface area is maximized. It was hypothesized that in doing so, the resulting MOFN would be more catalytically efficient on a per-total-Cu-atom basis as the active metal sites would be more readily accessible to substrates that are too large to diffuse through the pores of the MOF, like GSNO. This research also contributes building the foundation of synthesizing MOFNs for use as heterogeneous catalysis as a whole as there are many other reactions with substrates that would be too large to fit through the pores of the MOFs being used to catalyze them. This work resulted in the first reported synthesis of CuBDTri as a MOF (synthesized using solvothermal methods) and as a MOFN (synthesized using a three-layer, bottom-up method).

1.3.2 Chapter 3

Chapter 3 of this dissertation works to optimize the three-layer method used to synthesize the CuBDTri MOFN from Chapter 2. As previously mentioned, the goal in creating the CuBDTri MOFN was to increase catalytic efficiency by limiting the amount of copper sites in the MOF that would require diffusion to reach as not all substrates would be capable of readily accessing these sites. To this end, Chapter 3 lays the groundwork to optimize the synthesis of CuBDTri, attempting to create MOFN particles that are as thin as possible, ideally with just 1-2 building units thick, so that all of the copper sites are located on the external surface of the particle.

To do so, several variables such as temperature, time, metal to ligand ratio, and buffer layer thickness were all modified and tested. Due to the large (2700+) syntheses that would need to be performed to test all of the combinations of variables manually, it was instead planned to use a design of experiments approach to create a heat map based on a set of semi-randomly pre-

determined combinations of the conditions. Once these experiments are completed, the heatmap can then be used to predict the ideal set of conditions to use that would result in the thinnest nanosheets possible based on the parameters that were set.

Thus far, all of the syntheses required to provide data to create the initial heatmap has been completed and analyzed using SEM. Furthermore, as no standard procedure could be found for sample preparation and analysis of MOFNs using atomic force microscopy (AFM), a detailed method was experimentally determined for this project. AFM will be used to accurately determine the average thickness of the MOFN particles produced from each of the syntheses performed and provide the key set of data used to generate the heatmap. The approach used to optimize the synthesis of the CuBDTri MOFNs, using a design of experiments approach is one not commonly seen in the field of chemistry (especially relative to other fields like engineering), and this work hopes to provide an example of a more efficient way to optimize synthetic methods.

1.3.3 Chapter 4

Chapter 4 of this dissertation focuses on studying and understanding the breakdown of CuBTC (where BTC = benzene-1,3,5-tricarboxylate) in the Friedländer synthesis and determining the identity of the catalyst in the Friedländer synthesis for our system. The Friedländer synthesis is a reaction named after the German chemist Paul Friedländer that can be used to combine 2-aminobenzaldehydes with ketones to form quinoline derivatives.[98,99] Quinoline derivatives are one of the most common heterocycle moieties in drug research and have been shown to have pharmacological applications against bacteria, tuberculosis, malaria, inflammation, fungus, human immunodeficiency virus (HIV), hepatitis C, tumors, and fungus, making them key targets in synthetic research. [100–107]

In 2011, Pérez-Mayoral and Čejka reported the use of CuBTC as a heterogeneous catalyst for the Friedländer synthesis.[108] Based on their work, this project was originally developed to transfer the Friedländer synthesis from batch conditions to a continuous flow reactor so that CuBTC could be used to catalyze the Friedländer synthesis more efficiently. While initial efforts showed some success in that the continuous flow reactor was able to produce the desired product, it was found that the conditions being used for the Friedländer synthesis resulted in the breakdown of the CuBTC being used.

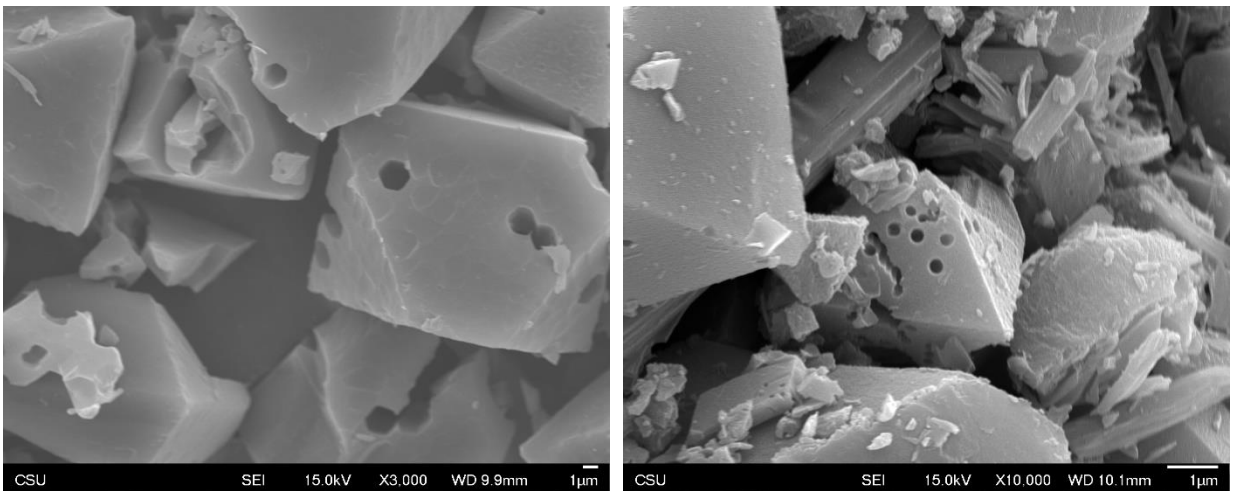

Figure 1.5. SEM images of some of the broken CuBTC particles with the "scaled" surfaces and hexagonal holes. In the image on the right, some of the unidentified crystalline material can also be seen as particles with a more rectangular morphology.

This redirected the work towards better understanding what may be causing the CuBTC in the Friedländer synthesis to be breaking down and what is the actual catalyst in this system. Towards achieving this, the CuBTC used to perform the Friedländer synthesis was analyzed using SEM and pXRD to track the breakdown of the MOF particles. The data collected showed that when exposed to the conditions used to perform the Friedländer synthesis, CuBTC develops a rougher surface (termed "scaled surfaces" in this dissertation) and hexagonal shaped holes that tunnel through the particle. It was also found that as the CuBTC breaks down, another crystalline material is formed that has yet to be definitively identified, though it is hypothesized, based on the

limited data obtained thus far that it is a copper-containing intermediate of the Friedländer synthesis being performed. Furthermore, the data collected suggests that the catalyst for this system is likely a compound that is formed in between this process of CuBTC breakdown and formation of the new crystalline material.

While this work creates a foundation towards understanding what is causing the CuBTC to break down and what is actually catalyzing the Friedländer synthesis in this system, there are still a lot of experiments that need to be completed to definitively answer these questions. Many of the key experiments that still need to be completed to achieve this goal are outlined in Chapter 4 as well.

1.3.4 Chapter 5

Chapter 5 again uses CuBTC MOFs in a continuous flow reactor, but this time to catalyze a condensation reaction to produce xanthene derivatives (that will be referred to as the "xanthene condensation" throughout this dissertation) more efficiently. While originally only used in dyes, xanthenes are a class of molecules that have recently gained a lot of attraction (starting mostly around 2019) when they were identified to be useful moieties in biodegradable agrochemicals, photodynamic therapies, solar cells, luminescent sensors, lasers, anti-inflammatory agents, antibacterial drugs, antinociceptives, antitumor treatments, and anti-virals.[55,109–114] Catalytic flow reactors offer a process to synthesize compounds that can be automated and scaled, facilitating the manufacture of key compounds.[115–118]

In 2021, Ghafri *et. al.* reported the use of CuBTC MOFs as an effective heterogeneous catalyst for creating xanthenes, using more mild conditions that most other processes.[119] This project aimed to transfer the described synthesis into a continuous flow process to help increase

the production efficiency of xanthene derivatives. From the preliminary experiments completed thus far, the results suggest that this has been successful in that the desired product is being formed under continuous flow. From SEM and pXRD analysis of the CuBTC used to catalyze the xanthene condensation, the data shows that the MOF has not been damaged by the reaction conditions.

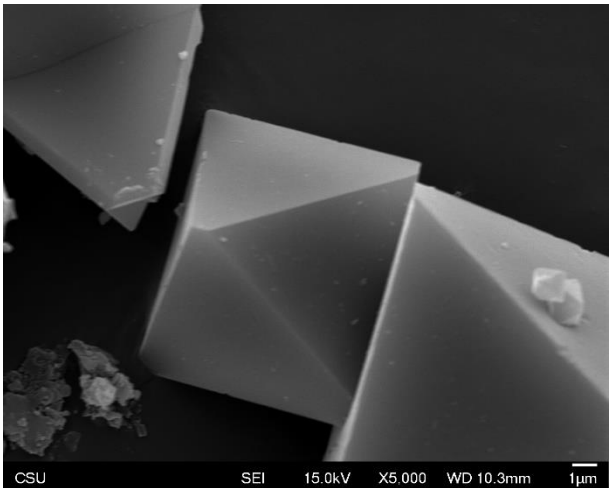

Figure 1.6. An SEM image showing the CuBTC after it was used to catalyze the xanthene condensation. It can be seen that the particles are still intact octahedra with smooth surfaces and have not been broken down.

The work discussed in Chapter 5 of this dissertation lays the groundwork towards developing a continuous flow reactor using CuBTC as a heterogeneous catalyst to complete the xanthene condensation and provides data to show preliminary success of this project. Additionally, by comparing the results obtained from this work, several key conclusions can be drawn to help further the understanding of the stability of CuBTC as a heterogeneous catalyst, providing insights for the goals set in Chapter 4 of this dissertation. However, there are still some key experiments that need to be completed to fully test and optimize this system and are outlined in this chapter.

1.3.5 Chapter 6

Chapter 6 summarizes the key findings from each chapter. It also provides suggestions for future key experiments that I have designed. Most importantly, it describes how the results in this dissertation inform future research directions in the field.

CHAPTER 1 – REFERENCES

(1) Motkuri, R.; Liu, J.; Fernandez, C.; Nune, S.; Thallapally, P.; Mcgrail, B. *Metal Organic Frameworks–Synthesis and Applications*; 2014. https://doi.org/10.1201/b17114-6.

(2) Neufeld, M. J.; Ware, B. R.; Lutzke, A.; Khetani, S. R.; Reynolds, M. M. Water-Stable Metal-Organic Framework/Polymer Composites Compatible with Human Hepatocytes. *ACS Appl Mater Interfaces* **2016**, *8* (30). https://doi.org/10.1021/acsami.6b05948.

(3) Doonan, C. J.; Sumby, C. J. Metal-Organic Framework Catalysis. *CrystEngComm* **2017**, *19* (29), 4045–4049. https://doi.org/10.1039/c7ce90106b.

(4) Xuan, W.; Zhu, C.; Liu, Y.; Cui, Y. Mesoporous Metal-Organic Framework Materials. *Chem Soc Rev* **2012**, *41* (5), 1677–1695. https://doi.org/10.1039/c1cs15196g.

(5) Klinowski, J.; Almeida Paz, F. A.; Silva, P.; Rocha, J. Microwave-Assisted Synthesis of Metal-Organic Frameworks. *Dalton Transactions* **2011**, *40* (2), 321–330. https://doi.org/10.1039/c0dt00708k.

(6) Yang, D.; Gates, B. C. Catalysis by Metal Organic Frameworks: Perspective and Suggestions for Future Research. *ACS Catalysis*. American Chemical Society March 1, 2019, pp 1779–1798. https://doi.org/10.1021/acscatal.8b04515.

(7) Liu, J.; Chen, L.; Cui, H.; Zhang, J.; Zhang, L.; Su, C. Y. Applications of Metal-Organic Frameworks in Heterogeneous Supramolecular Catalysis. *Chem Soc Rev* **2014**, *43* (16), 6011–6061. https://doi.org/10.1039/c4cs00094c.

(8) Zhao, M.; Wang, Y.; Ma, Q.; Huang, Y.; Zhang, X.; Ping, J.; Zhang, Z.; Lu, Q.; Yu, Y.; Xu, H.; Zhao, Y.; Zhang, H. Ultrathin 2D Metal-Organic Framework Nanosheets. *Advanced Materials* **2015**, *27* (45), 7372–7378. https://doi.org/10.1002/adma.201503648.

(9) Pascanu, V.; González Miera, G.; Inge, A. K.; Martín-Matute, B. Metal-Organic Frameworks as Catalysts for Organic Synthesis: A Critical Perspective. *J Am Chem Soc* **2019**, *141* (18), 7223–7234. https://doi.org/10.1021/jacs.9b00733.

(10) Corella-Ochoa, M. N.; Tapia, J. B.; Rubin, H. N.; Lillo, V.; González-Cobos, J.; Núñez-Rico, J. L.; Balestra, S. R. G.; Almora-Barrios, N.; Lledós, M.; Guëll-Bara, A.; Cabezas-Giménez, J.; Escudero-Adán, E. C.; Vidal-Ferran, A.; Calero, S.; Reynolds, M.; Martí-Gastaldo, C.; Galán-Mascarós, J. R. Homochiral Metal-Organic Frameworks for Enantioselective Separations in Liquid Chromatography. *J Am Chem Soc* **2019**, *141* (36), 14306–14316. https://doi.org/10.1021/jacs.9b06500.

(11) Zhao, M.; Huang, Y.; Peng, Y.; Huang, Z.; Ma, Q.; Zhang, H. Two-Dimensional Metal-Organic Framework Nanosheets: Synthesis and Applications. *Chem Soc Rev* **2018**, *47* (16), 6267–6295. https://doi.org/10.1039/c8cs00268a.

(12) Li, H.; Eddaoudi, M.; O'Keeffe, M.; Yaghi, O. M. Design and Synthesis of an Exceptionally Stable and Highly Porous Metal-Organic Framework. *Nature* **1999**, *402*, 276–279.

(13) Jiang, J.; Yaghi, O. M. Brønsted Acidity in Metal-Organic Frameworks. *Chemical Reviews*. 2015. https://doi.org/10.1021/acs.chemrev.5b00221.

(14) Thai, J. E.; Tuttle, R. R.; Deroo, J.; Cuchiaro, J.; Reynolds, M. M. Cu-Based Metal-Organic Framework Nanosheets Synthesized via a Three-Layer Bottom-Up Method for

the Catalytic Conversion of S-Nitrosoglutathione to Nitric Oxide. *ACS Appl Nano Mater* **2021**. https://doi.org/10.1021/acsanm.1c03313.

(15) Liu, D.; Gu, W.; Zhou, L.; Wang, L.; Zhang, J.; Liu, Y.; Lei, J. Recent Advances in MOF-Derived Carbon-Based Nanomaterials for Environmental Applications in Adsorption and Catalytic Degradation. *Chemical Engineering Journal*. Elsevier B.V. January 1, 2022. https://doi.org/10.1016/j.cej.2021.131503.

(16) Opanasenko, M.; Dhakshinamoorthy, A.; Shamzhy, M.; Nachtigall, P.; Horáček, M.; Garcia, H.; Čejka, J. Comparison of the Catalytic Activity of MOFs and Zeolites in Knoevenagel Condensation. *Catal Sci Technol* **2013**, *3* (2), 500–507. https://doi.org/10.1039/c2cy20586f.

(17) Cuchiaro, H.; Thai, J.; Schaffner, N.; Tuttle, R. R.; Reynolds, M. Exploring the Parameter Space of P-Cresyl Sulfate Adsorption in Metal-Organic Frameworks. *ACS Appl Mater Interfaces* **2020**, *12* (20), 22572–22580. https://doi.org/10.1021/acsami.0c04203.

(18) Groom, C. R.; Bruno, I. J.; Lightfoot, M. P.; Ward, S. C. The Cambridge Structural Database. *Acta Crystallogr B Struct Sci Cryst Eng Mater* **2016**, *72* (2), 171–179. https://doi.org/10.1107/S2052520616003954.

(19) Chakraborty, G.; Park, I. H.; Medishetty, R.; Vittal, J. J. Two-Dimensional Metal-Organic Framework Materials: Synthesis, Structures, Properties and Applications. *Chem Rev* **2021**, *121* (7), 3751–3891. https://doi.org/10.1021/acs.chemrev.0c01049.

(20) Dai, R.; Peng, F.; Ji, P.; Lu, K.; Wang, C.; Sun, J.; Lin, W. Electron Crystallography Reveals Atomic Structures of Metal-Organic Nanoplates with M12(M3-O)8(M3-

OH)8(M2-OH)6 (M = Zr, Hf) Secondary Building Units. *Inorg Chem* **2017**, *56* (14), 8128–8134. https://doi.org/10.1021/acs.inorgchem.7b00845.

(21) Liang, J.; Liang, Z.; Zou, R.; Zhao, Y. Heterogeneous Catalysis in Zeolites, Mesoporous Silica, and Metal–Organic Frameworks. *Advanced Materials*. Wiley-VCH Verlag August 11, 2017. https://doi.org/10.1002/adma.201701139.

(22) Gandhi, A.; Hasan, M. M. F. Machine Learning for the Design and Discovery of Zeolites and Porous Crystalline Materials. *Current Opinion in Chemical Engineering*. Elsevier Ltd March 1, 2022. https://doi.org/10.1016/j.coche.2021.100739.

(23) Moosavi, S. M.; Nandy, A.; Jablonka, K. M.; Ongari, D.; Janet, J. P.; Boyd, P. G.; Lee, Y.; Smit, B.; Kulik, H. J. Understanding the Diversity of the Metal-Organic Framework Ecosystem. *Nat Commun* **2020**, *11* (1). https://doi.org/10.1038/s41467-020-17755-8.

(24) Das, A. K.; Vemuri, R. S.; Kutnyakov, I.; McGrail, B. P.; Motkuri, R. K. An Efficient Synthesis Strategy for Metal-Organic Frameworks: Dry-Gel Synthesis of MOF-74 Framework with High Yield and Improved Performance. *Sci Rep* **2016**, *6* (June), 1–7. https://doi.org/10.1038/srep28050.

(25) Chi-Durán, I.; Enríquez, J.; Manquián, C.; Fritz, R. A.; Vega, A.; Serafini, D.; Herrera, F.; Singh, D. P. Azide-Based High-Energy Metal-Organic Frameworks with Enhanced Thermal Stability. *ACS Omega* **2019**. https://doi.org/10.1021/acsomega.9b01127.

(26) Tranchemontagne, D. J.; Mendoza-Cortés, J. L.; O'Keeffe, M.; Yaghi, O. M. Secondary Building Units, Nets and Bonding in the Chemistry of Metal-Organic Frameworks. *Chem Soc Rev* **2009**, *38* (5), 1257–1283. https://doi.org/10.1039/b817735j.

(27) Sabale, S.; Zheng, J.; Vemuri, R. S.; Yu, X.-Y.; Mcgrail, P.; Motkuri, R. K. Synthesis and Catalysis: Open Access Recent Advances in Metal-Organic Frameworks for Heterogeneous Catalyzed Organic Transformations. *Synthesis and Catalysis: Open Access* **2016**, *1* (5), 1–8.

(28) Bobbitt, N. S.; Mendonca, M. L.; Howarth, A. J.; Islamoglu, T.; Hupp, J. T.; Farha, O. K.; Snurr, R. Q. Metal-Organic Frameworks for the Removal of Toxic Industrial Chemicals and Chemical Warfare Agents. *Chemical Society Reviews*. 2017. https://doi.org/10.1039/c7cs00108h.

(29) Hai, G.; Jia, X.; Zhang, K.; Liu, X.; Wu, Z.; Wang, G. High-Performance Oxygen Evolution Catalyst Using Two-Dimensional Ultrathin Metal-Organic Frameworks Nanosheets. *Nano Energy* **2018**, *44* (October 2017), 345–352. https://doi.org/10.1016/j.nanoen.2017.11.071.

(30) Wu, H. bin; Lou, X. W. Metal-Organic Frameworks and Their Derived Materials for Electrochemical Energy Storage and Conversion: Promises and Challenges. *Science Advances*. 2017. https://doi.org/10.1126/sciadv.aap9252.

(31) Corma, A.; Iglesias, M.; Llabrés i Xamena, F. X.; Sánchez, F. Cu and Au Metal-Organic Frameworks Bridge the Gap between Homogeneous and Heterogeneous Catalysts for Alkene Cyclopropanation Reactions. *Chemistry - A European Journal* **2010**, *16* (32), 9789–9795. https://doi.org/10.1002/chem.201000278.

(32) Liu, B.; Vikrant, K.; Kim, K. H.; Kumar, V.; Kailasa, S. K. Critical Role of Water Stability in Metal-Organic Frameworks and Advanced Modification Strategies for the

Extension of Their Applicability. *Environ Sci Nano* **2020**, *7* (5), 1319–1347. https://doi.org/10.1039/c9en01321k.

(33) Oar-Arteta, L.; Wezendonk, T.; Sun, X.; Kapteijn, F.; Gascon, J. Metal Organic Frameworks as Precursors for the Manufacture of Advanced Catalytic Materials. *Materials Chemistry Frontiers*. 2017. https://doi.org/10.1039/c7qm00007c.

(34) Dhakshinamoorthy, A.; Navalon, S.; Asiri, A. M.; Garcia, H. Metal Organic Frameworks as Solid Catalysts for Liquid-Phase Continuous Flow Reactions. *Chemical Communications* **2019**, *56* (1), 26–45. https://doi.org/10.1039/c9cc07953j.

(35) Kuo, 2012 - Synthesis and Characterization of Porous HKUST-1 Metal Organic Frameworks for Hydrogen Storage.

(36) Dhakshinamoorthy, A.; Alvaro, M.; Garcia, H. Metal Organic Frameworks as Efficient Heterogeneous Catalysts for the Oxidation of Benzylic Compounds with T-Butylhydroperoxide. *J Catal* **2009**, *267* (1), 1–4. https://doi.org/10.1016/j.jcat.2009.08.001.

(37) Wu, Y.; Moorhouse, S. J.; O'Hare, D. Time-Resolved in Situ Diffraction Reveals a Solid-State Rearrangement during Solvothermal MOF Synthesis. *Chemistry of Materials* **2015**, *27* (21), 7236–7239. https://doi.org/10.1021/acs.chemmater.5b03085.

(38) Yu, Z. A Novel Mn(II) Coordination Polymer Based on Carboxylate and Tris[4-(1Himidazol-1-Yl)-Phenyl]Amine Coligands With a Rare Hms Topology: Solvothermal Synthesis, Crystal Structure, and Luminescent Property. *Synthesis and Reactivity in Inorganic, Metal-Organic and Nano-Metal Chemistry* **2016**, *46* (10), 1495–1498. https://doi.org/10.1080/15533174.2015.1136960.

(39) Bavykina, A.; Kolobov, N.; Khan, I. S.; Bau, J. A.; Ramirez, A.; Gascon, J. Metal-Organic Frameworks in Heterogeneous Catalysis: Recent Progress, New Trends, and Future Perspectives. *Chemical Reviews*. American Chemical Society August 26, 2020, pp 8468–8535. https://doi.org/10.1021/acs.chemrev.9b00685.

(40) Corma, A.; García, H.; Llabrés i Xamena, F. X. Engineering Metal Organic Frameworks for Heterogeneous Catalysis. *Chem Rev* **2010**, *110*, 4606–4655. https://doi.org/10.1021/cr9003924.

(41) Zhu, L.; Liu, X. Q.; Jiang, H. L.; Sun, L. B. Metal-Organic Frameworks for Heterogeneous Basic Catalysis. *Chem Rev* **2017**, *117* (12), 8129–8176. https://doi.org/10.1021/acs.chemrev.7b00091.

(42) Arnanz, A.; Pintado-Sierra, M.; Corma, A.; Iglesias, M.; Sánchez, F. Bifunctional Metal Organic Framework Catalysts for Multistep Reactions: MOF-Cu(BTC)-[Pd] Catalyst for One-Pot Heteroannulation of Acetylenic Compounds. *Adv Synth Catal* **2012**, *354* (7), 1347–1355. https://doi.org/10.1002/adsc.201100503.

(43) Ghosh, S.; Pahari, G.; Maiti, A.; Dinda, S.; Ghoshal, D. Designing of Three Mixed Ligand MOFs in Searching of Length Induced Flexibility in Ligand for the Creation of Interpenetration. *Polyhedron* **2022**, *218*. https://doi.org/10.1016/j.poly.2022.115763.

(44) Aljammal, N.; Jabbour, C.; Chaemchuen, S.; Juzsakova, T.; Verpoort, F. Flexibility in Metal–Organic Frameworks: A Basic Understanding. *Catalysts* **2019**, *9* (6). https://doi.org/10.3390/catal9060512.

(45) Ryzhikov, M. R.; Kozlova, S. G. Understanding Structural Flexibility of the Paddle-Wheel Zn-SBU Motif in MOFs: Influence of Pillar Ligands. *Physical Chemistry Chemical Physics* **2019**, *21* (22), 11977–11982. https://doi.org/10.1039/c9cp02483b.

(46) Tian, Y. Q.; Zhao, Y. M.; Chen, Z. X.; Zhang, G. N.; Weng, L. H.; Zhao, D. Y. Design and Generation of Extended Zeolitic Metal-Organic Frameworks (ZMOFs): Synthesis and Crystal Structures of Zinc(II) Imidazolate Polymers with Zeolitic Topologies. *Chemistry - A European Journal* **2007**, *13* (15), 4146–4154. https://doi.org/10.1002/chem.200700181.

(47) Park, K. S.; Ni, Z.; Cô, A. P.; Choi, J. Y.; Huang, R.; Uribe-Romo, F. J.; Chae, H. K.; O'keeffe, M.; Yaghi, O. M. *Exceptional Chemical and Thermal Stability of Zeolitic Imidazolate Frameworks*; 2006.

(48) Shi, Q.; Kang, X.; Shi, F. N.; Dong, J. Zn10(Im)20·4DBF: An Unprecedented 10-Nodal Zeolitic Topology with a 10-MR Channel and 10 Crystallographically Independent Zn Atoms. *Chemical Communications* **2015**, *51* (6), 1131–1134. https://doi.org/10.1039/c4cc07105k.

(49) Chughtai, A. H.; Ahmad, N.; Younus, H. A.; Laypkov, A.; Verpoort, F. Metal-Organic Frameworks: Versatile Heterogeneous Catalysts for Efficient Catalytic Organic Transformations. *Chem Soc Rev* **2015**, *44* (19), 6804–6849. https://doi.org/10.1039/c4cs00395k.

(50) Chen, B.; Yang, Z.; Zhu, Y.; Xia, Y. Zeolitic Imidazolate Framework Materials: Recent Progress in Synthesis and Applications. *J Mater Chem A Mater* **2014**, *2* (40), 16811–16831. https://doi.org/10.1039/c4ta02984d.

(51) Al-Janabi, N.; Hill, P.; Torrente-Murciano, L.; Garforth, A.; Gorgojo, P.; Siperstein, F.; Fan, X. Mapping the Cu-BTC Metal-Organic Framework (HKUST-1) Stability Envelope in the Presence of Water Vapour for CO2 Adsorption from Flue Gases. *Chemical Engineering Journal* **2015**, *281*, 669–677. https://doi.org/10.1016/j.cej.2015.07.020.

(52) Schlichte, K.; Kratzke, T.; Kaskel, S. Improved Synthesis, Thermal Stability and Catalytic Properties of the Metal-Organic Framework Compound Cu3(BTC)2. *Microporous and Mesoporous Materials* **2004**, *73* (1–2), 81–88. https://doi.org/10.1016/j.micromeso.2003.12.027.

(53) Ma, S.; Liu, Z. P. The Role of Zeolite Framework in Zeolite Stability and Catalysis from Recent Atomic Simulation. *Top Catal* **2022**, *65* (1–4), 59–68. https://doi.org/10.1007/s11244-021-01473-6.

(54) Schlögl, R. Heterogeneous Catalysis. *Angewandte Chemie - International Edition*. Wiley-VCH Verlag March 9, 2015, pp 3465–3520. https://doi.org/10.1002/anie.201410738.

(55) Ghamari Kargar, P.; Bagherzade, G.; Eshghi, H. Introduction of a Trinuclear Manganese(Iii) Catalyst on the Surface of Magnetic Cellulose as an Eco-Benign, Efficient and Reusable Novel Heterogeneous Catalyst for the Multi-Component Synthesis of New Derivatives of Xanthene. *RSC Adv* **2021**, *11* (8), 4339–4355. https://doi.org/10.1039/d0ra09420j.

(56) Widegren, J. A.; Finke, R. G. A Review of the Problem of Distinguishing True Homogeneous Catalysis from Soluble or Other Metal-Particle Heterogeneous Catalysis under Reducing Conditions. *Journal of Molecular Catalysis A: Chemical*. Elsevier May 1, 2003, pp 317–341. https://doi.org/10.1016/S1381-1169(02)00728-8.

(57) al Amery, N.; Abid, H. R.; Al-Saadi, S.; Wang, S.; Liu, S. Facile Directions for Synthesis, Modification and Activation of MOFs. *Materials Today Chemistry*. Elsevier Ltd September 1, 2020. https://doi.org/10.1016/j.mtchem.2020.100343.

(58) Prestipino, C.; Regli, L.; Vitillo, J. G.; Bonino, F.; Damin, A.; Lamberti, C.; Zecchina, A.; Solari, P. L.; Kongshaug, K. O.; Bordiga, S. Local Structure of Framework Cu(II) in HKUST-1 Metallorganic Framework: Spectroscopic Characterization upon Activation and Interaction with Adsorbates. *Chemistry of Materials* **2006**, *18* (5), 1337–1346. https://doi.org/10.1021/cm052191g.

(59) Alaerts, L.; Séguin, E.; Poelman, H.; Thibault-Starzyk, F.; Jacobs, P. A.; de Vos, D. E. Probing the Lewis Acidity and Catalytic Activity of the Metal-Organic Framework [Cu3(Btc)2] (BTC = Benzene-1,3,5-Tricarboxylate). *Chemistry - A European Journal* **2006**, *12* (28), 7353–7363. https://doi.org/10.1002/chem.200600220.

(60) Nguyen, L. T. L.; Nguyen, T. T.; Nguyen, K. D.; Phan, N. T. S. Metal-Organic Framework MOF-199 as an Efficient Heterogeneous Catalyst for the Aza-Michael Reaction. *Appl Catal A Gen* **2012**, *425–426*, 44–52. https://doi.org/10.1016/j.apcata.2012.02.045.

(61) Wang, Y.; Feng, L.; Pang, J.; Li, J.; Huang, N.; Day, G. S.; Cheng, L.; Drake, H. F.; Wang, Y.; Lollar, C.; Qin, J.; Gu, Z.; Lu, T.; Yuan, S.; Zhou, H. C. Photosensitizer-Anchored 2D MOF Nanosheets as Highly Stable and Accessible Catalysts toward Artemisinin Production. *Advanced Science* **2019**, *6* (11), 2–9. https://doi.org/10.1002/advs.201802059.

(62) Ramos-Fernandez, E. v.; Garcia-Domingos, M.; Juan-Alcañiz, J.; Gascon, J.; Kapteijn, F. MOFs Meet Monoliths: Hierarchical Structuring Metal Organic Framework Catalysts. *Appl Catal A Gen* **2011**, *391* (1–2), 261–267. https://doi.org/10.1016/j.apcata.2010.05.019.

(63) Gangu, K. K.; Jonnalagadda, S. B. A Review on Metal-Organic Frameworks as Congenial Heterogeneous Catalysts for Potential Organic Transformations. *Frontiers in Chemistry*. Frontiers Media S.A. December 17, 2021. https://doi.org/10.3389/fchem.2021.747615.

(64) Thommes, M.; Kaneko, K.; Neimark, A. v.; Olivier, J. P.; Rodriguez-Reinoso, F.; Rouquerol, J.; Sing, K. S. W. Physisorption of Gases, with Special Reference to the Evaluation of Surface Area and Pore Size Distribution (IUPAC Technical Report). *Pure and Applied Chemistry* **2015**, *87* (9–10), 1051–1069. https://doi.org/10.1515/pac-2014-1117.

(65) Eddaoudi, M.; Kim, J.; Rosi, N.; Vodak, D.; Wachter, J.; Keeffe, M. O.; Yaghi, O. M.; Eddaoudi, M.; Kimrn, J.; Rosi, N.; Yaghil, O. M. Systematic Design of Pore Size and Functionality in Isoreticular MOFs and Their Application in Methane Storage Published by : American Association for the Advancement of Science Linked References Are Available on JSTOR for This Article : Systematic Design. **2002**, *295* (5554), 469–472.

(66) Cheng, P.; Kim, M.; Lim, H.; Lin, J.; Torad, N. L.; Zhang, X.; Hossain, M. S. A.; Wu, C. W.; Wang, C.; Na, J.; Yamauchi, Y. A General Approach to Shaped MOF-Containing Aerogels toward Practical Water Treatment Application. *Adv Sustain Syst* **2020**, *4* (8), 1–7. https://doi.org/10.1002/adsu.202000060.

(67) Peterson, G. W.; Au, K.; Tovar, T. M.; Epps, T. H. Multivariate Cubtc Metal-Organic Framework with Enhanced Selectivity, Stability, Compatibility, and Processability.

Chemistry of Materials **2019**, *31* (20), 8459–8465. https://doi.org/10.1021/acs.chemmater.9b02756.

(68) McHugh, L. N.; McPherson, M. J.; McCormick, L. J.; Morris, S. A.; Wheatley, P. S.; Teat, S. J.; McKay, D.; Dawson, D. M.; Sansome, C. E. F.; Ashbrook, S. E.; Stone, C. A.; Smith, M. W.; Morris, R. E. Hydrolytic Stability in Hemilabile Metal–Organic Frameworks. *Nat Chem* **2018**, *10* (11), 1096–1102. https://doi.org/10.1038/s41557-018-0104-x.

(69) Rubin, H. N.; Neufeld, B. H.; Reynolds, M. M. Surface-Anchored Metal-Organic Framework-Cotton Material for Tunable Antibacterial Copper Delivery. *ACS Appl Mater Interfaces* **2018**, *10* (17), 15189–15199. https://doi.org/10.1021/acsami.7b19455.

(70) Rubin, H. N.; Reynolds, M. M. Functionalization of Metal-Organic Frameworks To Achieve Controllable Wettability. *Inorg Chem* **2017**, *56* (9), 5266–5274. https://doi.org/10.1021/acs.inorgchem.7b00373.

(71) Li, B.; Zhang, Y.; Ma, D.; Li, L.; Li, G.; Li, G.; Shi, Z.; Feng, S. A Strategy toward Constructing a Bifunctionalized MOF Catalyst: Post-Synthetic Modification of MOFs on Organic Ligands and Coordinatively Unsaturated Metal Sites. *Chemical Communications* **2012**, *48* (49), 6151–6153. https://doi.org/10.1039/c2cc32384b.

(72) Alegre-Requena, J. v.; Marqués-López, E.; Herrera, R. P.; Díaz, D. D. Metal-Organic Frameworks (MOFs) Bring New Life to Hydrogen-Bonding Organocatalysts in Confined Spaces. *CrystEngComm* **2016**, *18* (22), 3985–3995. https://doi.org/10.1039/c5ce02526e.

(73) McIndoe, J. S.; Vikse, K. L. Assigning the ESI Mass Spectra of Organometallic and Coordination Compounds. *Journal of Mass Spectrometry* **2019**, *54* (5), 466–479. https://doi.org/10.1002/jms.4359.

(74) Schlexer Lamoureux, P.; Winther, K. T.; Garrido Torres, J. A.; Streibel, V.; Zhao, M.; Bajdich, M.; Abild-Pedersen, F.; Bligaard, T. Machine Learning for Computational Heterogeneous Catalysis. *ChemCatChem* **2019**, *11* (16), 3581–3601. https://doi.org/10.1002/cctc.201900595.

(75) Masuda, K.; Ichitsuka, T.; Koumura, N.; Sato, K.; Kobayashi, S. Flow Fine Synthesis with Heterogeneous Catalysts. *Tetrahedron*. 2018. https://doi.org/10.1016/j.tet.2018.02.006.

(76) Davies, I. W.; Matty, L.; Hughes, D. L.; Reider, P. J. Are Heterogeneous Catalysts Precursors to Homogeneous Catalysts? [21]. *Journal of the American Chemical Society*. October 17, 2001, pp 10139–10140. https://doi.org/10.1021/ja016877v.

(77) Dhakshinamoorthy, A.; Alvaro, M.; Garcia, H. Metal-Organic Frameworks as Efficient Heterogeneous Catalysts for the Regioselective Ring Opening of Epoxides. *Chemistry - A European Journal* **2010**, *16* (28), 8530–8536. https://doi.org/10.1002/chem.201000588.

(78) Humphreys, C. J. The Significance of Braggs Law in Electron Diffraction and Microscopy, and Braggs Second Law. *Acta Crystallogr A* **2013**, *69* (1), 45–50. https://doi.org/10.1107/S0108767312047587.

(79) Yang, D.; Gates, B. C. Catalysis by Metal Organic Frameworks: Perspective and Suggestions for Future Research. *ACS Catalysis*. American Chemical Society March 1, 2019, pp 1779–1798. https://doi.org/10.1021/acscatal.8b04515.

(80) Brunauer, S.; Deming, L. S.; Deming, W. E.; Teller, E. On a Theory of the van Der Waals Adsorption of Gases. *J Am Chem Soc* **1940**, *62* (7), 1723–1732. https://doi.org/10.1021/ja01864a025.

(81) Gorren, A. C. F.; Schrammel, A.; Schmidt, K.; Mayer, B. *Decomposition of S-Nitrosoglutathione in the Presence of Copper Ions and Glutathione 1*; 1996; Vol. 330.

(82) Jit Singh, R.; Hogg, N.; Joseph, J.; Kalyanaraman, B. *Mechanism of Nitric Oxide Release from S-Nitrosothiols**; 1996; Vol. 271.

(83) Harding, J. L.; Reynolds, M. M. Combating Medical Device Fouling. *Trends in Biotechnology*. March 2014, pp 140–146. https://doi.org/10.1016/j.tibtech.2013.12.004.

(84) Singh, S. P.; Wishnok, J. S.; Keshive, M.; Deen, W. M.; Tannenbaum, S. R. *The Chemistry of the S-Nitrosoglutathioneglutathione System (Nitric Oxideglutathionyl RadicalsulfenamidetransnitrosationN-Nitrosomorpholine)*; 1996; Vol. 93.

(85) Guerra, D.; Ballard, K.; Truebridge, I.; Vierling, E. S-Nitrosation of Conserved Cysteines Modulates Activity and Stability of S-Nitrosoglutathione Reductase (GSNOR). *Biochemistry* **2016**, *55* (17), 2452–2464. https://doi.org/10.1021/acs.biochem.5b01373.

(86) Que, L. G.; Yang, Z.; Stamler, J. S.; Lugogo, N. L.; Kraft, M. S-Nitrosoglutathione Reductase: An Important Regulator in Human Asthma. *Am J Respir Crit Care Med* **2009**, *180* (3), 226–231. https://doi.org/10.1164/rccm.200901-0158OC.

(87) Broniowska, K. A.; Diers, A. R.; Hogg, N. S-Nitrosoglutathione. *Biochimica et Biophysica Acta - General Subjects*. May 2013, pp 3173–3181. https://doi.org/10.1016/j.bbagen.2013.02.004.

(88) Neufeld, M. J.; Lutzke, A.; Jones, W. M.; Reynolds, M. M. Nitric Oxide Generation from Endogenous Substrates Using Metal-Organic Frameworks: Inclusion within Poly(Vinyl Alcohol) Membranes to Investigate Reactivity and Therapeutic Potential. *ACS Appl Mater Interfaces* **2017**, *9* (41), 35628–35641. https://doi.org/10.1021/acsami.7b11846.

(89) Tuttle, R. R.; Rubin, H. N.; Rithner, C. D.; Finke, R. G.; Reynolds, M. M. Copper Ion vs Copper Metal–Organic Framework Catalyzed NO Release from Bioavailable S-Nitrosoglutathione En Route to Biomedical Applications: Direct 1H NMR Monitoring in Water Allowing Identification of the Distinct, True Reaction Stoichiometries and Thio. *J Inorg Biochem* **2019**, *199* (July), 110760. https://doi.org/10.1016/j.jinorgbio.2019.110760.

(90) Ochoa-Herrera, V.; León, G.; Banihani, Q.; Field, J. A.; Sierra-Alvarez, R. Toxicity of Copper(II) Ions to Microorganisms in Biological Wastewater Treatment Systems. *Science of the Total Environment* **2011**, *412–413*, 380–385. https://doi.org/10.1016/j.scitotenv.2011.09.072.

(91) Zhao, J.; Gao, W.; Yang, Z.; Li, H.; Gao, Z. Nitration of Amyloid-β Peptide (1–42) as a Protective Mechanism for the Amyloid-β Peptide (1–42) against Copper Ion Toxicity. *J Inorg Biochem* **2019**, *190*, 15–23. https://doi.org/10.1016/j.jinorgbio.2018.10.005.

(92) Liu, Y.; Wu, Y.; Guo, X.; Wen, Y.; Yang, H. Rapid and Selective Detection of Trace Cu2+ by Accumulation- Reaction-Based Raman Spectroscopy. *Sens Actuators B Chem* **2019**, *283*, 278–283. https://doi.org/10.1016/j.snb.2018.12.043.

(93) Neufeld, M. J.; Harding, J. L.; Reynolds, M. M. Immobilization of Metal − Organic Framework Copper (II) Benzene- 1 , 3 , 5-Tricarboxylate (CuBTC) onto Cotton Fabric as a Nitric Oxide Release Catalyst. **2015**, No. Ii. https://doi.org/10.1021/acsami.5b08773.

(94) Phan, N. T. S.; Vu, P. H. L.; Nguyen, T. T. Expanding Applications of Copper-Based Metal-Organic Frameworks in Catalysis: Oxidative C-O Coupling by Direct C-H Activation of Ethers over Cu2(BPDC)2(BPY) as an Efficient Heterogeneous Catalyst. *J Catal* **2013**, *306*, 38–46. https://doi.org/10.1016/j.jcat.2013.06.006.

(95) Neufeld, M. J.; Ware, B. R.; Lutzke, A.; Khetani, S. R.; Reynolds, M. M. Water-Stable Metal-Organic Framework/Polymer Composites Compatible with Human Hepatocytes. *ACS Appl Mater Interfaces* **2016**, *8* (30), 19343–19352. https://doi.org/10.1021/acsami.6b05948.

(96) Demessence, A.; D'Alessandro, D. M.; Foo, M. L.; Long, J. R. Strong CO2 Binding in a Water-Stable, Triazolate-Bridged Metal-Organic Framework Functionalized with Ethylenediamine. *J Am Chem Soc* **2009**, *131* (25), 8784–8786. https://doi.org/10.1021/ja903411w.

(97) Tuttle, R. R.; Folkman, S. J.; Rubin, H. N.; Finke, R. G.; Reynolds, M. M. Copper Metal-Organic Framework Surface Catalysis: Catalyst Poisoning, IR Spectroscopic, and Kinetic Evidence Addressing the Nature and Number of the Catalytically Active Sites En Route to Improved Applications. *ACS Appl Mater Interfaces* **2020**, *12* (35), 39043–39055. https://doi.org/10.1021/acsami.0c08961.

(98) Manske, R. H. *THE CHEMISTRY OF QUINOLINES*; 1941. https://doi.org/10.1021/cr60095a006.

(99) Cheng, C.-C.; Yan, S.-J. The Friedlander Synthesis of Quinolines. *Organic Reactions* **2005**, *28*, 37–201. https://doi.org/10.1002/0471264180.or028.02.

(100) Sales, E. M.; Daniel Figueroa-Villar, J. RECENT STUDIES ABOUT SYNTHESIS AND BIOLOGICAL ACTIVITY OF QUINOLONES AND DERIVATIVES: A REVIEW. *José et al. World Journal of Pharmacy and Pharmaceutical Sciences* **2016**, *5*, 253. https://doi.org/10.20959/wjpps20168-7411.

(101) Li, J.; Zheng, T.-C.; Jin, Y.; Xu, J.-G.; Yu, J.-G.; Lv, Y.-W. *Synthesis, Molecular Docking and Biological Evaluation of Quinolone Derivatives as Novel Anticancer Agents*; 2018; Vol. 66.

(102) Ahmed, A.; Daneshtalab, M. Nonclassical Biological Activities of Quinolone Derivatives. *J Pharm Pharmaceut Sci (www.cspsCanada.org)* **2012**, *15* (1), 52–72.

(103) Tabarrini, O.; Cecchetti, V.; Fravolini, A.; Nocentini, G.; Barzi, A.; Sabatini, S.; Miao, H.; Sissi, C. Design and Synthesis of Modified Quinolones as Antitumoral Acridones 1. **1999**. https://doi.org/10.1021/jm980324m.

(104) Kojima, H.; Kaita, K. D. E.; Hawkins, K.; Uhanova, J.; Minuk, G. Y. Use of Fluoroquinolones in Patients with Chronic Hepatitis C Virus-Induced Liver Failure. *Antimicrob Agents Chemother* **2002**, *46* (10), 3280–3282. https://doi.org/10.1128/AAC.46.10.3280-3282.2002.

(105) Fan, Y. L.; Cheng, X. W.; Wu, J. B.; Liu, M.; Zhang, F. Z.; Xu, Z.; Feng, L. S. Antiplasmodial and Antimalarial Activities of Quinolone Derivatives: An Overview. *European Journal of Medicinal Chemistry*. Elsevier Masson SAS February 25, 2018, pp 1–14. https://doi.org/10.1016/j.ejmech.2018.01.039.

(106) Sood, D.; Kumar, N.; Singh, A.; Sakharkar, M. K.; Tomar, V.; Chandra, R. Antibacterial and Pharmacological Evaluation of Fluoroquinolones: A Chemoinformatics Approach. *Genomics Inform* **2018**, *16* (3), 44–51. https://doi.org/10.5808/gi.2018.16.3.44.

(107) Pranger, A. D.; van der Werf, T. S.; Kosterink, J. G. W.; Alffenaar, · J W C. The Role of Fluoroquinolones in the Treatment of Tuberculosis in 2019. **2019**, *79*, 161–171. https://doi.org/10.1007/s40265-018-1043-y.

(108) Pérez-Mayoral, E.; Čejka, J. [Cu3(BTC)2]: A Metal-Organic Framework Catalyst for the Friedländer Reaction. *ChemCatChem* **2011**, *3* (1), 157–159. https://doi.org/10.1002/cctc.201000201.

(109) Abdel-Galil, F. M.; Riad, B. Y.; Sherif, S. M.; Elnagdi, M. H. *ACTIVATED NITRILES IN HETEROCYCLIC SYNTHESIS: A NOVEL SYNTHESIS OF 4-AZOLOYL-2-AMINOQUINOLINES*.

(110) Wei, W. J.; Zhong, Y. J.; Feng, Y. F.; Gao, L.; Tang, H. T.; Pan, Y. M.; Ma, X. L.; Mo, Z. Y. Electrochemically Mediated Direct C(Sp3)−H Sulfonylation of Xanthene Derivatives. *Adv Synth Catal* **2022**, *364* (4), 726–731. https://doi.org/10.1002/adsc.202101289.

(111) Cao, H. T.; Wan, J.; Li, B.; Zhang, H.; Xie, L. H.; Sun, C.; Feng, Q. Y.; Yu, W. J.; Huang, W. Highly Efficient Exciplex-Emission from Spiro[Fluorene-9,9′-Xanthene] Derivatives. *Dyes and Pigments* **2021**, *185*. https://doi.org/10.1016/j.dyepig.2020.108894.

(112) Rahnamafar, R.; Moradi, L.; Khoobi, M. Synthesis of Benzo[b]Xanthene-Triones and Tetrahydrochromeno[2,3-b]Xanthene Tetraones via Three- or Pseudo–Five-Component Reactions Using Fe3O4@SiO2/PEtOx as a Novel, Magnetically Recyclable, and Eco-

Friendly Nanocatalyst. *J Heterocycl Chem* **2020**, *57* (4), 1825–1837. https://doi.org/10.1002/jhet.3911.

(113) Xu, B.; Bi, D.; Hua, Y.; Liu, P.; Cheng, M.; Grätzel, M.; Kloo, L.; Hagfeldt, A.; Sun, L. A Low-Cost Spiro[Fluorene-9,9′-Xanthene]-Based Hole Transport Material for Highly Efficient Solid-State Dye-Sensitized Solar Cells and Perovskite Solar Cells. *Energy Environ Sci* **2016**, *9* (3), 873–877. https://doi.org/10.1039/c6ee00056h.

(114) Lee, D. Y.; Sivakumar, G.; Manju; Misra, R.; Seok, S. il. Carbazole-Based Spiro[Fluorene-9,9′-Xanthene] as an Efficient Hole-Transporting Material for Perovskite Solar Cells. *ACS Appl Mater Interfaces* **2020**, *12* (25), 28246–28252. https://doi.org/10.1021/acsami.0c06318.

(115) Jas, G.; Kirschning, A. Continuous Flow Techniques in Organic Synthesis. *Chemistry - A European Journal* **2003**, *9* (23), 5708–5723. https://doi.org/10.1002/chem.200305212.

(116) Plutschack, M. B.; Pieber, B.; Gilmore, K.; Seeberger, P. H. The Hitchhiker's Guide to Flow Chemistry Â¥. *Chemical Reviews*. 2017. https://doi.org/10.1021/acs.chemrev.7b00183.

(117) Hartman, R. L.; McMullen, J. P.; Jensen, K. F. Deciding Whether to Go with the Flow: Evaluating the Merits of Flow Reactors for Synthesis. *Angewandte Chemie - International Edition* **2011**, *50* (33), 7502–7519. https://doi.org/10.1002/anie.201004637.

(118) Akwi, F. M.; Watts, P. Continuous Flow Chemistry: Where Are We Now? Recent Applications, Challenges and Limitations. *Chemical Communications* **2018**, *54* (99), 13894–13928. https://doi.org/10.1039/c8cc07427e.

(119) Ghafuri, H.; Ganjali, F.; Hanifehnejad, P. Cu.BTC MOF as a Novel and Efficient Catalyst for the Synthesis of 1,8-Dioxo-Octa-Hydro Xanthene. In *Chemistry Proceedings*; MDPI AG, 2021; p 2. https://doi.org/10.3390/ecsoc-24-08359.

CHAPTER 2

DESIGNING AND SYNTHESIZING Cu-BASED METAL-ORGANIC FRAMEWORK NANOSHEETS FOR GREATER CATALYTIC EFFICIENCY

2.1 Overview

Metal-organic framework nanosheets (MOFNs) are promising materials for heterogeneous catalytic systems where active metal sites are positioned on the exterior surface of the particle. The hypothesis that intrapore metal sites are active for catalysis has been disproven for certain systems, and therefore the synthesis of MOF particles with increased external surface area and density of metal active sites is needed. MOFNs provided an increased proportion of metal sites accessible to substrates which experience limited or no diffusion into the MOF pores compared to MOF particles with other morphologies such as octahedra. However, developing synthetic methods to generate a variety of MOFNs remains an experimental challenge, particularly for water-stable materials. The work described in this study uses a three-layer method to synthesize nanosheet particles of a new MOF, CuBDTri (where H_2BDTri = 1,4-1*H*-1,2,3-triazol-5-yl)benzene). Scanning electron microscopy (SEM), powder X-ray diffraction (pXRD), Brunauer-Emmett-Teller (BET) analysis, inductively coupled plasma atomic emission spectroscopy (ICP-AES), and acid digestion with time-of-flight mass-spectrometry (TOF-MS) were used to characterize the newly synthesized CuBDTri nanosheets. Both the synthetic method and linker identity were shown to impact anisotropic growth of MOF particles with nanosheet morphologies. Importantly, this was the first report of using the three-layer method to synthesize MOFNs with Cu-N linkages, meaning the three-layer method is:

I. more broadly applicable than previously known (having only been used previously to synthesize nanosheets with Cu-oxo linkages)

II. (ii) can be used to synthesize water-stable Cu-MOFNs *in situ* (a key result, given MOFs with Cu-oxo linkages usually exhibit poor water stability).

The CuBDTri nanosheets are also more catalytically active on a per-total-Cu-atom basis for a standardized test reaction (nitric oxide (NO) generation from *S*-nitrosoglutathione (GSNO)) than previously studied octahedral particles of the MOF CuBTTri (where H_3BTTri = 1,3,5-tris(1*H*-1,2,3-triazol-5-yl)benzene), supporting the hypothesis that MOFNs are superior to particles with other morphologies for reactions where catalytic activity is limited to particle exterior surfaces (such as the NO generation reaction).

This work was originally published in ACS Applied Nano Materials (Thai, J. E., Tuttle R. R., DeRoo, J., Cuchiaro, J., Reynolds, M. M. Cu-Based Metal-Organic Framework Nanosheets Synthesized via a Three-Layer Bottom-Up Method for the Catalytic Conversion of *S*-Nitrosoglutathione to Nitric Oxide. *ACS Appl. Nano Mater.* **2022**, 5, 1, 486-496. This work has been reprinted (with minor edits to fit the format of this dissertation) with permission from the American Chemical Society (Copyright 2021). Preliminary catalytic experiments were completed by Robert Tuttle. Samples for the ICP-AES were prepared by Jacob DeRoo. BET analysis was completed by Jamie Cuchiaro. Jonathan Thai designed and carried out the synthetic procedure and completed the SEM, pXRD, and acid digestion TOF-MS analyses. Melissa M. Reynolds was the advisor on this project.

2.2 Introduction

The physical and chemical tunability, high surface area, and well-defined structural geometry makes MOFs interesting materials for study as heterogeneous catalysts.[1–14] However, for many catalytic MOF systems, *the pore apertures of MOFs can be too narrow to allow for facile substrate diffusion into the channels* to access intrapore metal sites, limiting catalytic activity to the metal sites on (or extremely close to) the external surfaces of MOF particles.[15–18]

Due to these limitations in metal site accessibility caused by substrate diffusion into the MOF pores, one current area of research focuses on developing strategies to synthesize low-dimensional MOF nanoparticles, often referred to as MOF nanosheets (MOFNs).[19–31] MOF particles with nanosheet morphologies are expected to contain a greater proportion of metal sites on or extremely close to the particle exterior surface versus particles with three-dimensional morphologies such as octahedra, cubes, rods, or spheres (when the particle size is held relatively constant). Hence, nanosheet MOFs are expected to exhibit an increased density of accessible catalytically active sites in systems where catalysis is limited to the exterior surface of MOF particles. Developing methods to synthesize a variety of MOFNs with different metal centers and organic linkers is therefore an important goal for generating new MOFs with improved catalytic performance.[32–35]

MOFN synthesis poses the significant challenge of suppressing particle growth to the nanometer scale and simultaneously promoting anisotropic growth in a two-dimensional plane to limit increase in thickness in a self-assembling particle.[19,36,37] Currently, there are two main strategies for producing MOFNs.[19,32,36–38] First, top-down methods where a layer-structured MOF is synthesized followed by various exfoliation techniques.[19,24,39–41] Top-down methods risk fragmentation, morphological damage, and re-aggregation of nanosheets.[41] Second, bottom-up

methods which directly synthesize MOFNs from metal nodes and organic ligands *in situ*. Bottom-up methods include, but are not limited to, three-layer, interfacial, surfactant-assisted, modulated, and sonication syntheses.[20,31,42–46] The main challenge associated with bottom-up methods is to be able to promote the anisotropic growth of MOF particles in two dimensions while suppressing growth of particles with other morphologies.[19,32] The three-layer method has been effective for synthesizing ultrathin MOFNs with Cu-oxo linkages.[20] However, the applicability of three-layer syntheses to Cu-MOFs with linkages beyond the Cu-oxo family has not been fully explored. Expanding the effectiveness of three-layer syntheses is necessary to synthesize MOFNs with hydrothermal stability for applications in water or biological media as MOFs with Cu-oxo linkages are known to not be stable in water.[47,48]

In 2020, the Reynolds group found and reported that just 1.3 ± 0.4% of the total Cu in the Cu-based MOF $H_3[(Cu_4Cl)_3(BTTri)_8]$ (where H_3BTTri = 1,3,5-tris(1*H*-1,2,3-triazol-5-yl)benzene, CuBTTri) is catalytically active for the generation of nitric oxide (NO) from *S*-nitrosoglutathione (GSNO) in water because the catalysis is completely confined to the exterior surface metal sites of the CuBTTri octahedral particles.[15,17] Hence, we sought to synthesize water-stable Cu-MOFNs with similar properties to CuBTTri to create a material with an increased proportion of Cu sites on particle exterior surfaces relative to CuBTTri octahedra to increase catalytic efficiency. CuBTTri is composed of Cu-N linkages, but no synthesis has previously been described for water-stable MOFNs with Cu-N linkages.

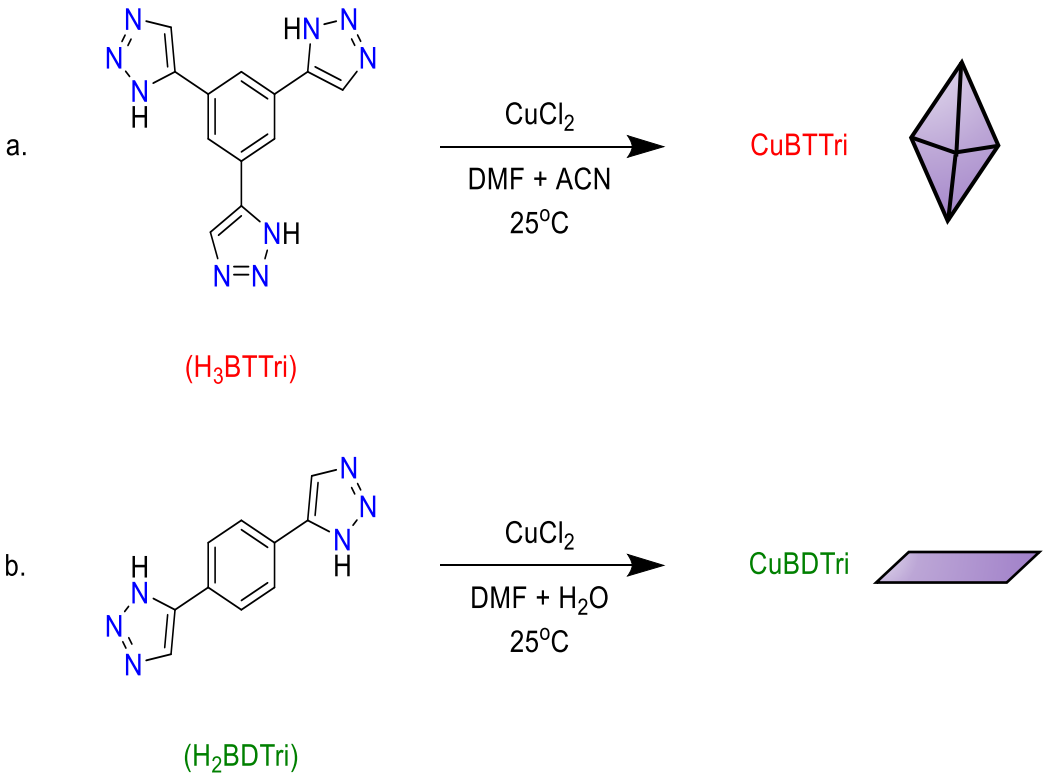

Figure 2.1. (a-b) General synthetic strategies for (a) CuBTTri MOF nanosheets (b) CuBDTri MOF nanosheets.

In this chapter, the use of a three-layer method (Figure 2.2) to synthesize nanosheets of a new MOF with Cu-N linkages, CuBDTri (where H_2BDTri = 1,4-di(1*H*-1,2,3-triazol-5-yl)benzene), (Figure 2.1) is reported. The CuBDTri MOFNs were compared to CuBDTri crystals which were synthesized using traditional solvothermal methods. Results show that the three-layer method is effective for the synthesis of MOFNs with Cu-N linkages and that the morphology of the Cu-MOF particles can be modulated by changing either the linker molecule or the synthetic method. These results yield the first synthesis of water-stable, discrete, Cu-based MOFNs *in situ*. The CuBDTri MOFNs are crystalline, porous, and composed of Cu^{2+} cations connected by H_2BDTri linkers. Preliminary catalytic data confirms that the CuBDTri nanosheets are active for catalytic generation of NO from bioavailable substrate, GSNO, and catalytically outperform CuBTTri octahedra on a per-total-Cu-atom-basis.

Figure 2.2. Layering of the different components used to synthesize the CuBDTri nanosheets. The labels i, ii, and iii correspond to H_2BDTri dissolved in a 2:1 mixture of water/DMF, a solvent spacer comprised of a 1:1 mixture of water/DMF, and then $CuCl_2 \cdot H_2O$ dissolved in a 1:2 mixture of water/DMF, respectively.

2.3 Experimental

2.3.1 Materials

All chemicals and solvents were purchased from commercial vendors and were then used without any further purification. *N*, *N*-dimethylformamide, >99.8%; methanol, >95%; trimethylsilylazide, >97%; acetonitrile, >99%; HCl (1M); and 1,4-diethynylbenzene, >97% were purchased from Fisher Scientific (Waltham, MA). Copper(I) iodide, >99.5%; and sodium nitrite >99.5% were purchased from Sigma-Aldrich (St. Louis, MO). Glutathione >98%; copper(II) chloride dihydrate, >99.5%; was purchased from VWR (Randor, PA). All deionized water used was purified by a Millipore Milli-Q IQ 7000 water purification system to 18.2 MΩ-cm resistivity prior to use.

2.3.2 Synthesis of CuBTTri MOFNs via Three-Layer Bottom-Up Synthesis

CuBTTri MOFNs were synthesized using a bottom-up three-later method adapted from the literature and modified to work with the reagents used in this synthesis.[20] In short, H_3BTTri ligand (0.11 mmol, 1.45 equiv.) was suspended in a mixture of DMF (2 mL) and CH_3CN (1 mL) in a 20 mL glass vial. This mixture was then sonicated for at least 1 hour to ensure all of the ligand was suspended. In a separate glass vial, $CuCl_2$•$2H_2O$ (0.118 mmol, 1 equiv.) was dissolved in a mixture of DMF (1 mL) and CH_3CN (2 mL). Once it was suspended and any large clumps were broken up, the ligand mixture was then added to a glass test tube (14 mm diameter). Over this mixture, a mixture of DMF and CH_3CN (1:1 ratio, 2 mL) was carefully added as to prevent premature mixing of the two layers. Finally, the solution containing the $CuCl_2$•$2H_2O$ was carefully added on top as to prevent it from mixing into the other layers. The synthesis was allowed to proceed at room temperature for 24 hours under static conditions. After the 24 hours, the reactions were centrifuged, the solvent was decanted, and the solid product was washed with copious amounts of DMF (at least 5 x 5 mL) via vacuum filtration. The collected product was then allowed to dry, yielding a purple solid that was analyzed using SEM.

2.3.3 Synthesis of H_2BDTri Ligand

To synthesize the H_2BDTri ligand, copper(I) iodide (1.011 g, 5.308 mmol) and 1,4-diethynylbenzene (5.429 g, 1 equiv.) were combined in a two-necked 500 mL round bottomed flask. DMF (180 mL) and methanol (20 mL) were then used to suspend the solid reagents. A reflux condenser was then set up with the vertical neck while a rubber septum was used to seal the other. The system was then purged with nitrogen. Trimethylsilylazide (12.5 mL, 2.18 equiv.) was then injected through the rubber septum, into the reaction. The dark brown mixture was then stirred at 300 rpm at 100°C for 48 hours. The reaction was then filtered hot through a coarse glass

filter frit, collecting a green solid and a golden-brown liquid. The collected liquid filtrate was then concentrated under reduced pressure until only about 10-20 mL was left. Then, deionized water (250 mL) was then added to the concentrated filtrate, producing a light green precipitate. The second mixture was then filtered through a fine glass filter frit. The collected solid was then washed with deionized water (6 x 250 mL) and diethyl ether (6 x 250 mL). The resulting solid was then dried under reduced pressure overnight, producing a pale green solid. The product was then analyzed via TOF-MS.

2.3.4 Synthesis of CuBDTri MOFs via Solvothermal Synthesis

The synthesized H_2BDTri ligand (5.154 mmol, 1 equiv.) and $CuCl_2 \cdot H_2O$ (12.374 mmol, 2.4 equiv.) were suspended in DMF (220 mL) in a sealable Pyrex bottle. The mixture was sonicated for at least 1 hour to fully disperse and suspend the reagents. The mixture was then placed into a pre-heated oven at 100°C for 72 hours. After 72 hours, the oven was turned off and the product was cooled to room temperature inside the oven naturally. Once cooled to room temperature, the solid product was then collected using a fine glass filter frit. The solid product was then washed with hot (<50°C) DMF (3 x 50 mL) and hot H_2O (3 x 50 mL). The solid was then dried under reduced pressure overnight, producing a pale blue-purple powder. The collected product was then characterized using SEM, pXRD, and BET analysis.

2.3.5 Synthesis of CuBDTri MOFNs via Bottom-Up Three-Layer Synthesis

H_2BDTri ligand (0.157 mmol, 1.33 equiv.) was suspended in a mixture of DMF (1 mL) and deionized water (2 mL) in a 20 mL glass vial. This mixture was then sonicated for at least 1 hour to ensure all of the ligand was suspended. In a separate glass vial, $CuCl_2 \cdot H_2O$ (0.118 mmol, 1 equiv.) was dissolved in a mixture of DMF (2 mL) and deionized water (1 mL). The ligand

mixture was then added to a glass test tube (14 mm diameter). Over this mixture, a mixture of DMF and deionized water (1:1 ratio, 1 mL) was carefully added as to prevent premature mixing of the two layers. Finally, the solution containing the $CuCl_2 \cdot H_2O$ was carefully added on top as to prevent it from mixing into the other layers. The synthesis was allowed to proceed at room temperature for 24 hours under static conditions. After the 24 hours, the reactions were centrifuged, the solvent was decanted, and the solid product was washed with copious amounts of DMF (at least 5 x 5 mL) via vacuum filtration. The collected product was allowed to dry, yielding a pale blue-purple solid. The product was then characterized using SEM, pXRD, BET analysis, elemental analysis, TEM and acid digestion followed by TOF-MS.

2.3.6 Characterization by Scanning Electron Microscopy (SEM) and Energy-Dispersive X-ray Spectroscopy (EDS)

SEM imaging was performed using a JEOL JSM-6500F microscope. An accelerating voltage of 15.0 kV was used to image all of the MOFs and MOFNs. All samples were prepared on a small piece of carbon tape which were then placed under vacuum and coated with 20 nm of gold prior to imaging. At least three representative images were taken with at least three different magnifications for each sample were taken. Energy-dispersive x-ray spectroscopy (EDS) images were obtained using the same instrument using an Oxford X-MAX 80 mm^2 EDS detector attachment. An accelerating voltage of 15.0 kV was used. Samples were prepared by being drop cast using deionized water onto aluminum stubs then placed under vacuum and coated with 20 nm of gold prior to imaging. EDS was used to then scan the image for carbon, copper, nitrogen, and oxygen collecting elemental data for at least 90 seconds. SEM images were imported into ImageJ and CuBDTri MOFN particle thicknesses were then measured manually on particles where the edge could be seen.

2.3.7 Characterization by Transmission Electron Microscopy (TEM)

TEM images were performed using a JEOL 2100 F which was operated at 200 kV under minimum dose operating conditions. The samples were inserted using a standard tilt holder. Images were taken using a Gatan Ultrascan 1000XP 2K x 2K pixel CCD camera at a variety of magnifications. Samples were scanned and pictures were taken manually upon finding the samples as it was found that the CuBDTri MOFNs were extremely beam sensitive and lost crystallinity after 1 second under the beam.

2.3.8 Characterization by Powdered X-Ray Diffraction (pXRD)

A Bruker D8 Discover DaVinci Powder X-ray Diffractometer with Cu Kα radiation (λ = 1.5406 Å was used, operated at 40 kV and 40 mA. A 0.6-mm divergent slit was placed on the primary beam sided and a high-resolution energy dispersive LYNXEYE-XE-T detector was placed on the diffracted beam side during the XRD studies. Samples were seated on a B-doped silicon zero-diffraction plate and held in place with a small amount of vacuum grease. The 2θ was set between 4-50 degrees and scanned at steps of 0.100 degrees.

2.3.9 Determination of CuBDTri Stability in Water

Water stability tests on the CuBDTri MOFNs were completed by conducting both a leaching study and determining the ability of the nanosheets to retain crystallinity after soaking in water. In the leaching study, the MOFNs were washed by suspending approximately 23 mg of CuBDTri MOFN in 10 mL of deionized water. The CuBDTri MOFN particles were vortexed to ensure all of the nanosheets were suspended into the water before it was allowed to sit for 24 hours under static conditions. Over these 24 hours, all of the nanosheets had settled to the bottom. An aliquot (3 mL) was taken from the center of the solution and the remaining solvent was discarded.

The MOFNs were then left to dry under reduced pressure at 110°C. Another 10 mL of deionized water was then added to the dried MOFNs, vortexed, and say for another 24 hours under static conditions. An aliquot (3 mL) was taken from the center of this solution as well. Both aliquots were then sent to Huffman Hazen Laboratories in Golden, CO for ICP-AES to determine the amount of copper present in these samples. The excess water was then removed from the samples and the MOFNs were left to dry under reduced pressure for 24 hours at 110°C. After 24 hours, pXRD of the nanosheets were taken to ensure that the crystallinity of the nanosheets remained intact.

2.3.10 Elemental Analysis of CuBDTri MOFNs

Using the dried MOFNs obtained from the "CuBDTri Stability in an Aqueous Medium" experiments, elemental analysis was conducted by Huffman Hazen in Golden, CO. The MOFNs were analyzed and the amount of carbon, hydrogen, nitrogen, and copper present in the sample was determined.

2.3.11 Acid Digestion and Time of Flight-Mass Spectrometry (TOF-MS) of CuBDTri MOFNs

To determine the presence of the H_2BDTri ligand in the CuBDTri MOFNs, the CuBDTri MOFNs were digested in 6 M HCl for 24 hours. A 1 mL aliquot was then taken from the middle of the solution and analyzed by direct injection using TOF-MS. TOF-MS was performed using an Agilent® 6224 time-of-flight mass spectrometer equipped with a dual ESI source. The detection range for the scans were set for 95-3200 *m/z*.

2.3.12 Synthesis of *S*-Nitrosoglutathione (GSNO)

A solution of glutathione (GSH) (1.53 g, 4.99 mmol) was prepared in Millipore filtered water (8 mL) containing 2 M HCl (2.5 mL). One equivalent of sodium nitrite (0.345 g, 4.99 mmol) was added, and the resulting mixture was stirred for 40 minutes at 5°C. Acetone (10 mL) was added to the resulting red solution and the mixture was stirred for another 10 minutes. The red precipitate was collected via vacuum filtration and washed with ice-cold deionized water (5 x 5 mL). The precipitate was dried under reduced pressure on a high vacuum line for at least 4 hours to afford *S*-nitrosoglutathione (1.4g, 4.12 mmol, 82%) (λmax) (H_2O) 335 nm (ε = 922, 15.9 cm^{-1} mM^{-1}).

2.3.13 Preliminary Catalytic Studies – Conversion of GSNO to NO Catalyzed by CuBDTri MOFNs

GSNO and GSH solutions were separately prepared from Millipore H_2O and solid GSNO or GSH under inert conditions (N_2) in 100 mL round bottomed flasks. CuBDTri was massed into a multi-neck, 50 mL round bottomed flask and dried overnight at 110°C. Once dried, the flask containing the CuBDTri MOFNs was placed under vacuum (<50 mtorr) on a Schlenk line and backfilled with N_2 (g) prior to reaction. GSNO (3 mM, 5 mL) and GSH (1.5 mM, 5 mL) solutions and H_2O (5 mL) were then injected into the reaction flasks containing dry CuBDTri, vigorous bubbling was established in the solution, and an exit needle was added to one neck of the flask. The initial concentration of GSNO in all reactions was 1 mM and the initial concentration of GSH in all reactions was 0.5 mM. Reaction flasks were wrapped in aluminum foil to prevent exposure to light and reactions were allowed to proceed for 20 minutes (the reaction time was chosen specifically to make comparison to rates previously measure at 20 minutes using CuBTTri octahedra as the catalyst). After 20 minutes, the reaction was quenched by removing the exit

needle to stop bubbling and the supernatant was decanted via a syringe. The supernatant was then immediately analyzed via UV-Vis spectroscopy to determine $[GSNO]_{20\ min}$. The value for [GSNO] after 20 minutes was determined by comparing the absorbance of the supernatant at 335 nm to the absorbance of a 1 mM GSNO standard (made fresh prior to use) at 335 nm. The mass of CuBDTri added to the reaction flasks (~1.3 mg) resulted in a ratio of 5 GSNO molecules for every Cu atom in the reaction flask (i.e., 5 GSNO:1 total Cu atoms). No unanticipated safety hazards were encountered over the course of all experiments.

2.3.14 Data Analysis

All data is reported as "average ± standard deviation". All data points that are reported were calculated from n = 3, unless noted otherwise.

2.4 Results and Discussion

2.4.1 Synthesis of Cu-Based Metal-Organic Framework Nanosheets Using Three-Layer Method and Initial Analysis of Particle Morphologies Using Scanning Electron Microscopy and Transmission Electron Microscopy

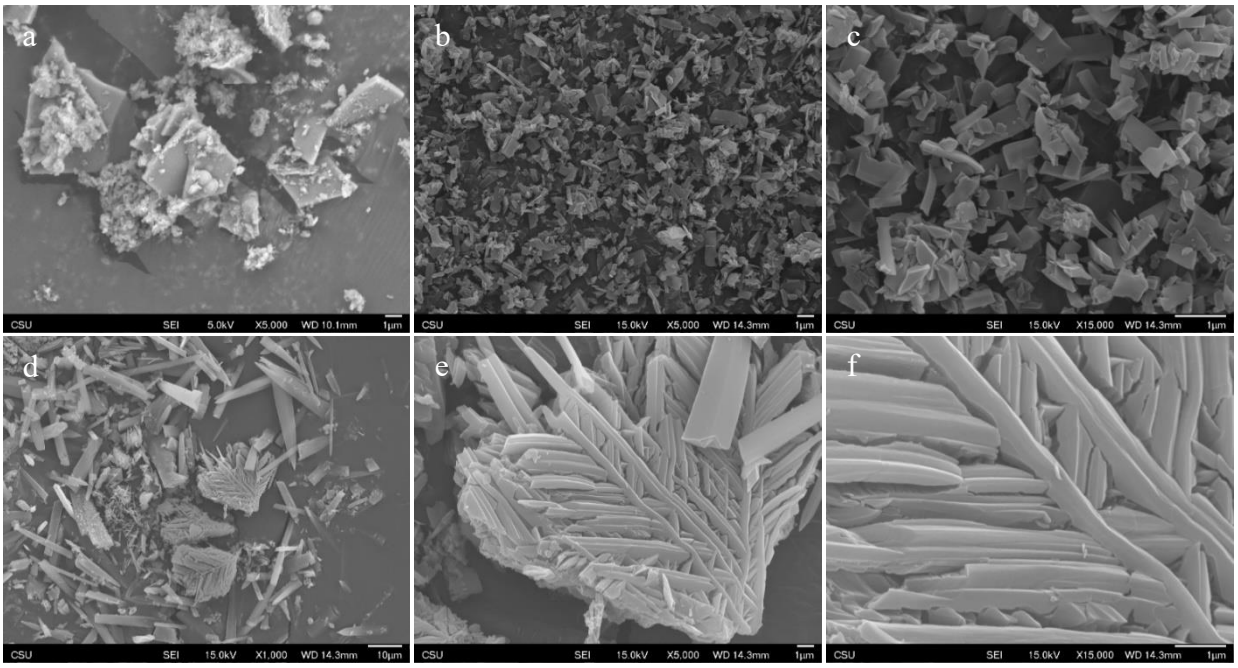

Figure 2.3. (a-f) SEM images of (a) CuBTTri MOF sheets synthesized using the three-layer method at x5000 magnification, (b, c) CuBDTri MOF nanosheets synthesized using the three-layer method at x5000 and x15,000 magnifications, respectively, (d-f) CuBDTri MOF synthesized using a solvothermal method, focusing on one of the "arrowhead" like masses of interwoven MOF at x1000, x5000, and x15,000 magnifications, respectively.

Previous work which had characterized the catalytically active sites in CuBTTri for NO generation from GSNO suggested that our initial efforts should be directed towards using a three-layer method to synthesize CuBTTri MOFNs. However, the yield by mass of CuBTTri nanosheets from the three-layer method was low (<1.0%, <1 mg). SEM images of the solid product from the three-layer synthesis (Figure 2.3a) starting with the CuBTTri precursors Cu^{2+} and H_3BTTri (Figure 2.1) showed that the solid collected was primarily comprised of particles with no discernable regular morphology and few possessed sheet-like morphologies. The few particles that possessed

morphologies that resembled sheets were observed to be large, approximately 2-6 µm across (close to CuBTTri octahedra synthesized using traditional solvothermal methods). Particles of 2-6 µm in length are hypothesized to have a lower proportion of metal sites present on external surfaces than is desirable for catalytic applications limited to particle exterior surfaces. Our own previous work shows that just 1.3 ± 0.4% of the total Cu is catalytically active in 600 ± 400 nm CuBTTri octahedra. The low yield and large particle sizes observed for the resulting solid from the three-layer synthesis using CuBTTri precursors suggested to us that a change in linker identity might be necessary to achieve Cu-MOFN synthesis. It was hypothesized that because H_3BTTri can initiate particle growth in three dimensions, a different linker molecule with fewer coordinating functional groups could better promote anisotropic growth of MOF crystals as nanosheets, illustrated in Figure 2.4. We turned to the H_2BDtri linker, which contains the same triazole moiety as H_3BTTri, but at only two sites on the linker molecule positioned *para* from one another (Figure 2.4).

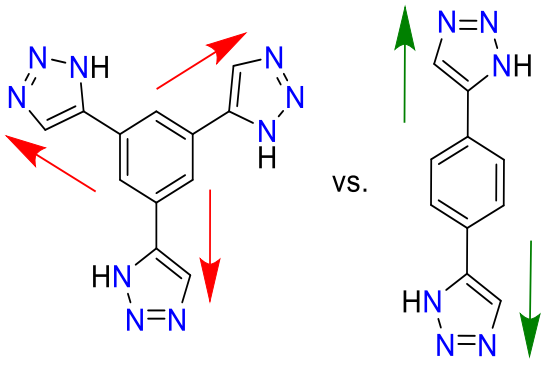

Figure 2.4. H_3BTTri (left) can allow for coordination to copper and growth in multiple directions, making it easier for "three-dimensional" morphologies to form. H_2BDTri (right) can only coordinate to copper in two directions, 180° away from each other, more readily promoting anisotropic growth, hence it is expected that the H_2BDTri can form MOFs with nanosheet morphology more readily.

Using the same three-layer method, the H_2BDTri linker was used to synthesize CuBDTri MOFNs. The yield of the CuBDTri product by mass improved (14 ± 2% (n=9) vs. <1.0%) relative to the synthesis employing CuBTTri precursors. SEM images (Figure 2.3b, 2.3c) show that CuBDTri particles from the three-layer synthesis possess nanosheet morphology, supporting the hypothesis that the H_2BDTri linker limits directional connectivity during particle growth. The CuBDTri nanosheets range from 40-600 nm in length with an average thickness of 40 ± 10 nm (n=101, from five different images), much smaller than the particles synthesized using H_3BTTri in the three-layer synthetic method. It is worthwhile to point out that the average thickness observed of 40 ± 10 nm observed includes the fact that the nanosheets were coated in 20 nm of gold, so thicknesses of the nanosheets may actually be closer to 20 ± 10 nm. This means the thickness of the particles are already observed to be quite low and further decreases in thicknesses are expected to be difficult to achieve synthetically. The large range in length of the CuBDTri nanosheets leaves room for improvement in the domain of controlling the aspect-ratios and size dispersity of the particles. The SEM images in Figure 2.3 and the relative yields of solid product obtained using H_2BDTri versus H_3BTTri show that both the synthetic method and ligand identity impact MOF particle synthesis yield, morphology, and size. While three-layer methods have previously been used to synthesize MOFNs with Cu-O linkages, this is the first report showing the method also works for synthesizing Cu-MOFNs with triaole linkers, and hence, Cu-MOFNs with improved hydrothermal stability (*vide infra*).

Table 2.1. A summary of the data used to compare the products from each of the syntheses. *Particle sizes measured for the CuBTTri synthesized via a three-layer bottom-up method was obtained by measuring the few nanosheets that could be found and do not consider the large particles with no regular morphology.

MOF	Synthetic Method	Linker Used	Dominant Particle Morphology	Particle Sizes (by width)	Yield
CuBTTri	Three-layer	H_3BTTri	No regular morphology	2-8 μm*	<1%
CuBDTri	Three-layer	H_2BDTri	Nanosheets	40-500 nm	13.81±2.21%
CuBDTri	Solvothermal	H_2BDTri	Elongated triangular and rhombical prisms	7 – 140 μm	N/A

The H_2BDTri ligand was also used to synthesize CuBDTri MOF using a traditional solvothermal method to produce crystals with a more three-dimensional morphology to address the question of if the H_2BDTri linker would promote nanosheet formation regardless of synthetic method. Representative Sem images of the CuBDTri particles obtained from a solvothermal synthesis (Figure 2.3d-f) show that the particle morphology is a mixture of very long sheet-like particles, triangular prisms, and rhombical prisms. Many of the particles are over 140 μm in length at 7 μm in width, large compared to the CuBDTri MOFNs synthesized using the three-layer method. Arrowhead-like aggregates composed of interwoven/intersecting sheets were also observed for CuBDTri particles synthesized using the solvothermal method. These results further support that the method of synthesis used (when linker identity is held constant) impacts the size and morphology of the resulting MOF particles. A summary of the observed particle morphology, size, and yield for the different linker and synthetic method pairings reported herein are summarized in Table 2.1.

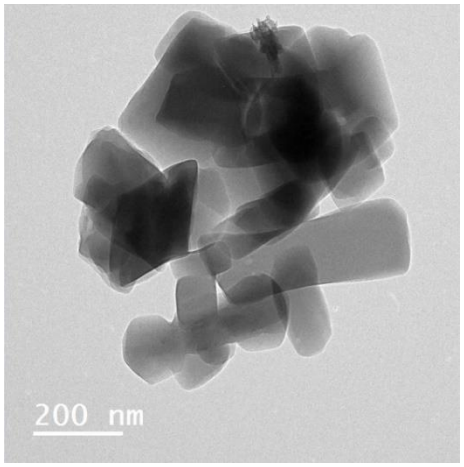

Figure 2.5. TEM image showing overall geometry of some CuBDTri MOF nanosheets.

TEM images of the CuBDTri MOFNs synthesized via the three-layer method were also collected (Figure 2.5). The morphology of the particles of the particles observed by TEM resembles sheets, which can be loosely defined as flat quadrilaterals. This is consistent with what is seen under SEM for the CuBDTri MOFNs. Unfortunately, TEM could not be used to further characterize the CuBDTri MOFNs more extensively via electron diffraction as the samples were observed to be extremely beam sensitive with the crystal lattice breaking down after approximately 1 second of beam exposure. With the equipment that was currently available, this was not an issue that could be avoided. However, it can be seen that several of the nanosheets observed in Figure 2.5 via TEM appear transparent and nanosheets can be observed underneath/above one another. The observed transparency of the nanosheets via TEM is well in line with our measured average thickness of 40 ± 10 nm (potentially 20 ± 10 nm), as particles less than 100 nm thick are known to exhibit transparency in TEM images.

2.4.2 Characterization to Ascertain CuBDTri as a MOF

This is the first report of synthesizing a MOF using the H_2BDTri linker and by extension, the first report of synthesizing a Cu-based MOF using the H_2BDTri linker. Hence, we also

collected data to test whether the solid synthesized using the H_2BDTri linker was indeed a MOF. For this purpose, a MOF is defined as a crystalline, porous material composed of metal cations and organic linkers. To do this, pXRD was used to determine the crystallinity of the material. BET analysis was used to determine the surface area of the material and by extension, the porosity of the material. Elemental analysis, EDS mapping, and acid digestion TOF-MS were then used to confirm the presence of copper and the H_2BDTri linker in the solid.

2.4.2.1 Characterization and Comparison of CuBDTri MOFN and CuBTTri MOF via pXRD

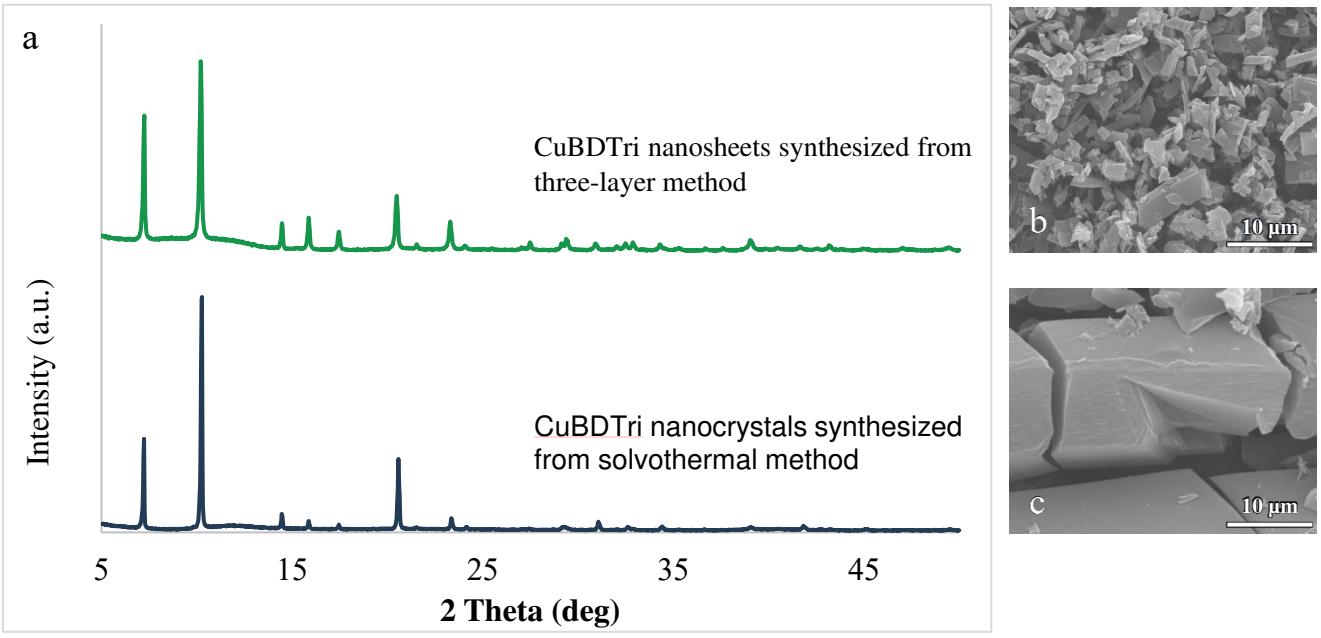

Figure 2.6. (a) Diffraction patterns obtained using pXRD, of CuBDTri MOF nanosheets synthesized using three-layer method (top) and CuBDTri MOF nanocrystals synthesized using traditional solvothermal methods (bottom). The identical positions of the peaks in the diffraction patterns confirm that both materials are crystalline and possess the same bulk crystal structure. (b) SEM image at x15000 magnification of CuBDTri MOF nanosheets synthesized using the three-layer method. (c) SEM image at x15000 magnification of CuBDTri MOF synthesized using solvothermal methods.

X-ray diffraction patterns were collected for the CuBDTri products of the three-layer and the solvothermal methods (Figure 2.6). The diffraction patterns in Figure 2.6a show that the products from both syntheses are crystalline based upon the presence of sharp, distinct peaks. Furthermore, the position of the peaks in the diffraction patterns are identical, indicating that both

materials are isotypic and exhibit similar, if not identical, bulk crystal structures. The relative intensities of the peaks in Figure 2.6a differ between the two CuBDTri samples, which may be caused by the difference in particle morphology. As observed in SEM, CuBDTri nanosheets synthesized using the three-layer method are rectangular and flat, while the CuBDTri synthesized using solvothermal methods grow more readily in three dimensions. Different particle morphologies of materials with the same bulk crystal structure will exhibit slight difference in peak intensity in diffraction patterns because different lattice planes will be present for diffraction patterns because different lattice planes will be present for diffraction events at different ratios. Ultimately, the pXRD data in Figure 2.6a shows that the solid CuBDTri products synthesized using the three-layer method meet the requirement of crystallinity for being defined as a MOF.

2.4.2.2 Characterization of CuBDTri MOFNs as a Porous Material via BET Analysis to Measure Surface Area

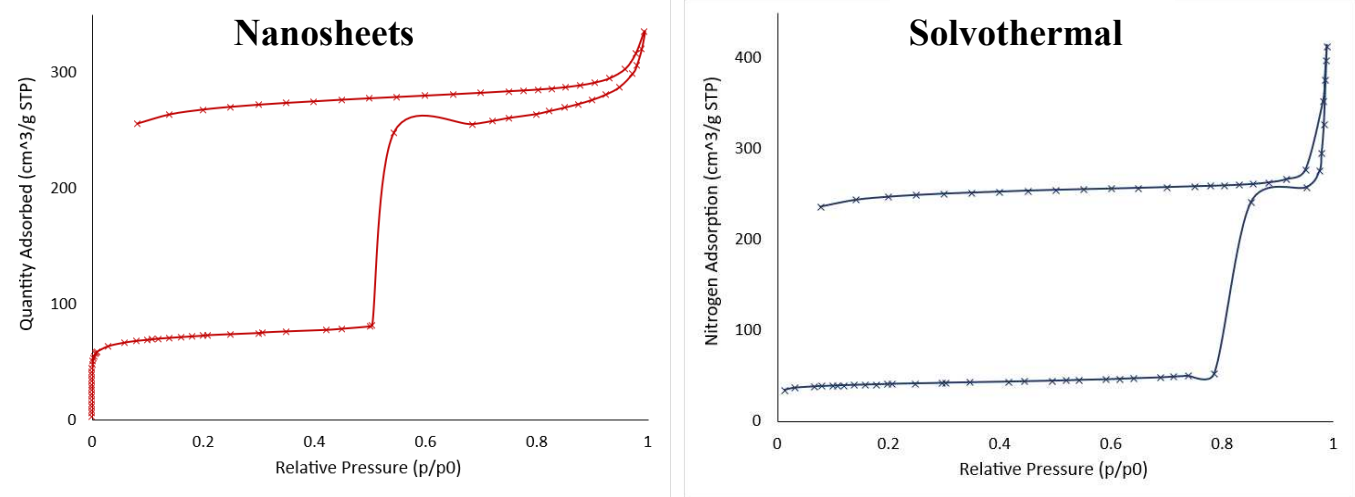

Figure 2.7. Characteristic two-step N_2 adsorption isotherms on CuBDTri MOF nanosheets synthesized using the three-layer method and CuBDTri MOF nanocrystals synthesized using a solvothermal method. Future experiments will be necessary to determine whether this observation results from pressure-induced pore accessibility to the adsorbate, diffusion of adsorbate between layers, or an alternative hypothesis.

The BET surface area of the CuBDTri MOFNs produced from the three-layer method was determined to be 246 ± 30 m^2/g (n = 4), and a typical isotherm is shown in Figure 2.7. The overall shape is congruent with a type II isotherm, having more than one inflection point, and dV / d(p/P^*) is increasing, where po/P^* = 1.[49,50] A sharp increase in adsorption was observed at 0.488 ± 0.05 (p/p°), creating a stepwise affection in the isotherm. The region prior to the sharp increase is congruent with a type I isotherm, and the region following the sharp increase is congruent with a type III isotherm. A serial, two-step process suggests that N_2 adsorption is initially limited to a very near the MOF surface at low pressures, followed by a second, pressure-dependent adsorption process at higher pressures. The second process may be indicative of N_2 penetration into the bulk of the MOF. This two-step profile and corresponding hysteresis were observed over four experiments on three batches of CuBDTri nanosheets over a 9-month period. The approximate increase in adsorbed gas was consistent between experiments. The relative pressures at which the absorbance increase occurred varied, and we attribute the variance to variations in average nanosheet thickness/aspect ratio between synthetic batches. A greater thickness would likely correspond to higher pressure absorbance increase due to increased net activation energy required for conformation change or, alternatively, the increased number of pores the adsorbate diffuses into.

The observation of a stepwise adsorption profile is not well understood. The hysteresis isotherms of porous coordination polymers have been reported and are congruent with the desorption profiles we report here. A two-step isotherm was also reported for another 2D MOF [{$Cu(BF_4)_2$(4,4'-bypyridine)$_2$}$_n$].[51] There is evidence that suggest stepwise isotherms indicate flexibility within the framework, and guest inclusion into the framework only occurs once some threshold pressure is reached.[52] It is believed this indicates that the framework may be in a

"closed" conformation below the threshold pressure and "open" at pressures above the threshold. The large hysteresis observed may indicate slow egress of trapped N_2 from the MOF in the "open" conformation, which would then be further hindered when the framework transitions to the "closed" conformation at lower pressures.

Additional studies are necessary to determine the rigidity and pore dimensions of the CuBDTri MOFNs. Although pore sizes were measured, they were calculated from the overall isotherm. It is likely that pore size would vary if a conformational change was what causes the two-step adsorption that is observed. The observation of capillary condensation may also be related to conformational changes, but additional studies are necessary to evaluate this hypothesis properly and thoroughly. The pore size of the CuBDTri MOFNs synthesized using the three-layer method and the CuBDTri MOFs synthesized using solvothermal methods were measured to be 9.4 ± 1.0 Å (n = 4) and 17.5 Å, respectively. These measurements indicate the presence of micropores, but are inconclusive whether CuBDTri MOFNs are strictly meso-, microporous, or some combination thereof, depending on the confirmational state of the MOFNs.

If the framework is indeed inflexible, then the two-step isotherm may be explained by physisorbed nitrogen aggregating on the exterior surface of the MOF particles and initially blocking the pore aperture. This blockage of the pore aperture would then be overcome by an increase in pressure, and V_{ads} increases as N_2 diffuses into the framework. A similar hypothesis was recently reported for two-step C_2H_2 and CO adsorption isotherms.[53]

Regardless, the BET analysis shows that the material synthesized using the three-layer method with H_2BDTri produced a porous material with a high surface area, meeting that criterion for being identified as a MOF.

2.4.2.3 Using Elemental Analysis, EDS, and Acid Digestion TOF-MS to Confirm the Presence of Cu, C, N, and H in the CuBDTri MOFNs

Table 2.2. Data table showing the mg/L of copper found in each of the samples once the CuBDTri MOF nanosheets synthesized vie the three-layer bottom-up method were soaked for 24 hours. The "Control" is just the deionized water. The "Sample Wash" refers to the first aliquot from the sample after the CuBDTri MOF nanosheets were soaked in water for 24 hours for the first time, showing how much loose copper was removed. The "Sample" refers to the aliquot from the sample after the CuBDTri MOF nanosheets were soaked in water for another 24 hours, showing a reduced amount of copper found in solution.

Sample ID	Amount of Copper Found in Solution (mg/L)
Control	<0.05
Sample Wash 1	0.98
Sample Wash 2	0.59
Sample Wash 3	0.89
Sample 1	0.49
Sample 2	0.32
Sample 3	0.35

Elemental analysis of CuBDTri MOFNs revealed that C, H, N, and Cu are all present in approximately a 30:39:16:2 ratio (Table 2.2). The H_2BDTri ligand itself has a molecular formula of $C_{10}H_8N_6$. Based on ratios from the elemental analysis, we are unable to determine the exact molecular formula of CuBDTri MOFNs. However, elemental analysis confirms that the CuBDTri MOFNs are composed of C, N, H, and Cu, as expected based on the identity of the precursors used. Despite the use of a $CuCl_2$ precursor, no significant amount of Cl was observed to be present in the solid by elemental analysis. With this, the elemental analysis data confirms that Cu and the elements in the H_2BDTri ligand (C, N, and H) are present in the nanosheets.

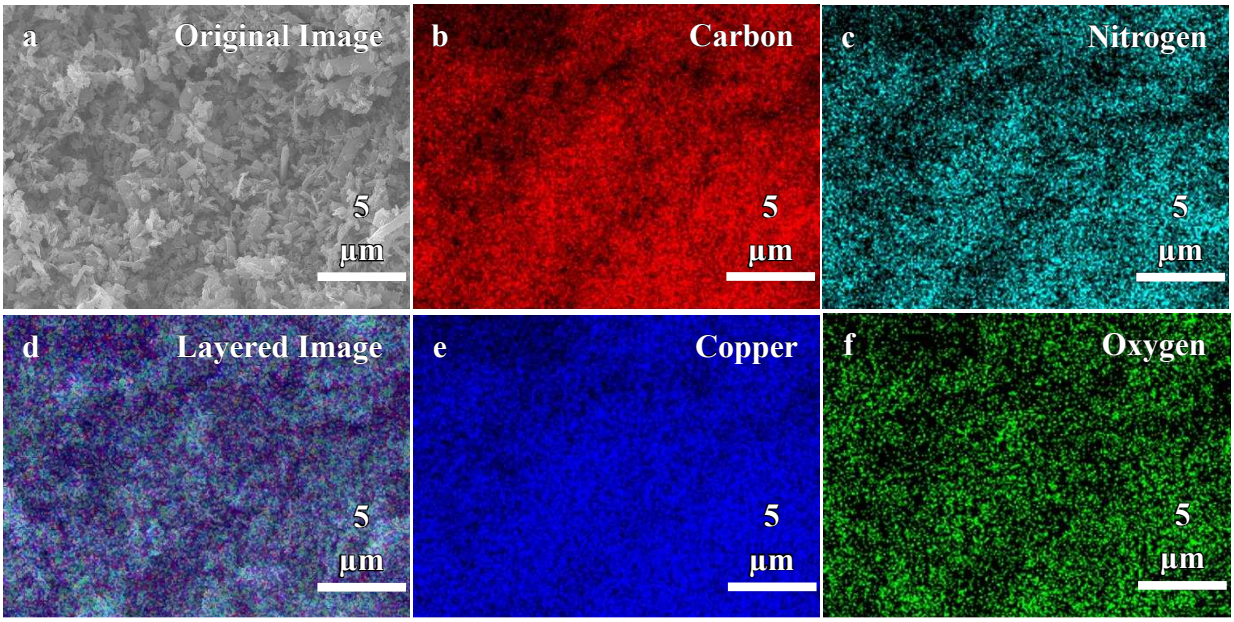

Figure 2.8. (a-f) SEM image and elemental maps obtained form CuBTTri MOF nanosheets synthesized using the three-layer method. Sample was drop cast onto an aluminum pin stub. (a) Original SEM image of CuBTTri MOF sheets synthesized using the three-layer method, (b) EDS map image of carbon, copper, nitrogen, and oxygen all layered on top of each other (c) EDS map of carbon (d) EDS map of copper (e) EDS map of nitrogen (f) EDS map of oxygen.

Using EDS, mapping of the CuBDTri MOFNs showed that C, Cu, N, and O are all present on the MOF (Figure 2.8). Oxygen is likely present due to adventitious water vapor of O_2 gas molecules adsorbed on the CuBDTri particle surfaces as oxygen was confirmed to not be present in the dried CuBDTri via analysis (vide supra). Based on the EDS data, CuBDTri MOFN surfaces contain approximately 50.76% C, 37.62% N, .01% Cu, and 3.62 O by mass. Again, more experiments were required to determine the molecular formula of the CuBDTri MOFNs. With the EDS data, the presence of Cu and the H_2BDTri linker in the CuBDTri MOFN is further supported.

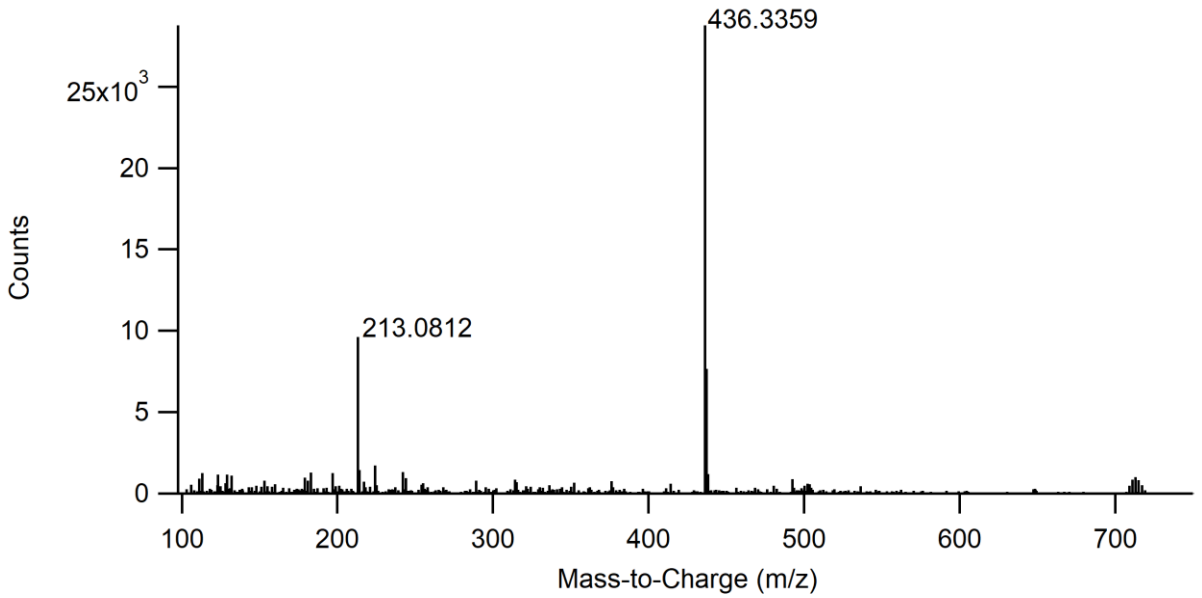

Figure 2.9. Mass spectrum of the 6M HCl solution after MOF nanosheets that were synthesized via the three-layer bottom-up method were digested for 24 hours. The mass of the H_2BDTri is observed at 213 *m/z*, accounting for the proton present from running the sample under position ion mode.

The CuBDTri MOFNs were digested in 6 M HCl and a filter (0.2 μm) was used to remove any undissolved particulates, leaving behind a solution with the dissolved ligand. TOF-MS was used to test this solution for the presence of the H_2BDTri ligand in the CuBDTri MOFNs synthesized via the three-layer method (Figure 2.9). The mass spectrum obtained reveals the presence of a distinct peak at 213 *m/z*, confirming that the MOFN contained the H_2BDTri ligand. There were no other major detectable components inside the solution via TOF-MS.

2.4.3 Determining Stability of CuBDTri MOFNs in Water

Soaking studies of CuBDTri nanosheets support the hydrothermal stability of the material. When 23 mg of CuBDTri MOFNs were soaked in 10 mL of deionized water for 24 hours, an average of 0.39 mg/L of Cu was observed via elemental analysis. Comparing the Cu content of the soaking solution to the Cu content in the CuBDTri MOFN sample reveals that approximately

0.11% of Cu was lost over 24 hours, confirming that the CuBDTri MOFNs do no leach a significant amount of Cu cations under aqueous conditions.

2.4.4 Preliminary Catalytic Performance of CuBDTri MOFNs in Reaction to Convert GSNO to NO

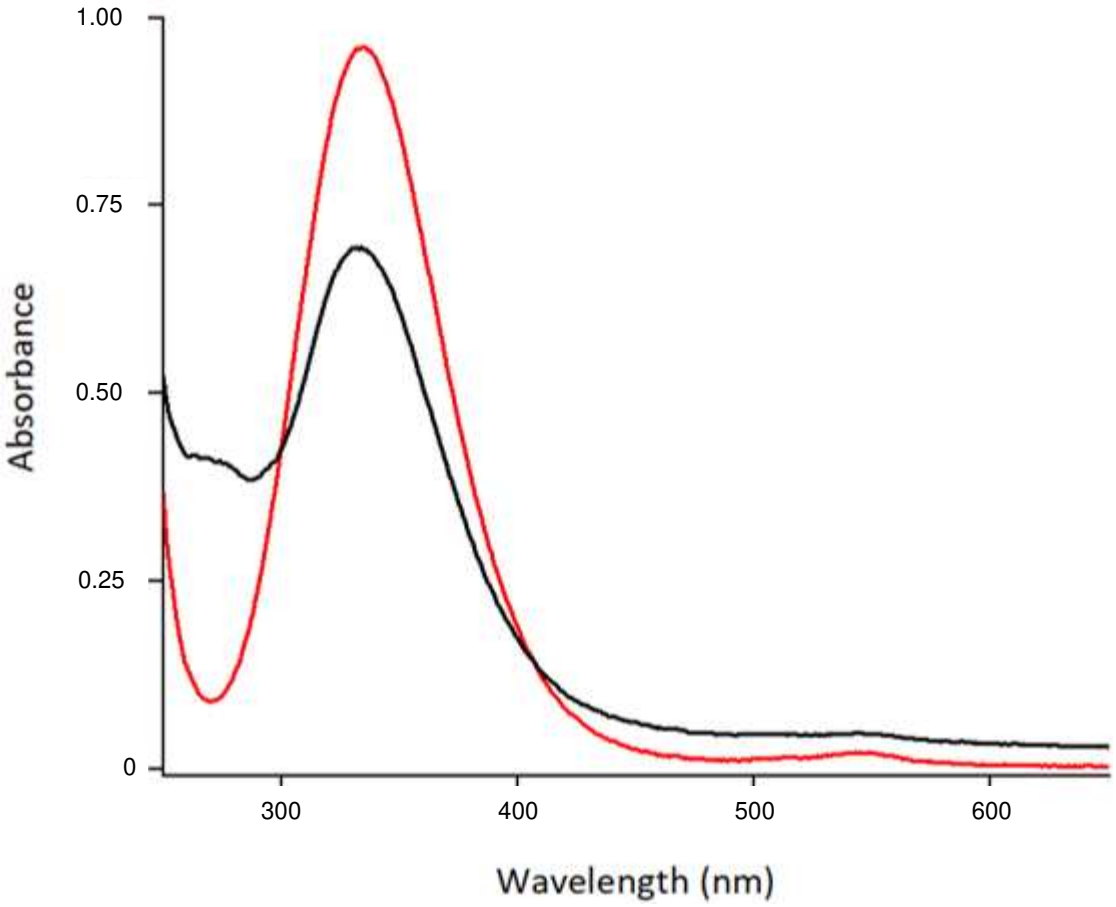

Figure 2.10. Red (top), the UV-VIS spectrum for a 1.0 mM GSNO standard in H_2O (Abs. at 335 nm is 0.961). Black (bottom), the UV-VIS spectrum for the supernatant from a reaction between GSNO and CuBDTri nanosheets (1.3 mg) in H_2O after 20 min (Abs. at 335 nm is 0.692, corresponding to [GSNO] = 0.72 mM). The CuBDTri nanosheets were confirmed to be active for GSNO to NO conversion catalysis.

The CuBDTri MOFNs synthesized via the three-layer method were evaluated with respect to their catalytic performance for GSNO to NO conversion in H_2O. GSNO to NO conversion was chosen as a catalytic test reaction to compare CuBDTri MOFNs and CuBTTri octahedra because the behavior of CuBTTri as a GSNO to NO conversion catalyst has been accurately benchmarked. Previously, our group has reported that the rate of loss of GSNO ([-d-GSNO]/dt]) over 20 minutes of the reaction in H_2O when using CuBTTri as the catalyst was $(2.9 \pm 0.3) \times 10^{-4}$ mM s^{-1} (Table 3).[15,17] Those previous CuBTTri experiments were carried out using a mass of CuBTTri (2.7 mg), resulting in a ratio of two GSNO molecules per-each-Cu-atom basis for catalysis because the CuBDTri nanosheets may contain a greater proportion of metal sites on the exterior surface of the particle in comparison to CuBTTri octahedra.

Table 2.3. The observed rate at 20 minutes for GSNO to NO conversion for CuBTTri and CuBDTri under identical experimental conditions (other than the ratio of GSNO Cu per GSNO, the CuBDTri nanosheets operate at the same rate, within experimental error, as the CuBTTri octahedra.to total Cu). The key finding is that, despite 2.5 fewer equivalents of Cu per GSNO, the CuBDTri MOFN catalyzed the reaction at the same rate, within the experimental error, as CuBTTri octahedra.

MOF Catalyst	**GSNO:Cu_{Total}**	**[-d-GSNO]/dt]$_{20\ minutes}$ mM s^{-1}**
CuBTTri	2:1	$(2.0 \pm 0.3) \times 10^{-4}$
CuBDTri	5:1	$(2.3 \pm 0.4) \times 10^{-4}$

CuBDTri nanosheets were exposed to 1 mM GSNO in H_2O and allowed to react for 20 minutes under identical experimental conditions from previous work using CuBTTri.[15,17] The mass of CuBDTri used (1.3 mg) resulted in a ratio of five GSNO molecules per-each-Cu-atm in the nanosheet sample (based upon the amount of Cu reported via elemental analysis of CuBDTri. At 20 minutes, [-d[GSNO]/dt] was determined using UV-Vis spectroscopy to measure $[GSNO]_{20\ min}$ (Figure 2.10). The spectrum shows that at 20 minutes, (in a representative experiment), the

concentration of GSNO had decreased from 1 to 0.72 mM. Three trials using CuBDTri MOFNs for catalysis resulted in an average $[-d[GSNO]/dt]_{nanosheets} = (2.3 \pm 0.4 \times 10^{-4}$ mM s^{-1} (Table 3). The observed rate for GSNO oxidation catalyzed by CuBDTri nanosheets is equal, within experimental error to the observed rate for CuBTTri octahedra (Table 3). However, experiments using CuBDTri nanosheets were carried out with 2/5 fewer equivalents of total Cu per GSNO than CuBTTri experiments. This means that the CuBDTri MOFNs achieve the same catalytic rate as CuBTTri octahedra with less total Cu, and therefore CuBDTri MOFNs are superior catalysts to CuBTTri octahedra for GSNO to NO conversion in H_2O on a per-total-Cu-atom basis. It is also important to note that in Figure 10, at a wavelength of approximately 280 nm, there is an increase in absorbance between the red (standard 1.0 mM GSNO in H_2O) and black (after 1.0 mM GSNO in H_2O was exposed to the CuBDTri MOFN for 20 minutes). This increase is indicative of the production of GSSG, a byproduct of the conversion of GSNO to NO.

It is important to note that the catalysis results herein are preliminary and mainly serve to confirm that the CuBDTri MOFNs are catalytically active for a biomedically important reaction (NO generation) and is worthy of further study. Future experiments are needed to determine what proportion of any improvement in catalytic performance comes from:

I. That CuBDTri MOFNs exhibit an increased density of active sites versus CuBTTri octahedra due to their relatively greater external surface area, leading to a greater proportion of the Cu to be readily accessible
II. That the Cu surface sites in CuBDTri are kinetically differentiable from, and catalyze GSNO to NO conversion at a greater rate than the Cu surface sites in CuBTTri

However, further experimentation and a more thorough understanding of the crystal structure and catalytic sites of the CuBDTri MOFNs would be required to be able to draw these conclusions.

Analysis of the CuBDTri MOFN pre- and post-catalysis as shown that the MOFN likely retains crystallinity after being used to oxidize GSNO to produce NO based on the retention of a sharp peak a little above 5 2θ. However, other peaks cannot be clearly seen. We hypothesize that this is likely due to the adherence of GSNO, GSSH, NO, or a combination thereof to the MOFN, resulting in the disappearance of these peaks in the diffraction pattern. The fact that the park just above 5 2θ is still present however makes it seem unlikely that the crystal structure itself is being destroyed completely and this further experimentation is required to determine the exact cause of this.

2.5 Conclusions

In summary, CuBDTri MOFNs were successfully synthesized using a three-layer method for the first time. These CuBDTri MOFNs were confirmed to be crystalline, porous, water-stable, and catalytic active for GSNO to NO conversion in H_2O. The CuBDTri MOFNs were observed to be more catalytically active in the conversion of GSNO to NO on a per-total-Cu-atom basis than CuBTTri nanosheets. The successful synthesis of CuBDTri MOFNs using the three-layer method suggests that this method is useful for synthesizing MOFs using a wider variety of linkers than previously established. The H_2BDTri ligand more readily promotes the growth of particles with sheet-like morphologies than the H_3BTTri ligand. This suggests that ligand identity must be considered when trying to control the crystal morphology in MOF particles as illustrated by the differences observed in the morphology of the CuBDTri products synthesized using the three-layer method and the CuBTTri products synthesized using the three-layer method. Furthermore, the synthetic method used has an observable effect as well so must also be considered when trying to

control the crystal morphology in MOF particles which was illustrated by the differences observed in the morphology of the CuBDTri products synthesized using the three-layered method and the CuBDTri products synthesized using solvothermal methods.

The methods used to confirm CuBDTri as a MOF (pXRD, BET, elemental analysis, and acid digestion TOF-MS) should serve as an example of a standard to use that does not currently exist in the MOF literature. With this combination of analytical techniques, it can be confirmed that the material is indeed crystalline, porous, and posses the intended metal center(s) and organic linker(s). With appropriate standardization of confirming materials as MOFs, a level of consistency can be reached in the MOF literature.

CHAPTER 2 - REFERENCES

(1) Liu, J.; Chen, L.; Cui, H.; Zhang, J.; Zhang, L.; Su, C. Y. Applications of Metal-Organic Frameworks in Heterogeneous Supramolecular Catalysis. *Chem Soc Rev* **2014**, *43* (16), 6011–6061. https://doi.org/10.1039/c4cs00094c.

(2) Farha, O. K.; Eryazici, I.; Jeong, N. C.; Hauser, B. G.; Wilmer, C. E.; Sarjeant, A. A.; Snurr, R. Q.; Nguyen, S. T.; Yazaydin, A. Ö.; Hupp, J. T. Metal-Organic Framework Materials with Ultrahigh Surface Areas: Is the Sky the Limit? *J Am Chem Soc* **2012**, *134* (36), 15016–15021. https://doi.org/10.1021/ja3055639.

(3) Nugent, P.; Giannopoulou, E. G.; Burd, S. D.; Elemento, O.; Giannopoulou, E. G.; Forrest, K.; Pham, T.; Ma, S.; Space, B.; Wojtas, L.; Eddaoudi, M.; Zaworotko, M. J. Porous Materials with Optimal Adsorption Thermodynamics and Kinetics for Co2separation. *Nature* **2013**, *495* (7439), 80–84. https://doi.org/10.1038/nature11893.

(4) Cui, Y.; Li, B.; He, H.; Zhou, W.; Chen, B.; Qian, G. Metal-Organic Frameworks as Platforms for Functional Materials. *Acc Chem Res* **2016**, *49* (3), 483–493. https://doi.org/10.1021/acs.accounts.5b00530.

(5) Sabale, S.; Zheng, J.; Vemuri, R. S.; Yu, X.-Y.; Mcgrail, P.; Motkuri, R. K. Synthesis and Catalysis: Open Access Recent Advances in Metal-Organic Frameworks for Heterogeneous Catalyzed Organic Transformations. *Synthesis and Catalysis: Open Access* **2016**, *1* (5), 1–8.

(6) Gascon, J.; Corma, A.; Kapteijn, F.; Llabrés I Xamena, F. X. Metal Organic Framework Catalysis: Quo Vadis? *ACS Catal* **2014**, *4* (2), 361–378. https://doi.org/10.1021/cs400959k.

(7) Masoomi, M. Y.; Morsali, A.; Dhakshinamoorthy, A.; Garcia, H. Mixed-Metal MOFs: Unique Opportunities in Metal–Organic Framework (MOF) Functionality and Design. *Angewandte Chemie - International Edition* **2019**, *58* (43), 15188–15205. https://doi.org/10.1002/anie.201902229.

(8) Kim, B.; Na, J.; Lim, H.; Kim, Y.; Kim, J.; Kim, E. Robust High Thermoelectric Harvesting Under a Self-Humidifying Bilayer of Metal Organic Framework and Hydrogel Layer. *Adv Funct Mater* **2019**, *29* (7). https://doi.org/10.1002/adfm.201807549.

(9) Cheng, P.; Wang, C.; Kaneti, Y. V.; Eguchi, M.; Lin, J.; Yamauchi, Y.; Na, J. Practical MOF Nanoarchitectonics: New Strategies for Enhancing the Processability of MOFs for Practical Applications. *Langmuir* **2020**, *36* (16), 4231–4249. https://doi.org/10.1021/acs.langmuir.0c00236.

(10) Das, A. K.; Vemuri, R. S.; Kutnyakov, I.; McGrail, B. P.; Motkuri, R. K. An Efficient Synthesis Strategy for Metal-Organic Frameworks: Dry-Gel Synthesis of MOF-74 Framework with High Yield and Improved Performance. *Sci Rep* **2016**, *6* (June), 1–7. https://doi.org/10.1038/srep28050.

(11) Tranchemontagne, D. J.; Mendoza-Cortés, J. L.; O'Keeffe, M.; Yaghi, O. M. Secondary Building Units, Nets and Bonding in the Chemistry of Metal-Organic Frameworks. *Chem Soc Rev* **2009**, *38* (5), 1257–1283. https://doi.org/10.1039/b817735j.

(12) Opanasenko, M.; Dhakshinamoorthy, A.; Shamzhy, M.; Nachtigall, P.; Horáček, M.; Garcia, H.; Čejka, J. Comparison of the Catalytic Activity of MOFs and Zeolites in Knoevenagel Condensation. *Catal Sci Technol* **2013**, *3* (2), 500–507. https://doi.org/10.1039/c2cy20586f.

(13) Xuan, W.; Zhu, C.; Liu, Y.; Cui, Y. Mesoporous Metal-Organic Framework Materials. *Chem Soc Rev* **2012**, *41* (5), 1677–1695. https://doi.org/10.1039/c1cs15196g.

(14) Thorarinsdottir, A. E.; Harris, T. D. Metal-Organic Framework Magnets. *Chem Rev* **2020**, *120* (16), 8716–8789. https://doi.org/10.1021/acs.chemrev.9b00666.

(15) Tuttle, R. R.; Rubin, H. N.; Rithner, C. D.; Finke, R. G.; Reynolds, M. M. Copper Ion vs Copper Metal–Organic Framework Catalyzed NO Release from Bioavailable S-Nitrosoglutathione En Route to Biomedical Applications: Direct 1H NMR Monitoring in Water Allowing Identification of the Distinct, True Reaction Stoichiometries and Thio. *J Inorg Biochem* **2019**, *199* (July), 110760. https://doi.org/10.1016/j.jinorgbio.2019.110760.

(16) Cuchiaro, H.; Thai, J.; Schaffner, N.; Tuttle, R. R.; Reynolds, M. Exploring the Parameter Space of P-Cresyl Sulfate Adsorption in Metal-Organic Frameworks. *ACS Appl Mater Interfaces* **2020**, *12* (20), 22572–22580. https://doi.org/10.1021/acsami.0c04203.

(17) Tuttle, R. R.; Folkman, S. J.; Rubin, H. N.; Finke, R. G.; Reynolds, M. M. Copper Metal-Organic Framework Surface Catalysis: Catalyst Poisoning, IR Spectroscopic, and Kinetic Evidence Addressing the Nature and Number of the Catalytically Active Sites En Route to Improved Applications. *ACS Appl Mater Interfaces* **2020**, *12* (35), 39043–39055. https://doi.org/10.1021/acsami.0c08961.

(18) Yang, D.; Gates, B. C. Catalysis by Metal Organic Frameworks: Perspective and Suggestions for Future Research. *ACS Catalysis*. American Chemical Society March 1, 2019, pp 1779–1798. https://doi.org/10.1021/acscatal.8b04515.

(19) Zhao, M.; Huang, Y.; Peng, Y.; Huang, Z.; Ma, Q.; Zhang, H. Two-Dimensional Metal-Organic Framework Nanosheets: Synthesis and Applications. *Chem Soc Rev* **2018**, *47* (16), 6267–6295. https://doi.org/10.1039/c8cs00268a.

(20) Rodenas, T.; Luz, I.; Prieto, G.; Seoane, B.; Miro, H.; Corma, A.; Kapteijn, F.; Llabrés I Xamena, F. X.; Gascon, J. Metal-Organic Framework Nanosheets in Polymer Composite Materials for Gas Separation. *Nat Mater* **2015**, *14* (1), 48–55. https://doi.org/10.1038/nmat4113.

(21) Das, S. K.; Chatterjee, S.; Bhunia, S.; Mondal, A.; Mitra, P.; Kumari, V.; Pradhan, A.; Bhaumik, A. A New Strongly Paramagnetic Cerium-Containing Microporous MOF for CO2 Fixation under Ambient Conditions. *Dalton Transactions* **2017**, *46* (40), 13783–13792. https://doi.org/10.1039/c7dt02040f.

(22) Gumilar, G.; Kaneti, Y. V.; Henzie, J.; Chatterjee, S.; Na, J.; Yuliarto, B.; Nugraha, N.; Patah, A.; Bhaumik, A.; Yamauchi, Y. General Synthesis of Hierarchical Sheet/Plate-like M-BDC (M = Cu, Mn, Ni, and Zr) Metal-Organic Frameworks for Electrochemical Non-Enzymatic Glucose Sensing. *Chem Sci* **2020**, *11* (14), 3644–3655. https://doi.org/10.1039/c9sc05636j.

(23) Tan, C.; Cao, X.; Wu, X. J.; He, Q.; Yang, J.; Zhang, X.; Chen, J.; Zhao, W.; Han, S.; Nam, G. H.; Sindoro, M.; Zhang, H. Recent Advances in Ultrathin Two-Dimensional

Nanomaterials. *Chem Rev* **2017**, *117* (9), 6225–6331. https://doi.org/10.1021/acs.chemrev.6b00558.

(24) Coleman, J. N.; Lotya, M.; Neill, A. O.; Bergin, S. D.; King, P. J.; Khan, U.; Young, K.; Gaucher, A.; De, S.; Smith, R. J.; Shvets, I. v; Arora, S. K.; Stanton, G.; Kim, H.; Lee, K.; Kim, G. T.; Duesberg, G. S.; Hallam, T.; Boland, J. J.; Wang, J. J.; Donegan, J. F.; Grunlan, J. C.; Moriarty, G.; Shmeliov, A.; Nicholls, R. J.; Perkins, J. M.; Grieveson, E. M.; Theuwissen, K.; Mccomb, D. W.; Nellist, P. D.; Nicolosi, V. Two-Dimensional Nanosheets Produced by Liquid Exfoliation of Layered Materials. *Science (1979)* **2011**, *331* (6017), 568–571.

(25) Wang, J.; Li, N.; Xu, Y.; Pang, H. Two-Dimensional MOF and COF Nanosheets: Synthesis and Applications in Electrochemistry. *Chemistry - A European Journal*. Wiley-VCH Verlag May 20, 2020, pp 6402–6422. https://doi.org/10.1002/chem.202000294.

(26) Peng, Y.; Li, Y.; Ban, Y.; Yang, W. Two-Dimensional Metal–Organic Framework Nanosheets for Membrane-Based Gas Separation. *Angewandte Chemie - International Edition* **2017**, *56* (33), 9757–9761. https://doi.org/10.1002/anie.201703959.

(27) Chakraborty, G.; Park, I. H.; Medishetty, R.; Vittal, J. J. Two-Dimensional Metal-Organic Framework Materials: Synthesis, Structures, Properties and Applications. *Chem Rev* **2021**, *121* (7), 3751–3891. https://doi.org/10.1021/acs.chemrev.0c01049.

(28) Zhao, W.; Peng, J.; Wang, W.; Liu, S.; Zhao, Q.; Huang, W. Ultrathin Two-Dimensional Metal-Organic Framework Nanosheets for Functional Electronic Devices. *Coord Chem Rev* **2018**, *377*, 44–63. https://doi.org/10.1016/j.ccr.2018.08.023.

(29) Xu, M.; Yang, S. S.; Gu, Z. Y. Two-Dimensional Metal-Organic Framework Nanosheets: A Rapidly Growing Class of Versatile Nanomaterials for Gas Separation, MALDI-TOF Matrix and Biomimetic Applications. *Chemistry - A European Journal* **2018**, *24* (57), 15131–15142. https://doi.org/10.1002/chem.201800556.

(30) Zhang, H. Ultrathin Two-Dimensional Nanomaterials. *ACS Nano* **2015**, *9* (10), 9451–9469. https://doi.org/10.1021/acsnano.5b05040.

(31) Zhao, M.; Wang, Y.; Ma, Q.; Huang, Y.; Zhang, X.; Ping, J.; Zhang, Z.; Lu, Q.; Yu, Y.; Xu, H.; Zhao, Y.; Zhang, H. Ultrathin 2D Metal-Organic Framework Nanosheets. *Advanced Materials* **2015**, *27* (45), 7372–7378. https://doi.org/10.1002/adma.201503648.

(32) Zhao, M.; Lu, Q.; Ma, Q.; Zhang, H. Two-Dimensional Metal–Organic Framework Nanosheets. *Small Methods* **2017**, *1* (1–2), 1–8. https://doi.org/10.1002/smtd.201600030.

(33) Wang, B.; Jin, J.; Ding, B.; Han, X.; Han, A.; Liu, J. General Approach to Metal-Organic Framework Nanosheets With Controllable Thickness by Using Metal Hydroxides as Precursors. *Front Mater* **2020**, *7* (February), 1–7. https://doi.org/10.3389/fmats.2020.00037.

(34) Bligaard, T.; Bullock, R. M.; Campbell, C. T.; Chen, J. G.; Gates, B. C.; Gorte, R. J.; Jones, C. W.; Jones, W. D.; Kitchin, J. R.; Scott, S. L. Toward Benchmarking in Catalysis Science: Best Practices, Challenges, and Opportunities. *ACS Catalysis*. American Chemical Society April 1, 2016, pp 2590–2602. https://doi.org/10.1021/acscatal.6b00183.

(35) Cancino, P.; Paredes-García, V.; Aguirre, P.; Spodine, E. A Reusable CuII Based Metal-Organic Framework as a Catalyst for the Oxidation of Olefins. *Catal Sci Technol* **2014**, *4* (8), 2599–2607. https://doi.org/10.1039/c4cy00152d.

(36) Liu, W.; Yin, R.; Xu, X.; Zhang, L.; Shi, W.; Cao, X. Structural Engineering of Low-Dimensional Metal–Organic Frameworks: Synthesis, Properties, and Applications. *Advanced Science*. John Wiley and Sons Inc. June 19, 2019. https://doi.org/10.1002/advs.201802373.

(37) Yuan, S.; Feng, L.; Wang, K.; Pang, J.; Bosch, M.; Lollar, C.; Sun, Y.; Qin, J.; Yang, X.; Zhang, P.; Wang, Q.; Zou, L.; Zhang, Y.; Zhang, L.; Fang, Y.; Li, J.; Zhou, H. C. Stable Metal–Organic Frameworks: Design, Synthesis, and Applications. *Advanced Materials* **2018**, *30* (37). https://doi.org/10.1002/adma.201704303.

(38) Lente, G. Comment on "'turning over' Definitions in Catalytic Cycles." *ACS Catalysis*. American Chemical Society March 1, 2013, pp 381–382. https://doi.org/10.1021/cs300846b.

(39) Nicolosi, V.; Chhowalla, M.; Kanatzidis, M. G.; Strano, M. S.; Coleman, J. N. Liquid Exfoliation of Layered Materials. *Science (1979)* **2013**, *340* (6139), 72–75. https://doi.org/10.1126/science.1226419.

(40) Coleman, J. N. Liquid Exfoliation of Defect-Free Graphene. *Acc Chem Res* **2013**, *46* (1), 14–22. https://doi.org/10.1021/ar300009f.

(41) Junggeburth, S. C.; Diehl, L.; Werner, S.; Duppel, V.; Sigle, W.; Lotsch, B. v. Ultrathin 2D Coordination Polymer Nanosheets by Surfactant-Mediated Synthesis. *J Am Chem Soc* **2013**, *135* (16), 6157–6164. https://doi.org/10.1021/ja312567v.

(42) Huang, L.; Zhang, X.; Han, Y.; Wang, Q.; Fang, Y.; Dong, S. In Situ Synthesis of Ultrathin Metal-Organic Framework Nanosheets: A New Method for 2D Metal-Based

Nanoporous Carbon Electrocatalysts. *J Mater Chem A Mater* **2017**, *5* (35), 18610–18617. https://doi.org/10.1039/c7ta05821g.

(43) Jiang, Y.; Liu, H.; Tan, X.; Guo, L.; Zhang, J.; Liu, S.; Guo, Y.; Zhang, J.; Wang, H.; Chu, W. Monoclinic ZIF-8 Nanosheet-Derived 2D Carbon Nanosheets as Sulfur Immobilizer for High-Performance Lithium Sulfur Batteries. *ACS Appl Mater Interfaces* **2017**, *9* (30), 25239–25249. https://doi.org/10.1021/acsami.7b04432.

(44) Dai, R.; Peng, F.; Ji, P.; Lu, K.; Wang, C.; Sun, J.; Lin, W. Electron Crystallography Reveals Atomic Structures of Metal-Organic Nanoplates with M12(M3-O)8(M3-OH)8(M2-OH)6 (M = Zr, Hf) Secondary Building Units. *Inorg Chem* **2017**, *56* (14), 8128–8134. https://doi.org/10.1021/acs.inorgchem.7b00845.

(45) Liang, W.; Li, L.; Hou, J.; Shepherd, N. D.; Bennett, T. D.; D'Alessandro, D. M.; Chen, V. Linking Defects, Hierarchical Porosity Generation and Desalination Performance in Metal-Organic Frameworks. *Chem Sci* **2018**, *9* (14), 3508–3516. https://doi.org/10.1039/c7sc05175a.

(46) Kambe, T.; Sakamoto, R.; Hoshiko, K.; Takada, K.; Miyachi, M.; Ryu, J. H.; Sasaki, S.; Kim, J.; Nakazato, K.; Takata, M.; Nishihara, H. π-Conjugated Nickel Bis(Dithiolene) Complex Nanosheet. *J Am Chem Soc* **2013**, *135* (7), 2462–2465. https://doi.org/10.1021/ja312380b.

(47) Schäfer, P.; Kapteijn, F.; van der Veen, M. A.; Domke, K. F. Understanding the Inhibiting Effect of BTC on CuBTC Growth through Experiment and Modeling. *Cryst Growth Des* **2017**, *17* (11), 5603–5607. https://doi.org/10.1021/acs.cgd.7b00938.

(48) Al-Janabi, N.; Hill, P.; Torrente-Murciano, L.; Garforth, A.; Gorgojo, P.; Siperstein, F.; Fan, X. Mapping the Cu-BTC Metal-Organic Framework (HKUST-1) Stability Envelope in the Presence of Water Vapour for CO2 Adsorption from Flue Gases. *Chemical Engineering Journal* **2015**, *281*, 669–677. https://doi.org/10.1016/j.cej.2015.07.020.

(49) Thommes, M.; Kaneko, K.; Neimark, A. v.; Olivier, J. P.; Rodriguez-Reinoso, F.; Rouquerol, J.; Sing, K. S. W. Physisorption of Gases, with Special Reference to the Evaluation of Surface Area and Pore Size Distribution (IUPAC Technical Report). *Pure and Applied Chemistry* **2015**, *87* (9–10), 1051–1069. https://doi.org/10.1515/pac-2014-1117.

(50) Brunauer, S.; Deming, L. S.; Deming, W. E.; Teller, E. On a Theory of the van Der Waals Adsorption of Gases. *J Am Chem Soc* **1940**, *62* (7), 1723–1732. https://doi.org/10.1021/ja01864a025.

(51) Kondo, A.; Noguchi, H.; Ohnishi, S.; Kajiro, H.; Tohdoh, A.; Hattori, Y.; Xu, W. C.; Tanaka, H.; Kanoh, H.; Kaneko, K. Novel Expansion/Shrinkage Modulation of 2D Layered MOF Triggered by Clathrate Formation with CO2 Molecules. *Nano Lett* **2006**, *6* (11), 2581–2584. https://doi.org/10.1021/nl062032b.

(52) Uemura, K.; Yamasaki, Y.; Komagawa, Y.; Tanaka, K.; Kita, H. Two-Step Adsorption/Desorption on a Jungle-Gym-Type Porous Coordination Polymer. *Angewandte Chemie* **2007**, *119* (35), 6782–6785. https://doi.org/10.1002/ange.200702390.

(53) Wang, H.; Behera, N.; Wang, S.; Dong, Q.; Wang, Z.; Zheng, B.; Wang, D.; Duan, J. Optimized Nanospace of Coordination Isomers with Selenium Sites for Acetylene

Separation. *Inorg Chem Front* **2020**, *7* (17), 3195–3203.

https://doi.org/10.1039/d0qi00518e.

CHAPTER 3

OPTIMIZING THE THREE-LAYER BOTTOM-UP SYNTHETIC METHOD FOR MAKING CuBDTri METAL-ORGANIC FRAMEWORK NANOSHEETS STREAMLINED USING COMPUTATIONAL HEATMAPS

3.1 Overview

As discussed in Chapter 2 of this dissertation, Cu-based metal-organic framework nanosheets (MOFNs) have been synthesized for CuBDTri (where H_2BDTri = 1,4-1*H*-1,2,3-triazol-5-yl)benzene) using a three-layer, bottom-up method. The CuBDTri MOFN offers the advantage over other heterogeneous catalytic MOF systems in that the active sites are positioned on the exterior surface of the particle. Ideally, MOFNs can be synthesized to possess two-dimensional morphology with only 1 or 2 layers of the MOF. This would mean that every Cu-site in the MOFN is located on the exterior surface of the particle and the Cu site would be accessible without needing substrates to diffuse into the pores. By designing and synthesizing catalytic MOFNs in this way, the catalytic efficiency of MOFNs as heterogeneous catalysts would be maximized on a per-atom-basis.

As discussed at the end of Chapter 2 of this dissertation, CuBDTri MOFNs are more catalytically active on a per-total-Cu-atom basis in a standardized test reaction, generating nitric oxide (NO) from *S*-nitrosoglutathione, relative to previously studied octahedral particles of the MOF CuBTTri (where H_3BTTri = 1,3,5-tris(1*H*-1,2,3-triazol-5-yl)benzene. Understanding the factors that lead to the increase in catalytic efficiency is important for moving forward in

redesigning MOFs for higher catalytic efficiency. The improvement in catalytic performance is due to either one or both of the following reasons:

I. The CuBDTri MOFNs exhibit an increased density of active sites versus CuBTTri octahedra due to having a higher external surface area on the particle, resulting in a larger proportion of the Cu-sites being readily accessible.

II. The Cu surface sites on the CuBDTri MOFNs are kinetically different from those seen on CuBTTri octahedra. This difference then causes the Cu sites in the CuBDTri MOFNs to catalyze the GSNO to NO conversion at a faster rate than those in CuBTTri octahedra.

By synthesizing CuBDTri MOFNs with thinner morphological structures, the hypotheses can be tested to determine whether the increased density of active sites on the surface is a factor in the improved catalytic performance. To test this, CuBDTri MOFNs of varying average thicknesses would be used to catalyze a standardized test reaction where nitric oxide (NO) is generated from *S*-nitrosoglutathione. The reaction rates could then be measured and compared to determine whether the increased density of active sites on the exterior surface of the MOFN particle is a factor in the improved catalytic performance that was observed. It would be expected that the thinner the MOFNs are, the higher the catalytic efficiency should be on a per-total-Cu-atom basis, as there would be a greater active site density due to an increased external surface area to volume ratio in thinner MOFN particles.

Determination of the synthetic conditions to be used was done by Jonathan Thai and Jacob DeRoo. The syntheses performed to test each of the set of conditions and SEM imaging were carried out by Jonathan Thai and Andrea Selkow. Development of sample prep, AFM methods,

and obtaining of AFM images were done by Jonathan Thai and Adam Sherrer. Melissa M. Reynolds was the advisor on this project.

3.2 Introduction

Metal-organic frameworks (MOFs) are a class of materials that boast a high level of physical and chemical tunability, high surface area, and well-defined structural geometry, making them an interesting material for study as heterogeneous catalysts.[1–13] However, reports show that for many catalytic systems involving MOFs, the pore apertures of the MOF particle can be too narrow for substrates to diffuse into the channels of the MOF to access intrapore catalytic sites, severely limiting the catalytic activity to the sites on (or extremely close to) to the external surface of the MOF particle.[14–17] This limitation in accessibility to the catalytic sites has motivated scientists interested in using MOFs in heterogeneous catalytic systems to investigate ways to optimize the catalytic efficiency of MOFs.[18–35]

As discussed in Chapter 2, our previous work designed and synthesized the first instance of water-stable Cu-based metal-organic framework nanosheets (MOFNs) that were capable of catalyzing the conversion of *S*-nitrosoglutathione (GSNO) to nitric oxide (NO).[15] It was hypothesized that MOF particles with nanosheet morphologies position a greater proportion of metal sites on, or extremely close to the exterior surface of the particle relative to particles with extended three-dimensional morphologies such as octahedra, cubes, rods, or spheres (when the size of the particle is held relatively constant). Hence, MOFNs are expected to exhibit an increase in catalytically active sites that are significantly more accessible in cases where catalytic activity is limited to the exterior surface of the MOF particle. In an ideal situation, these MOFNs synthesized would only be 1-2 layers thick so that there is no internal volume in the MOF particle and every metal site is positioned on the external surface of the MOF particle. This would result

in every metal site being accessible to any substrate without need for diffusion through the pore apertures of the MOF particles.

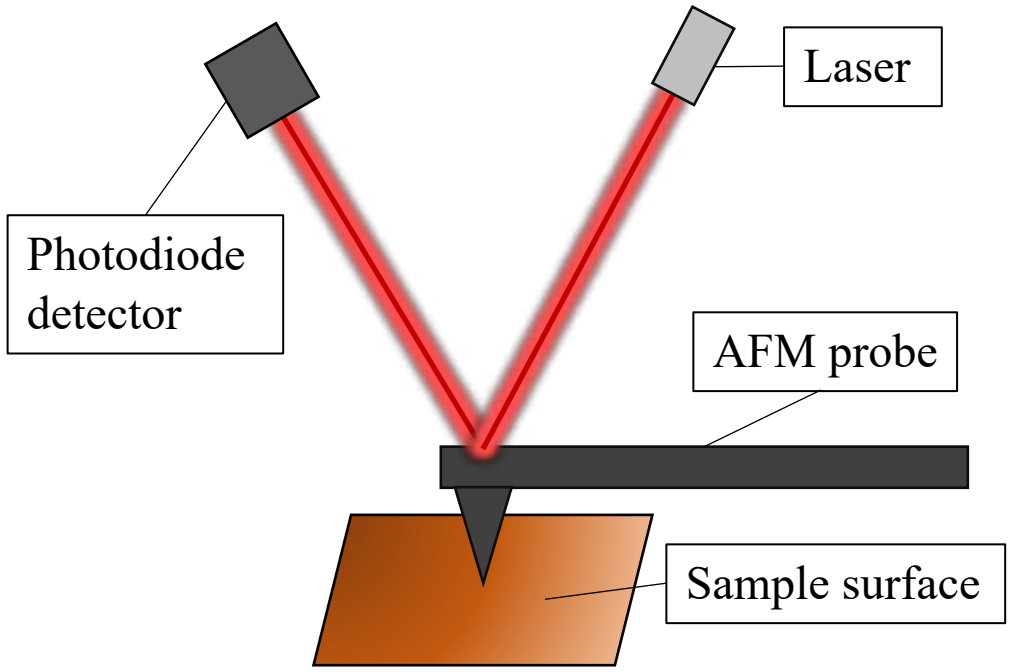

Figure 3.1. General schematic of an atomic force microscope.

To accurately determine the thickness of the MOFNs to ensure we were getting them as thin as possible, atomic force microscopy (AFM) was used as is possess high sensitivity, capable of determining differences down to the nanometer scale. AFM is a high-resolution technique where an AFM probe (akin to a "needle") on the free end of a cantilever scans the surface of a sample in a raster pattern (Figure 3.1).[36] A laser reflecting off of the AFM probe and into a position-sensitive photodiode detector is then used to determine the changes in height of the AFM probe.[36] Collectively, this data generates a three-dimensional topographic map of the surface of a sample.[36]

While there are several instances in the literature where AFM is used to image nanomaterials, including MOFs and MOFNs, there does not appear to be a standard set of methods

and many of the images obtained are of very low quality, showing only parts of the AFM image and/or only one particle in the image.[37–41] For the purpose of this project where averages of several nanosheets would be required, just trying to replicate what others have done in the literature would be insufficient. This meant that to properly image the CuBDTri MOFNs with AFM, the sample preparation and specific conditions used had to be determined experimentally. In doing so, I aimed to create a thorough set of experiments to determine the optimal set of conditions to use to properly image the CuBDTri MOFNs using AFM where several individual particles can be measured in a single AFM image so that statistical significance can be achieved, even with from just a single sample.

In this chapter, we discuss the use of the three-layer method to synthesize CuBDTri MOFNs was run at various conditions so that they could be used to generate a heatmap that can predict the ideal conditions to use to synthesize CuBDTri to create MOFN particles that are as this as possible. The specific conditions that were modified in these reactions were metal to ligand ratio (amount of ligand used), buffer volume, and temperature. A method was developed to accurately measure MOFN particle thickness using AFM so that it could be used to determine the average thickness (and other dimensions) of the CuBDTri MOFNs produced from each set of synthetic conditions. However, since all three conditions were semi-randomly changed through each experiment, no definitive trends can be drawn from these experiments until AFM experiments are completed. Definitive trends based on each of the variables will be determined in future experiments once a heatmap has been generated. Instead, this chapter will draw generalized trends based on observations during the synthetic process, images obtained from scanning electron microscopy (SEM), and preliminary AFM data.

3.3 Experimental

3.3.1 Materials

All chemicals and solvents were purchased from commercial vendors and were then used without any further purification. *N*, *N*-dimethylformamide, >99.8%, methanol, >95%; trimethylsilylazide, >97%; acetonitrile, 99%; and 1,4-diethynylbenzene, >97% were purchased from Fisher Scientific (Waltham, MA). Copper(I) iodide, >99.5% was purchased from Sigma-Aldrich (St. Louis, MO). Muscovite Mica Sheets (9.55 mm diameter) were purchased from Electron Microscopy Sciences (Hatfield, PA). All deionized water used was purified by a Millipore Milli-Q IQ 7000 water purification system to 18.2 MΩ-cm resistivity prior to use.

3.3.2 Synthesis of H_2BDTri Ligand

To synthesize the H_2BDTri ligand, copper(I) iodide (1.011 g, 5.308 mmol) and 1,4-diethynylbenzene (5.429 g, 1 equiv.) were combined in a two-necked 500 mL round bottomed flask. DMF (180 mL) and methanol (20 mL) were then used to suspend the solid reagents. A reflux condenser was then set up with the vertical neck while a rubber septum was used to seal the other. The system was then purged with nitrogen. Trimethylsilylazide (12.5 mL, 2.18 equiv.) was then injected through the rubber septum, into the reaction. The dark brown mixture was then stirred at 300 rpm at 100 °C for 48 hours under nitrogen. The reaction was then filtered hot through a coarse glass filter frit, collecting a green solid and a golden-brown liquid. The collected liquid filtrate was then concentrated under reduced pressure until only about 10-20 mL was left. Then, deionized water (250 mL) was then added to the concentrated filtrate, producing a light green precipitate. The second mixture was then filtered through a fine glass filter frit. The collected solid was then washed with deionized water (6 x 250 mL) and diethyl ether (6 x 250 mL). The

resulting solid was then dried under reduced pressure overnight, producing a pale green solid. The product was then analyzed via TOF-MS in positive mode.

3.3.3 Synthesis of CuBDTri MOFNs via Bottom-Up Three-Layer Synthesis

In this experiment, CuBDTri MOFNs were synthesized using a various combination of conditions (Table 3.1) that were determined semi-randomly to be able to provide the necessary information to create a heatmap that could then use the data to predict the ideal conditions to be used for CuBDTri MOFN synthesis, producing the thinnest nanosheets possible with the three-layer method. Variables that were changed are marked (a-c) throughout this procedure to correlate with that variable in Table 1. H_2BDTri ligand (a) was suspended in a mixture of DMF (1 mL) and deionized water (2 mL) in a 20 mL glass vial. The amount of H_2BDTri ligand used was determined by taking the metal to ligand ratio (a) and multiplying it by the equiv. of $CuCl_2 \cdot H_2O$ used. This mixture was then sonicated for at least 1 hour to ensure all of the ligand was suspended. In a separate glass vial, $CuCl_2 \cdot H_2O$ (0.118 mmol) was dissolved in a mixture of DMF (2 mL) and deionized water (1 mL). The ligand mixture was then added to a glass test tube (14 mm diameter). Over this mixture, a mixture of DMF and deionized water (1:1 ratio, b) was carefully added as to prevent premature mixing of the two layers. Finally, the solution containing the $CuCl_2 \cdot H_2O$ was carefully added on top as to prevent it from mixing into the other layers. The synthesis was allowed to proceed under static conditions at various temperatures (c). After 24 hours, the reactions were centrifuged, the solvent was decanted, and the solid product was washed with copious amounts of DMF (at least 5 x 5 mL) via vacuum filtration. The collected product was allowed to dry, yielding a pale blue-purple solid. The product was then characterized using SEM, pXRD and AFM.

Table 3.1. The set of experimental conditions that were determined to be used to perform the three-layer synthesis of CuBDTri.

Experiment	a. Metal to Ligand ratio	b. Buffer Volume (mL)	c. Temperature (°C)
1	0.8	1	15
2	2	1.5	15
3	1.2	3	15
4	1.2	2	20
5	2.4	2.5	20
6	0.8	3	20
7	1.2	1	25
8	2.4	1.5	25
9	0.8	2	25
10	2.4	1	30
11	1.6	2	30
12	2	3	30
13	2	1	35
14	0.8	1.5	35
15	1.6	2.5	35

3.3.4 Characterization by Scanning Electron Microscopy (SEM)

SEM imaging was performed using a JEOL JSM-6500F microscope. An accelerating voltage of 15.0 kV was used to image all of the MOFNs synthesized. All samples were prepared on a small piece of carbon tape which were then placed under vacuum and coated with 20 nm of gold prior to imaging. Images were taken from at least three randomly picked areas within the sample with at least three different magnifications for each, and a representative image is then provided.

3.3.5 Characterization by Powder X-ray Diffraction (pXRD)

A Bruker D8 Discover DaVinci Powder X-ray Diffractometer with Cu Kα radiation (λ = 1.5406 Å was used, operated at 40 kV and 40 mA. A 0.6-mm divergent slit was placed on the primary beam sided and a high-resolution energy dispersive LYNXEYE-XE-T detector was placed on the diffracted beam side during the XRD studies. Samples were seated on a B-doped silicon zero-diffraction plate and held in place with a small amount of vacuum grease. The 2θ was set between 4-50 degrees and scanned at steps of 0.100 degrees.

3.3.6 Characterization by Atomic Force Microscopy (AFM)

AFM was performed using a Bruker Bioscope Resolve. All images and force curves were collected using SCANASYST Air tips (Bruker). Samples of the CuBDTri MOFNs were suspended in deionized water, making specific mass of MOFN to deionized water ratios before they were drop cast onto freshly cleaved mica sheets that were mounted onto glass slides. The AFM line scan rate was 0.996 Hz and the peak force tapping frequency was set to 2 kHz. The peak force set point was set to 999 pN.

3.3.7 Data Analysis

All data is reported as "average ± standard deviation". All data points that are reported were calculated from n = 3, unless noted otherwise.

3.4 Results and Discussion

3.4.1 Determining the Synthetic Conditions for CuBDTri MOFNs to Optimize

Previous work had indicated that the conditions used to synthesize CuBDTri were unlikely to have been 1 or 2 layers of MOF, indicating that optimization would be possible. Ideally, CuBDTri MOFNs would be synthesized in a way so that every Cu-site would be positioned on the exterior surface of the particle so that they would all be easily accessible regardless of whether or not the substrates could easily diffuse through the pores of the MOF. This would allow for the CuBDTri to be as efficient as possible for use as a heterogeneous catalyst. Based on the three-layer method being used, the potential variables to be considered would be:

I. Time – how long will the reaction be run for
II. Metal to ligand ratio – how much of the ligand (H_2BDTri) is being used relative to metal ($CuCl_2 \cdot H_2O$). In this case, the amount of metal used was always held constant and the amount of ligand was modified relative to it.
III. Buffer volume – how much of the 1:1 DMF and deionized water buffer layer was going to be put in between the layer containing the metal and the ligand.
IV. Temperature – at what temperature the reaction was left to proceed at under static conditions.

Upper and lower boundaries were then chosen based on feasibility (based on what could be executed) for each of these variables (detailed in Table 1) and then semi-randomly chosen for

each experiment so that a heat map could be generated once the thicknesses of the MOFN particles produced from each synthesis is determined using AFM. After some preliminary experiments however, the conditions were modified based on the results obtained and feasibility of the experiments. These modified conditions are provided in Table 2. In Figures 3.2 and 3.3, SEM images from each set of conditions (as described in Table 2) are provided. However, since multiple conditions were changed between each of the syntheses, no definitive trends can be determined without the heat map. Furthermore, the lack of AFM data for each of these syntheses means that we do not currently have accurate enough measurements to determine exact changes and can only generalize trends that can be seen via SEM.

3.4.1.1 SEM Images from Each of the Three-Layer Syntheses

The three-layer method was used to synthesize CuBDTri MOFNs using different metal to ligand ratios, buffer volumes, and temperatures (Table 3.2). After they were rinsed with DMF and dried under vacuum, SEM images of the solid products were obtained. SEM images of the CuBDTri MOFNs are provided at x5000 magnification (Figure 3.2) to show a general overview of the material and then at x15,000 magnification (Figure 3.3) of a different area of the sample to show consistency between multiple instances of the synthesis and to show greater detail of the MOFN particles.

Table 3.2. Actual synthetic conditions used for each of the syntheses. Due to restrictions on being able to maintain a specific temperature while the reactions were being run, temperature points had to be modified to what could be accomplished experimentally.

Associated SEM image	Metal to Ligand ratio	Buffer Volume (mL)	Temperature (°C)
a	0.8	1	11
b	2	1.5	11
c	1.2	3	11
d	1.2	2	25
e	2.4	2.5	25
f	0.8	3	25
g	1.2	1	25
h	2.4	1.5	25
i	0.8	2	25
j	2.4	1	31.2
k	1.6	2	31.2
l	2	3	31.2
m	2	1	35
n	0.8	1.5	35
o	1.6	2.5	35

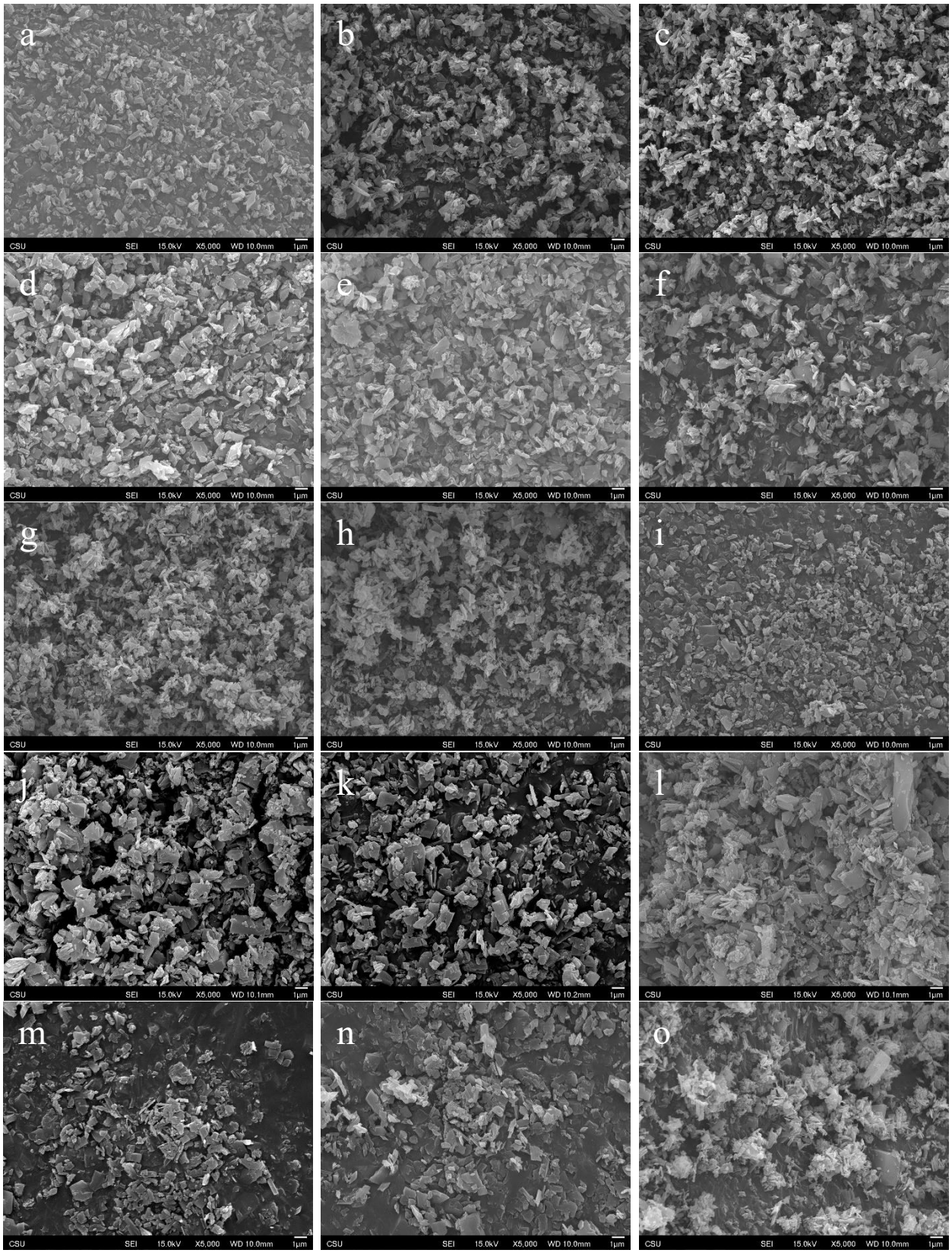

Figure 3.2. Representative SEM images at x5000 magnification of the CuBDTri MOFNs produced from the synthetic conditions as detailed in Table 3.2.

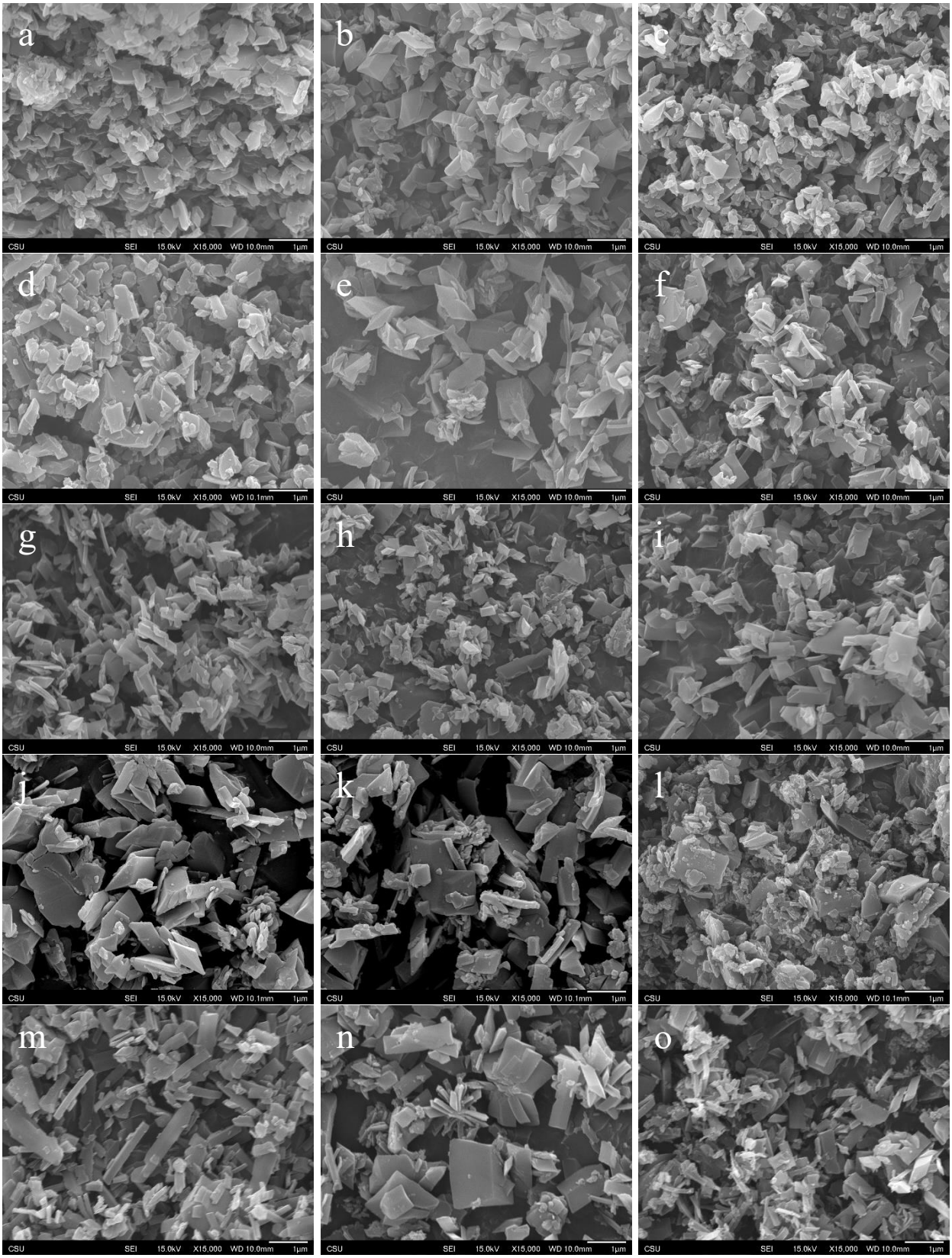

Figure 3.3. Representative SEM images at x15,000 magnification of the CuBDTri MOFNs produced from the synthetic conditions as detailed in Table 3.2.

3.4.2 Towards the Understanding of the Formation of the CuBDTri MOF Nanosheets Based on the Synthetic Conditions Used

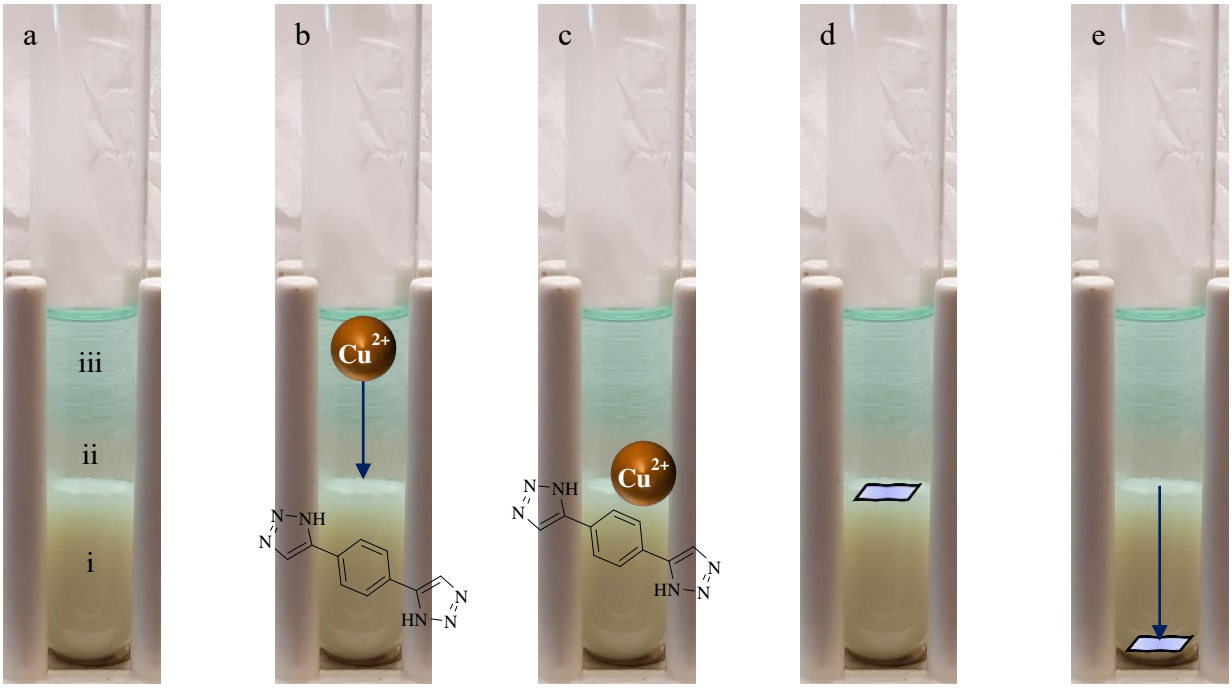

Figure 3.4. (a) The layering of the different components used to synthesize the CuBDTri nanosheets. The labels i, ii, and iii correspond to H_2BDTri dissolved in a 2:1 mixture of water/DMF, a solvent spacer comprised of a 1:1 mixture of water/DMF, and then $CuCl_2 \cdot H_2O$ dissolved in a 1:2 mixture of water/DMF, respectively. (b-f) the process at which the synthesis takes place through the layers. (b) Copper ions from the top layer diffuse down through the solvent spacer. (c) The copper ion contacts the ligand layer (this can be seen with the slight blue tinge lying right on top of the ligand layer). (d) The ligand and copper ion come together to form a nanosheet at this interface. (e) The ligand eventually sinks to the bottom of the test tube, exposing more of the interface to allow the reaction to keep going.

Based on the hypothesized process of formation of the nanosheets (Figure 3.4) synthesized using the three-layer method, predictions can be made on how each of the variables will affect the size of the CuBDTri MOFNs. The hypothesized process of nanosheet formation is as follows:

I. From bottom to top, the reagents are layered with the ligand, buffer, and metal.

II. Copper ions from $CuCl_2 \cdot H_2O$ diffuse downwards through the buffer layer

a. It can be seen in Figure 3.4 that the top of the ligand layer is slightly blue. This is indicative that the Cu does diffuse through this middle layer and then stops on top of the ligand layer.

III. Copper ions then react with the H_2BDTri ligand at this interface, forming the MOFN particles

IV. The formed MOFN particles then sink, exposing more of the interface to allow the reaction to keep progressing.

If this hypothesized formation of CuBDTri MOFNs is true, it would be consistent with the fact that shorter amounts of time may just not allow enough time for enough particles to be formed and longer amounts of time would not result in a higher yield or larger particles. Since the preliminary experiments showed that varying time had little to no effect on the thickness or yield of the MOFNs, it was removed as a consideration.

3.4.1.1 Time

Originally, the length of reaction time was going to be a variable that was tested, but based on the results, this was removed. Reactions were allowed to run at time points of 6, 12, 24, 48, and 72 hours. The original method as described in the literature to synthesize MOFNs was completed in 24 hours.[42] Shorter time points were tested as it was hypothesized that they would result in thinner nanosheets but would potentially produce lower yields. Longer time points were tested as it was hypothesized that they would generate higher yields but would potentially produce thicker nanosheets.

It was expected that shorter time periods (6 and 12 hours) would result in smaller and thinner MOFN particles relative to the 24-hour time point. However, particles were either too

small or not fully formed at the 6- and 12-hour time points to be collected, resulting in a yield too low to allow for analysis. The 48- and 72-hour time points did produce products but there were no noticeable differences in yield or particle sizes based on SEMs obtained. These preliminary results lead me to hypothesize that the 24-hour time point is ideal for the three-layer synthesis of CuBDTri and was then removed as a tested variable in the experiments.

3.4.1.2 Metal to Ligand Ratio

By varying the concentration of the ligand when synthesizing CuBDTri MOFNs, it was hypothesized that lower concentrations of the ligand would result in smaller/thinner MOFN particles. Specifically, this is because by lowering the concentration of the ligand in the bottom layer, there should theoretically be less ligand available at the interface to react with the metal ions that had diffused from the top layer. This should result in a lower rate of formation of the CuBDTri MOFNs, which I hypothesized should produce thinner MOFN particles. Hence, in each of these experiments, the amount of $CuCl_2 \cdot H_2O$ was held constant while the amount of H_2BDtri ligand was changed in the experiments. Relative to $CuCl_2 \cdot H_2O$, the mols of H_2BDTri ligand used were 0.8, 1.6, 2, and 2.4. These values were chosen so that the effects of both increasing and decreasing the concentration of the H_2BDTri ligand could be observed and by accounted for by the heatmap. However, preliminary observations based on the SEM images does not show and obvious trends in particle size and thickness based on the changes made to the metal to ligand ratio. Hence, the completion of the AFM experiments and heatmap will be required to draw any meaningful conclusions on how the metal to ligand ratio affects particle size and thickness.

3.4.1.3 Buffer Volume

By using different volumes of 1:1 DMF to water buffer solution used to separate the two layers containing the $CuCl_2 \cdot H_2O$ and the H_2BDTri ligand, it was hypothesized that a larger buffer volume would result in smaller/thinner MOFN particles. This is based on the idea that a larger buffer volume being used would create a longer path of diffusion between the two layers, resulting in the particles forming more slowly, thus likely to be smaller/thinner. This should functionally reduce the concentrations of the reactants reaching the reaction interface at a given time. Reactions were run using 1:1 DMF to water buffer volumes of 1, 1.5, 2, 2.5, and 3 mL. Preliminary observations made from the SEM images obtained do not show any obvious trends in particle thickness or size based on the changes made to the buffer volume and thus the completion of the AFM experiments and heat map must be completed before any conclusions can be made.

As a side note, it was observed that larger 1:1 DMF to water buffer volumes used would make layering on top of this layer more easily and less likely to break the layers. While this doesn't necessarily have a direct effect the thickness of nanosheets produced, it does suggest that using a larger buffer volume makes the layering process easier.

3.4.1.4 Temperature

By synthesizing CuBDTri MOFNs using the three-layer bottom-up method at different temperatures, it was hypothesized that running the reaction at lower temperatures would result in smaller/thinner particles. This is due to the idea that at lower temperatures, the formation of the CuBDTri MOFN particles would be slower. It should also be noted that temperature will have a direct impact on the rate of diffusion both by increasing the thermal energy of the reactants and potentially also reducing viscosity of the solvents at higher temperatures. To test this, reactions

were set to run at approximately 15, 20, 25, 30, and 35 °C. However, due to limitations in being able to maintain certain temperatures consistently over 24-hour periods, some of these temperatures had to be adjusted to fit what could be achieved experimentally, resulting in the reactions being run at 11, 25, 31.2, and 35 °C instead.

It is important to note that in the original design of the experiment, reactions were planned to be carried out at 5, 15, 25, 35, and 45 °C. However, when run at 5 °C no solid particles were collected. This was likely due to the yield being too low and/or the particles that were formed being too small so that they could not be collected. This led to the reasoning that when the synthesis of CuBDTri MOFNs using the three-layer method was performed at too low of a temperature, the formation of the MOFNs would be too slow and the layers could diffuse into each other before the reaction could properly be run to completion.

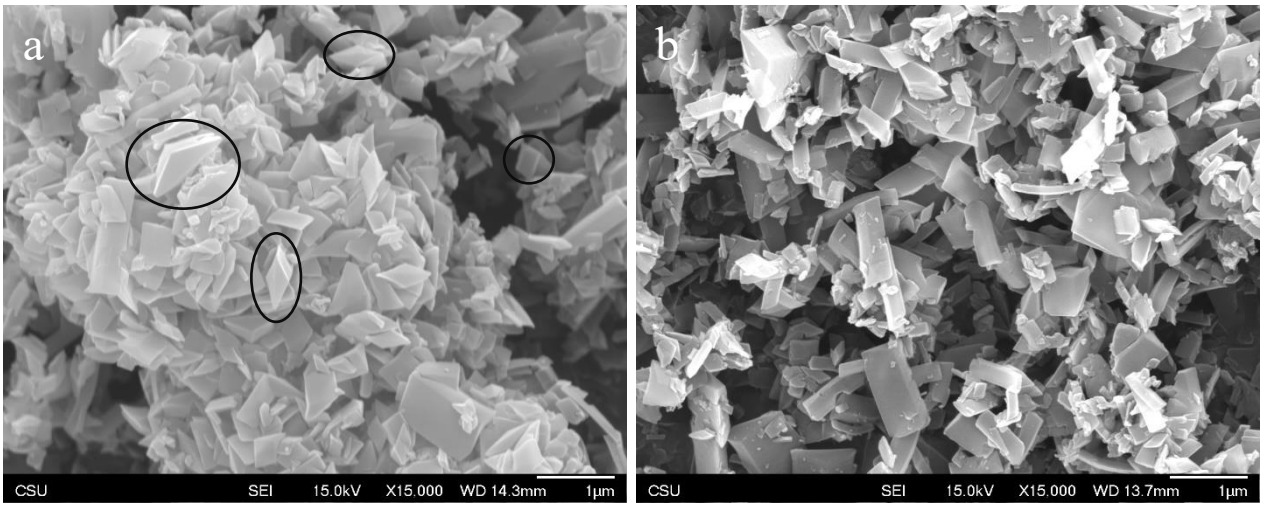

Figure 3.5. SEM images of (a) MOFN particles produced from a preliminary experiment where the three-layer method was performed at 15 °C to test the effects of temperature on MOFN formation. Black circles are used to highlight some of the MOF particles that have triangular or rhombical prism (three dimensional) morphologies (b) MOFN particles produced using the conditions as described in Chapter 2.

With the layers diffused into each other, there would be no reaction interface for the MOFNs to form and more three-dimensional particle morphologies can be observed in the SEM

(Figure 3.5). While most particles do seem to form nanosheets at lower temperatures, there are some particles with morphologies that more closely resemble those of triangular and rhombical prisms, and these are more commonly seen in the SEM images of the MOFN products obtained from performing the three-layer synthesis at lower temperatures. It is hypothesized that the lower temperatures slow down the diffusion and thus reaction rate between the ligand and the metal more than it slows down the diffusion of the layers together. This could then result in some sheets forming, but then having excess metal and ligand after the layers have diffused into each other, resulting in more three-dimensional morphologies, like those seen when CuBDTri is synthesized using solvothermal methods.

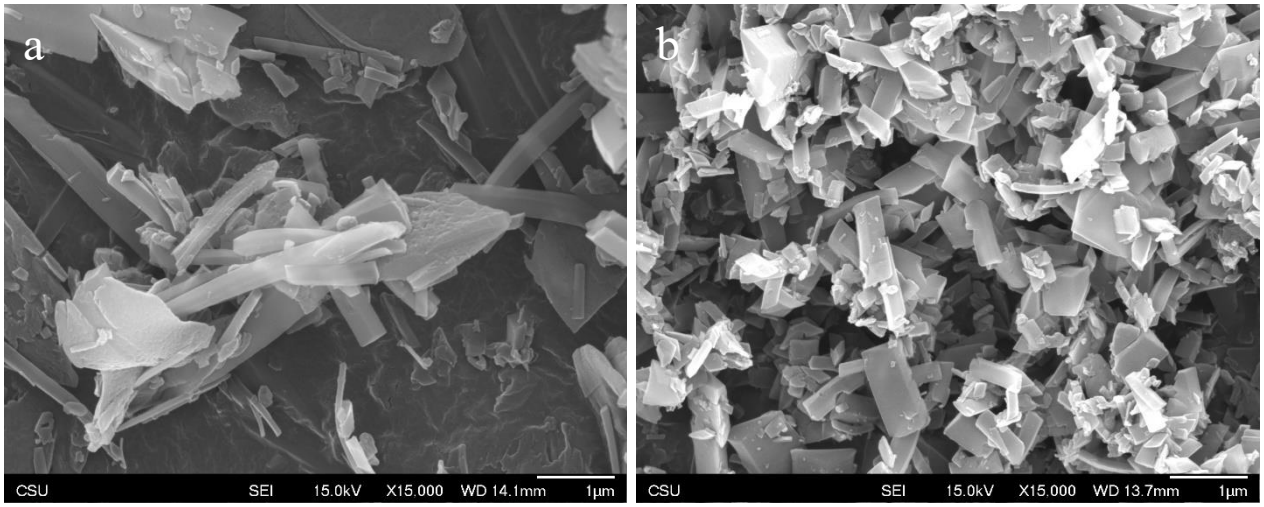

Figure 3.6. SEM images of (a) MOFN particles produced from a preliminary experiment where the three-layer method was performed at 45 °C to test the effects of temperature on MOFN formation (b) MOFN particles produced using the conditions as described in Chapter 2.

Interestingly, it can be seen in the SEM images that particles synthesized at higher temperatures typically form longer and thicker particles, showing that the CuBDTri MOFNs preferentially grow in one dimension (Figure 3.6). This is consistent with the hypotheses discussed in Chapter 2 that the shape of the H_2BDTri ligand limits the potential directions of growth due to the triazoles being positioned on the 1 and 4 positions of the benzene ring of the ligand. This is

likely due to the fact that when performed at higher temperatures, the three layers that are created for the synthesis tend to break faster (as the heat increases the rate of them diffusing into each other) and so there is much less time for the MOFNs to form at the interface between layers. Instead, it is hypothesized that very small MOFNs form in the short time before the layers diffuse into each other and those crystals then act as seeds for the MOFN to grow from. Then, once the layers are broken, the conditions would be very similar to those used to synthesize the CuBDTri MOF under solvothermal conditions, but due to the presence of these "seed crystals", the resulting MOF particles still resemble those of the nanosheets, except elongated due to rapid growth in one dimension and slower growth in the other two, dictated by the shape of the ligand.

Some preliminary experiments performed the reaction using the three-layer method at 45 °C heated the reaction too much and resulted in the layers breaking and mixing into each other in under 10 minutes, not allowing for the reaction to progress properly. Since solid was still able to be collected, CuBDTri MOFNs were synthesized using the same methods as described in our previous work, except with the temperature modified to 45 °C rather than room temperature.[15] From this experiment, it can be seen that by increasing the temperature by 20 °C, the resulting particles did not resemble the sheets as much as they resembled the elongated particles seen when CuBDTri was synthesized via solvothermal methods.

3.4.3 Development of AFM Methods

Initial AFM images obtained were unable to obtain any usable data since no discrete CuBDTri MOFN particles with sheet morphologies could be found. Upon looking at the samples using SEM that were prepared by drop casting using deionized water onto aluminum stubs, it was found that very few of the CuBDTri MOFNs were adhered as individual particles and there were

large aggregates of MOFNs on the edges of where the drop had dried. Samples were originally prepared using 0.1 mg of CuBDTri MOFN per 1 mL of deionized water.

3.4.3.1 Effect of Lowering Concentration of CuBDTri MOFNs for AFM

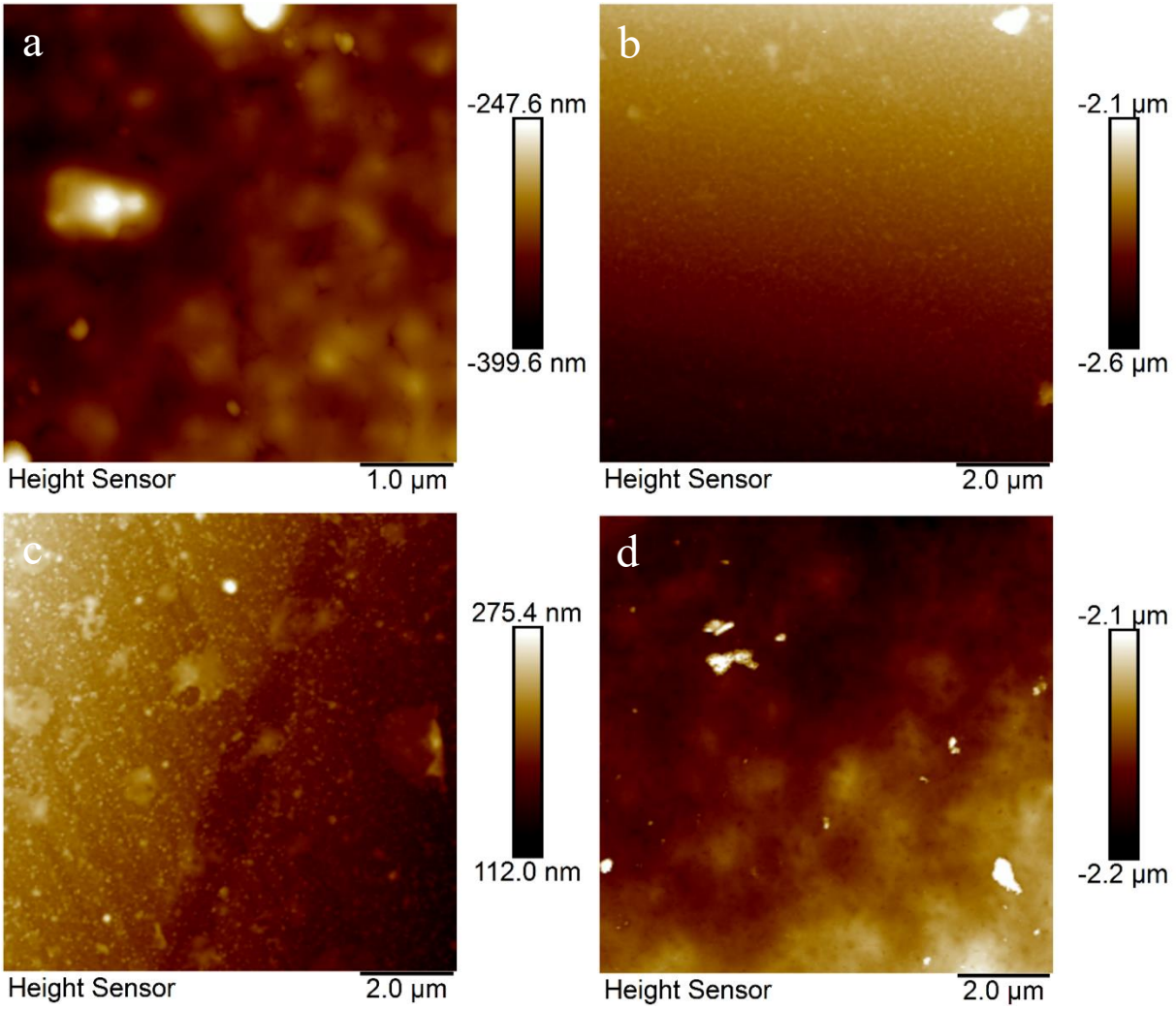

Figure 3.7. Representative AFM images of the CuBDTri MOFN using (a) 0.1 mg (10%), (b) 0.05 mg (5%), (c) 0.01 mg (1%), and (d) 0.001 mg (0.1%) of MOFN per mL of water.

To try and get samples with individual particles that could be measured by the AFM, the concentration of CuBDTri MOFN particles in the drop casting solutions were varied. It was observed that at a concentration of 0.1 mg of MOFN per 1 mL of DI water resulted in clumps of particles that could not be properly measure by the AFM. The hypothesis was that with fewer

particles in solution, it would be less likely for them to come together and aggregate into large groups of particles. To test this, concentrations of the samples being drop casted were decreased, using, 0.1 (10%), 0.05 (5%), 0.01 (1%), and 0.001 mg (0.1%) per 1 mL of deionized water, shaken vigorously and then the sample was drop casted onto mica sheets. Once the water had evaporated off, AFM images were then obtained to see if by just decreasing the concentration being used had any effect (Figure 3.7).

It can be seen in all of the AFM images used in Figure 3.7 that each of the images still have CuBDTri MOFNs that have clumped together so that accurate measurements for particle thickness could not easily be obtained, especially in Figure 3.7a and 3.7b, where no individual particles were found. In Figure 3.7c and 3.7d however, there are some areas that look like that could potentially be individual particles, but more needed to be done to create more individual MOFN particles so that they could be properly measured to determine particle thickness. Ultimately, from this set of experiments, while both the 1% and 0.01% solutions possessed individual particles and clumps of particles, it was concluded to use the 1% solution as the sample for 0.01% solution required more extensive searching to find the sample under AFM.

3.4.3.2 Effect of Sonication on Preparing CuBDTri MOFNs for AFM

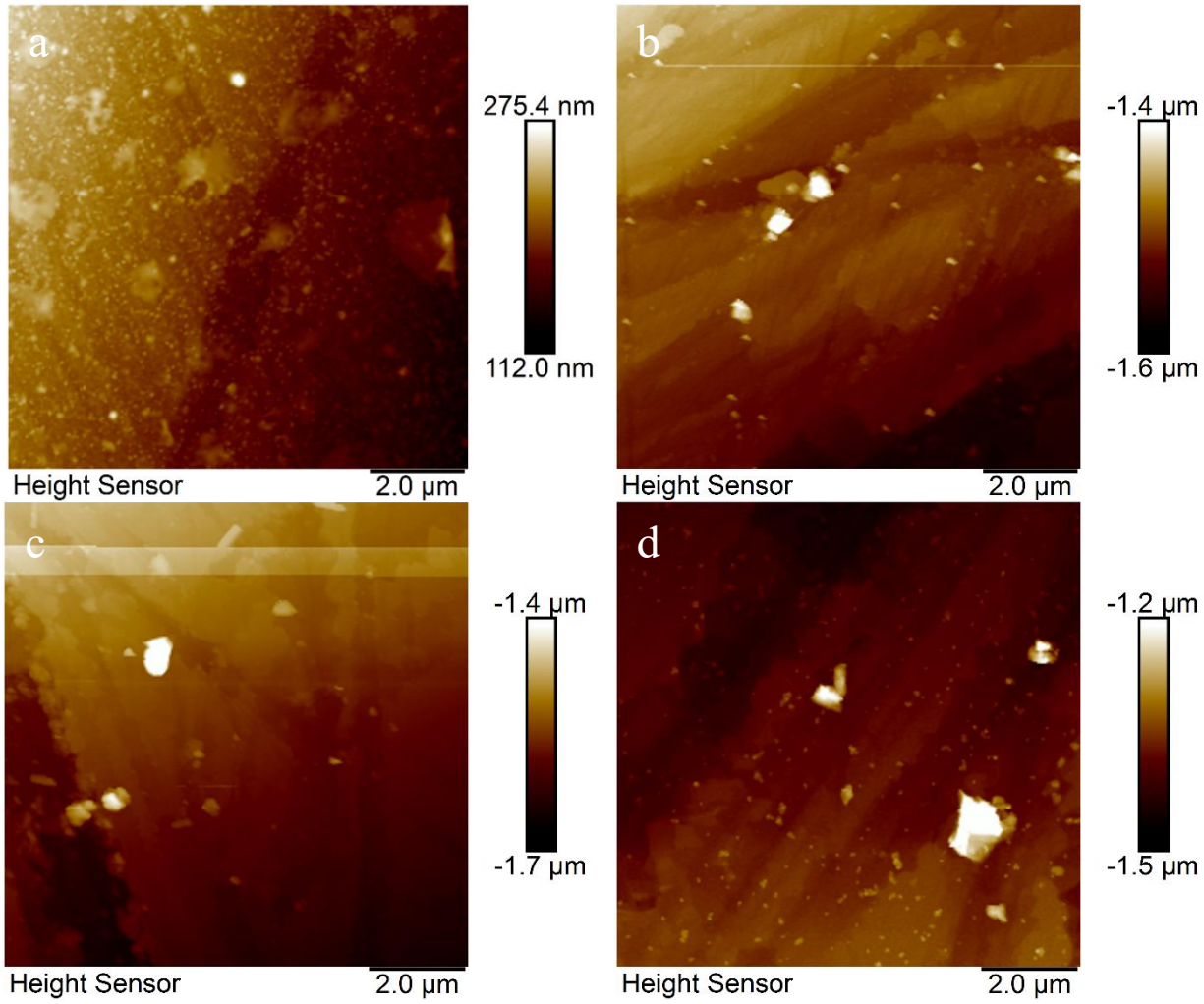

Figure 3.8. Representative AFM images of the CuBDTri MOFN using (a) 0.01 mg/1 mL water (1%), not sonicated, (b) 0.01 mg/1 mL water (1%), sonicated for 10 seconds, (c) 0.01 mg/1 mL water (1%), sonicated for 20 seconds, and (d) 0.001 mg (0.1%), sonicated for 30 seconds.

In another attempt to break apart the aggregated particles, the suspended CuBDTri MOFN particles were sonicated for 10, 20, and 30 seconds. It has been shown in the literature that certain MOF and MOFN particles can break down under sonication, so the amount of time the MOFN particles were sonicated were purposefully limited to very short time points.[18,24,25,43,44] Based on what is seen in the AFM images taken (Figure 3.8), it did seem like the CuBDTri MOFN particles did break apart after being sonicated, the particles seemed to fragment into pieces in a way that

didn't affect the thickness of the CuBDTri MOFN particles and thus the use of sonication as a method to break apart aggregates of the MOFN particles was investigated.

All sonication experiments used the 1% solution, thus were compared to a 1% solution drop casted on mica sheets that was not sonicated as a reference point. When analyzed, 30 seconds of sonication was excessive (Figure 3.8d), leading to almost all particles being broken down and it was uncertain whether any particles stayed fully intact. Although it should not have affected the thickness of the particle, it was decided that it would be easier to confirm consistency if more particles were found individual and whole. After 20 seconds of sonication, there were some clumps of materials left, but it seemed like the majority of particles were now separated and individual particles could be found fairly frequently and not too many of the particles seem to have been broken too severely. Lastly, under 10 seconds, most particles seemed to still be aggregated together and few individual particles were seen. It can be noted that very few particles were damaged. Ultimately, it was concluded that 20 seconds of sonication would be ideal as it was long enough to separate the aggregated particles while not damaging the particles too severely for AFM imaging.

3.4.3.3 Effect of Drop Casting on Oxygen Plasma Treatment on CuBDTri MOFNs for AFM

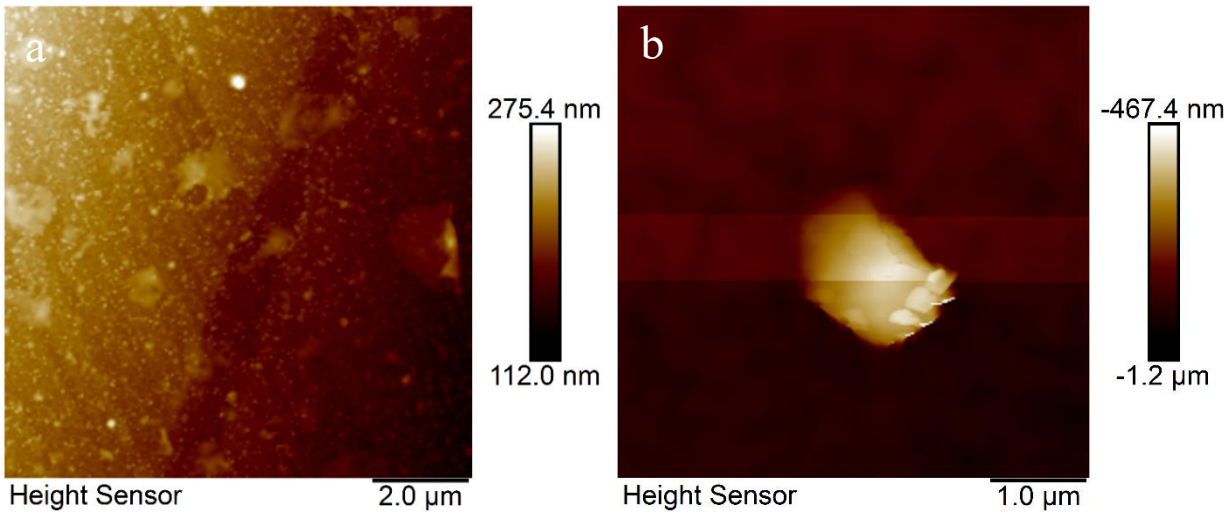

Figure 3.9. Representative AFM images of the CuBDTri MOFN using (a) 0.01 mg/1 mL water (1%), not sonicated, was not treated with oxygen plasma (b) 0.01 mg/1 mL water (1%), not sonicated, treated with oxygen plasma

An oxygen plasma treatment was performed on the CuBDTri MOFNs in an attempt to make them hydrophilic so that they would not aggregate together. By making the MOFN particles hydrophilic, it is expected that they would interact more strongly with the water creating a "shell" of water molecules to prevent them from aggregating together during the drop casting process. The oxygen plasma treated CuBDTri MOFNs were then suspended in water and drop casted immediately after the treatment, allowed to dry, and then analyzed via AFM (Figure 3.9). Based on the AFM images obtained, there was no clear improvement seen using oxygen plasma treatment on the CuBDTri MOFNs in respect to preventing clustering. It can be seen there is still clearly particles on top of each other in Figure 3.9b. Due to this, treating the CuBDTri MOFNs with oxygen plasma was removed as a consideration as no progress towards separating particles was observed from using it.

3.4.3.4 Effect of Drop Casting on Freshly Cleaved Mica Surfaces on Prepping CuBDTri MOFNs for AFM

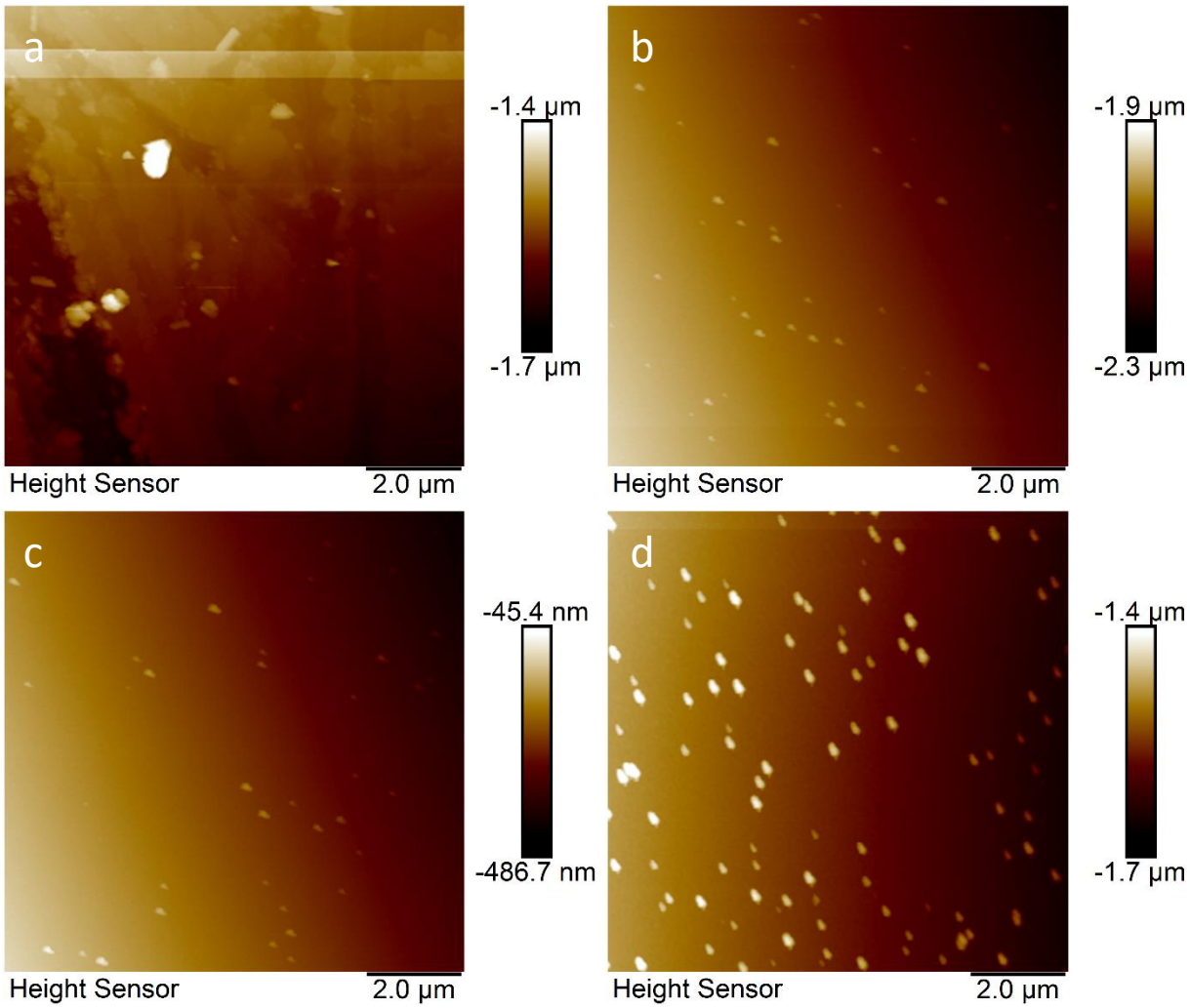

Figure 3.10. Representative AFM images of the CuBDTri MOFN using (a) 0.01 mg/1 mL water (1%), sonicated for 20 seconds, drop casted on un-cleaved mica (b, c, d) 0.01 mg/1 mL water (1%), sonicated for 20 seconds, drop casted on freshly cleaved mica

It has been shown in the literature that freshly cleaved mica is a hydrophilic surface.[45] This was done by taking mica sheets and carefully splitting along the edge with a razor blade to expose a fresh hydrophilic surface. CuBDTri suspended in 1% MOFN solutions were then immediately drop casted on the newly exposed surface. Once dried, the samples were analyzed via AFM

(Figure 3.10). On initial visual observations, it can be noted that the sample drop casted on the freshly cleaved mica surface spread out much more readily relative to mica surfaces that were not freshly cleaved. Once analyzed by AFM, it can be seen that there is a clear improvement in sample preparation relative to reducing clustered particles and finding isolated particles that could be properly measured by AFM. In Figure 3.10b-d, it can be seen that there is a noticeable reduction in aggregated particles and most particles seen under AFM are individual nanosheets. The use of freshly cleaved mica sheets has had the most noticeable effect of any of the other changes that have been tested previously and it was concluded that the MOFN samples would ideally be drop casted on freshly cleaved mica.

3.4.3.5 Finalized Conditions to Prepare CuBDTri MOFN Samples for AFM

From the experiments that tested different concentrations of the CuBDTri MOFN solution, sonication of the sample, treating the CuBDTri MOFN with oxygen plasma, and drop casting the sample onto freshly cleaved mica, I believe that we have determined an ideal set of conditions to use that successfully provides AFM images of several individual particles in a single image. This would allow for even just one good AFM image to provide data of statistically significance on the thickness of the CuBDTri MOF nanosheets and give visual indication that there is consistency between each of the individual MOFN particles. In future experiments to obtain all of these measurements for the heatmap we are trying to create from this project, all AFM images will use CuBDTri MOFN samples with a concentration of 0.01 mg of CuBDTri MOFN per mL of DI water, sonicated for 20 seconds, and then drop casted onto a freshly cleaved sheet of mica.

3.5 Conclusions

The experiments discussed in this chapter lay the groundwork required to create a heatmap that can determine the optimal conditions to use with the three-layer synthesis to synthesize CuBDTri MOFNs to create the thinnest particles possible based on the synthetic conditions modified. Towards this goal, all of the initial syntheses to obtain an initial set of data modifying temperature, middle-layer buffer thickness, and the metal to ligand ratio were finished. The MOFNs produced from each of the syntheses are being analyzed using a set of AFM conditions that have also been successfully developed and tested to be able to clearly show multiple CuBDTri MOFN particles per image.

From this, this work thus far has contributed significantly towards the goal of creating CuBDTri MOFNs that are as thin as possible so that internal volume of the MOFN is minimized while the external surface area is maximized. This will result in CuBDTri MOFNs that are as efficient on a per-total-Cu-atom-basis as possible. Towards this goal, the work in this chapter has accomplished:

I. Completing all of the syntheses required to help create the initial set of AFM data that would be required to accurately measure the thickness of the individual CuBDTri MOFN particles.
II. Experimentally determining a set of conditions that clearly shows a large amount of CuBDTri MOFN particles per image using the AFM so that large data sets can be collected quickly.

While there is still much work to be done on this project, I strongly believe the work that is completed thus far has laid a strong foundation so that this project can continue to move forward

to produce optimal CuBDTri MOFNs for heterogeneous catalytic processes restricted to the surface of the MOFN particles.

3.6 Future Directions

Experiments are currently being run using the AFM to accurately determine the thickness of the CuBDTri MOFNs using the AFM conditions determined in this chapter. Once the average thicknesses of the CuBDTri MOFNs produced under each of these conditions has been determined, the data can be used to create a heatmap that should predict the optimal set of conditions to be used to create MOFNs that are as thin as possible. The predicted conditions will then be used to synthesize CuBDTri MOFNs to test the accuracy of the heatmap. If the results from the synthesis are inconsistent with the prediction, the data will be put into the heatmap, and the process will be repeated using the heatmap to keep predicting the optimal set of conditions until they are consistent with what is observed experimentally.

Using computational processes like these can help streamline the processes of optimizing the conditions for synthetic methods where there are multiple variables that need to be tested without the need for manually running each of the experiments. Furthermore, I believe this work can serve as a precedent on how to streamline the process of optimizing the development of new materials in the future, especially with MOFs and MOFNs.

CHAPTER 3 – REFERENCES

(1) Farha, O. K.; Eryazici, I.; Jeong, N. C.; Hauser, B. G.; Wilmer, C. E.; Sarjeant, A. A.; Snurr, R. Q.; Nguyen, S. T.; Yazaydin, A. Ö.; Hupp, J. T. Metal-Organic Framework Materials with Ultrahigh Surface Areas: Is the Sky the Limit? *J Am Chem Soc* **2012**, *134* (36), 15016–15021. https://doi.org/10.1021/ja3055639.

(2) Sabale, S.; Zheng, J.; Vemuri, R. S.; Yu, X.-Y.; Mcgrail, P.; Motkuri, R. K. Synthesis and Catalysis: Open Access Recent Advances in Metal-Organic Frameworks for Heterogeneous Catalyzed Organic Transformations. *Synthesis and Catalysis: Open Access* **2016**, *1* (5), 1–8.

(3) Corma, A.; García, H.; Llabrés i Xamena, F. X. Engineering Metal Organic Frameworks for Heterogeneous Catalysis. *Chem Rev* **2010**, *110*, 4606–4655. https://doi.org/10.1021/cr9003924.

(4) Zhu, L.; Liu, X. Q.; Jiang, H. L.; Sun, L. B. Metal-Organic Frameworks for Heterogeneous Basic Catalysis. *Chem Rev* **2017**, *117* (12), 8129–8176. https://doi.org/10.1021/acs.chemrev.7b00091.

(5) Liu, J.; Chen, L.; Cui, H.; Zhang, J.; Zhang, L.; Su, C. Y. Applications of Metal-Organic Frameworks in Heterogeneous Supramolecular Catalysis. *Chem Soc Rev* **2014**, *43* (16), 6011–6061. https://doi.org/10.1039/c4cs00094c.

(6) Pal, N.; Bhaumik, A. Mesoporous Materials: Versatile Supports in Heterogeneous Catalysis for Liquid Phase Catalytic Transformations. *RSC Advances*. 2015. https://doi.org/10.1039/c4ra13077d.

(7) Tanimu, A.; Jaenicke, S.; Alhooshani, K. Heterogeneous Catalysis in Continuous Flow Microreactors: A Review of Methods and Applications. *Chemical Engineering Journal* **2017**, *327*, 792–821. https://doi.org/10.1016/j.cej.2017.06.161.

(8) Phan, N. T. S.; Vu, P. H. L.; Nguyen, T. T. Expanding Applications of Copper-Based Metal-Organic Frameworks in Catalysis: Oxidative C-O Coupling by Direct C-H Activation of Ethers over Cu2(BPDC)2(BPY) as an Efficient Heterogeneous Catalyst. *J Catal* **2013**, *306*, 38–46. https://doi.org/10.1016/j.jcat.2013.06.006.

(9) Dhakshinamoorthy, A.; Alvaro, M.; Garcia, H. Metal Organic Frameworks as Efficient Heterogeneous Catalysts for the Oxidation of Benzylic Compounds with T-Butylhydroperoxide. *J Catal* **2009**, *267* (1), 1–4. https://doi.org/10.1016/j.jcat.2009.08.001.

(10) Nguyen, L. T. L.; Nguyen, T. T.; Nguyen, K. D.; Phan, N. T. S. Metal-Organic Framework MOF-199 as an Efficient Heterogeneous Catalyst for the Aza-Michael Reaction. *Appl Catal A Gen* **2012**, *425–426*, 44–52. https://doi.org/10.1016/j.apcata.2012.02.045.

(11) Nugent, P.; Giannopoulou, E. G.; Burd, S. D.; Elemento, O.; Giannopoulou, E. G.; Forrest, K.; Pham, T.; Ma, S.; Space, B.; Wojtas, L.; Eddaoudi, M.; Zaworotko, M. J. Porous Materials with Optimal Adsorption Thermodynamics and Kinetics for Co2separation. *Nature* **2013**, *495* (7439), 80–84. https://doi.org/10.1038/nature11893.

(12) Cui, Y.; Li, B.; He, H.; Zhou, W.; Chen, B.; Qian, G. Metal-Organic Frameworks as Platforms for Functional Materials. *Acc Chem Res* **2016**, *49* (3), 483–493. https://doi.org/10.1021/acs.accounts.5b00530.

(13) Masoomi, M. Y.; Morsali, A.; Dhakshinamoorthy, A.; Garcia, H. Mixed-Metal MOFs: Unique Opportunities in Metal–Organic Framework (MOF) Functionality and Design. *Angewandte Chemie - International Edition* **2019**, *58* (43), 15188–15205. https://doi.org/10.1002/anie.201902229.

(14) Cuchiaro, H.; Thai, J.; Schaffner, N.; Tuttle, R. R.; Reynolds, M. Exploring the Parameter Space of P-Cresyl Sulfate Adsorption in Metal-Organic Frameworks. *ACS Appl Mater Interfaces* **2020**, *12* (20), 22572–22580. https://doi.org/10.1021/acsami.0c04203.

(15) Thai, J. E.; Tuttle, R. R.; Deroo, J.; Cuchiaro, J.; Reynolds, M. M. Cu-Based Metal-Organic Framework Nanosheets Synthesized via a Three-Layer Bottom-Up Method for the Catalytic Conversion of S-Nitrosoglutathione to Nitric Oxide. *ACS Appl Nano Mater* **2021**. https://doi.org/10.1021/acsanm.1c03313.

(16) Tuttle, R. R.; Folkman, S. J.; Rubin, H. N.; Finke, R. G.; Reynolds, M. M. Copper Metal-Organic Framework Surface Catalysis: Catalyst Poisoning, IR Spectroscopic, and Kinetic Evidence Addressing the Nature and Number of the Catalytically Active Sites En Route to Improved Applications. *ACS Appl Mater Interfaces* **2020**, *12* (35), 39043–39055. https://doi.org/10.1021/acsami.0c08961.

(17) Tuttle, R. R.; Rubin, H. N.; Rithner, C. D.; Finke, R. G.; Reynolds, M. M. Copper Ion vs Copper Metal–Organic Framework Catalyzed NO Release from Bioavailable S-Nitrosoglutathione En Route to Biomedical Applications: Direct 1H NMR Monitoring in

Water Allowing Identification of the Distinct, True Reaction Stoichiometries and Thio. *J Inorg Biochem* **2019**, *199* (July), 110760. https://doi.org/10.1016/j.jinorgbio.2019.110760.

(18) Coleman, J. N.; Lotya, M.; Neill, A. O.; Bergin, S. D.; King, P. J.; Khan, U.; Young, K.; Gaucher, A.; De, S.; Smith, R. J.; Shvets, I. v; Arora, S. K.; Stanton, G.; Kim, H.; Lee, K.; Kim, G. T.; Duesberg, G. S.; Hallam, T.; Boland, J. J.; Wang, J. J.; Donegan, J. F.; Grunlan, J. C.; Moriarty, G.; Shmeliov, A.; Nicholls, R. J.; Perkins, J. M.; Grieveson, E. M.; Theuwissen, K.; Mccomb, D. W.; Nellist, P. D.; Nicolosi, V. Two-Dimensional Nanosheets Produced by Liquid Exfoliation of Layered Materials. *Science (1979)* **2011**, *331* (6017), 568–571.

(19) Zhang, H. Ultrathin Two-Dimensional Nanomaterials. *ACS Nano* **2015**, *9* (10), 9451–9469. https://doi.org/10.1021/acsnano.5b05040.

(20) Zhao, M.; Lu, Q.; Ma, Q.; Zhang, H. Two-Dimensional Metal–Organic Framework Nanosheets. *Small Methods* **2017**, *1* (1–2), 1–8. https://doi.org/10.1002/smtd.201600030.

(21) Chhowalla, M.; Liu, Z.; Zhang, H. Two-Dimensional Transition Metal Dichalcogenide (TMD) Nanosheets. *Chem Soc Rev* **2015**, *44* (9), 2584–2586. https://doi.org/10.1039/c5cs90037a.

(22) Tan, C.; Cao, X.; Wu, X. J.; He, Q.; Yang, J.; Zhang, X.; Chen, J.; Zhao, W.; Han, S.; Nam, G. H.; Sindoro, M.; Zhang, H. Recent Advances in Ultrathin Two-Dimensional Nanomaterials. *Chem Rev* **2017**, *117* (9), 6225–6331. https://doi.org/10.1021/acs.chemrev.6b00558.

(23) Tan, C.; Zhang, H. Two-Dimensional Transition Metal Dichalcogenide Nanosheet-Based Composites. *Chem Soc Rev* **2015**, *44* (9), 2713–2731. https://doi.org/10.1039/c4cs00182f.

(24) Zhao, M.; Huang, Y.; Peng, Y.; Huang, Z.; Ma, Q.; Zhang, H. Two-Dimensional Metal-Organic Framework Nanosheets: Synthesis and Applications. *Chem Soc Rev* **2018**, *47* (16), 6267–6295. https://doi.org/10.1039/c8cs00268a.

(25) Wang, J.; Li, N.; Xu, Y.; Pang, H. Two-Dimensional MOF and COF Nanosheets: Synthesis and Applications in Electrochemistry. *Chemistry - A European Journal*. Wiley-VCH Verlag May 20, 2020, pp 6402–6422. https://doi.org/10.1002/chem.202000294.

(26) Peng, Y.; Li, Y.; Ban, Y.; Yang, W. Two-Dimensional Metal–Organic Framework Nanosheets for Membrane-Based Gas Separation. *Angewandte Chemie - International Edition* **2017**, *56* (33), 9757–9761. https://doi.org/10.1002/anie.201703959.

(27) Chakraborty, G.; Park, I. H.; Medishetty, R.; Vittal, J. J. Two-Dimensional Metal-Organic Framework Materials: Synthesis, Structures, Properties and Applications. *Chem Rev* **2021**, *121* (7), 3751–3891. https://doi.org/10.1021/acs.chemrev.0c01049.

(28) Zhao, W.; Peng, J.; Wang, W.; Liu, S.; Zhao, Q.; Huang, W. Ultrathin Two-Dimensional Metal-Organic Framework Nanosheets for Functional Electronic Devices. *Coord Chem Rev* **2018**, *377*, 44–63. https://doi.org/10.1016/j.ccr.2018.08.023.

(29) Hai, G.; Jia, X.; Zhang, K.; Liu, X.; Wu, Z.; Wang, G. High-Performance Oxygen Evolution Catalyst Using Two-Dimensional Ultrathin Metal-Organic Frameworks Nanosheets. *Nano Energy* **2018**, *44* (October 2017), 345–352. https://doi.org/10.1016/j.nanoen.2017.11.071.

(30) Yin, H.; Tang, Z. Ultrathin Two-Dimensional Layered Metal Hydroxides: An Emerging Platform for Advanced Catalysis, Energy Conversion and Storage. *Chem Soc Rev* **2016**, *45* (18), 4873–4891. https://doi.org/10.1039/c6cs00343e.

(31) Hu, Z.; Mahdi, E. M.; Peng, Y.; Qian, Y.; Zhang, B.; Yan, N.; Yuan, D.; Tan, J. C.; Zhao, D. Kinetically Controlled Synthesis of Two-Dimensional Zr/Hf Metal-Organic Framework Nanosheets via a Modulated Hydrothermal Approach. *J Mater Chem A Mater* **2017**, *5* (19), 8954–8963. https://doi.org/10.1039/c7ta00413c.

(32) Xu, M.; Yang, S. S.; Gu, Z. Y. Two-Dimensional Metal-Organic Framework Nanosheets: A Rapidly Growing Class of Versatile Nanomaterials for Gas Separation, MALDI-TOF Matrix and Biomimetic Applications. *Chemistry - A European Journal* **2018**, *24* (57), 15131–15142. https://doi.org/10.1002/chem.201800556.

(33) Zhuang, L.; Ge, L.; Liu, H.; Jiang, Z.; Jia, Y.; Li, Z.; Yang, D.; Hocking, R. K.; Li, M.; Zhang, L.; Wang, X.; Yao, X. MOF Nanosheets Very Important Paper A Surfactant-Free and Scalable General Strategy for Synthesizing Ultrathin Two-Dimensional Metal – Organic Framework Nanosheets for the Oxygen Evolution Reaction Research Articles. **2019**, *4300*, 13565–13572. https://doi.org/10.1002/anie.201907600.

(34) Das, S. K.; Chatterjee, S.; Bhunia, S.; Mondal, A.; Mitra, P.; Kumari, V.; Pradhan, A.; Bhaumik, A. A New Strongly Paramagnetic Cerium-Containing Microporous MOF for CO2 Fixation under Ambient Conditions. *Dalton Transactions* **2017**, *46* (40), 13783–13792. https://doi.org/10.1039/c7dt02040f.

(35) Gumilar, G.; Kaneti, Y. V.; Henzie, J.; Chatterjee, S.; Na, J.; Yuliarto, B.; Nugraha, N.; Patah, A.; Bhaumik, A.; Yamauchi, Y. General Synthesis of Hierarchical Sheet/Plate-like M-BDC (M = Cu, Mn, Ni, and Zr) Metal-Organic Frameworks for Electrochemical Non-Enzymatic Glucose Sensing. *Chem Sci* **2020**, *11* (14), 3644–3655. https://doi.org/10.1039/c9sc05636j.

(36) Binnig, G.; Quate' ', C. F.; Gi, E. L.; Gerber, C. *Atomic Force Microscope*.

(37) Makiura, R. Creation of Metal–Organic Framework Nanosheets by the Langmuir-Blodgett Technique. *Coordination Chemistry Reviews*. Elsevier B.V. October 15, 2022. https://doi.org/10.1016/j.ccr.2022.214650.

(38) Han, M.; Zhang, X.; Gao, H.; Chen, S.; Cheng, P.; Wang, P.; Zhao, Z.; Dang, R.; Wang, G. In Situ Semi-Sacrificial Template-Assisted Growth of Ultrathin Metal–Organic Framework Nanosheets for Electrocatalytic Oxygen Evolution. *Chemical Engineering Journal* **2021**, *426*. https://doi.org/10.1016/j.cej.2021.131348.

(39) Duan, J.; Li, Y.; Pan, Y.; Behera, N.; Jin, W. Metal-Organic Framework Nanosheets: An Emerging Family of Multifunctional 2D Materials. *Coordination Chemistry Reviews*. Elsevier B.V. September 15, 2019, pp 25–45. https://doi.org/10.1016/j.ccr.2019.05.018.

(40) Koyappayil, A.; Yeon, S. ho; Chavan, S. G.; Jin, L.; Go, A.; Lee, M. H. Efficient and Rapid Synthesis of Ultrathin Nickel-Metal Organic Framework Nanosheets for the Sensitive Determination of Glucose. *Microchemical Journal* **2022**, *179*. https://doi.org/10.1016/j.microc.2022.107462.

(41) Li, H.; Gao, K.; Mo, B.; Meng, Q.; Li, K.; Wu, J.; Hou, H. Construction of Porous 2D MOF Nanosheets for Rapid and Selective Adsorption of Cationic Dyes. *Dalton Transactions* **2021**, *50* (9), 3348–3355. https://doi.org/10.1039/d0dt04143b.

(42) Rodenas, T.; Luz, I.; Prieto, G.; Seoane, B.; Miro, H.; Corma, A.; Kapteijn, F.; Llabrés I Xamena, F. X.; Gascon, J. Metal-Organic Framework Nanosheets in Polymer Composite Materials for Gas Separation. *Nat Mater* **2015**, *14* (1), 48–55. https://doi.org/10.1038/nmat4113.

(43) Nicolosi, V.; Chhowalla, M.; Kanatzidis, M. G.; Strano, M. S.; Coleman, J. N. Liquid Exfoliation of Layered Materials. *Science (1979)* **2013**, *340* (6139), 72–75. https://doi.org/10.1126/science.1226419.

(44) Coleman, J. N. Liquid Exfoliation of Defect-Free Graphene. *Acc Chem Res* **2013**, *46* (1), 14–22. https://doi.org/10.1021/ar300009f.

(45) Keller, A.; Fritzsche, M.; Ogaki, R.; Bald, I.; Facsko, S.; Dong, M.; Kingshott, P.; Besenbacher, F. Tuning the Hydrophobicity of Mica Surfaces by Hyperthermal Ar Ion Irradiation. *Journal of Chemical Physics* **2011**, *134* (10). https://doi.org/10.1063/1.3561292.

CHAPTER 4

TOWARDS THE UNDERSTANDING OF THE BREAKDOWN OF CuBTC METAL-ORGANIC FRAMEWORKS BY FRIEDLÄNDER SYNTHESIS AND REIDENTIFICATION OF THE CATALYST

4.1 Overview

While there is a lot of work in synthesizing and developing new metal-organic frameworks (MOFs) for heterogeneous catalysis for different reactions, there is not a proportional amount of work being done in determining how exactly this catalysis is being done. This has led to a lack of understanding towards the mechanisms, active site, and catalyst identity in many catalytic MOF systems. One example of such a gap in understanding, is the use of CuBTC (where BTC = benzene-1,3,5-tricarboxylate) to catalyze the Friedländer synthesis between 2-aminobenzophenones and ketones to form quinolines. From attempts to perform this reaction system under continuous flow to increase the production efficiency of these quinolines, it was found that the CuBTC MOF was being broken down and producing a new crystalline material. The work in this chapter works towards understanding the breakdown of CuBTC under these conditions and towards determining what is actually catalyzing the Friedländer synthesis in this system.

Development, conception, and construction of the modified flow reactor used for all continuous flow syntheses was done by Jonathan Thai and Jesus Tapia. The syntheses performed to test the Friedländer synthesis under batch conditions and continuous flow were performed by Jonathan Thai. Characterization and analysis of the CuBTC MOFs by powder x-ray diffraction

(pXRD) and scanning electron microscopy (SEM) were done by Jonathan Thai. Time-of-flight mass spectrometry (TOF-MS) data was obtained by Jesus Tapia, Jonathan Thai, and Madeline Roach. Melissa M. Reynolds was the advisor on this project.

4.2 Introduction

4.2.1 Quinolines and the Friedländer Synthesis

Quinolines are a class of molecules that belong to the benzo-pyridine family and have several derivatives that are among of the most common heterocycle moieties in drug research (Figure 4.1).[1–5] Quinoline derivatives have shown pharmacological activity against bacteria, tuberculosis, malaria, human immunodeficiency virus (HIV), hepatitis C, tumors, inflammation, and fungus while also being able to be used in other biological activities.[2,6–13] Friedlieb Ferdinand Runge first extracted quinoline from coal tar in 1834 and this has been the main source of natural quinoline since as it is not very commonly found in nature.[14] Instead, quinoline and quinoline derivatives are more commonly synthesized from several well-known reactions such as, but not limited to the Camps quinoline synthesis, Combes quinoline synthesis, Conrad-Limpach synthesis, Doebner reaction, Doebner-Miller reaction, Friedländer synthesis, Gould-Jacobs reaction, Knorr quinoline synthesis, Niementowski quinoline synthesis, Pfitzinger reaction, Povarov reaction, and Skraup synthesis.[3–5,14–19]

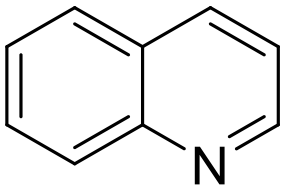

Figure 4.1. Structure of quinoline

The Friedländer synthesis is a well-known reaction, named after German chemist Paul Friedländer that combines 2-aminobenzaldehydes and ketones to form quinoline derivatives (Figure 4.2).[3,4] Many quinoline derivatives produced by the Friedländer synthesis are known intermediates in synthetic processes used for antimalarials and other parasitic agents, making them extremely high-value pharmaceutical targets.[11,14,20–22] This utility has led to many research efforts to develop more efficient methods for performing the Friedländer Synthesis, as many traditional methods use harsh synthetic conditions. This has led to many turning to the use of heterogeneous catalysis to allow for the use of more mild conditions.

4.2.2 Reported Use of CuBTC as a Catalyst for the Friedländer Synthesis

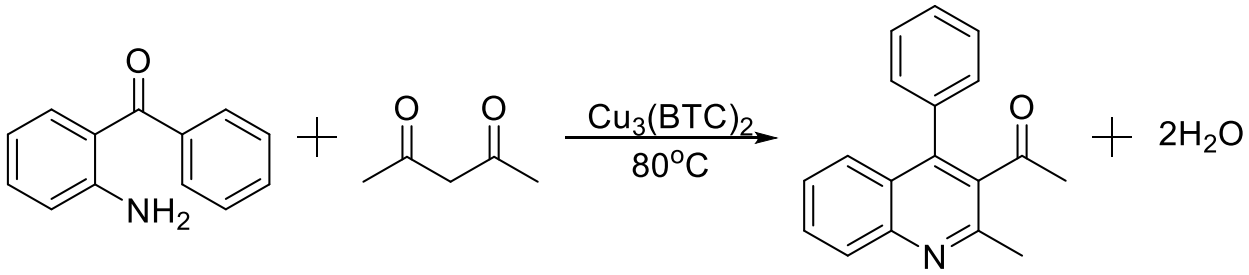

Figure 4.2. Reaction scheme for the Friedländer synthesis between 2-aminobenzophenone and acetylacetone to produce 3-aceyl-2-methyl-4-phenylquinoline. This is the reaction originally performed by Pérez-Mayoral and Cejka, done under continuous flow with CuBTC on silica monoliths by Sachse *et al.*, and then used in our continuous flow system.

In 2011, it was reported by Pérez-Mayoral and Čejka that the Friedländer synthesis could be carried out by using the CuBTC (BTC = benzene-1,3,5-tricarboxylate) metal-organic framework (MOFs) as a heterogeneous catalyst.[23] This was accomplished between 2-aminobenzophenone derivatives and acetylacetone to produce 3-acetyl-2-methyl-4-phenylquinolines (Figure 4.2). This led them to continue the use of CuBTC to catalyze the Friedländer synthesis, expanding the substrate scope and optimizing the process.[24–26]

In 2012, after the initial publication by Pérez-Mayoral and Čejka, CuBTC MOFs were reported to be synthesized as nanoparticles inside the pores of silica monoliths to create a fixed-bed catalyst to allow for use of the MOF to catalyze the Friedländer synthesis using the same reagents under continuous flow conditions.[27,28] By using MOFs synthesized onto mesoporous silica monoliths, backpressure generated by the continuous flow system can be reduced and simplify the process of packing a catalytic column.[27] This brought into question on whether or not CuBTC could be used on a continuous flow system with a direct packed column as direct packing would allow for the highest volume of MOF to be used, thus theoretically allow for a microreactor to maximize production efficiency.

4.2.3 Developing a Continuous Flow Reactor for the Friedländer Synthesis Using CuBTC as the Catalyst

The original goal of this work was to create a catalytic system capable of carrying out high-throughput organic transformations under continuous flow conditions using MOFs. The model system being developed needed to follow these guidelines:

I. Reaction must be catalyzed by a MOF that is readily available so that it can be cost efficient and allow for scale up to be used in high-throughput production
II. The MOF must be stable (not break down both physically and chemically) under the reaction conditions so that the catalytic bed can be reused
III. The transformation being performed must be easily detectable with conventional analytical methods such as nuclear magnetic resonance (NMR), infrared spectroscopy (IR), and/or mass spectrometry (MS)

IV. A high (>70%) percent conversion must be achievable within a relatively short (<24 hours) reaction time as contact between the reagents and the MOF catalysts will be limited under continuous flow conditions

Due to the previous precedents showing that the Friedländer synthesis followed each of these points, it was chosen to act as the model reaction for this continuous flow system.

4.2.4 Towards a Better Understanding of the Role of CuBTC in the Friedländer Synthesis

Initial results performing the Friedländer synthesis under batch and continuous flow conditions were promising in that the reaction conditions published in the work of Pérez-Mayoral and Čejka were reproducible and that when put under continuous flow conditions, product could be seen in the mass spectra obtained from the eluted product. However, while studying the Friedländer synthesis under continuous flow conditions, the direction of this project changed as it was observed that:

I. The eluent being collected from the continuous flow system would initially come out green and then turn blue, even though none of the reactants or products were blue.

II. There was a large amount of back pressure that would build up (upwards of 300 atm) after about 30 mL of eluent was collected. This pressure was due to the accumulation of a solid in the tubing going form the column to the collection vessel and would suddenly drop once the pressure reached around 380 atm, resulting in rapid elution.

III. The collected eluent would contain solid. It was expected that these small bits of solid were responsible for clogging the tubing and pressurizing the system.

IV. Large (up to 4-5mm in length) blue crystalline needles would recrystallize from the eluent when left sitting at room temperature (after 12+ hours). When analyzed via pXRD and SEM, these crystals did not match any of the data obtained for CuBTC. When analyzed using TOF-MS, the blue crystalline needles possessed mass-to-charge ratios that would match those expected of intermediates of the Friedländer synthesis being performed, connected to copper (confirmed via isotopic ratios) and the 1,3,5-benznetricarboxylic acid. This data will be discussed in further detail later in this chapter.

V. When analyzed by pXRD, the CuBTC still in the column matched the diffraction pattern expected of CuBTC. However, when analyzed via SEM, the CuBTC particles, which typically have an octahedral morphology, had several hexagonal-shaped holes in the particle, with some particles looking like they were shredded by these "hexagonal holes".

VI. The amount of CuBTC that was originally packed into the column was reduced after it was used to perform the Friedländer synthesis under continuous flow conditions. It would get to the point of having no MOF left in the column after 10 equivalents of the reaction was performed.

Due to these points, it was hypothesized that CuBTC was being broken down by the Friedländer synthesis and that CuBTC may not be the true catalyst of the Friedländer synthesis in this system. Instead, it is hypothesized that the CuBTC is functionally a pre-catalyst. The true catalyst of the Friedländer synthesis in this system is likely to be a yet-to-be-identified copper-containing species that was extracted from the MOF lattice. This project was consequently redirected towards

identifying what is the actual catalyst in this Friedländer synthesis system and whether or not this is truly a heterogeneous catalytic system.

There are several potential factors that may be causing the breakdown of CuBTC that need to be considered. These factors include:

I. There is an inherent issue with the Friedländer synthesis that leads to the breakdown of CuBTC.
II. As water is known to be capable of breaking down CuBTC, the production of water from the Friedländer synthesis may be leading to the breakdown of the MOF.
III. The use of 2-aminobenzophenone and DMF may be leading to a displacement of the benzene-1,3,5-tricarboxylic acid ligand as the nitrogen-containing groups may have a higher affinity for the Cu(II) centers.
IV. There is an inherent issue with the setup for the continuous flow reactor that is leading to the breakdown of the CuBTC.

While not an exhaustive list, these are the key factors that need to be considered and tested first to form a basis of understanding as to what is causing the observed breakdown of the CuBTC in this system.

MOFs as heterogeneous catalysts is a growing field of research due to their uniform structure, high porosity, large surface area, and tunability.[29–38] However, the catalyst identity is largely assumed in many of these cases and the actual mechanism of catalysis is not fully understood in most cases.[39–42] The ability to definitively identify and understand the catalytic process are key points towards improving and optimizing catalytic processes and makes the ability to determine catalyst identity and catalytic mechanisms an extremely important goal.[43–45] By

developing this level of understanding of MOF catalysis, it would make it easier to accurately compare the catalytic efficiency between different MOF species and allow for more targeted design of MOFs for heterogeneous catalysis, facilitating the process of converting more of the reactions to more efficient, continuous flow processes. Thus, the work discussed in this chapter moves towards understanding the breakdown of CuBTC MOFs when used as a catalyst for the Friedländer synthesis between 2-aminobenzophenone and acetylacetone as well as towards understanding what the identity of the catalyst is for this system.

4.3 Experimental

4.3.1 Materials

All chemicals and solvents were purchased from commercial vendors and were then used without any further purification. *N*, *N*-dimethylformamide, >99.6%; 2-aminobenzophenone, 98%; and ethanol, 100% was purchased from Fisher Scientific (Waltham, MA). 1,3,5-benzenetricarboxylic acid, >98%; and copper(II) nitrate trihydrate, >99%; and acetylacetone >99% were purchased from Sigma-Aldrich (St. Louis, MO). All deionized water used was purified by a Millipore Milli-Q- IQ 7000 water purification system to 18.2 MΩ-cm resistivity prior to use.

4.3.2 Synthesis of CuBTC MOF

The synthesis to create the CuBTC MOF used was adapted from the literature.[32] In short, 1,3,5-benzenetricarboxylic acid (12.85 mmol, 0.62 equiv.) and copper(II) nitrate trihydrate (20.695 mmol, 1.0 equiv.) were suspended in a mixture of deionized water (23 mL), DMF (33 mL), and ethanol (36 mL) in a sealable Pyrex bottle. The mixture was sonicated for at least 1 hour to fully disperse and suspend the reagents. The mixture was then placed into a pre-heated oven at 90°C for 24 hours. After 24 hours, the oven was turned off and the product was cooled to room

temperature inside the oven naturally. Once cooled to room temperature, the solid product was then collected using a fine glass filter frit. The solid product was then rinsed with DMF (3 x 50 mL). The solid product was then washed in ethanol using Soxhlet extraction for at least 24 hours. The solid product was then collected using a fine glass filter frit. The solid was then collected and dried at 150°C under reduced pressure, producing a dark blue powder. The collected product was then characterized using SEM and pXRD.

4.3.3 Using CuBTC to Catalyze the Friedländer Synthesis Between 2-Aminobenzophenone and Acetylacetone Under Batch Conditions

The reaction conditions used were adapted from the literature.[23,46] In short, CuBTC (0.05g, 0.083 mmol) was weighed out into a 100 mL round bottomed flask. The CuBTC was then activated in a vacuum oven at 150°C under reduced pressure overnight. The oven was then turned off and the CuBTC was then allowed to cool naturally to room temperature before it was taken out. Acetylacetone (20.0 mmol, 10 equiv.) and 2-aminobenzophenone (2.0 mmol, 1 equiv.) were then measured out into the RBF with the CuBTC. The reaction mixture was then stirred and heated to 100°C for 24 hours in a reflux apparatus. Ethanol (10 mL in 2-3 mL portions) was then used to rinse the contents of the RBF into a centrifuge tube. The solid (unidentified crystal) and supernatant were then separated via centrifugation. The supernatant was then transferred to a vial and the solvent was then removed under reduced pressure (to produce the product mixture). The unidentified crystal was then rinsed with ethanol (10 mL) and vortexed to ensure no remnants of the reagents or products from the reaction were still present and the solid and supernatant were then separated again via centrifugation. The supernatant was then combined with the product mixture and had the solvents removed under reduced pressure, yielding a green solid. The unidentified crystal was collected and dried under reduced pressure for 24 hours, yielding a pale

blue solid. The product mixture was analyzed using TOF-MS. The unidentified crystal was analyzed using TOF-MS, pXRD, and SEM.

4.3.4 Using CuBTC to Catalyze the Friedländer Synthesis Between 2-Aminobenzophenone and Acetylacetone Under Continuous Flow Conditions

The procedure described here is referred to as "1 equivalent" of the Friedländer synthesis under continuous flow conditions, though the same column may have been used several times for some experiments (in that case, the "equivalents" following the first start at the preheating step). CuBTC was activated at 150 °C under pressure overnight in a vacuum oven. The oven was then turned off and the CuBTC was allowed to cool down to room temperature before it was taken out. A stainless-steel HPLC column (I.D. x L, 4.6 x 50 mm) was then directly packed with CuBTC and connected to a HPLC pump via stainless steel tubing. The column was than pre-heated to 80 °C while rinsed with DMF at 0.3 mL/min for at least 30 minutes prior to running the reaction. A reaction mixture was created using by dissolving 2-aminobenzophenone (2.0 mmol, 1 equiv.) in acetylacetone (10.0 mmol, 5 equiv.), yielding a yellow liquid. The reaction mixture was then drawn into a 5 mL gas-tight glass syringe and injected into the reactor at 0.3 mL/min. The reaction was rinsed with DMF and the product eluent was collected in 4 mL fractions. Each of the fractions collected were then analyzed using TOF-MS.

4.3.5 Characterization by Scanning Electron Microscopy (SEM)

SEM imaging was performed using a JEOL JSM-6500F microscope. An accelerating voltage of 15.0 kV was used to image the MOFs. All samples were prepared on a small piece of carbon tape which were then placed under vacuum and coated with 20 nm of gold prior to imaging.

At least three representative images were taken with at least three different magnifications for each sample were taken.

4.3.6 Characterization by Powder X-Ray Diffraction (pXRD)

A Bruker D8 Discover DaVinci Powder X-ray Diffractometer with Cu Kα radiation (λ = 1.5406 Å was used, operated at 40 kV and 40 mA. A 0.6-mm divergent slit was placed on the primary beam sided and a high-resolution energy dispersive LYNXEYE-XE-T detector was placed on the diffracted beam side during the XRD studies. Samples were seated on a B-doped silicon zero-diffraction plate and held in place with a small amount of vacuum grease. The 2θ was set between 4-50 degrees and scanned at steps of 0.100 degrees.

4.3.7 Characterization by Time of Flight-Mass Spectrometry (TOF-MS)

TOF-MS was performed using an Agilent® 6224 time-of-flight mass spectrometer equipped with a dual ESI source. All data shown in this chapter was collected while operating the TOF-MS under positive mode. The detection range for the scans were set for 95-3200 *m/z*.

4.3.8 Data Analysis

All data is reported as "average ± standard deviation". All data points that are reported were calculated from n = 3, unless noted otherwise.

4.4 Results and Discussion

4.4.1 Proof of Concept for the Friedländer Synthesis Catalyzed by CuBTC Between 2-Aminobenzophenone and Acetylacetone & Determining Parameters for Performing the Reaction Under Continuous Flow

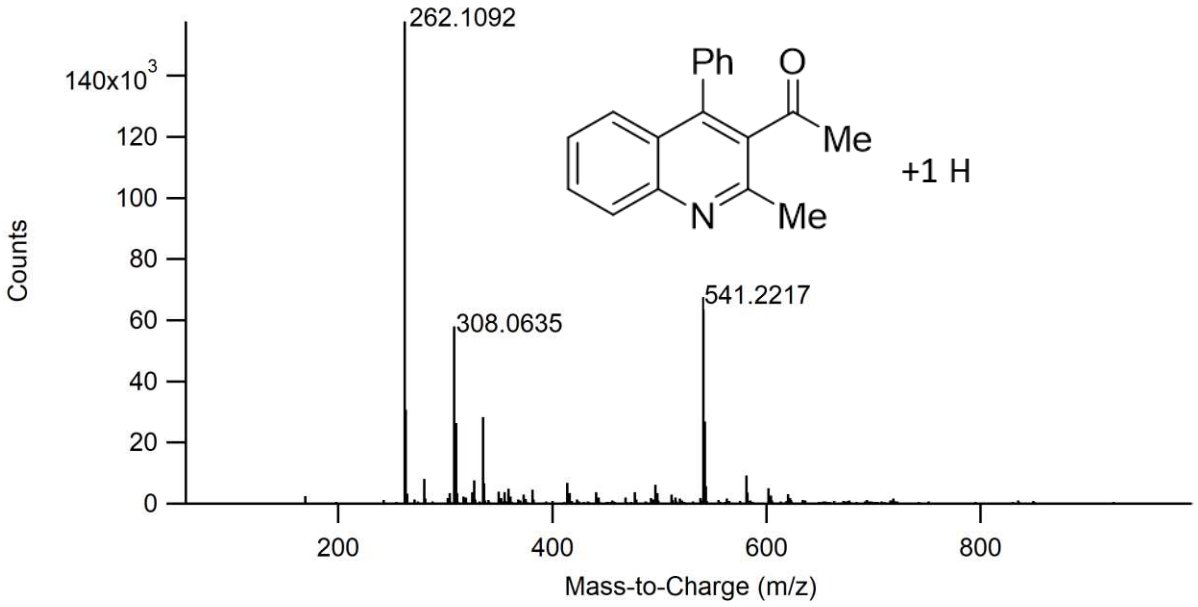

Figure 4.3. Mass spectrum of the product obtained after performing the Friedländer synthesis between acetylacetone and 2-aminobenzophenone in the presence of CuBTC and the structure of the product that correlates with the 262 *m/z* peak. This figure was created with the help of Madeline C. Roach.

To see how well the Friedländer synthesis would run under batch conditions and to determine what, if any changes needed to be made to the reaction conditions when converting the reaction to continuous flow conditions, the reaction reported in the literature was replicated.[23] When the Friedländer synthesis between 2-aminobenzophenone and acetylacetone was run using batch conditions and the parameters as described in the literature, the results were consistent with what was reported in the literature. Using TOF-MS, it can be seen that the majority of the reactant (2-aminobenzophenone) was consumed as the 198 *m/z* is observed to be relatively low and the most prominent signal is that of 262 *m/z*, representative of the protonated product (Figure 4.3).

However, no mass balance experiment was performed, so this cannot be definitively claimed. It should be noted that there is a peak at 308 *m/*z has a shoulder at 310 *m/*z and is hypothesized to be a copper-containing intermediate of the reaction and will be discussed more thoroughly later in this chapter. Overall, due to the consistency with the literature, it was decided that moving forward with converting this reaction to continuous flow conditions was viable.

The initial challenge that arose however, is that the reaction mixture created according to the literature procedure for batch conditions ran the reaction neat in acetylacetone, which created a slurry, meaning it could not be injected into a continuous flow system. Therefore, to optimize the reaction for use under continuous flow conditions, 2 mL of DMF was added into the reaction

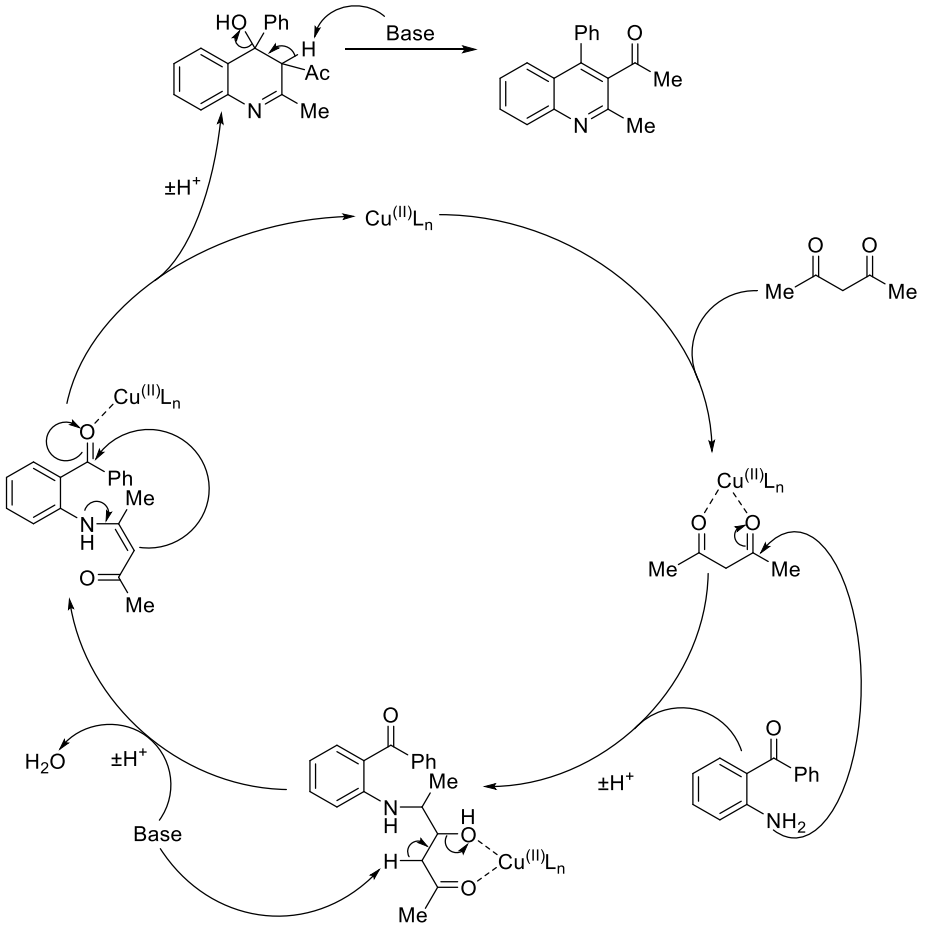

Figure 4.4. Proposed mechanism for the Friedländer synthesis between 2-aminobenzophenone

mixture to dissolve the 2-aminobenzophenone. Furthermore, to better understand the system parameters, experiments were conducted at lower temperatures and with smaller amounts of acetylacetone (the initial ratio of 2-aminobenzoephnone to acetylacetone was 1:5 and was then reduced to 1:2). These experiments were designed to test whether these parameters could be modified without decreasing yields before moving to continuous flow conditions. However, both of these changes also resulted in decreased yields. Based on the proposed mechanism (Figure 4.4), it is expected that the lower temperature resulted in a decrease in yield as the lowered temperature makes it more difficult to form the secondary enolate. Furthermore, from the data obtained, it is hypothesized the acetylacetone is likely part of the rate-determining step. This is supported by the fact that reducing the amount of acetylacetone decreased percent conversion when given the same amount of time to react.

Based on these results, it was determined that the reaction conditions should be modified as little as possible prior to injecting the reactant mixture into the column. With this in mind, the reaction mixture containing the 2-aminobenzophenone and acetylacetone in a 1:5 mol ratio was heated to 40 °C to allow for the 2-aminobenzophenone to completely dissolve into the acetylacetone right before injection into the continuous flow system, yielding a bright yellow mixture. It was found that even when the mixture was left in a scintillation vial on the benchtop for 7 days, no visible solid formed, so it was determined that this should be a sufficient method for creating a liquid reactant mixture that could be injected into the continuous flow system without and major issues.

4.4.2 The Breakdown of CuBTC in the Friedländer System

When performing the Friedländer synthesis under continuous flow conditions, a major unexpected observation was made: the eluent being collected would start off green but would then

turn blue. The green color was consistent with what was observed during the reaction being run in batch conditions, however, the blue was new and was only seen starting in fraction 2 of running the reaction under continuous flow conditions. After running the 10 equivalents of the reaction through the continuous flow system, this was consistent in each instance of the reaction. Even more shockingly though, when the column was opened at the end of running the 10 equivalents of the reaction through, there was little to no solid left inside the column that was originally packed with over half a gram of the CuBTC MOF. Upon close inspection of the fractions that were collected, there were small, blue particles that appeared to be crystalline in some of the fractions, typically fractions 1-6. These observations led me to hypothesize that the CuBTC was being broken down by something in the system.

4.4.2.1 Further Investigations into the CuBTC MOF Still in Column After Undergoing Friedländer Synthesis

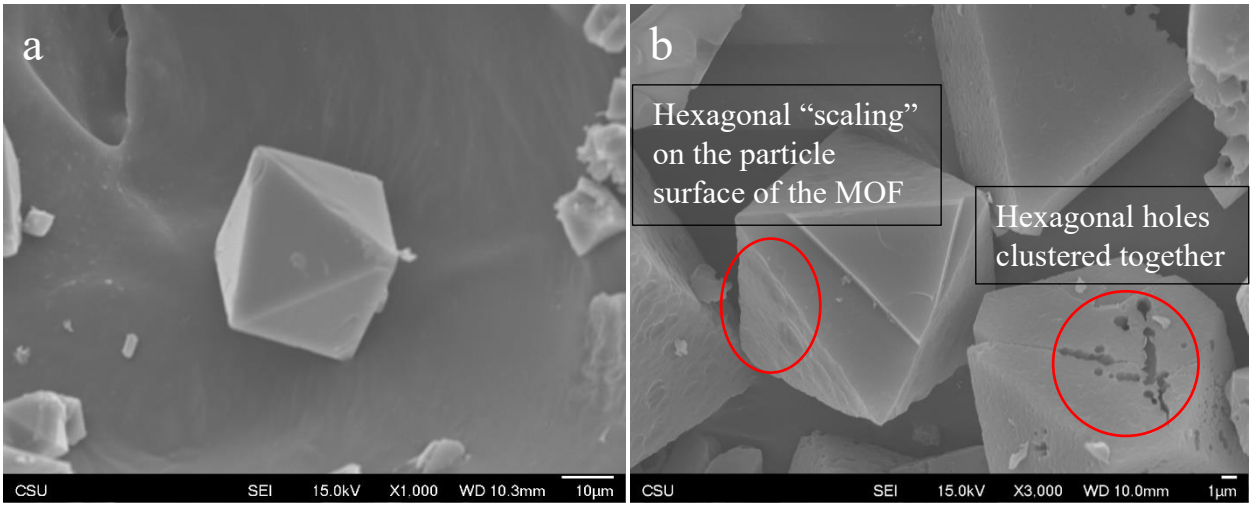

Figure 4.5. SEM images taken of: (a) CuBTC right after it has been synthesized and washed with ethanol. Note the particle surface appears to be smooth. (b) CuBTC that has been used for the Friedländer synthesis under continuous flow conditions and then washed with ethanol. Note how the surfaces of the MOF particles appear rough and the surfaces now has "scaling" (where parts of the MOF seem to have been shaved off in roughly hexagonal shapes) and possess hexagonal shaped holes.

Since it was shown that running 10 equivalents of the Friedländer synthesis would result in the loss of all of the CuBTC MOF packed into the column, experiments were done using only 1 equivalent and 7 equivalents of the Friedländer synthesis under continuous flow synthesis. This led to very interesting results, where the CuBTC MOF that was still inside the column after it had been used to run the Friedländer Synthesis under continuous flow had hexagonal-shaped holes in the MOF particles, indicating that there was breakdown of the MOF (Figure 4.5). The Friedländer synthesis was then performed under batch conditions at various time points to see if it was possible to catch the MOF particles with the hexagonal shaped holes in them when run under batch conditions as well. This would show that the breakdown of the CuBTC due to the reaction itself and not due to performing the reaction using continuous flow conditions. These results are what

redirected this study towards understanding the system and determining "if CuBTC is being broken down by the Friedländer synthesis, and if so, how/why" and "is CuBTC actually the catalyst of the Friedländer synthesis in this system" rather than developing the Friedländer synthesis to progress under continuous flow conditions. It also brings into question whether the catalysis happening in this system is homogenous or heterogeneous.

4.4.2.2 Using CuBTC for One Equivalent of the Friedländer Synthesis Under Continuous Flow Conditions

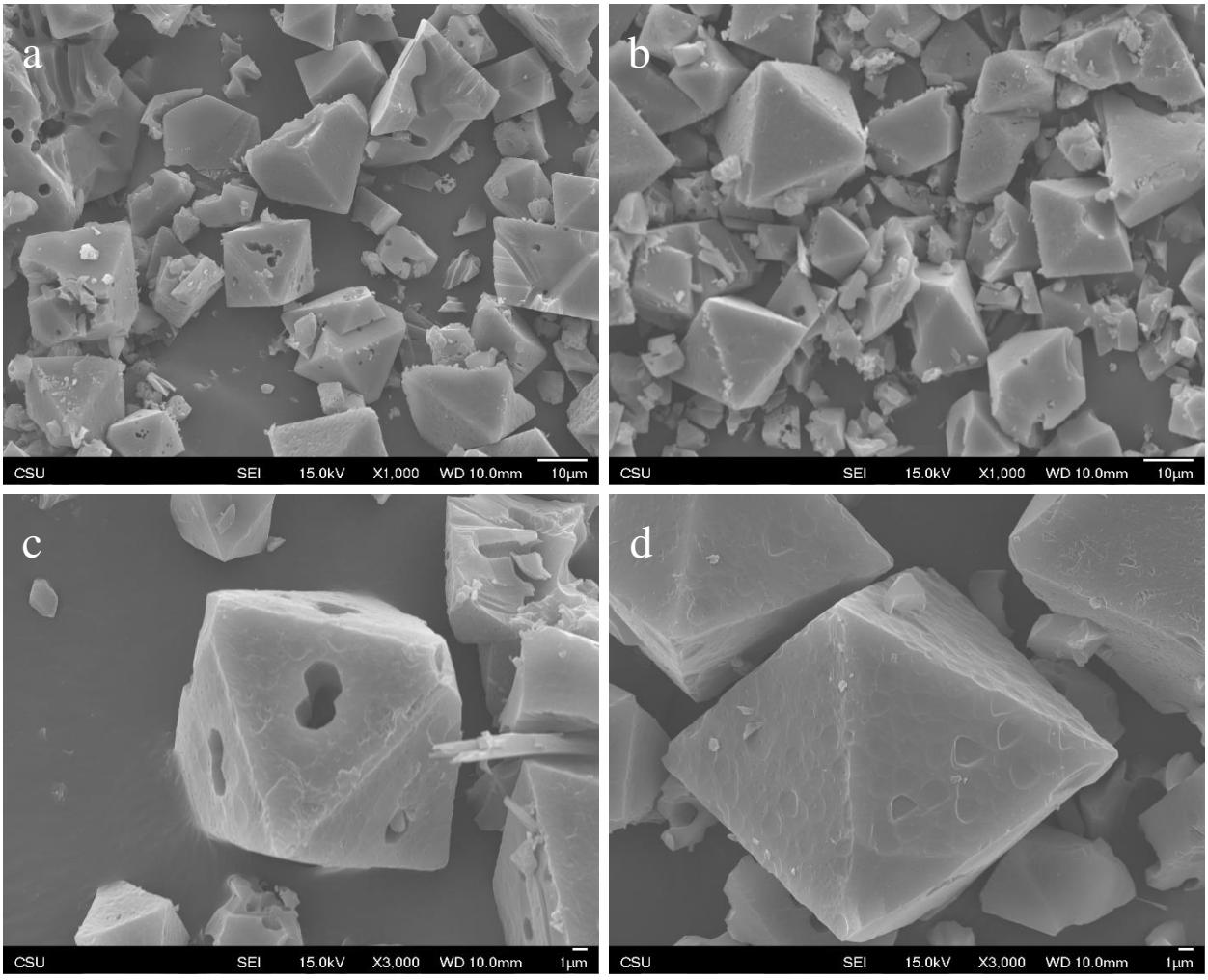

Figure 4.6. SEM images showing the scaling and hexagonal holes on CuBTC MOF particles after they were used for one equivalent of the Friedländer synthesis under continuous flow conditions.

After performing one equivalent of the Friedländer synthesis under continuous flow conditions using CuBTC packed directly into a column, most of the CuBTC (roughly 90% left, by visual inspection) was still present in the column. From the SEM images, it can be seen that even with only one equivalent of the reaction being run through about half a gram of CuBTC MOF, there is already evidence of the MOF being broken down (Figure 4.6). From these images, it can be seen that most, if not all particles have begun the process of breaking down, having this "scaling" effect appear, creating a rougher surface. Many particles can also be seen developing hexagonal-shaped holes. In Figure 4.6a and 4.6b, the SEM images show that most of the particles do not seem to possess the hexagonal shaped holes. However, in all of the SEM images, especially with the higher magnification from Figure 4.6c and 4.6d, the MOF particles possess the "scaled" surface which is hypothesized to be the initial step towards the breakdown of the CuBTC MOF before the hexagonal shaped holes are formed. The hexagonal holes in the MOF particles were all sized at about 2 μm or below.

The eluent from these reactions, when collected in 4 mL fractions, start off green, but by fraction 2 turn blue. The blue coloration is indicative that copper is making it through the column and being collected in these fractions. It should be noted however that since the reaction mixture starts of yellow, it is possible that the green coloration observed in the first fraction could be due to the presence of the reactant mixture (yellow) with the copper (blue) to produce the green solution observed. Based on the fact that parts of the CuBTC MOF seems to have broken off, leaving the "scaling" and hexagonal shaped holes, it is hypothesized that the breakdown of the CuBTC MOF happens fairly quickly as after ~5 mL has been run through the column, the blue coloration and small, blue particles already appear in the collected fractions.

4.4.2.3 Using CuBTC for Seven Equivalents of the Friedländer Synthesis Under Continuous Flow Conditions

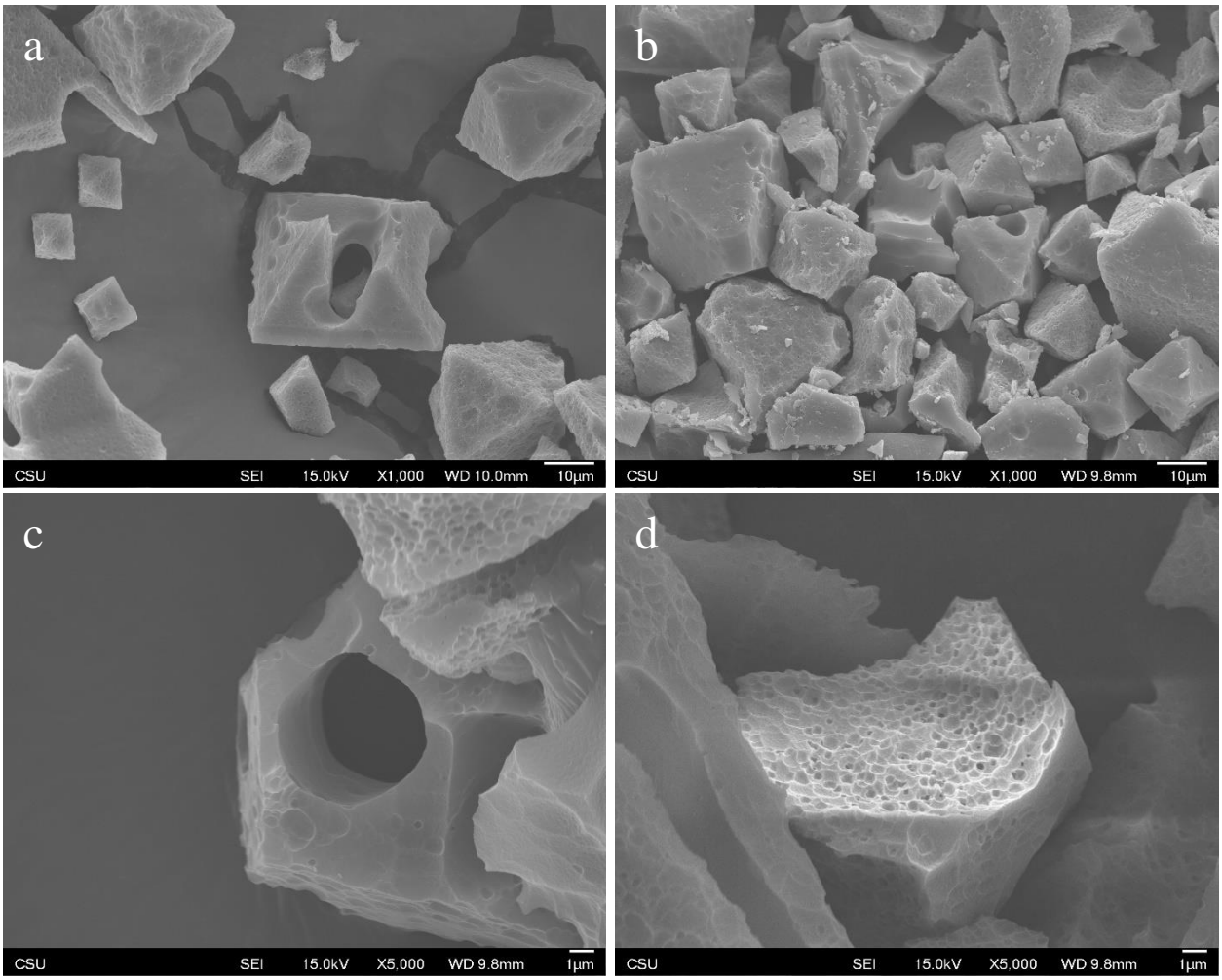

Figure 4.7. SEM images showing the scaling and hexagonal holes on CuBTC MOF particles after they were used for seven equivalents of the Friedländer synthesis under continuous flow conditions.

After performing seven equivalents of the Friedländer synthesis under continuous flow conditions using CuBTC, most of the CuBTC that was originally packed in the column would have disappeared from the column (roughly 20-30% left, by visual inspection). Relative to the SEM images seen in Figure 4.6, a more thorough breakdown of the CuBTC MOF can be seen (Figure 4.7). In Figures 4.7a and 4.7c, you can see the MOF particles that have been tunneled through

entirely while still retaining some small resemblance of the original octahedral morphology. In general, these hexagonal holes were bigger than those observed when only 1 equivalent of the Friedländer synthesis was performed using CuBTC, with many of these hexagonal holes being 2 μm or larger. However, it can be noted that in general, there are fewer holes observed in general and it is hypothesized that this is due to the fact that the holes broke apart the MOF particles entirely (as observed in the bottom right SEM image) and/or had joined together to form larger holes.

4.4.2.4 pXRD of the CuBTC After Being Used for the Friedländer Synthesis Under Continuous Flow Conditions

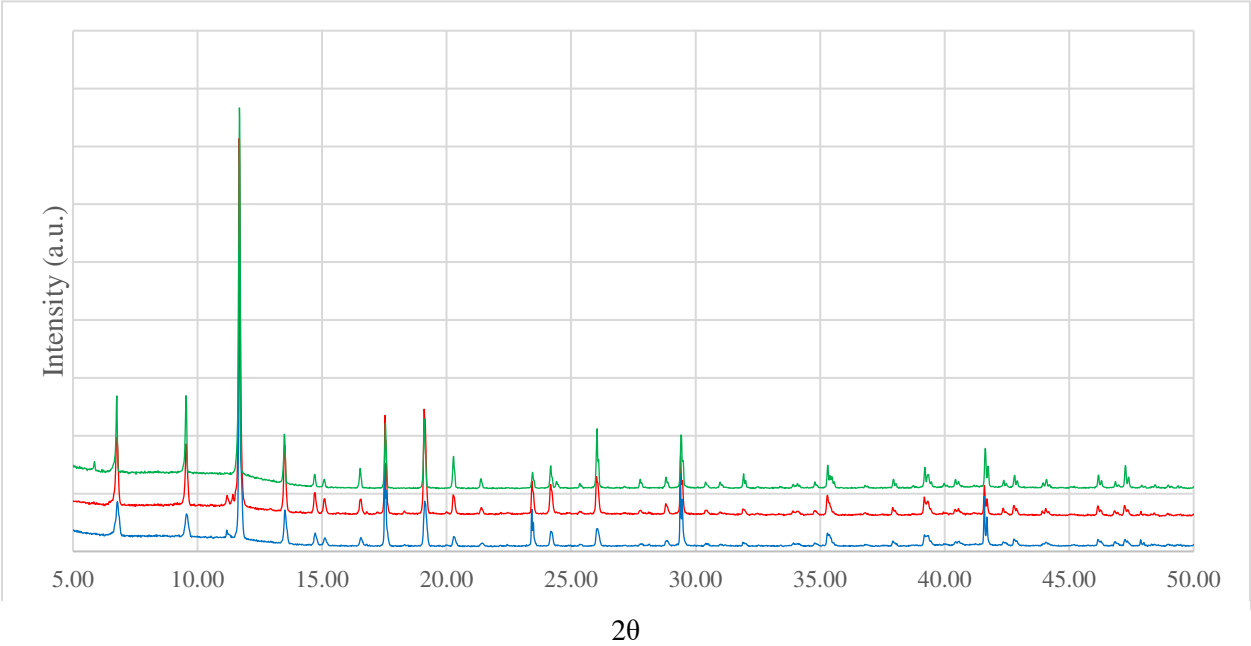

Figure 4.8. pXRD of CuBTC after it was just synthesized, washed, and dried (green), CuBTC from the column after it was used for 1 equivalent of the Friedländer synthesis under continuous flow conditions (red), and CuBTC from the column after it was used for 7 equivalents of the Friedländer synthesis under continuous flow conditions (blue).

When the CuBTC that was used in the continuous flow system was analyzed and compared to fresh CuBTC using pXRD (Figure 4.8), it can be seen that there is very little change in the diffraction pattern with only some minor changes in the ratios between some signals. These slight

changes in signal ratios would be consistent with the fact that the CuBTC particles are breaking down bit by bit, but the bulk of the crystal is still intact, thus diffracting in the same way as fresh CuBTC. This is also consistent with the pXRD data from the literature, showing that the bulk of the MOF is still intact after being used for the Friedländer synthesis. However, from the SEM data, we know for a fact that the MOF particles are not wholly intact still and that there is breakdown of the MOF particles that cannot be seen using x-ray diffraction as there are still crystalline particles to diffract.

4.4.2.5 Friedländer Synthesis with CuBTC Under Batch Conditions for 24 Hours

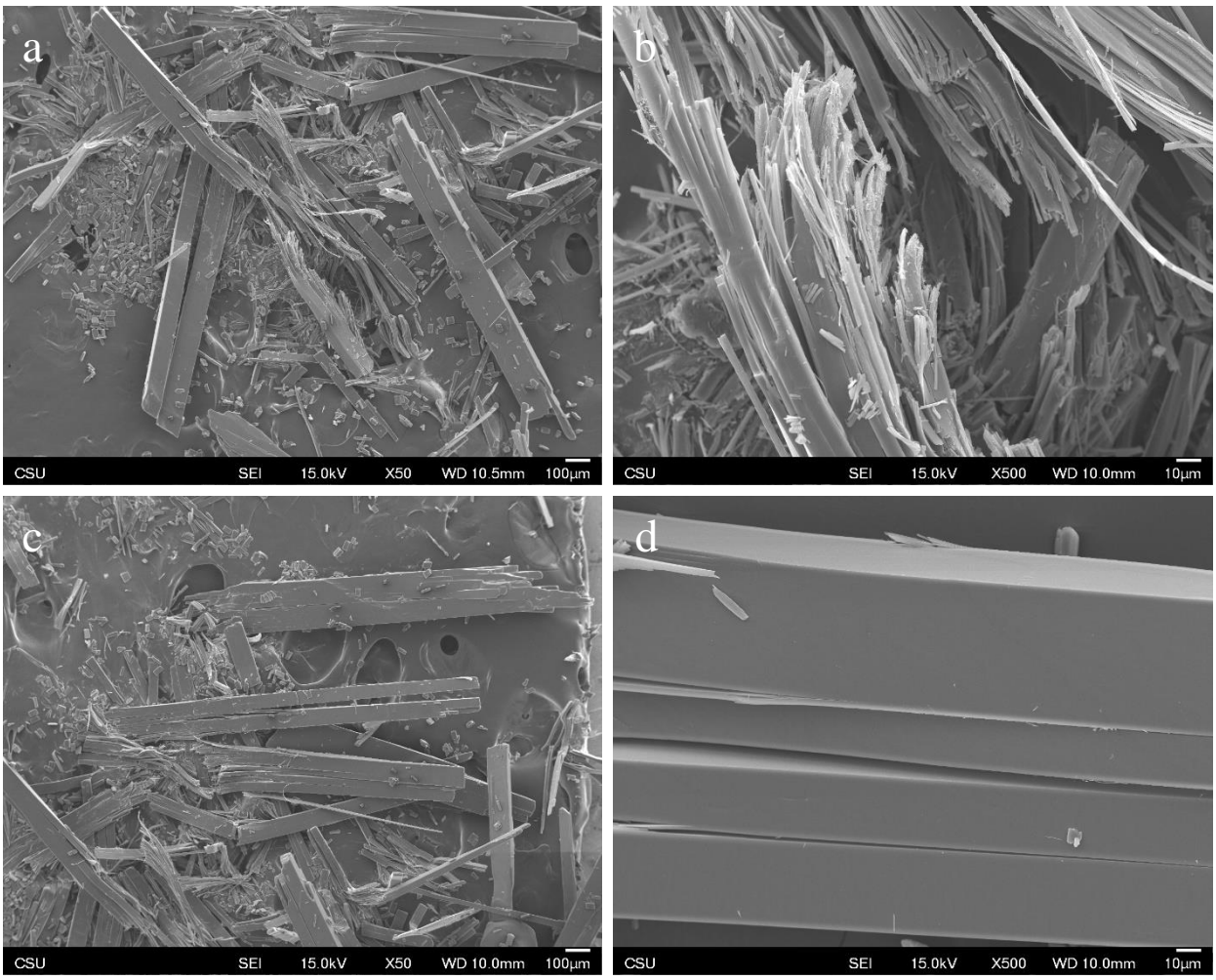

Figure 4.9. SEM images showing the solids isolated and collected from running the Friedländer synthesis under batch conditions for 24 hours.

In an attempt to see if the CuBTC MOF particles with "scaling" and the hexagonal holes were from how the reaction was performed or whether an artifact of the reaction itself, the Friedländer synthesis with CuBTC under batch conditions. After 24 hours of heating, the blue solids "unidentified crystals" that formed during the reaction were collected, washed, and dried before they were imaged using SEM. Under SEM, there are clear differences, the most profound differences being the size and shape of the particles.

The CuBTC synthesized with the method described in this work generally produces particles in the 10-20 μm range. However, to the naked eye, these crystals obtained from running the Friedländer synthesis for 24 hours resemble blue needles, whereas CuBTC MOF typically looks like a fine blue powder. Under SEM, in Figure 4.9, the particles seen are several hundred μm (many reaching into mm range) at their longest length. The SEM image in Figure 4.9d is representative of what these particles look like when zoomed in and this is consistent across the entire particle, indicating that these long particles are indeed a singular particle and not multiple particles clustered together.

When synthesized using traditional solvothermal methods, CuBTC forms into octahedra. However, there were no octahedra to be found anywhere in these samples, rather, they are long, rectangular particles, some of which look like they have been shredded or ripped apart at the ends (especially in Figure 4.9b). This drastic difference from that of CuBTC coupled with the fact we have seen CuBTC being broken down when used for the Friedländer synthesis under continuous flow conditions leads me to hypothesize that these particles are not actually CuBTC.

These differences lead me to hypothesize that there is a chemical-level breakdown of the CuBTC that occurs when it is in the presence of the Friedländer synthesis followed by a recrystallization of those broken-down parts of CuBTC into these crystals. However, further experiments would be required to confirm this hypothesis and if shown to be true, whether:

I. CuBTC is indeed broken down on a chemical level

II. What CuBTC is broken down into – is it just fragmented into small MOF particles or is it being chemically broken down and changed into another compound entirely and if so, what is this compound and is it the actual catalyst for the Friedländer synthesis in this system?

III. What these new crystals are – whether they are intermediates of the reaction or some other unidentified byproduct

As of now, it is hypothesized that these crystals are some copper-containing intermediate of the Friedländer synthesis and/or the actual catalyst that is being used in the catalytic cycle of the Friedländer synthesis.

This does not however address the initial goal of trying to see if the CuBTC with the rough, "scaled" surfaces and hexagonal holes were being produced by the Friedländer synthesis itself or not. Based on the observations that were made however, it was hypothesized that 24 hours may be too long of an exposure time to the conditions used for the Friedländer synthesis as under continuous flow conditions, the exposure time is very short. To remedy this, the reaction time was shortened down to 30 minutes to see if that would allow us to see results consistent with what was seen under continuous flow.

4.4.2.6 Friedländer Synthesis with CuBTC Under Batch Conditions for Thirty Minutes

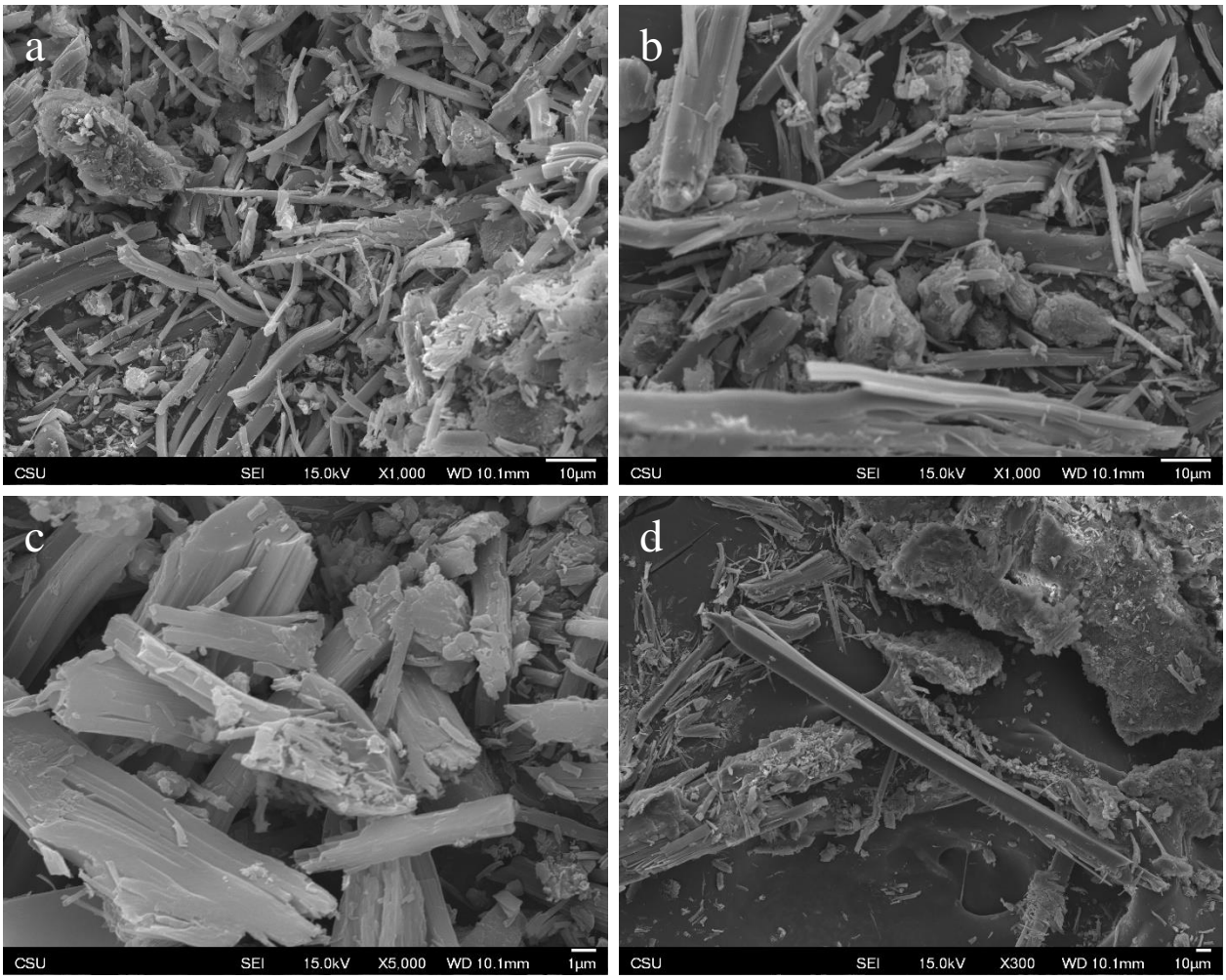

Figure 4.10. SEM images showing the solids isolated and collected from running the Friedländer synthesis under batch conditions for 30 minutes.

When shortened down to 30 minutes, the CuBTC used to run the Friedländer synthesis under batch conditions were again, not observed visually. In the SEM images (Figure 4.10), there are no particles that bear any resemblance to the octahedra expected of CuBTC. The majority of the particles observed have similar morphologies to those seen in Figure 4.9, being long and rectangular. Most of these particles were smaller though, the majority ranging from 1 µm -100 µm, though some were well over 100 µm (like the particle seen in Figure 4.9d, though these were few). The presence of the several small particles supports the hypothesis that there is a chemical

breakdown of the CuBTC and that these particles are different crystals that are being newly grown. Again however, no octahedra or particles resembling pieces of an octahedra are observed and no particles seem to possess a similar "scaling" effect, or the hexagonal holes seen from the CuBTC used under continuous flow conditions. So, the amount of reaction time was again reduced, this time to 15 minutes.

4.4.2.7 Friedländer Synthesis with CuBTC Under Batch Conditions for Fifteen Minutes

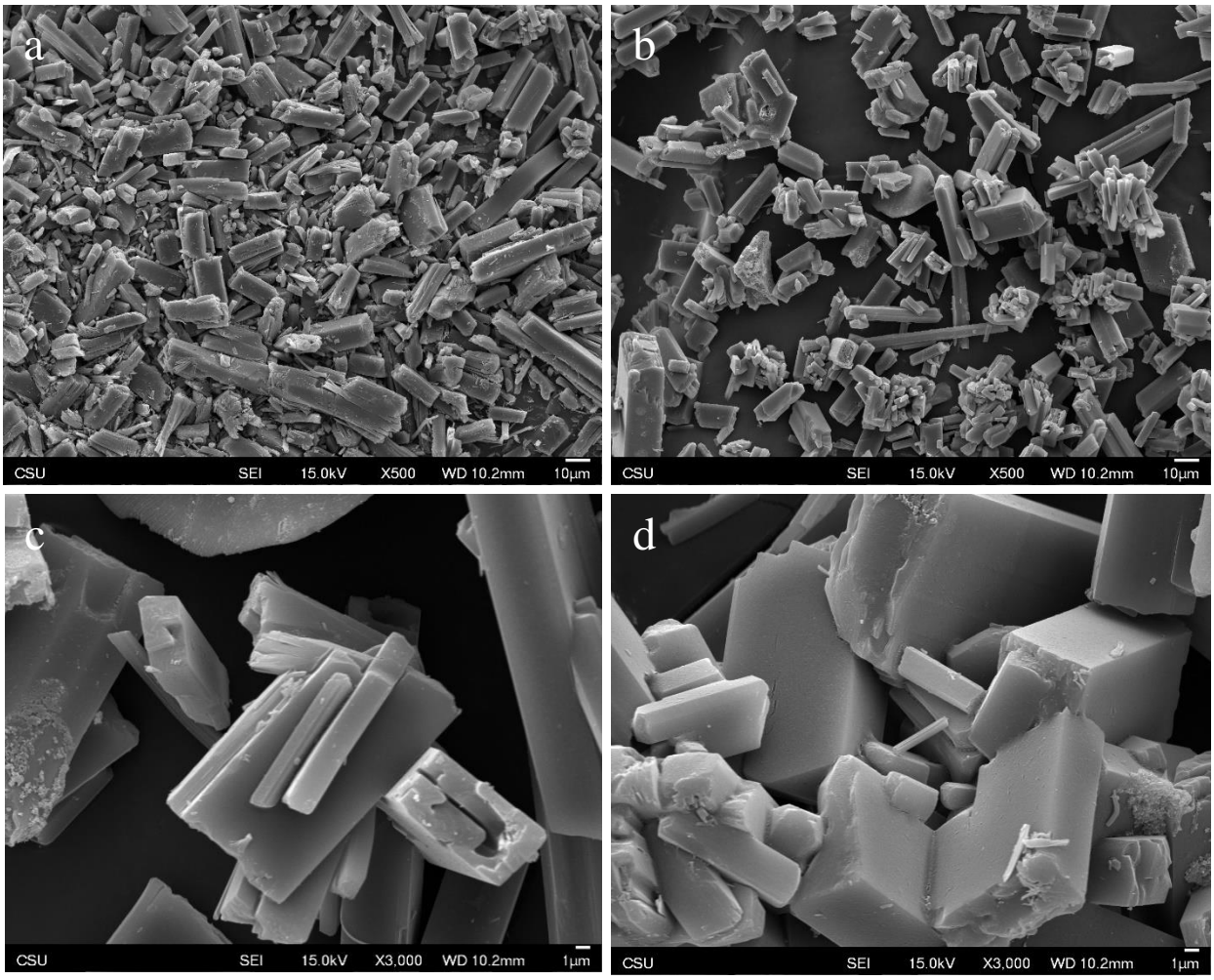

Figure 4.11. SEM images showing the solids isolated and collected from running the Friedländer synthesis under batch conditions for 15 minutes.

When shortened down to 15 minutes, the CuBTC used to run the Friedländer synthesis were still not seen in the SEM images (Figure 4.11). In the SEM images, there are no particles

that resemble the octahedra expected of CuBTC. The majority of the particles observed here have morphologies that resemble small, rectangular pellets, mostly ranging from 1 μm – 50 μm. However, there were some areas that had particles like those seen in Figure 4.11d, where they look almost cubic and a single side with a rough edge, while the others are very smooth. Based on size however, these are likely to just be broken pieces of the rectangular pellets that clustered together. Further experimentation would be required to definitively determine whether this is the case or not, however. The main point that can be taken from this though is that none of these particles resemble octahedra or pieces of an octahedra and none of the particles resemble the "scaling" or hexagonal holes seen from the CuBTC obtained after being exposed to the Friedländer synthesis under continuous flow conditions. Because of this, the reaction time was again shortened, this time down to 1 minute.

4.4.2.8 Friedländer Synthesis with CuBTC Under Batch Conditions for One Minute

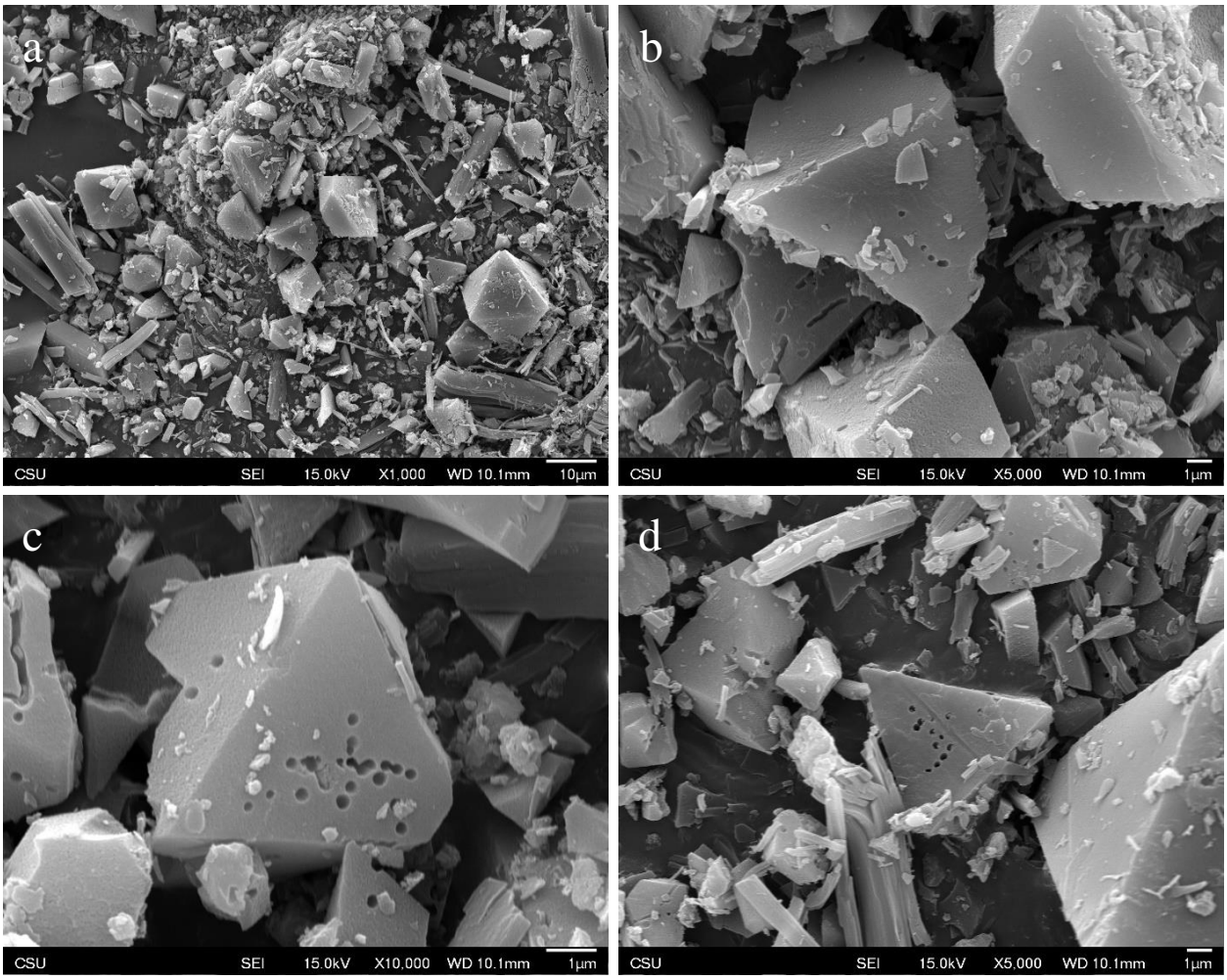

Figure 4.12. SEM images showing the solids isolated and collected from running the Friedländer synthesis under batch conditions for 1 minute.

When shortened down to a runtime of 1 minute, the CuBTC used to run the Friedländer synthesis could be seen as deformed octahedral particles. While most of the particles seen in the SEM images (Figure 4.12), didn't resemble the octahedra of the CuBTC, resembling the rectangular particles seen in Figures 4.9, 4.10, and 4.11 (as seen in Figure 4.12a and 4/12d), there were still some remnants of the octahedra to be found in the sample. Some of the rough, "scaling" effect can be seen on these particles and several of the hexagonal holes are present on the particles throughout each of the image sin Figure 4.12. It can also be seen that almost none of these particles

are whole octahedra anymore and are just pieces of the octahedra broken off. The formation of the rectangular particles seen in Figure 4.9 and 4.11 can also be found throughout the sample, indicating that the breakdown of the CuBTC octahedra and the formation of these rectangular particles happen very quickly (under 1 minute after the reaction mixture is heated). These images confirm that the breakdown of CuBTC in this way is not due to the fact the Friedländer synthesis was being performed under continuous flow conditions with the CuBTC but is likely a result of the Friedländer synthesis itself as they can be found after performing the Friedländer synthesis under batch conditions.

To further confirm this claim, experimental controls would need to be conducted where CuBTC is subjected to the same conditions used to perform the Friedländer synthesis that causes it to break down with each of the reagents being removed. These controls would provide evidence to show that the reagents themselves do not cause the breakdown of the CuBTC used in the reaction and that only when the Friedländer synthesis itself is being performed with those reagents that the MOF breaks down in this way.

4.4.2.9 Friedländer Synthesis with CuBTC Under Batch Conditions for Forty-Eight Hours

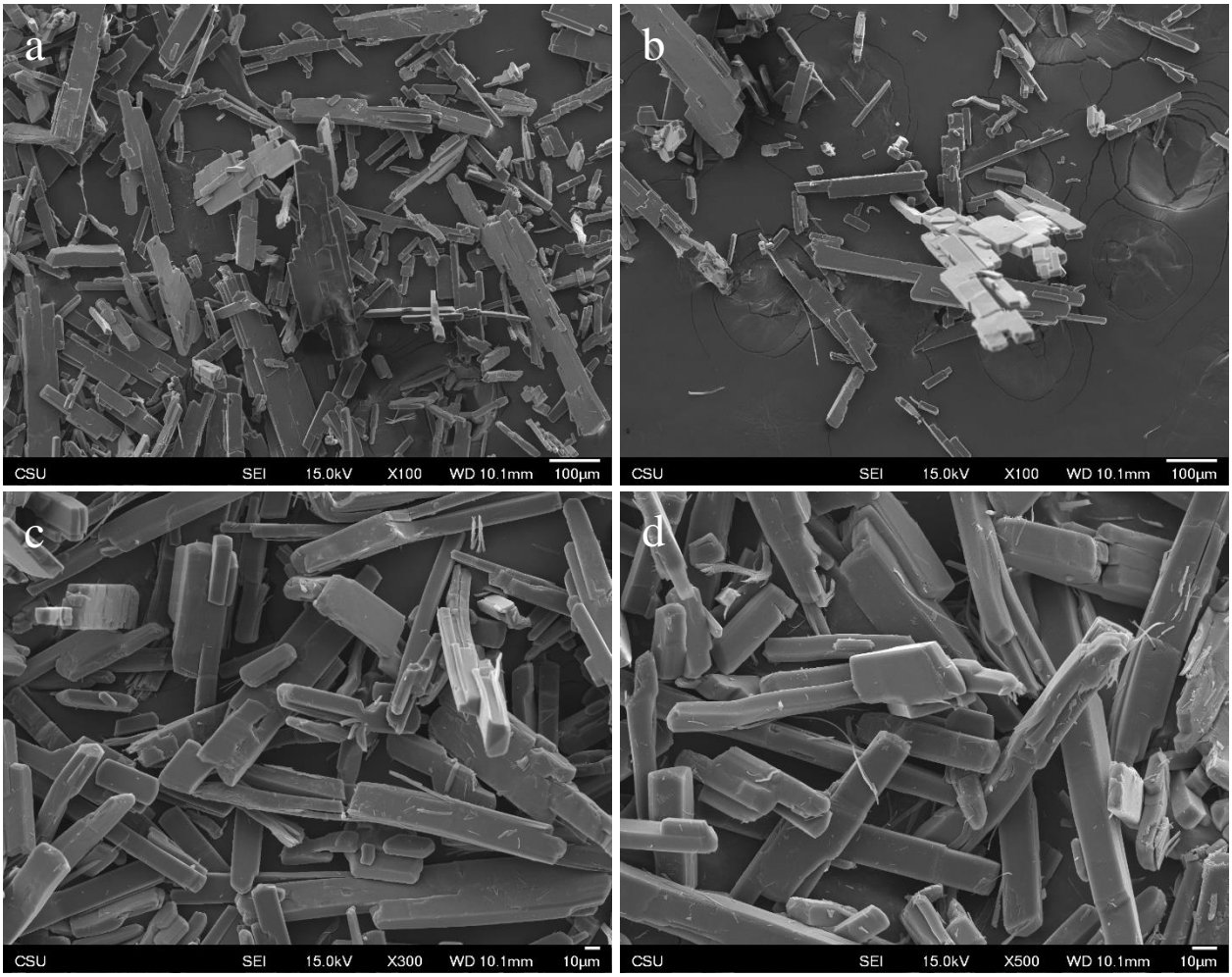

Figure 4.13. SEM images showing the solids isolated and collected from running the Friedländer synthesis under batch conditions for 48 hours.

To see if CuBTC octahedra would have the potential to reform if given enough time after the reaction should have run to completion, the reaction was allowed to run for 48 hours. However, it can be seen in the SEM (Figure 4.13) that when given 48 hours, no semblance of the CuBTC octahedra had reformed. Instead, the same rectangular particles are still present though as whole, they are larger than the particles seen after 24 hours. Interestingly, in Figure 4.13a and 4.13b, you can see what looks like separate particles coming together and forming a single, larger particle. This leads me to hypothesize that the particles likely go through a process where they form many

small particles (as seen in Figures 4.9, 4.11, and 4.12) and then come together, recrystallizing into larger particles as seen here.

4.4.2.10 Friedländer Synthesis with CuBTC Under Batch Conditions for Seventy-Two Hours

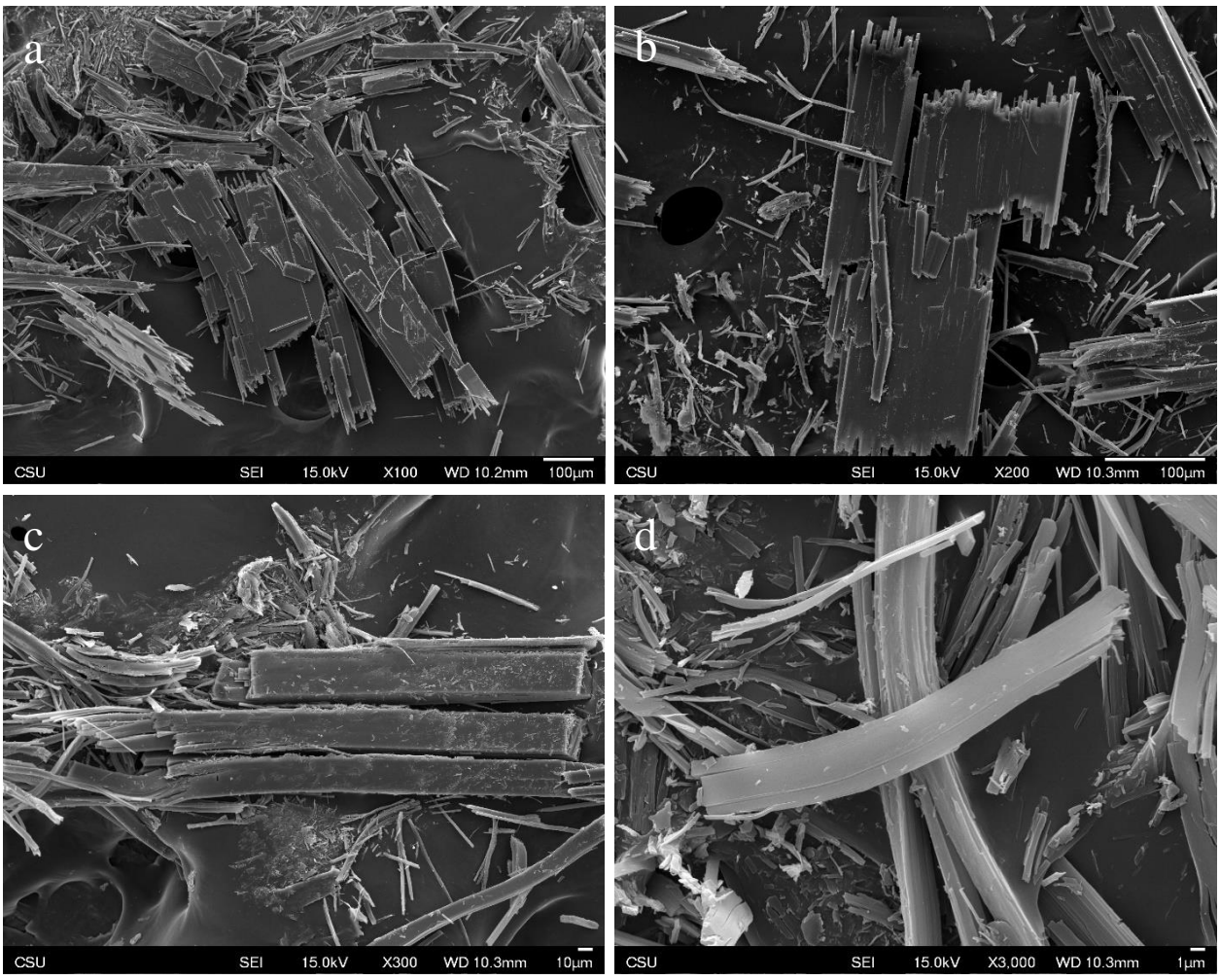

Figure 4.14. SEM images showing the solids isolated and collected from running the Friedländer synthesis under batch conditions for 72 hours.

To give an excessive amount of time for CuBTC to potentially reform, the reaction was again run, this time for 72 hours. From the SEM images (Figure 4.14), it is clear to see that there is no indication that the CuBTC octahedra are being reformed. Instead. The rectangular particles are now much bigger as a whole, many being much wider than we have seen previously, where they are surpassing 100 µm in width where they were typically 10-20 µm wide after 48 hours.

Similar to the images seen after 48 hours (Figure 4.13), you can see that it looks like many of the long rectangular particles are recrystallizing into each other to form these much larger rectangular structures. In the image on the bottom right, you can even see a particle where it looks like it has mostly fused into the larger particle, but notice that it has not yet fully done so at the ends.

Another key point to note is that since CuBTC does not seem to have reformed, it is unlikely that there are free-floating Cu centers or ligands from broken down CuBTC. While it is expected that the CuBTC is broken down due to these SEM images, none of the components seem to be present in the end solution as the conditions used in the reaction are very similar to those used in synthesizing the CuBTC. While not definitive and further experimentation would be required to confirm this, this hypothesis does have some evidence suggesting that it may be true. If true, it would be key to then identify where those components are to work towards understanding the breakdown of CuBTC in this process. Achieving that understanding would then allow for this process to be modified so that it could potentially work under continuous flow conditions as intended or even better understand the stability of CuBTC MOF.

4.4.2.11 Analysis of the Blue Solids ("Unidentified Crystal") Collected from Batch Conditions Using X-Ray Diffraction

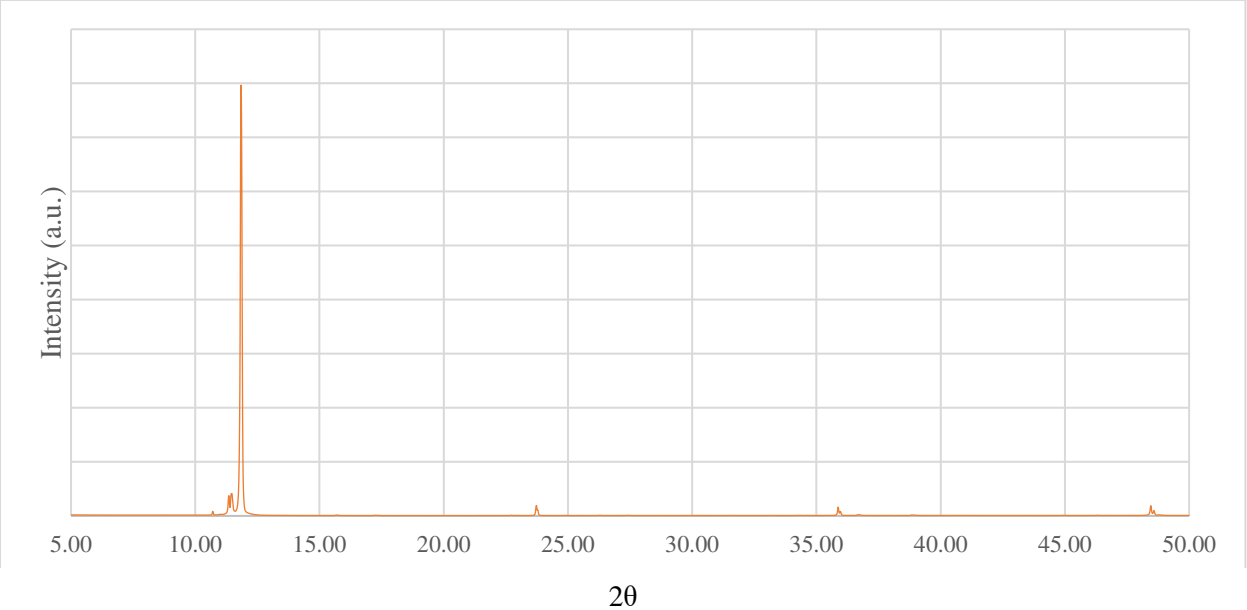

Figure 4.15. Representative pXRD of the blue solid "unidentified crystal" after it had Friedländer synthesis was performed with CuBTC under batch conditions for 24 hours. Diffraction patterns of the blue solid "unidentified crystals" obtained from the other experiments produced similar diffraction patterns.

As a different particle morphology doesn't definitively confirm that these "unidentified crystals" obtained from running the Friedländer synthesis under batch conditions were not CuBTC, pXRD was done to determine the crystal structure of these particles. The diffraction pattern obtained (Figure 4.15) was drastically different from that seen for CuBTC, indicating that the crystals obtained after the Friedländer synthesis was performed were different than the CuBTC initially used. In this diffraction pattern, one major signal is observed at 11.82 2θ with some minor peaks, indicating that the crystal structure is extremely uniform throughout the particle.

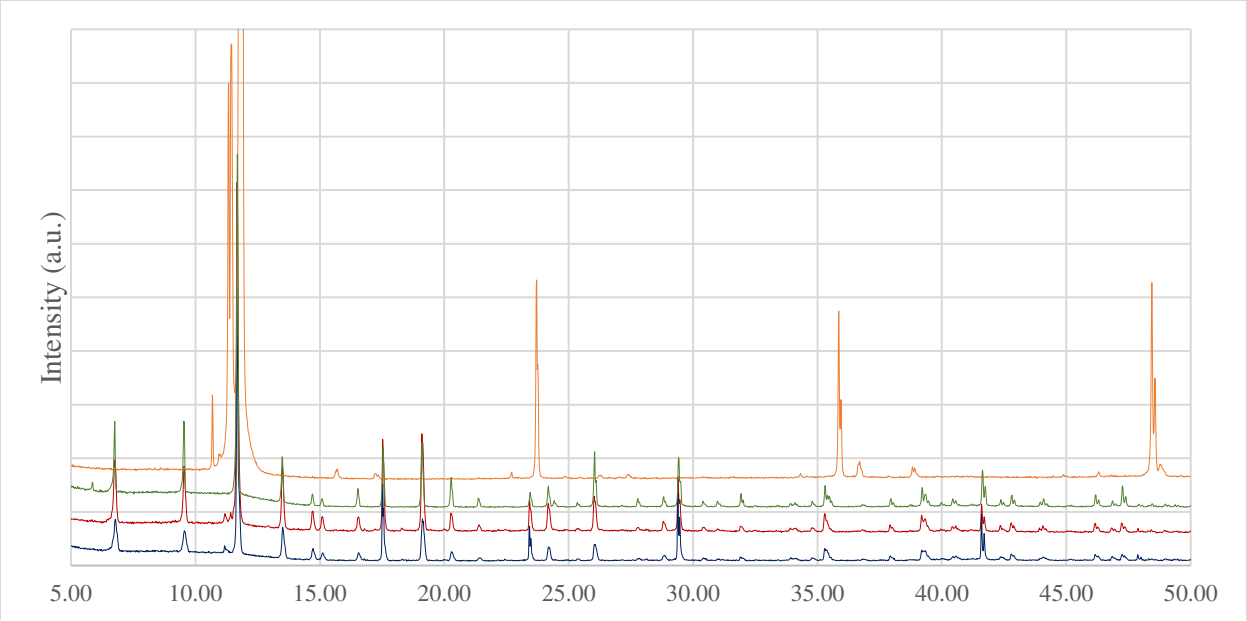

Figure 4.16. Representative pXRD of the blue solid "unidentified crystal" after it had Friedländer synthesis was performed with CuBTC under batch conditions for 24 hours (orange) overlaid on top of pXRDs of CuBTC after it was just synthesized, washed, and dried (green), CuBTC from the column after it was used for 1 equivalent of the Friedländer synthesis under continuous flow conditions (red), and CuBTC from the column after it was used for 7 equivalents of the Friedländer synthesis under continuous flow conditions (blue). It should be noted that the diffraction pattern for the blue solid "unidentified crystal" is zoomed in to ensure the other diffraction patterns were clearly visible and so the majority of the major peak at 11.82 2θ has been cut off.

In comparison to the diffraction patterns of CuBTC (Figure 4.16), it can be seen that the blue solid "unidentified crystal" has a very different crystal structure. Essentially, none of the peaks from the diffraction pattern of the blue solid "unidentified crystal" match up with any of the peaks from the CuBTC in respect to the 2θ or peak ratios. The major peaks of each of the diffraction patterns are all around the 11-12 2θ area, but if you look closely, you can see that the peaks of the CuBTC that was freshly synthesized and from the inside of the column when the Friedländer synthesis was performed under continuous flow conditions peak at slightly different points (you can see the CuBTC peaks appearing in between two of the peaks from the blue solid "unidentified crystal" at a 11-12 2θ area). This confirms that the blue solid "unidentified crystal"

is of a different identity relative to CuBTC MOF and that it only appears in the eluent collected from performing the Friedländer synthesis using the continuous flow system and the remaining solution from the Friedländer synthesis when run using batch conditions.

4.4.3 Investigations into the Blue Solids ("Unidentified Crystal") Collected in the Eluent After Undergoing Friedländer Synthesis Under Continuous Flow

4.4.3.1 Analysis of the Fractions Collected from Performing the Friedländer Synthesis with CuBTC Under Continuous Flow Conditions

When the Friedländer synthesis was performed under continuous flow conditions using the CuBTC column, the eluent was collected in 4 mL fractions and then analyzed using TOF-MS. Representative mass spectra are shown to provide examples of what different fractions looked like, showing each of the major peaks that appeared (Figure 4.17). In these spectra, there were major peaks that could not be directly linked to the reactants or expected products (Figure 4.17a and 4.17b). Instead, these are peaks tentatively identified with intermediates of the Friedländer synthesis being performed suggesting that the elution of the reagents/product is not at the expected rate.

It would be expected that since only about 4 mL of the reaction mixture is injected, it should be collected within the first two fractions as that would mean 8 mL of eluent has been collected. However, the fractions collected are still observed to be blue, suggesting that copper (and potentially other compounds) are still coming off of the column, even after the reactant mixture should have already have completely eluted from the column. This suggests that the reactants are interacting with the CuBTC in the column, likely breaking it down, and causing a copper-containing compound to elute from the column, resulting in the blue eluent. The hypothesis that

the compounds eluting from the column contain copper are supported by the TOF-MS data as there are peaks that suggest the presence of copper.

In the first spectrum (Figure 4.17a), a tentative structure was put together was constructed for the major peak observed in the first fraction collected when running the Friedländer synthesis under continuous flow conditions, based on the observed *m/z*. Due to the presence of the m_1 and m_1+2 peaks, it is expected that copper (due to copper isotopes adding 2 to the observed mass) must be present in this structure and the predicted structure provided was constructed with that in mind (Figure 4.17a).[47,48] This structure is based on one of the expected intermediates of the Friedländer synthesis being performed, so if true, it would mean that it is likely that the reagents did not have enough time to reach the desired product with the conditions being used while fraction 1 was being collected.

It is important to note that in Figure 4.3, the control of the Friedländer synthesis performed based on the conditions reported in the literature, there is also a peak at 308 *m/z* with a shoulder (at 310 *m/z*). The fact that this peak is also present in the control experiment supports the idea that this is likely a copper-containing intermediate of the reaction as it is now observed as a peak when performing the Friedländer synthesis under batch conditions and under continuous flow conditions.

In the second spectra (Figure 4.17b), a tentative structure has been proposed for the major peak observed in sixth fraction collected, again based on the observed *m/z* of 308 (and 310). The m_2 and m_2+2 peak pattern is observed again, so the predicted structure was constructed with that in mind again. This structure was also based on an expected intermediate based on the expected reaction mechanism of the Friedländer synthesis being performed with a copper and BTC ligand still attached to it. This is consistent in the sense that this intermediate should also only appear

after the intermediate hypothesized to be present in fraction 1 based on the reaction mechanism. Since the CuBTC is observed to be breaking down, the presence of the ligand as part of this predicted structure would also be consistent with the fact that no free ligand is observed to be present in any of the fractions based on the spectra obtained.

In the third spectra (Figure 4.17c), it is predicted that the ninth fraction collected now contains the desired product with a sodium ion attached to it (284 *m/z*). Again, based on the sequence of the fractions and the proposed reaction mechanism, it would be possible that the product did not fully form under the conditions used to perform the Friedländer synthesis under continuous flow before ~32 mL of the reaction mixture and solvent eluted and only starting at fraction 9 do we see product come off of the column.

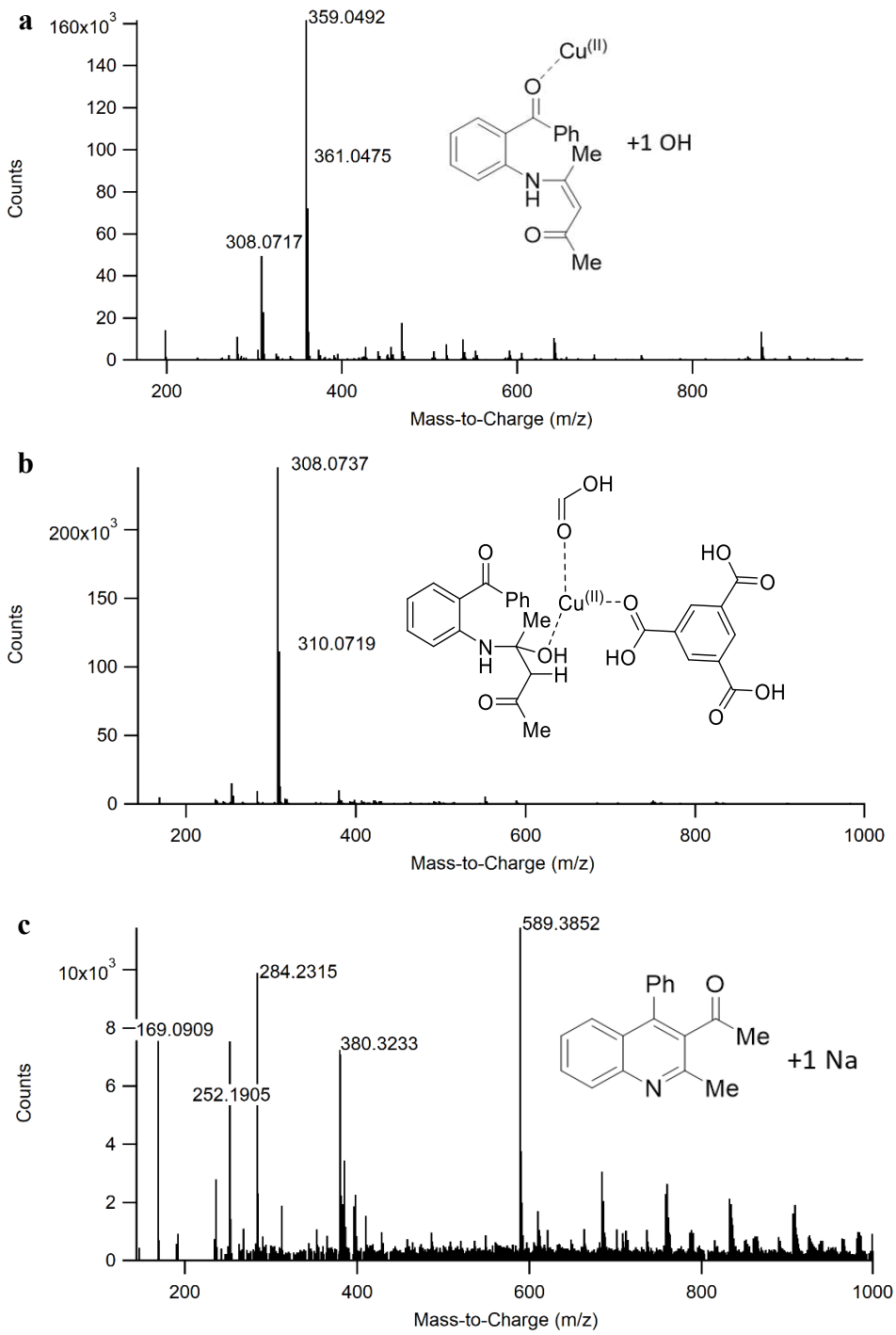

Figure 4.17. Mass spectra obtained from (a) fraction 1 of an equivalent of the Friedländer synthesis under continuous flow and a predicted structure for the peak at 359 (m_1) and 361 (m_1+2) *m/z*, (b) fraction 6 an equivalent of the Friedländer synthesis under continuous flow and a predicted structure for the 308 (m_2) and 310 (m_2+2) *m/z*, (c) fraction 9 of an equivalent of the Friedländer synthesis under continuous flow and the predicted structure of the 284 (m_3) *m/z*, which would match the desired product with a sodium ion. This figure was created with the help of Madeline C. Roach.

4.4.3.2 Comparing the Mass Spectrum Obtained for the Blue Solids ("Unidentified crystal") with the Collected Fractions

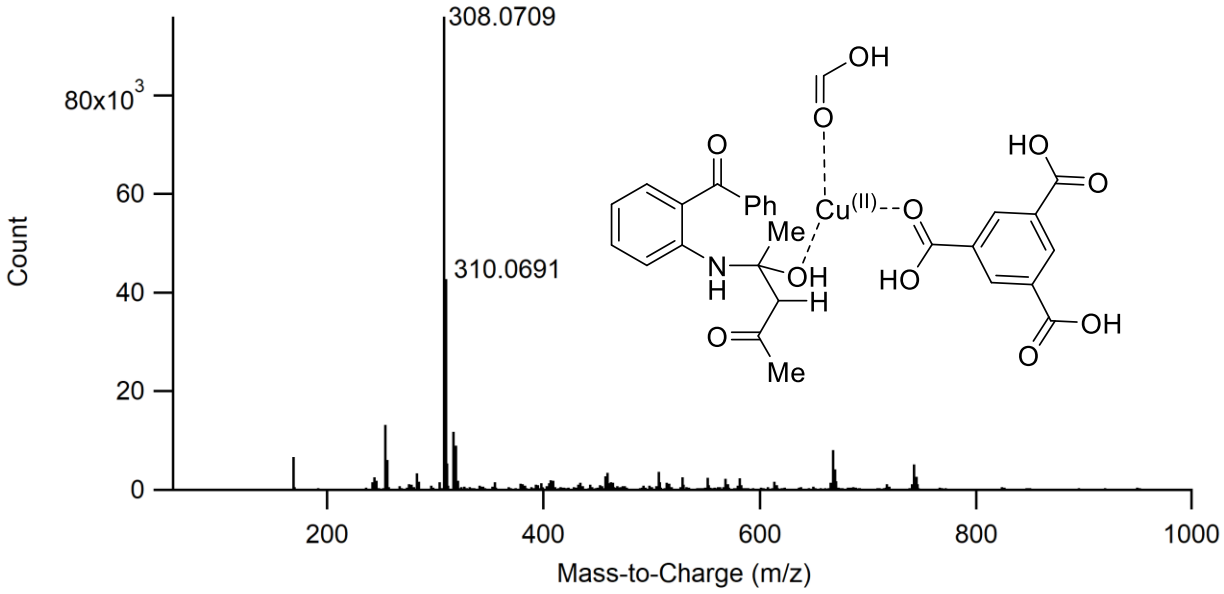

Figure 4.18. Mass spectra obtained from dissolving the blue solid ("unidentified crystal") in ethanol. A predicted structure for the 308 (m) and 310 (m_2+2) *m/z* is provided. This figure was created with the help of Madeline C. Roach.

Interestingly, when the "unidentified crystal" that can be collected when the Friedländer synthesis is performed in the presence of CuBTC under batch conditions and from some fractions when performed under continuous flow conditions, it can be dissolved in ethanol. Due to its solubility, mass spectra data was obtained (Figure 4.18) and it was found that the major peak observed matches the one observed in fraction 6 (Figure 4.17b).

The spectrum seen in Figure 4.18 possess the m and m+2 peaks (308 and 310 *m/*z), indicating that there is likely copper present in the compound. The fact that it recrystallizes out of solution suggests that there is a fairly stable compound. As stated earlier, it is hypothesized that the compound that is crystallizing out of solution is an intermediate of the Friedländer synthesis (hypothesized structure provided in Figure 4.18). The fact that this crystallized spontaneously at room temperature under static conditions out of some of the fractions collected when performing

the Friedländer synthesis under continuous flow conditions suggest that there is a high enough concentration of that specific compound in that fraction and that it is fairly pure to create such large (up to 4-5 mm in length) crystals. Furthermore, this supports a hypothesis where the Friedländer synthesis is occurring in the continuous flow column with in what seems to be like stages. The reagents adhere to the MOF, react, and then break off of the MOF particle, with some of them breaking off at certain stages of the reaction, allowing us to "see" the different steps of the reaction from the proposed mechanism through the collected fractions. However, further experiments (such as NMR, IR, and ultraviolet-visible (UV-Vis) spectroscopy) would be required to definitively identify this compound as MS alone is not enough to draw any concrete conclusions from in this case.

4.4.4 Towards Reidentifying the Catalyst in the System for the Friedländer Synthesis

As it was observed that the CuBTC is being broken down by the conditions used to perform the Friedländer synthesis and then confirmed that it does not reform, it is hypothesized that CuBTC is not actually the catalyst for the reaction and is instead, a pre-catalyst. In other words, I hypothesize that CuBTC is being broken down and in that process, the actual catalyst that is part of the catalytic cycle is created. These are some preliminary control experiments to try and determine what it might be.

4.4.4.1 Controls: Using Copper Nitrate Trihydrate

Since the CuBTC used in all of the experiments in this project were synthesized using copper nitrate trihydrate, it was a potential candidate as the catalytic agent in this system. Furthermore, it was stated in the paper from Pérez-Mayoral and Čejka that $Cu(NO_3)•3H_2O$ was just as effective as CUBTC for the catalysis of the Friedländer synthesis.[23]

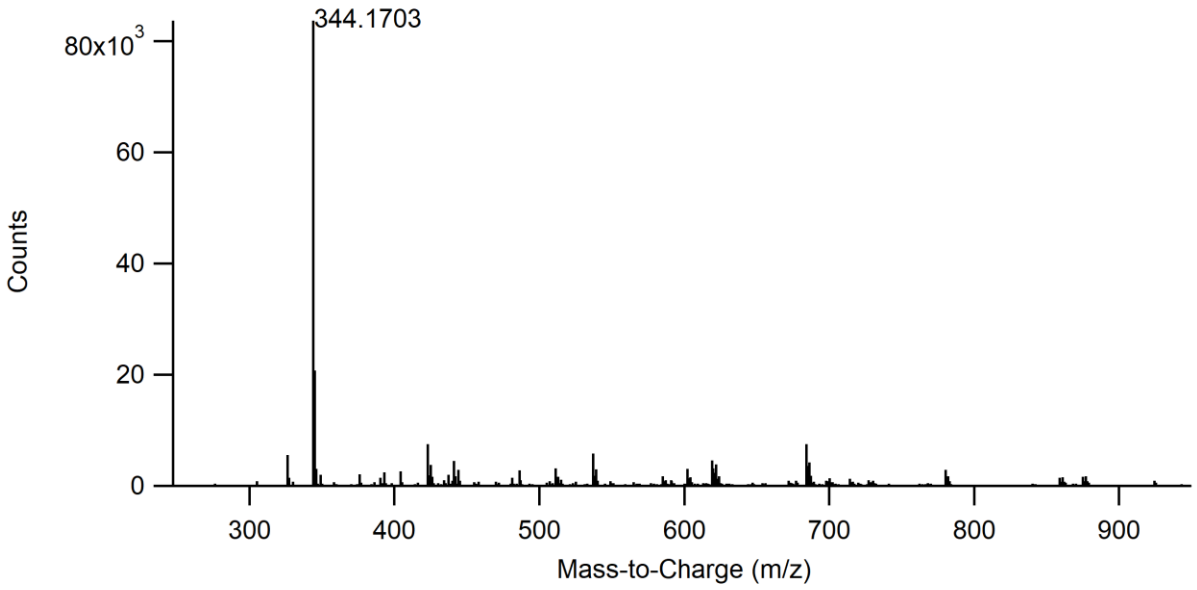

Figure 4.19. Mass spectra obtained after trying to catalyze the Friedländer synthesis between acetylacetone and 2-aminobenzophenone using $Cu(NO_3)•3H_2O$. This figure was created with the help of Madeline C. Roach.

A control was run using the same exact conditions used to perform the Friedländer synthesis with the only change being the CuBTC being replaced by $Cu(NO_3)•3H_2O$. Based on the mass spectrum produced however, the reaction did not progress as expected with none of the desired product being seen in the mass spectrum (Figure 4.19). It should be noted that not even a suspected intermediate with the copper still attached is observed. The results suggest that $Cu(NO_3)•3H_2O$ itself is incapable of catalyzing the Friedländer synthesis. However, since it was stated in the literature that experiments by Pérez-Mayoral and Čejka that it could, uncertain whether or not $Cu(NO_3)•3H_2O$ is actually capable of catalyzing the Friedländer synthesis.[23] However, the experiment done here was only performed once, so would need to be repeated for statistical significance and to fully confirm the results are reproducible before definitively claiming that the Friedländer synthesis cannot be catalyzed using $Cu(NO_3)•3H_2O$.

4.4.4.2 Controls: Using the Supernatant Collected

Figure 4.20. Fractions (20 mL) collected from performing the Friedländer synthesis under continuous flow conditions. On the fraction on the right, you can see "unidentified crystal" that had recrystallized out of the fraction after it sat at room temperature for about 24 hours.

As mentioned in previous sections, when performing the reaction under continuous flow conditions, some of the fractions collected were colored bright blue (Figure 4.20). Since it is hypothesized that the blue coloration of the eluent from some of the fractions collected from running the Friedländer synthesis under continuous flow conditions was due to a copper-containing intermediate, this intermediate could be part of the catalytic cycle. This means that the catalyst for the reaction could be present within the supernatant. Thus, a reaction was set up with 2 mL of the supernatant added as the only copper source and was run under batch conditions.

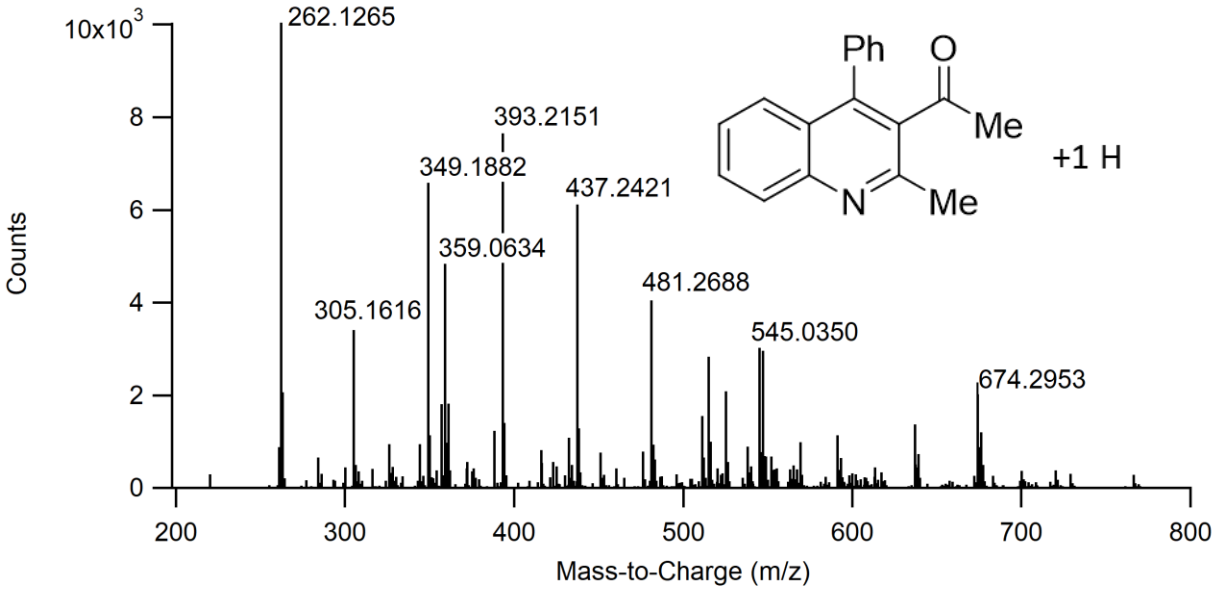

Figure 4.21. Mass spectra obtained after trying to catalyze the Friedländer synthesis between acetylacetone and 2-aminobenzophenone using the supernatant from the continuous flow synthesis. The structure for the product that is present, indicated by the 262 *m/z* peak is also provided.This figure was created with the help of Madeline C. Roach.

Based on the mass spectrum produced (Figure 4.21), it can be seen that the there is a clear peak at 262 *m/z*, perfectly matching the peak seen in Figure 4.3, indicating the presence of the desired product. The presence of the product suggests that the supernatant contains the catalyst for the Friedländer synthesis which could potentially be the hypothesized intermediate with the copper and ligand attached (Figure 4.17b). This is a key finding in that no CuBTC was added to this reaction and the supernatant used contained no visible solids, indicating that no CuBTC was present. This supports the hypothesis that CuBTC is not actually the catalyst for the Friedländer synthesis in this system and that it does indeed breakdown into another copper-containing compound that acts as the actual catalyst for the reaction.

However, there are several other unidentified peaks in this spectrum and the exact copper intermediate that is present has not been definitively identified. Thus, further experiments would be required to determine what actually acted as the catalyst in this case.

4.4.4.3 Controls: Using the "Unidentified crystal"

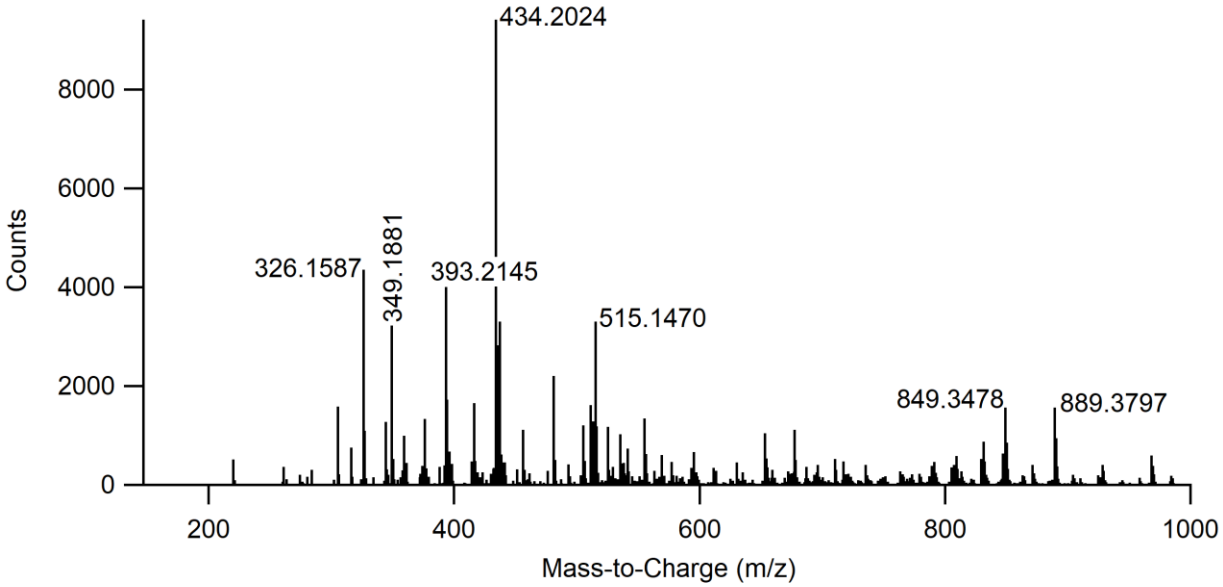

Figure 4.22. Mass spectra obtained after trying to catalyze the Friedländer synthesis between acetylacetone and 2-aminobenzophenone using the "unidentified crystal" from the continuous flow synthesis. This figure was created with the help of Madeline C. Roach.

When using the "unidentified crystal" in place of CuBTC in an attempt to catalyze the Friedländer synthesis, there was no product found in the mass spectrum (Figure 4.22). This is interesting as it was suspected that the "unidentified crystal" was recrystallizing out of the supernatant solution and based on the data (Figure 4.17b and 4.17c), it was hypothesized that this "unidentified crystal" was the compound responsible for catalyzing the Friedländer synthesis. However, this does not seem to be true and there is likely to be another compound that may not be accounted for that is actually responsible for catalyzing the Friedländer synthesis. A hypothesis could be that a precursor to this "unidentified crystal" is the active catalyst and that once the "unidentified crystal" forms, it cannot regenerate the catalyst, explaining why the supernatant the "unidentified crystal" recrystallized from is capable of catalyzing the Friedländer synthesis, but the "unidentified crystal" itself cannot.

It is important to note however that with this experiment, there was not enough of the "unidentified crystal" to match the mass of CuBTC used in the batch condition control of the Friedländer synthesis. This may be a contributing factor to the data, but it is unlikely. If the "unidentified crystal" was indeed catalytic, it should have catalytic turnover and thus still produce the desired product, just at a slower rate. Further experiments would be required to draw more definitive conclusions however and repeating this experiment with more "unidentified crystal" would also be required to ensure this data is statistically significant.

4.5 Conclusions

In this chapter, a project that initially aimed to transfer the Friedländer synthesis from the benchtop to a continuous flow reactor was redirected to identifying how and why CuBTC was being broken down by the reaction conditions and to try and reidentify the catalyst of the Friedländer synthesis in this system.

With the current data and work completed, we can confirm that CuBTC is indeed breaking down in the current system based on the SEM images and TOF-MS data where they show the broken down CuBTC particles and the presence of copper detached from the MOF, respectively. It can also be confirmed that the observed breakdown of the CuBTC is caused by a specific effect in the Friedländer synthesis and not a change from transferring the reaction from batch conditions to continuous flow conditions.

Additionally, this work lays the foundation towards better understanding why CuBTC is breaking down in the conditions used to perform the Friedländer synthesis when it was believed to be the catalyst beforehand. Better understanding of why CuBTC is being broken down by this system is important because it will help better determine what reactions CuBTC, and potentially

other MOFs, are capable of catalyzing. Furthermore, it can help chemists understand what causes CuBTC to break down, allowing them to better design reaction conditions around these limitations for use in other reactions.

This work also lays the foundation for reidentifying the actual catalyst for the Friedländer synthesis in this system, further providing a better understanding of Cu-catalyzed systems for the Friedländer synthesis. Understanding what the active catalyst is in a reaction is fundamental when trying to optimize and improve the reaction. By determining the active catalyst in this system, it can also lead to better understanding of how MOF catalysts work and help determine whether this system uses homogeneous or heterogeneous MOF catalysis.

There are still many experiments that could be performed to confirm many of the new hypotheses and questions that arose during the course of this project. Some of the experiments to perform to answer these questions more definitively, include, but are not limited to:

I. Running a control to determine what, if any, specific reagent is leading to the breakdown of the CuBTC
    a. Use the reaction conditions for the Friedländer synthesis with just CuBTC and DMF
    b. Use the reaction conditions for the Friedländer synthesis with CuBTC in DMF and 2-aminobenzophenone
    c. Use the reaction conditions for the Friedländer synthesis with CuBTC in DMF and acetylacetone

II. Use Cu(I) and Cu(II) specific chelating agents in the supernatant that catalyzed the Friedländer synthesis to determine whether the copper-containing compound hypothesized to catalyze the reaction contains either Cu(I) or Cu(II) using UV-Vis

III. Compare the reaction rates of the Friedländer synthesis when run using CuBTC vs. the supernatant

IV. Determining the rate of loss of CuBTC from the column used for performing the Friedländer synthesis and comparing that to the amount of copper present in the collected eluent

V. Analyzing the green fractions collected from continuous flow to confirm whether or not copper is present already in those fractions and try to confirm whether or not it might be responsible for the green color (using UV-Vis)

By performing these experiments, and likely others, it would be possible to further narrow down what is causing the CuBTC to breakdown in this system and what the actual catalyst for the Friedländer synthesis is.

Lastly, this work makes a statement on the need for more thorough and standardized analysis of MOF catalysts in the literature. While most scientists do use pXRD pre- and post-catalysis to confirm the retention of crystal structure, there are very few, if any, instances in the literature where MOFs used in heterogeneous catalysts are analyzed pre- and post-catalysis using SEM to ensure there is not a breakdown of the MOF particle that cannot be observed using pXRD. It has been shown through this work that using solely XRD techniques is not sufficient as it can miss partial breakdown of the MOF as long as the bulk of the crystal is still intact and that imaging techniques such as SEM is necessary to ensure the MOF is still fully intact.

CHAPTER 4 – REFERENCES

(1) Andriole, V. T. *The Quinolones: Past, Present, and Future*; 2005. https://doi.org/10.1086/428051.

(2) Aly, A. A.; Ramadan, M.; Abuo-Rahma, G. E. D. A.; Elshaier, Y. A. M. M.; Elbastawesy, M. A. I.; Brown, A. B.; Bräse, S. Quinolones as Prospective Drugs: Their Syntheses and Biological Applications. In *Advances in Heterocyclic Chemistry*; Academic Press Inc., 2021; Vol. 135, pp 147–196. https://doi.org/10.1016/bs.aihch.2020.08.001.

(3) Manske, R. H. *THE CHEMISTRY OF QUINOLINES*; 1941. https://doi.org/10.1021/cr60095a006.

(4) Cheng, C.-C.; Yan, S.-J. The Friedlander Synthesis of Quinolines. *Organic Reactions* **2005**, *28*, 37–201. https://doi.org/10.1002/0471264180.or028.02.

(5) Marella, A.; Tanwar, O. P.; Saha, R.; Ali, M. R.; Srivastava, S.; Akhter, M.; Shaquiquzzaman, M.; Alam, M. M. Quinoline: A Versatile Heterocyclic. *Saudi Pharmaceutical Journal*. January 2013, pp 1–12. https://doi.org/10.1016/j.jsps.2012.03.002.

(6) Li, J.; Zheng, T.-C.; Jin, Y.; Xu, J.-G.; Yu, J.-G.; Lv, Y.-W. *Synthesis, Molecular Docking and Biological Evaluation of Quinolone Derivatives as Novel Anticancer Agents*; 2018; Vol. 66.

(7) Sales, E. M.; Daniel Figueroa-Villar, J. RECENT STUDIES ABOUT SYNTHESIS AND BIOLOGICAL ACTIVITY OF QUINOLONES AND DERIVATIVES: A REVIEW. *José*

et al. World Journal of Pharmacy and Pharmaceutical Sciences **2016**, *5*, 253. https://doi.org/10.20959/wjpps20168-7411.

(8) Ahmed, A.; Daneshtalab, M. Nonclassical Biological Activities of Quinolone Derivatives. *J Pharm Pharmaceut Sci (www.cspsCanada.org)* **2012**, *15* (1), 52–72.

(9) Tabarrini, O.; Cecchetti, V.; Fravolini, A.; Nocentini, G.; Barzi, A.; Sabatini, S.; Miao, H.; Sissi, C. Design and Synthesis of Modified Quinolones as Antitumoral Acridones 1. **1999**. https://doi.org/10.1021/jm980324m.

(10) Kojima, H.; Kaita, K. D. E.; Hawkins, K.; Uhanova, J.; Minuk, G. Y. Use of Fluoroquinolones in Patients with Chronic Hepatitis C Virus-Induced Liver Failure. *Antimicrob Agents Chemother* **2002**, *46* (10), 3280–3282. https://doi.org/10.1128/AAC.46.10.3280-3282.2002.

(11) Fan, Y. L.; Cheng, X. W.; Wu, J. B.; Liu, M.; Zhang, F. Z.; Xu, Z.; Feng, L. S. Antiplasmodial and Antimalarial Activities of Quinolone Derivatives: An Overview. *European Journal of Medicinal Chemistry*. Elsevier Masson SAS February 25, 2018, pp 1–14. https://doi.org/10.1016/j.ejmech.2018.01.039.

(12) Pranger, A. D.; van der Werf, T. S.; Kosterink, J. G. W.; Alffenaar, · J W C. The Role of Fluoroquinolones in the Treatment of Tuberculosis in 2019. **2019**, *79*, 161–171. https://doi.org/10.1007/s40265-018-1043-y.

(13) Sood, D.; Kumar, N.; Singh, A.; Sakharkar, M. K.; Tomar, V.; Chandra, R. Antibacterial and Pharmacological Evaluation of Fluoroquinolones: A Chemoinformatics Approach. *Genomics Inform* **2018**, *16* (3), 44–51. https://doi.org/10.5808/gi.2018.16.3.44.

(14) Matada, B. S.; Pattanashettar, R.; Yernale, N. G. A Comprehensive Review on the Biological Interest of Quinoline and Its Derivatives. *Bioorg Med Chem* **2021**, *32*. https://doi.org/10.1016/j.bmc.2020.115973.

(15) Liu, X. H.; Fang, Y. M.; Xie, F.; Zhang, R. R.; Shen, Z. H.; Tan, C. X.; Weng, J. Q.; Xu, T. M.; Huang, H. Y. Synthesis and in Vivo Fungicidal Activity of Some New Quinoline Derivatives against Rice Blast. *Pest Manag Sci* **2017**, *73* (9), 1900–1907. https://doi.org/10.1002/ps.4556.

(16) Gupta, V. K.; Mittal, A.; Gajbe, V. Adsorption and Desorption Studies of a Water Soluble Dye, Quinoline Yellow, Using Waste Materials. *J Colloid Interface Sci* **2005**, *284* (1), 89–98. https://doi.org/10.1016/j.jcis.2004.09.055.

(17) Ahmed, W.; Zhang, S.; Yu, X.; Yamamoto, Y.; Bao, M. Brønsted Acid-Catalyzed Metal- and Solvent-Free Quinoline Synthesis from: N -Alkyl Anilines and Alkynes or Alkenes. *Green Chemistry* **2018**, *20* (1), 261–265. https://doi.org/10.1039/c7gc03175k.

(18) Wu, Y. C.; Liu, L.; Li, H. J.; Wang, D.; Chen, Y. J. Skraup-Doebner-Von Miller Quinoline Synthesis Revisited: Reversal of the Regiochemistry for γ-Aryl-β,γ-Unsaturated α-Ketoesters. *Journal of Organic Chemistry* **2006**, *71* (17), 6592–6595. https://doi.org/10.1021/jo060290n.

(19) Graves, P. R. Discovery of Novel Targets of Quinoline Drugs in the Human Purine Binding Proteome. *Mol Pharmacol* **2002**, *62* (6), 1364–1372. https://doi.org/10.1124/mol.62.6.1364.

(20) Foley, M.; Tilley, L. Quinoline Antimalarials: Mechanisms of Action and Resistance and Prospects for New Agents. *Pharmacol Ther* **1998**, *79* (1), 55–87. https://doi.org/10.1016/S0163-7258(98)00012-6.

(21) Foley, M.; Tilley, L. Quinoline Antimalarials: Mechanisms of Action and Resistance. *Int J Parasitol* **1997**, *27* (2), 231–240. https://doi.org/10.1016/S0020-7519(96)00152-X.

(22) Kaur, K.; Jain, M.; Reddy, R. P.; Jain, R. Quinolines and Structurally Related Heterocycles as Antimalarials. *Eur J Med Chem* **2010**, *45* (8), 3245–3264. https://doi.org/10.1016/j.ejmech.2010.04.011.

(23) Pérez-Mayoral, E.; Čejka, J. [Cu3(BTC)2]: A Metal-Organic Framework Catalyst for the Friedländer Reaction. *ChemCatChem* **2011**, *3* (1), 157–159. https://doi.org/10.1002/cctc.201000201.

(24) Položij, M.; Pérez-Mayoral, E.; Čejka, J.; Hermann, J.; Nachtigall, P. Theoretical Investigation of the Friedländer Reaction Catalysed by CuBTC: Concerted Effect of the Adjacent Cu2+ Sites. *Catal Today* **2013**, *204*, 101–107. https://doi.org/10.1016/j.cattod.2012.08.025.

(25) Pérez-Mayoral, E.; Musilová, Z.; Gil, B.; Marszalek, B.; Položij, M.; Nachtigall, P.; Čejka, J. Synthesis of Quinolines via Friedländer Reaction Catalyzed by CuBTC Metal-Organic-Framework. *Dalton Transactions* **2012**, *41* (14), 4036–4044. https://doi.org/10.1039/c2dt11978a.

(26) Domínguez-Fernández, F.; López-Sanz, J.; Pérez-Mayoral, E.; Bek, D.; Martín-Aranda, R. M.; López-Peinado, A. J.; Čejka, J. Novel Basic Mesoporous Catalysts for the Friedländer

Reaction from 2-Aminoaryl Ketones: Quinolin-2(1H)-Ones versus Quinolines. *ChemCatChem* **2009**, *1* (2), 241–243. https://doi.org/10.1002/cctc.200900097.

(27) Sachse, A.; Ameloot, R.; Coq, B.; Fajula, F.; Coasne, B.; de Vos, D.; Galarneau, A. In Situ Synthesis of Cu-BTC (HKUST-1) in Macro-/Mesoporous Silica Monoliths for Continuous Flow Catalysis. *Chemical Communications* **2012**, *48* (39), 4749–4751. https://doi.org/10.1039/c2cc17190b.

(28) Galarneau, A.; Sachse, A.; Said, B.; Pelisson, C. H.; Boscaro, P.; Brun, N.; Courtheoux, L.; Olivi-Tran, N.; Coasne, B.; Fajula, F. Les Monolithes Siliciques à Porosité Hiérarchique: Une Nouvelle Classe de Microréacteurs Pour l'Intensification Des Procédés En Catalyse et En Adsorption. *Comptes Rendus Chimie* **2016**, *19* (1–2), 231–247. https://doi.org/10.1016/j.crci.2015.05.017.

(29) Bavykina, A.; Kolobov, N.; Khan, I. S.; Bau, J. A.; Ramirez, A.; Gascon, J. Metal-Organic Frameworks in Heterogeneous Catalysis: Recent Progress, New Trends, and Future Perspectives. *Chemical Reviews*. American Chemical Society August 26, 2020, pp 8468–8535. https://doi.org/10.1021/acs.chemrev.9b00685.

(30) Liang, J.; Liang, Z.; Zou, R.; Zhao, Y. Heterogeneous Catalysis in Zeolites, Mesoporous Silica, and Metal–Organic Frameworks. *Advanced Materials*. Wiley-VCH Verlag August 11, 2017. https://doi.org/10.1002/adma.201701139.

(31) Arnanz, A.; Pintado-Sierra, M.; Corma, A.; Iglesias, M.; Sánchez, F. Bifunctional Metal Organic Framework Catalysts for Multistep Reactions: MOF-Cu(BTC)-[Pd] Catalyst for One-Pot Heteroannulation of Acetylenic Compounds. *Adv Synth Catal* **2012**, *354* (7), 1347–1355. https://doi.org/10.1002/adsc.201100503.

(32) Nguyen, L. T. L.; Nguyen, T. T.; Nguyen, K. D.; Phan, N. T. S. Metal-Organic Framework MOF-199 as an Efficient Heterogeneous Catalyst for the Aza-Michael Reaction. *Appl Catal A Gen* **2012**, *425–426*, 44–52. https://doi.org/10.1016/j.apcata.2012.02.045.

(33) Opanasenko, M.; Dhakshinamoorthy, A.; Shamzhy, M.; Nachtigall, P.; Horáček, M.; Garcia, H.; Čejka, J. Comparison of the Catalytic Activity of MOFs and Zeolites in Knoevenagel Condensation. *Catal Sci Technol* **2013**, *3* (2), 500–507. https://doi.org/10.1039/c2cy20586f.

(34) Gascon, J.; Corma, A.; Kapteijn, F.; Llabrés I Xamena, F. X. Metal Organic Framework Catalysis: Quo Vadis? *ACS Catal* **2014**, *4* (2), 361–378. https://doi.org/10.1021/cs400959k.

(35) Sabale, S.; Zheng, J.; Vemuri, R. S.; Yu, X.-Y.; Mcgrail, P.; Motkuri, R. K. Synthesis and Catalysis: Open Access Recent Advances in Metal-Organic Frameworks for Heterogeneous Catalyzed Organic Transformations. *Synthesis and Catalysis: Open Access* **2016**, *1* (5), 1–8.

(36) Phan, N. T. S.; Vu, P. H. L.; Nguyen, T. T. Expanding Applications of Copper-Based Metal-Organic Frameworks in Catalysis: Oxidative C-O Coupling by Direct C-H Activation of Ethers over Cu2(BPDC)2(BPY) as an Efficient Heterogeneous Catalyst. *J Catal* **2013**, *306*, 38–46. https://doi.org/10.1016/j.jcat.2013.06.006.

(37) Doonan, C. J.; Sumby, C. J. Metal-Organic Framework Catalysis. *CrystEngComm* **2017**, *19* (29), 4045–4049. https://doi.org/10.1039/c7ce90106b.

(38) Martín-Aranda, R. M.; Čejka, J. Recent Advances in Catalysis over Mesoporous Molecular Sieves. *Top Catal* **2010**, *53* (3–4), 141–153. https://doi.org/10.1007/s11244-009-9419-6.

(39) Cuchiaro, H.; Thai, J.; Schaffner, N.; Tuttle, R. R.; Reynolds, M. Exploring the Parameter Space of P-Cresyl Sulfate Adsorption in Metal-Organic Frameworks. *ACS Appl Mater Interfaces* **2020**, *12* (20), 22572–22580. https://doi.org/10.1021/acsami.0c04203.

(40) Tuttle, R. R.; Rubin, H. N.; Rithner, C. D.; Finke, R. G.; Reynolds, M. M. Copper Ion vs Copper Metal–Organic Framework Catalyzed NO Release from Bioavailable S-Nitrosoglutathione En Route to Biomedical Applications: Direct 1H NMR Monitoring in Water Allowing Identification of the Distinct, True Reaction Stoichiometries and Thio. *J Inorg Biochem* **2019**, *199* (July), 110760. https://doi.org/10.1016/j.jinorgbio.2019.110760.

(41) Thai, J. E.; Tuttle, R. R.; Deroo, J.; Cuchiaro, J.; Reynolds, M. M. Cu-Based Metal-Organic Framework Nanosheets Synthesized via a Three-Layer Bottom-Up Method for the Catalytic Conversion of S-Nitrosoglutathione to Nitric Oxide. *ACS Appl Nano Mater* **2021**. https://doi.org/10.1021/acsanm.1c03313.

(42) Tuttle, R. R.; Folkman, S. J.; Rubin, H. N.; Finke, R. G.; Reynolds, M. M. Copper Metal-Organic Framework Surface Catalysis: Catalyst Poisoning, IR Spectroscopic, and Kinetic Evidence Addressing the Nature and Number of the Catalytically Active Sites En Route to Improved Applications. *ACS Appl Mater Interfaces* **2020**, *12* (35), 39043–39055. https://doi.org/10.1021/acsami.0c08961.

(43) Widegren, J. A.; Finke, R. G. A Review of the Problem of Distinguishing True Homogeneous Catalysis from Soluble or Other Metal-Particle Heterogeneous Catalysis

under Reducing Conditions. *Journal of Molecular Catalysis A: Chemical*. Elsevier May 1, 2003, pp 317–341. https://doi.org/10.1016/S1381-1169(02)00728-8.

(44) Davies, I. W.; Matty, L.; Hughes, D. L.; Reider, P. J. Are Heterogeneous Catalysts Precursors to Homogeneous Catalysts? [21]. *Journal of the American Chemical Society*. October 17, 2001, pp 10139–10140. https://doi.org/10.1021/ja016877v.

(45) Siegel, S. *Alkene Hydrogenation and Related Reactions A Comparison of Heterogeneous with Homogeneous Catalysis*; 1973; Vol. 30.

(46) Heyrovsky, J. [Cu 3 (BTC) 2]: A Metal – Organic Framework Catalyst for the Friedländer Reaction. **2011**, *3*, 157–159. https://doi.org/10.1002/cctc.201000201.

(47) Tsednee, M.; Huang, Y. C.; Chen, Y. R.; Yeh, K. C. Identification of Metal Species by ESI-MS/MS through Release of Free Metals from the Corresponding Metal-Ligand Complexes. *Sci Rep* **2016**, *6*. https://doi.org/10.1038/srep26785.

(48) McIndoe, J. S.; Vikse, K. L. Assigning the ESI Mass Spectra of Organometallic and Coordination Compounds. *Journal of Mass Spectrometry* **2019**, *54* (5), 466–479. https://doi.org/10.1002/jms.4359.

CHAPTER 5

TOWARDS USING CuBTC METAL-ORGANIC FRAMEWORKS TO CATALYZE CONDENSATIONS BETWEEN DIMEDONE AND BENZALDEHYDE TO FORM 1,8-DIOXO-OCTA-HYDRO-XANTHENE UNDER CONTINUOUS FLOW CONDITIONS

5.1 Overview

In Chapter 4, original goal was to create a continuous flow reactor capable of catalyzing an organic transformation using CuBTC (where BTC = benzene-1,3,5-tricarboxylate). However, when unexpected crystals were observed in the eluent and CuBTC we found to be missing from the packed column, the project was redirected towards understanding the factors that led to CuBTC decomposing and to identify the catalyst of that system. In this chapter, I discuss preliminary experiments and results that are working towards achieving the same goal of trying to perform a reaction using the continuous flow reactor that I had developed. This reaction is a condensation to produce a xanthene derivative. The preliminary results discussed in this chapter also provide some insights towards the stability of CuBTC when used as a catalyst under continuous flow conditions and when used as a catalyst for condensation reactions.

The continuous flow reactor used for this research is the same system used for the Friedländer synthesis in Chapter 4 of this dissertation and was developed and constructed by Jonathan Thai and Jesus Tapia. All reactions both under batch conditions and continuous flow conditions were performed by Jonathan Thai. The CuBTC metal-organic framework (MOF) was synthesized and characterized (via SEM and pXRD) by Jonathan Thai. Analysis of the products

from the reactions were done using time-of-flight mass-spectrometry (TOF-MS) and were performed by Madeline C. Roach. Melissa M. Reynolds was the advisor on this project.

5.2 Introduction

Heterocycles are commonly found moieties in present day pharmaceuticals, making them high-value synthetic targets due to their versatility.[1–7] While originally only used as dyes, xanthene derivatives have gained increased interest in recent years due to discoveries that have expanded their known applications, both in materials and medicinal chemistry. Xanthene derivatives have found uses in areas such as biodegradable agrochemicals, photodynamic therapy, solar cells, luminescent sensors, lasers, anti-inflammatory agents, antibacterial drugs, antinociceptives, antitumor, and anti-viral treatments.[8–20] Because of this, new synthetic methods to produce xanthenes and their derivatives have been a focus of many scientists in recent years.[20,21]

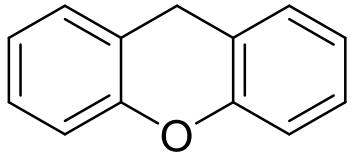

Figure 5.1. The structure of xanthene

Continuous flow reactors are a growing area of interest due to the advantages they can offer over performing syntheses under more traditional batch conditions.[22–25] These reactors can allow chemists to automate synthetic processes, reducing the amount of benchwork required while also improving consistency and achieving greater reaction efficiency relative to both speed and cost. Currently, many micro-reactors use nanotubes to force interactions between chemicals, allowing them to react more efficiently due to improved mass transfer.[23,26] Continuous flow reactors have also been used with heterogeneous catalysts in the form of packed columns, catalyst coated tubular reactors, and monolithic columns.[22,27–31] While in recent years, continuous flow processes are

slowly making their way into more industrial processes, there are still several obstacles that continuous flow processes face that limit their broader integration into industrial processes.[22,25,32] These obstacles include, but are not limited to:

I. The inability to catalyze reactions with insoluble starting materials, products, or byproducts
II. Required changes in the solvent being used in multi-step processes
III. Production of unwanted byproducts that interfere with the reaction in multi-step processes
IV. The requirement of expensive equipment to perform reactions under continuous flow conditions, which can stagnate improvements in production processes due to emerging technologies and large pieces of equipment
V. The inability to easily scale reactions

Most of these challenges are typically specific to the reaction someone would want to perform, but the latter two are universal across continuous flow systems and I believe they must be addressed to facilitate the use of continuous flow systems in industrial production processes.

To this end, I aimed to design and develop a fixed-bed catalytic reactor where a stainless-steel column is directly packed with metal-organic frameworks (MOFs). This design would be similar to those used for columns used in separations that also use MOFs.[30,33–36] When equipped with a sufficient pump, reactants would be pushed through the catalytic MOF column under continuous flow conditions. This system will be designed to be:

I. Smaller – should be easily placed and used on a benchtop so that it can be used in various lab settings

II. Composed of easily replaceable parts – the column and other parts used in this reactor can be easily interchanged so that the reactor would be able to accommodate different reactions and be improved as technologies improve

While this may not entirely eliminate the need for large, expensive pieces of equipment, it would allow for users to improve the system they already possess, helping them avoid stagnation. Furthermore, since the parts are made to be replaceable, they could potentially be manufactured at lower costs as well.

MOFs were chosen to be the catalytic material used in these systems due to their large surface area, scalable production, ability to be created using low-cost materials, high versatility as catalytic materials, and high level of tunability that allows them to be designed to catalyze specific reactions. Within the 20 years since MOFs have gained traction in the chemical field, new structures and applications have been reported almost daily, with well over 90,000 unique structural entries for MOFs being reported, indicating over 4500 new MOF structures being reported annually.[37–40] This is much larger relative to similar materials such as zeolites, where only about 252 unique zeolites have been identified, which has not changed since 2018.[41–45]

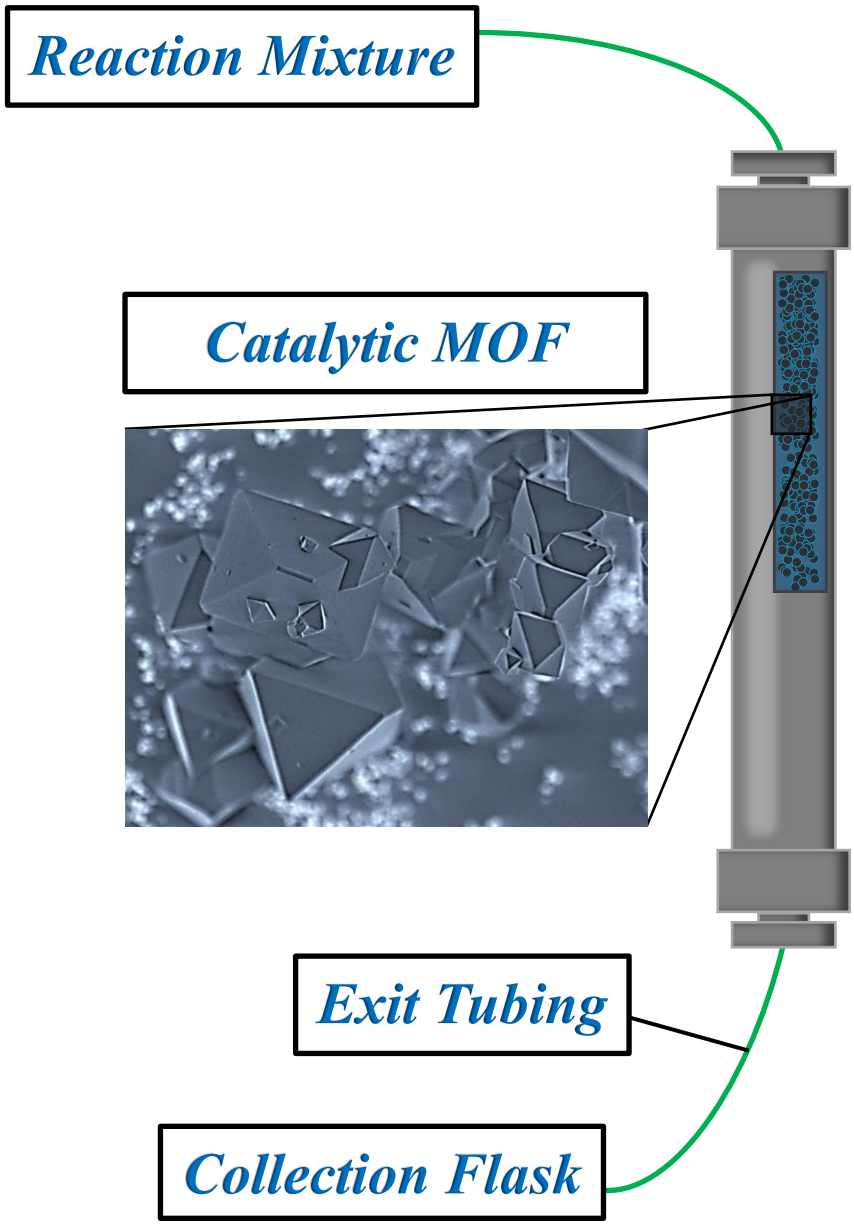

Figure 5.2. A schematic showing the continuous flow system around the catalytic column with an SEM image of the CuBTC MOF packed inside of the column. In the schematic, the reaction mixture is pumped through the system using an HPLC pump, into the column where it flows down through the catalyst packed into the column, into a collection flask.

This project focuses on increasing the production efficiency for xanthene derivatives. It does so by transferring the reaction to the continuous flow process could offer several advantages. This is done by using a pump to push the reagents through a direct-packed column, where a stainless-steel column is packed directly with MOF (Figure 5.2). The major advantages that

performing reactions under continuous flow offer over reactions performed using batch conditions include, but are not limited to:

I. Sustainability – heterogeneous catalysts used in packed column reactors are very easy to reuse, allowing for the catalysts in the column to be reused with little to no effort needed to recycle the catalyst

II. Speed – direct packed columns create very small spaces for the reactants to interact with each other, resulting in better mass transfer, similar to microfluidic tubing

III. Costs – by performing reactions faster and being able to easily reuse the catalyst, this helps reduce the cost of chemical production

IV. Ease-of-use – by design, the reactor setup in this project is made to be very easy to use, where one would just need to be capable of loading reagents and then starting hitting a “start” button, allowing for anyone to be able to perform the reaction without high-levels knowledge of organic synthesis

V. Automation – with further development, the continuous flow reactor system could easily be put into a part of a larger multi-step process, helping take steps towards automating the process of chemical synthesis

VI. Safety – if automated, the reaction can be done without a person being directly present, limiting their exposure to potentially dangerous chemicals and reducing the potential for accidents

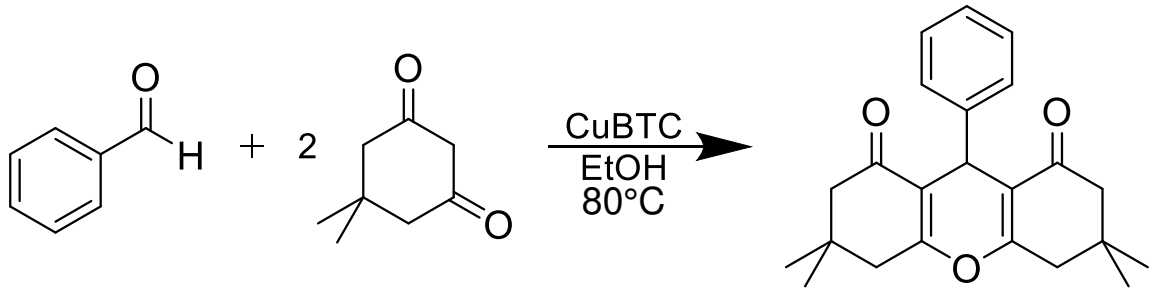

Figure 5.3. Reaction scheme for the condensation between benzaldehyde and two equivalents of dimedone to produce 3,3,6,6-tetramethyl-9-phenyl-3,4,5,6,7,9-hexahydro-1*H*-xanthene-1,8(2*H*)-dione. This reaction was originally reported using a CuBTC catalyst by Ghafuri *et al.* and then used in our continuous flow system.

In this chapter, I discuss the use of a continuous flow system using CuBTC to catalyze a condensation between benzaldehyde and dimedone to produce 3,3,6,6-tetramethyl-9-phenyl-3,4,5,6,7,9-hexahydro-1*H*-xanthene-1,8(2*H*)-dione (Figure 5.3 and 5.4). This reaction will be referred to as the "xanthene condensation". This xanthene was specifically chosen because it had been identified by Merck & Co., Inc. to be a valuable target as it is a moiety for pharmaceuticals that can be used for antivirals and antibacterials.[21,46] While this system is still in development, the preliminary data suggests that this system is working as intended and will perform the reaction without breaking down the CuBTC. Furthermore, both the Friedländer synthesis discussed in Chapter 4 of this dissertation and the reaction being performed here are condensations, thus key conclusions can be drawn based on the results obtained from the experiments discussed in this chapter.

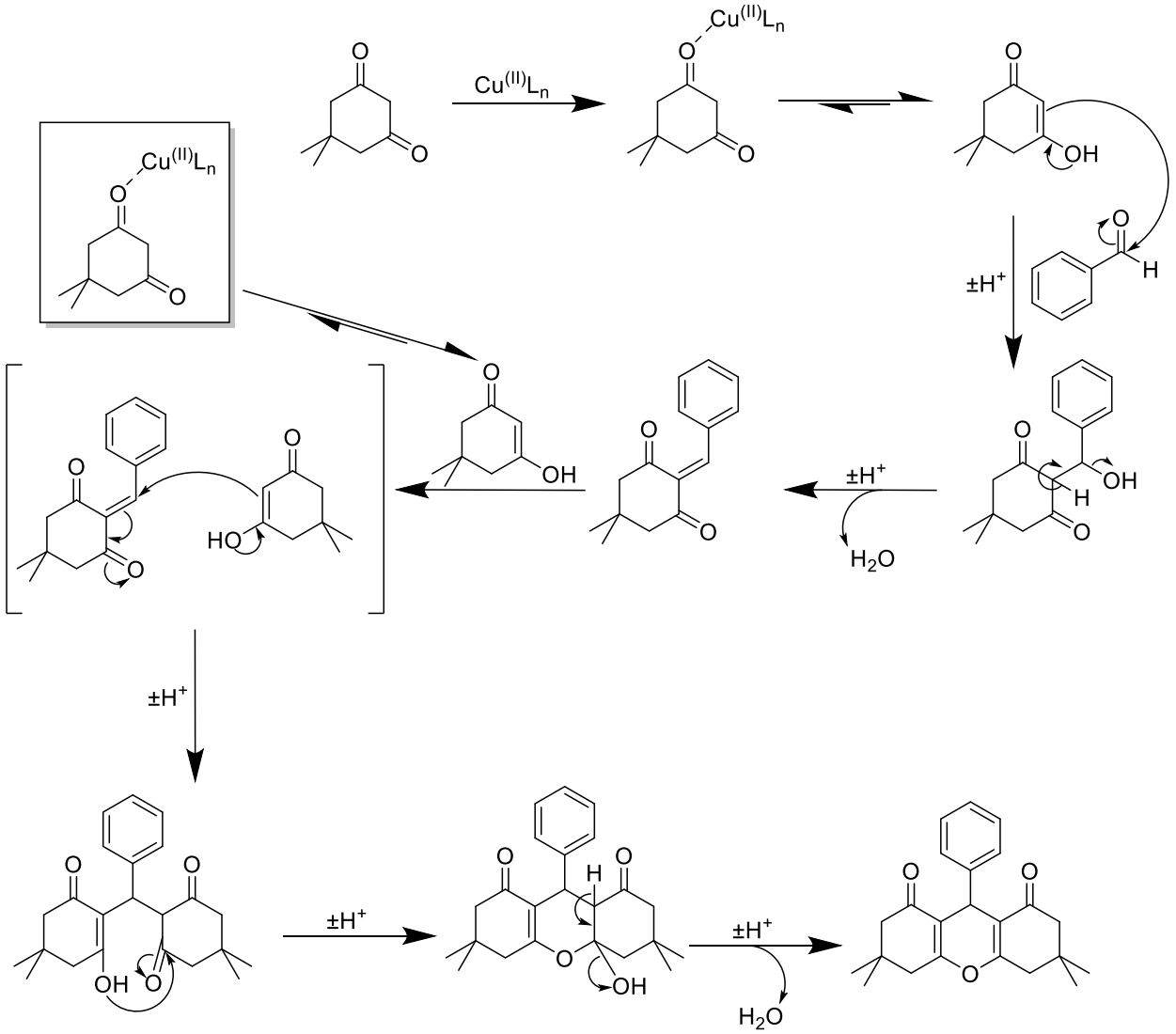

Figure 5.4. Proposed mechanism for the condensation between benzaldehyde and two equivalents of dimedone to produce 3,3,6,6-tetramethyl-9-phenyl-3,4,5,6,7,9-hexahydro-1*H*-xanthene-1,8(2*H*)-dione. This reaction was originally reported using a CuBTC catalyst by Ghafuri *et al.* and then used in our continuous flow system.

5.3 Experimental

5.3.1 Materials

All chemicals and solvents were purchased from commercial vendors and were then used without any further purification. *N*, *N*-dimethylformamide, >99.6%; dimedone, 98%; and ethanol, 100% was purchased from Fisher Scientific (Waltham, MA). 1,3,5-benzenetricarboxylic acid,

>98%; and copper(II) nitrate trihydrate, >99%; 3,3,6,6,-tetramethyl-9-phenyl-3,4,5,6,7,9-hexahydro-1*H*-xanthene-1,8(2*H*)-dione, and benzaldehyde >99% were purchased from Sigma-Aldrich (St. Louis, MO). All deionized water used was purified by a Millipore Milli-Q- IQ 7000 water purification system to 18.2 MΩ-cm resistivity prior to use.

5.3.2 Synthesis of CuBTC MOF

The synthesis to create the CuBTC MOF used was adapted from the literature.[47] In short, 1,3,5-benzenetricarboxylic acid (12.85 mmol, 0.62 equiv.) and copper(II) nitrate trihydrate (20.695 mmol, 1.0 equiv.) were suspended in a mixture of deionized water (23 mL), DMF (33 mL), and ethanol (36 mL) in a sealable Pyrex bottle. The mixture was sonicated for at least 1 hour to fully disperse and suspend the reagents. The mixture was then placed into a pre-heated oven at 90 °C for 24 hours. After 24 hours, the oven was turned off and the product was cooled to room temperature inside the oven naturally. Once cooled to room temperature, the solid product was then collected using a fine glass filter frit. The solid product was then rinsed with DMF (3 x 50 mL). The solid product was then washed in ethanol using Soxhlet extraction for at least 24 hours. The solid product was then collected using a fine glass filter frit. The solid was then collected and dried at 150°C under reduced pressure, producing a dark blue powder. The collected product was then characterized using SEM and pXRD.

5.3.3 Using CuBTC to Catalyze the Condensation Between Dimedone and Benzaldehyde Under Batch Conditions

The reaction conditions used were adapted from the literature.[21] In short, CuBTC (0.05g, 0.083 mmol) was weighed out into a 100 mL round bottomed flask. The CuBTC was then activated in a vacuum oven at 150 °C under reduced pressure overnight. The oven was then turned

off and the CuBTC was then allowed to cool naturally to room temperature before it was taken out. Acetylacetone (20.0 mmol, 10 equiv.) and 2-aminobenzophenone (2.0 mmol, 1 equiv.) were then measured out into the RBF with the CuBTC. The reaction mixture was then stirred and heated to 80 °C for 20 minutes in a reflux apparatus. Ethanol (10 mL in 2-3 mL portions) was then used to rinse the RBF into a centrifuge tube. The solid (unidentified crystal) and supernatant were then separated via centrifugation. The supernatant was then transferred to a vial and the solvent was then removed under reduced pressure (to produce the product mixture). The unidentified crystal was then rinsed with ethanol (10 mL) and vortexed to ensure no remnants of the reagents or products from the reaction were still present and the solid and supernatant were then separated again via centrifugation. The supernatant was then combined with the product mixture and had the solvents removed under reduced pressure, yielding a green solid. The unidentified crystal was collected and dried under reduced pressure for 24 hours, yielding a pale blue solid. The product mixture was analyzed using TOF-MS. The unidentified crystal was analyzed using TOF-MS, pXRD, and SEM.

5.3.4 Using CuBTC to Catalyze the Condensation Between Dimedone and Benzaldehyde Under Continuous Flow Conditions

The procedure described here is referred to as "1 equivalent" of the condensation between dimedone and benzaldehyde under continuous flow conditions, though the same column may have been used several times for some experiments (in that case, the "equivalents" following the first start at the preheating step). CuBTC was activated at 150°C under pressure overnight in a vacuum oven. The oven was then turned off and the CuBTC was allowed to cool down to room temperature before it was taken out. A stainless-steel HPLC column (I.D. x L, 4.6 x 50 mm) was then directly packed with CuBTC and connected to a HPLC pump via stainless steel tubing. The column was

than pre-heated to 80°C while rinsed with ethanol at 0.5 mL/min for at least 30 minutes prior to running the reaction. A reaction mixture was created using by dissolving dimedone (2.0 mmol, 2 equiv.) in benzaldehyde (1.0 mmol, 1 equiv.), yielding a clear liquid. The reaction mixture was then drawn into a 5 mL gas-tight glass syringe and injected into the reactor at 0.5 mL/min. The reaction was rinsed with ethanol and the product eluent was collected in 4 mL fractions. Each of the fractions collected were then analyzed using TOF-MS.

5.3.5 Characterization by Scanning Electron Microscopy (SEM)

SEM imaging was performed using a JEOL JSM-6500F microscope. An accelerating voltage of 15.0 kV was used to image the MOFs. All samples were prepared on a small piece of carbon tape which were then placed under vacuum and coated with 20 nm of gold prior to imaging. At least three representative images were taken with at least three different magnifications for each sample were taken.

5.3.6 Characterization by Powdered X-ray Diffraction (pXRD)

A Bruker D8 Discover DaVinci Powder X-ray Diffractometer with Cu Kα radiation (λ = 1.5406 Å was used, operated at 40 kV and 40 mA. A 0.6-mm divergent slit was placed on the primary beam sided and a high-resolution energy dispersive LYNXEYE-XE-T detector was placed on the diffracted beam side during the XRD studies. Samples were seated on a B-doped silicon zero-diffraction plate and held in place with a small amount of vacuum grease. The 2θ was set between 4-50 degrees and scanned at steps of 0.100 degrees.

5.3.7 Characterization by Time of Flight-Mass Spectrometry (TOF-MS)

TOF-MS was performed using an Agilent® 6224 time-of-flight mass spectrometer equipped with a dual ESI source. All data shown in this chapter was collected while operating the TOF-MS under positive mode. The detection range for the scans were set for 95-3200 *m/z*.

5.3.8 Data Analysis

All data is reported as "average ± standard deviation". All data points that are reported were calculated from n = 3, unless noted otherwise.

5.4 Results and Discussion

5.4.1 Analysis of Products Obtained After Performing the Xanthene Condensation Under Batch Conditions

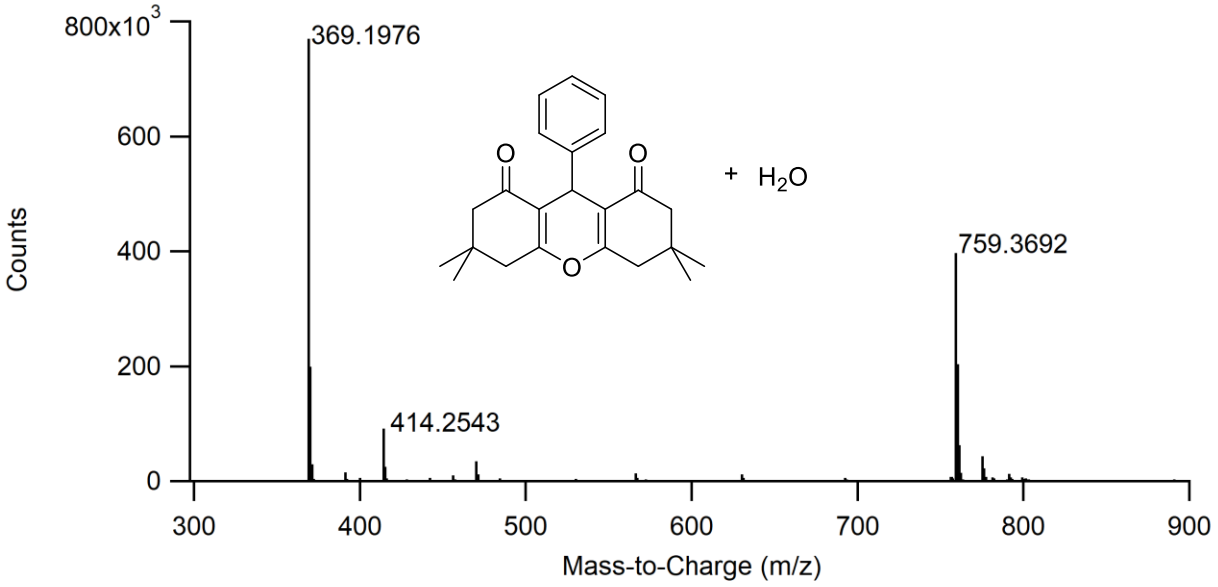

Figure 5.5. A representative mass spectrum of the xanthene condensation after work up and recrystallization. The predicted structure has been provided, based on the 369 *m/z*, which would account for with M + H_2O. The 759 *m/z* can also be accounted for with [2M + 2H_2O + Na^+]. Since there were no major differences between the mass spectra, only a representative one is provided here. This xanthene condensation was performed at 80 °C. This figure was created with the help of Madeline C. Roach.

The xanthene condensation was performed under batch conditions using the conditions as described in the literature.[21] This was to ensure the robustness of the literature procedure and to understand how the reaction works prior to converting it to the continuous flow system. As excess dimedone was found in the collected product prior to removal of the solvent under reduced pressures and recrystallization, the batch condition reactions were performed at 80, 85, 90, and 95 °C to determine if increasing the reaction temperature could drive the reaction to completion. However, no differences were observed under TOF-MS (Figure 5.5), so the lowest temperature point, 80°C was chosen to be used under continuous flow conditions for the following reasons:

I. To reach temperatures higher than room temperature, the continuous flow system needs to preheat with the packed column installed. By using a lower temperature, it can reach that temperature more quickly.

II. This would allow for the xanthene condensation to be performed at the same temperature used to perform the Friedländer synthesis from Chapter 4. This consistency between the experiments would allow for me to compare the results of the two experiments.

It should be noted that in the mass spectrum, the 369 *m/z* being associated with the xanthene product is not exactly as expected as the product was expected to be at 350 *m/z* (351 *m/z* to account for the experiment being performed in positive mode, so would be protonated). The 369 *m/z* does however correlate with the 351 + 18, which could be indicative of water being attached to the molecule. To try and see if this is consistent with a standard, a standard was purchased (From Sigma, synthesized by Merck) and analyzed using TOF-MS so that it could be compared to the product obtained from the xanthene condensation performed and discussed in this chapter.

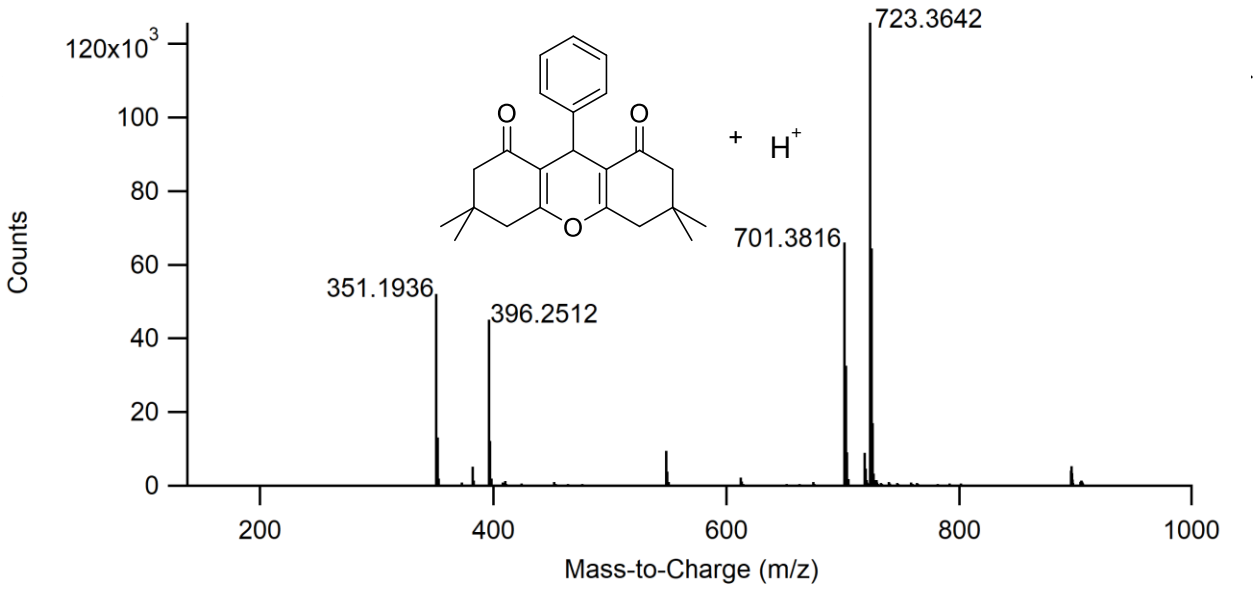

Figure 5.6. A mass spectrum of a 3,3,6,6,-tetramethyl-9-phenyl-3,4,5,6,7,9-hexahydrp-1*H*-xanthene-1,8(2*H*)dione standard. The structure of the compound has been provided and appears as the peak at 351 *m/z* ($M + H^+$). The peaks are 701 and 723 *m/z* are expected to be $2M + H^+$ and $2M + Na^+$, respectively. This figure was created with the help of Madeline C. Roach.

5.4.2 Analysis of Products Obtained After Performing the Xanthene Condensation Under Continuous Flow Conditions

When the xanthene condensation was performed under continuous flow conditions, the product eluting from the reactor was collected in ~4 mL fractions. From the TOF-MS data (Figure 5.7), it can be seen that the product was completely eluted from the column was collected entirely in the first fraction (369 and 391 *m/z*), and no peaks of interest were observed in the following fractions. This was consistent even after four equivalents of the xanthene condensation under

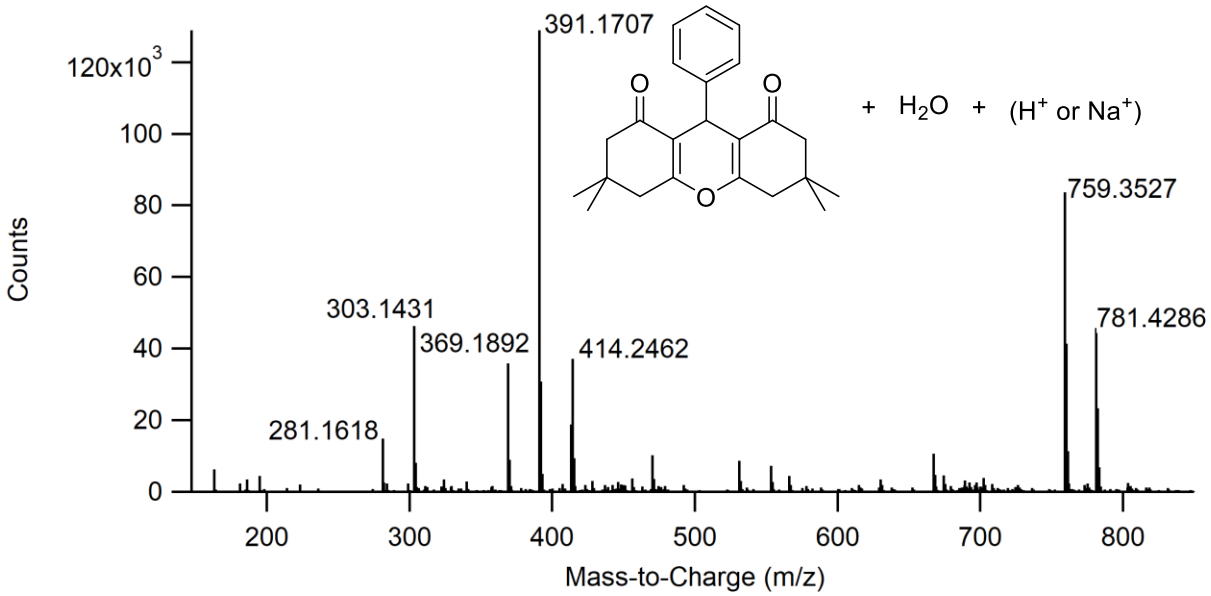

Figure 5.7. A representative mass spectrum of the first fraction collected from the xanthene condensation performed under continuous flow conditions after work up and recrystallization. Since there were no major differences between the mass spectra, only a representative one is provided here. The structure of the product is also provided which is expected to be associated with the 369 *m/z* [M + H_2O + H^+] and the 391 *m/z* [M + H_2O + Na^+]. It is also possible to account for the 759 *m/z* and 781 *m/z* in this mass spectrum with [2M + 2H_2O + Na^+] and [2M + 2H_2O + 2Na^+]. This figure was created with the help of Madeline C. Roach.

continuous flow using the same CuBTC-packed column. Between each of these equivalents, the column was rinsed with about 30 mL of ethanol to ensure nothing was still present on the column prior to being used for the next equivalent of the reaction.

5.4.3 Analysis of the CuBTC MOF Used to Catalyze the Xanthene Condensation to Ensure it is Still Intact

To ensure this reaction was suitable for continuous flow conditions and to confirm that the CuBTC was indeed catalytic and being regenerated by the reaction (and not being broken down), the CuBTC was analyzed using pXRD and SEM. There were key visual indications however that suggested there was no breakdown of the CuBTC by the xanthene condensation when it was performed under batch and continuous flow conditions.

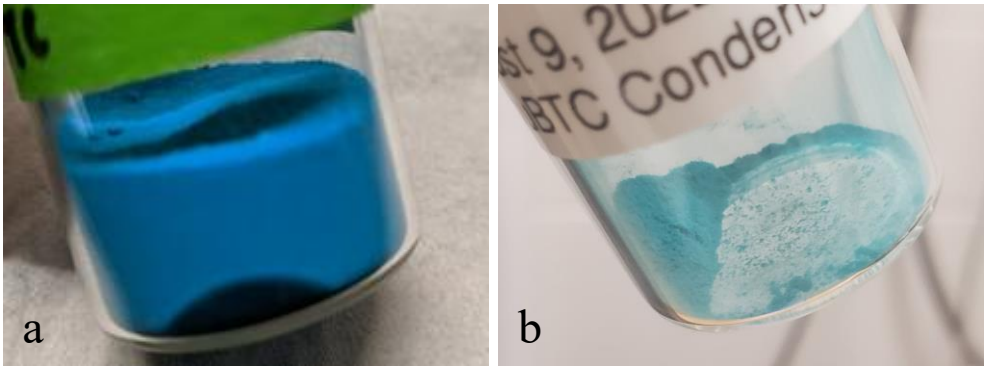

Figure 5.8. Picture of (a) CuBTC that had just been synthesized and activated for >24 hours under reduced pressure at 150 °C (b) CuBTC retrieved from the packed column after it had been used to catalyze four equivalents of the xanthene condensation and then dried under reduced pressure.

Firstly, the CuBTC MOF crystals collected after performing the reaction under batch conditions still resembled a fine, blue powder (Figure 5.8). While the CuBTC used for the Friedländer synthesis looked similar (also resembled a fine, blue powder) when it was collected from inside the column, there was a clear decrease in the amount of CuBTC (it was not tightly packed) in the catalytic column. This was because the CuBTC used in the Friedländer synthesis from Chapter 4 was determined to have broken down and recrystallized into long (>1 mm) blue needles. However, under continuous flow conditions, the CuBTC packed into the column did not seem to leave the column and under visual inspection, the column was still fully and tightly packed

with the MOF. This would be consistent with the fact that there were no crystals (outside of the clear/white crystals of the product) visible in the collected fractions.

The product collected under both batch conditions and continuous flow conditions were very different between the Friedländer synthesis and the xanthene condensation as well. Under batch conditions, the Friedländer synthesis would result in a dark green solution. When set up, the Friedländer synthesis would appear yellow and the green it turns into is hypothesized to be due to the breakdown of the CuBTC releasing copper into the solution, resulting in a green solution, though this has yet to be confirmed. However, the xanthene condensation starts off as a colorless reaction and ends clear as well, with no indication of copper being released into the reaction. This is consistent under continuous flow as well. As discussed in Chapter 4, the fractions collected when the Friedländer synthesis was performed under continuous flow were initially green and then turn blue, indicative of copper being leeched from the CuBTC in the column. In contrast, the fractions collected from the xanthene condensation are clear and colorless in all fractions, giving a visual indication that no copper was being leeched from the CuBTC.

Lastly, when performed under continuous flow, the pressure reported by the pump used was very different when performing the Friedländer synthesis versus the xanthene condensation. When the Friedländer synthesis was performed under continuous flow, it was commonly seen that the pressure would build soon after the fractions started turning blue, reaching as high as 380 atm. When above 300 atm, there was no elution from the column until reaching a pressure of 380 atm, at which point a small (~1-2 mL) amount of eluent would come out in a spurt all at once and the pressure would then drop again. This led me to hypothesize that the broken-down pieces of the CuBTC MOF and potentially some product was clogging the tubing between the column and the collection tube. In contrast, when the xanthene condensation was performed under continuous

flow, there was never an observed increase in pressure from the pump and a steady, continuous flow was maintained throughout each of the reactions. Based on the lack of pressure being built up and the clear, colorless eluent, visual indications strongly suggest that the CuBTC being used to catalyze the xanthene condensation was not breaking down.

5.4.3.1 Analysis of the CuBTC MOF Using pXRD

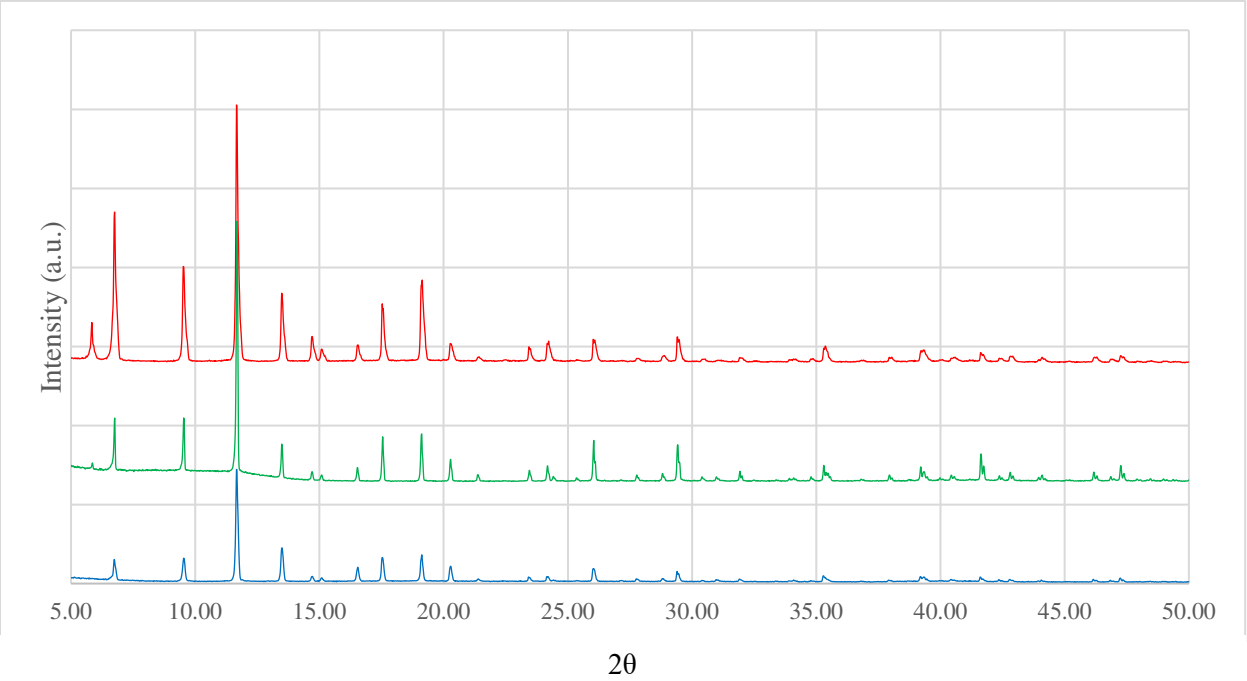

Figure 5.9. pXRD patterns of CuBTC after it had been used to run four equivalents of the xanthene condensation (red), unused CuBTC (green), and CuBTC after it had been used to run the xanthene condensation under batch conditions (blue).

To confirm that the visual observations were correct, the CuBTC from used to catalyze the xanthene condensation under batch conditions and from inside the column after it was used to catalyze the four equivalents of the xanthene condensation were analyzed using pXRD (Figure 5.9). By analyzing the crystal structure this way, I would be able to determine whether the crystallinity of the CuBTC was indeed intact. From the diffraction pattern, it can be clearly seen that the peaks are consistently in the same place and have roughly the same ratios between peaks,

indicating that there were no major changes to the crystal structure of the CuBTC MOF. This is true of the MOF after it was used to catalyze the xanthene condensation regardless of whether the xanthene condensation was performed using continuous flow or batch conditions. This is consistent with what was visually observed of the CuBTC after it was isolated after the reaction was completed, under both continuous flow and batch conditions.

5.4.3.2 Analysis of the CuBTC MOF Using SEM

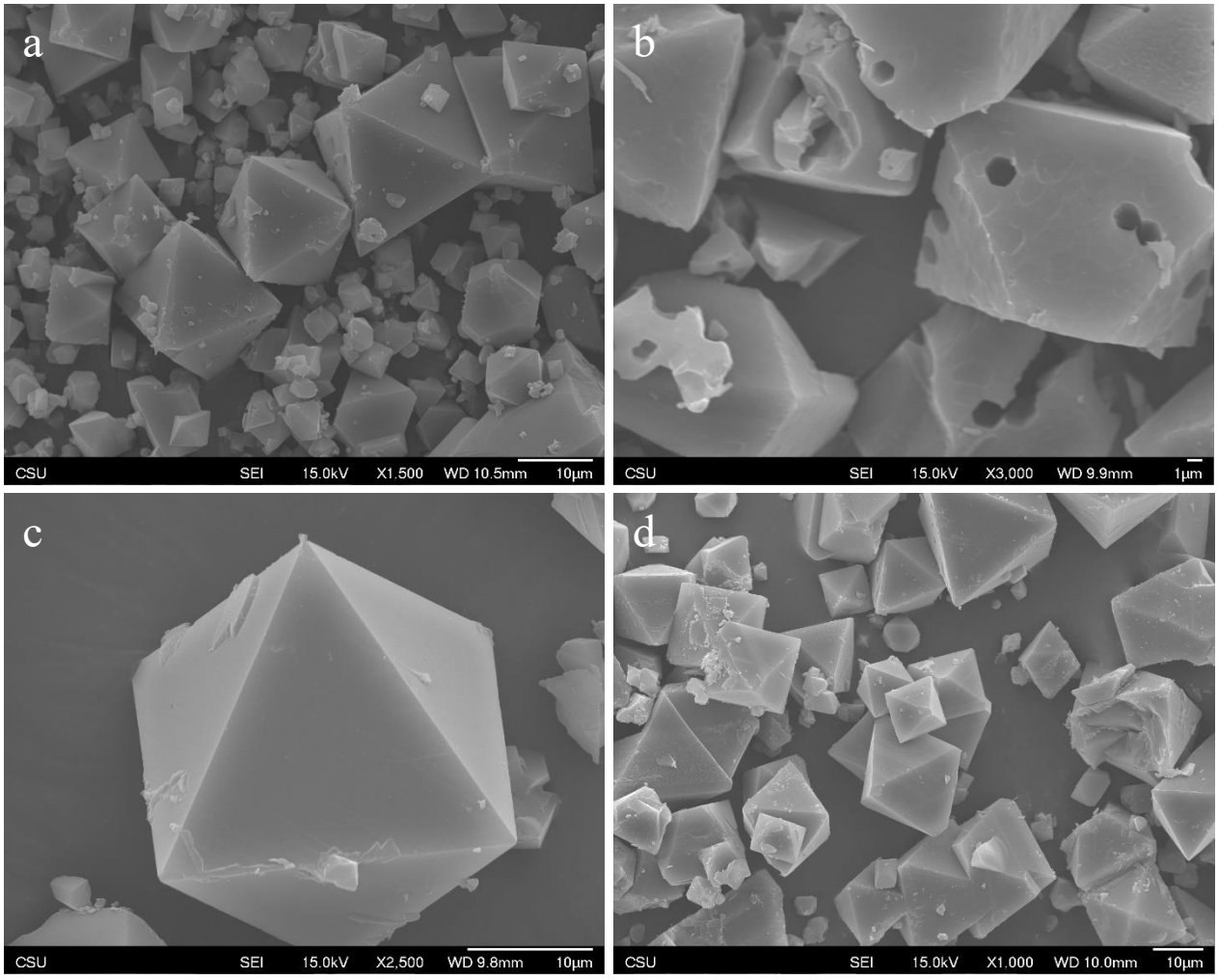

Figure 5.10. SEM images of (a) Freshly synthesized CuBTC at x1500 magnification (b) CuBTC that had been used to catalyze the Friedländer synthesis under continuous flow conditions at x3000 magnification (c) CuBTC that had been used to catalyze the xanthene condensation under batch conditions at x2500 magnification (d) CuBTC that had been used to catalyze the xanthene condensation under continuous flow conditions at x1000 magnification.

To ensure that there was no breakdown of the CuBTC that could not be seen via pXRD (as seen in Chapter 4), SEM images were also taken of the CuBTC used to catalyze the xanthene condensation under batch conditions and four equivalents of the xanthene condensation under continuous flow conditions (Figure 5.10). Based on the SEM images obtained of the CuBTC before and after it was used to catalyze the xanthene condensation, there is very little difference between the two (Figure 5.10). None of the CuBTC MOF particles used to catalyze the xanthene condensation possess any of the "scaling" or hexagonal shaped holes observed in the CuBTC particles after they were exposed to the conditions of the Friedländer synthesis from Chapter 4. Figure 5.10a provides a representative look at the CuBTC being used, showing octahedra particles with smooth surfaces around 5-20 μm long across the edge of the MOF particle. In contrast, the CuBTC used to catalyze the Friedländer synthesis from Chapter 4 shows what seems to be the remains of octahedral particles around 5-20 μm long across the edge with very rough surfaces ("scaled" surfaces) that have hexagonal shaped holes in the particles (Figure 5.10b). The CuBTC used to catalyze the xanthene condensation show octahedra particles of similar size (5-20 μm across the edge) with smooth surfaces (Figure 5.10c and 5.10d), matching those seen in the SEM images of freshly synthesized CuBTC. Any particles in these images that seem to be broken down seem to be broken down mechanically (similar to what CuBTC MOF particles look like if lightly crushed physically) and do not possess any indication of the "scaling" on its surfaces or hexagonal holes like the ones seen in Figure 5.10b. This supports the hypothesis that CuBTC is stable under the conditions used to perform the xanthene condensation. Additionally, it also supports the hypothesis that the CuBTC MOF itself is the catalyst inside the catalytic cycle as it is regenerated and is not broken down or changed to another compound by the catalytic process. To this end, the

SEM images provide promising preliminary data towards the conclusion that the xanthene condensation has been successfully transferred from a batch process to continuous flow conditions.

While different magnifications were used in each of these images, they are able to provide the desired details of the CuBTC MOF particles, specifically that Figure 5.10a, 5.10b, and 5.10d all show octahedral particles with smooth surfaces and no hexagonal holes in any of the particles. In contrast, Figure 5.10b clearly shows multiple particles that resemble the remnants of octahedra with rough surfaces that possess the "scaling" and hexagonal shaped holes in the particles. Ultimately, the SEM images along with the pXRD confirms that the CuBTC used to catalyze the xanthene condensation is not being damaged or losing crystallinity, supporting the notion that this reaction is being successfully performed catalytically under continuous flow conditions.

5.4.3.3 Comparison of Results with the CuBTC Used to Catalyze the Friedländer Synthesis

As discussed in Chapter 4, CuBTC was also used in an attempt to catalyze the Friedländer synthesis under continuous flow conditions, but it was found that the MOF was breaking down under the reaction conditions. It is important to note that the Friedländer synthesis is essentially a condensation reaction as well, so the reaction is similar to the xanthene condensation performed here.

As seen in the previous sections of this chapter, the pXRD and SEM data both support the fact that the CuBTC used to catalyze the xanthene condensation between dimedone and benzaldehyde is stable under the reaction conditions. The pXRD data shows that the crystal structure of the CuBTC MOF used to catalyze the xanthene condensation to produce the xanthene derivative has retained its crystal structure. The SEM images show that it is not just the bulk structure that is conserved, but the particle itself has no visible differences from freshly synthesized

CuBTC. This allows for several key conclusions to be drawn about the stability of CuBTC as a catalyst.

Since the Friedländer is essentially a series of condensations, it can be considered to be within the same class of reactions as the xanthene condensation performed and discussed in this chapter. It can be concluded that there is nothing inherent in a condensation reaction that results in the breakdown of the CuBTC MOFs used to catalyze them since the breakdown of the CuBTC MOF is only observed when used to catalyze the Friedländer synthesis, but not when used to catalyze a condensation to produce xanthenes. This is observed to be true regardless of whether the xanthene condensation is performed using batch conditions or under continuous flow conditions.

Early on, it was hypothesized that the breakdown of CuBTC may be due to the production of water as a byproduct of the condensation as water is known to be capable of breaking down CuBTC.[48–51] However, since both the Friedländer synthesis performed in Chapter 4 and the xanthene condensation performed in this chapter both produce water as a byproduct (in equivalent amounts relative to mol of water per mol of reaction), it is unlikely the production of water as a byproduct is the cause of the breakdown of CuBTC.

Furthermore, both the Friedländer synthesis from Chapter 4 and the xanthene condensation discussed in this chapter are performed using very similar conditions. Both reactions are performed at 80°C, use catalytic amounts of CuBTC MOF, and are on similar scales (both reaction mixtures are about 3-4 mL in volume). This further strengthens the ability to compare the two reaction systems as there are such clear differences between the SEM and pXRD data between the two experiments.

It is also important to note that the Friedländer synthesis uses an amino-containing reagent, 2-aminobenzophenone and uses an amide-containing solvent, DMF. In contrast, none of the reagents, solvents, or products used in the xanthene condensation contain nitrogen in any form. This is an important note because nitrogen has a higher bonding affinity to Cu(II) which is something that must also be considered as these nitrogen-containing groups may be coordinating to the copper centers of the CuBTC and breaking the bond between the copper and benzene-1,3,5-tricrboxylic acid ligand in CuBTC, resulting in the breakdown of the MOF and preventing its regeneration. Further investigations would be required to determine whether this is a factor in the breakdown of CuBTC under the conditions used to perform the Friedländer synthesis and not the xanthene condensation. If successful in making this distinction, a rule could then be established to more easily determine whether CuBTC can be used as a catalyst for reactions.

5.5 Conclusions

While the transferring the xanthene condensation to continuous flow conditions is very much still a work in progress and it still in the preliminary stages, there are already many interesting results that can be drawn from these experiments. Towards developing the reaction to be performed under continuous flow conditions to be able to produce xanthene derivatives via CuBTC catalyzed condensations, it can be said that:

I. The reaction seems to work under continuous flow. The desired product is being obtained (as seen via TOF-MS).

II. There is no evidence that the xanthene condensation breaks down CuBTC. The SEM, pXRD, and TOF-MS data suggest that the CuBTC is intact after being used to catalyze the xanthene condensation and that the CuBTC is indeed acting as a catalyst in this reaction. This means that it is likely that the CuBTC column could

be used indefinitely with little to no effort as it was being reused in the experiments performed already for multiple equivalents of the xanthene condensation with just an ethanol wash being done in between each use.

Future experiments with the xanthene condensation under continuous flow would aim to perform at least 10 equivalents of the xanthene condensation can be performed using the same column with little to no decrease in efficiency as this would be well past ensuring catalytic turnover of the CuBTC under continuous flow conditions. Furthermore, it would show the robustness of the system that it can be reused several times, allowing the CuBTC catalyst to be used without the requirement of more complex techniques to recover the catalyst, as would be required if the reaction was performed under batch conditions. Lastly, to test if the reaction can be performed under continuous flow even more efficiently, higher flow rates could be used to see if the reaction can be performed even faster, producing xanthene derivatives that much faster than doing them under batch conditions.

Moving forward, a more thorough analysis of the product would need to be conducted to provide more evidence of the success of the preliminary experiments. Using nuclear magnetic resonance (NMR) and infrared spectroscopy (IR) would help provide more data to support that the intended product was indeed obtained from the xanthene condensation when performed using both the batch conditions and continuous flow conditions. It could also be a good idea to perform TOF-MS using negative mode as all previous experiments have only used positive mode. This could help ensure there are no other unwanted byproducts present in the experiment that could not be detected using positive mode. Elemental analysis can also be done on the collected eluent from the xanthene condensation performed under continuous flow conditions to ensure there is no

copper present, providing further confirmation that there is no breakdown of the CuBTC being used to catalyze the xanthene condensation.

As is, it can be tentatively claimed with the preliminary experiments completed thus far that the continuous flow reactor used here can produce the xanthenes over twice as fast as doing it under batch conditions when considering only the reaction and set up times. This excludes any preparatory work and post-reaction work ups that would be required which is required under batch conditions but can be skipped when performing under continuous flow conditions such as such as activation of the CuBTC MOF in the oven (approximately a 24-hour process) and recovery of the CuBTC MOF after the reaction (>30-minute process). These preliminary results are very promising and show that there is a high chance that the xanthene condensation can be successfully transferred to a continuous flow process, making the production of xanthene derivatives via condensation a much more efficient process. Regardless, more experiments would be required to confirm and optimize the reaction under continuous flow conditions.

The results of the xanthene condensation can also be used to draw several conclusions about the stability of CuBTC under continuous flow conditions, especially when paired with the results and conclusions discussed in Chapter 4 of this dissertation. They key conclusions that can be drawn would be:

I. Condensation reactions do not inherently break down CuBTC. As both the Friedländer synthesis and xanthene condensation are both condensation reactions, it can be concluded that condensation reactions do not break down CuBTC inherently as the breakdown of the CuBTC MOF is only observed when in the presence of the Friedländer synthesis.

II. Continuous flow conditions do not inherently break down CuBTC. Again, as both the Friedländer synthesis and xanthene condensation were both performed under continuous flow conditions, it can be concluded that the conditions used to perform these reactions under continuous flow do not inherently break down the CuBTC as the break down is only observed with the Friedländer synthesis.

These conclusions are especially strengthened by the fact that when performed under continuous flow conditions, both the Friedländer synthesis from Chapter 4 and the xanthene condensation from this chapter were both performed at 80°C and have been performed at the same flow rate. This contributes key insights to the understanding of the stability of CuBTC MOF as a catalyst for organic reactions. This understanding is important towards the goal of transferring organic reactions catalyze by CuBTC and potentially even other MOF catalysts to continuous flow conditions. This knowledge would be key in allowing scientists to make progress towards automating more reactions and creating a more efficient future in chemical manufacturing.

Furthermore, it is important to note that the Friedländer synthesis discussed in Chapter 4 of this dissertation uses 2-aminobenzophenone as one of the reactants and DMF as the solvent. Both of these compounds possess nitrogen (amino and amide groups) which means they could have a greater binding affinity to the copper centers of the CuBTC MOF than the oxygen from the benzene-1,3,5-tricarboxylic acid linkers. This could provide another factor to explain why the CuBTC MOF breaks down when being used to perform the Friedländer synthesis discussed in Chapter 4 while it appears to be stable when used to perform the xanthene condensation discussed in this chapter as the xanthene condensation does not use or create any reagents or products that possess nitrogen or amino groups.

The understanding of why the catalytic MOF in these systems is important towards the goal of transferring organic reactions catalyze by CuBTC and potentially even other MOF catalysts to continuous flow conditions. This knowledge would be key in allowing scientists to make progress towards automating more reactions and creating a more efficient future in chemical manufacturing.

CHAPTER 5 – REFERENCES

(1) Zhang, W.; Xiang, X. X.; Chen, J.; Yang, C.; Pan, Y. L.; Cheng, J. P.; Meng, Q.; Li, X. Direct C–H Difluoromethylation of Heterocycles via Organic Photoredox Catalysis. *Nat Commun* **2020**, *11* (1). https://doi.org/10.1038/s41467-020-14494-8.

(2) Norwood, V. M.; Huigens, R. W. Harnessing the Chemistry of the Indole Heterocycle to Drive Discoveries in Biology and Medicine. *ChemBioChem*. Wiley-VCH Verlag September 16, 2019, pp 2273–2297. https://doi.org/10.1002/cbic.201800768.

(3) Martins, P.; Jesus, J.; Santos, S.; Raposo, L. R.; Roma-Rodrigues, C.; Baptista, P. V.; Fernandes, A. R. Heterocyclic Anticancer Compounds: Recent Advances and the Paradigm Shift towards the Use of Nanomedicine's Tool Box. *Molecules*. MDPI AG September 1, 2015, pp 16852–16891. https://doi.org/10.3390/molecules200916852.

(4) Nasreen, A. Cupric Nitrate Catalyzed Efficient and Facile Synthesis of 1,8-Dioxo-Octahydroxanthene Derivatives. *Asian Journal of Chemistry* **2013**, *25* (13), 7535–7538. https://doi.org/10.14233/ajchem.2013.15076.

(5) Kaur, K.; Jain, M.; Reddy, R. P.; Jain, R. Quinolines and Structurally Related Heterocycles as Antimalarials. *Eur J Med Chem* **2010**, *45* (8), 3245–3264. https://doi.org/10.1016/j.ejmech.2010.04.011.

(6) Colella, M.; Degennaro, L.; Luisi, R. Continuous Flow Synthesis of Heterocycles: A Recent Update on the Flow Synthesis of Indoles. *Molecules* **2020**, *25* (14). https://doi.org/10.3390/molecules25143242.

(7) Dhakshinamoorthy, A.; Garcia, H. Metal-Organic Frameworks as Solid Catalysts for the Synthesis of Nitrogen-Containing Heterocycles. *Chem Soc Rev* **2014**, *43* (16), 5750–5765. https://doi.org/10.1039/c3cs60442j.

(8) Ghamari Kargar, P.; Bagherzade, G.; Eshghi, H. Introduction of a Trinuclear Manganese(Iii) Catalyst on the Surface of Magnetic Cellulose as an Eco-Benign, Efficient and Reusable Novel Heterogeneous Catalyst for the Multi-Component Synthesis of New Derivatives of Xanthene. *RSC Adv* **2021**, *11* (8), 4339–4355. https://doi.org/10.1039/d0ra09420j.

(9) Abdel-Galil, F. M.; Riad, B. Y.; Sherif, S. M.; Elnagdi, M. H. *ACTIVATED NITRILES IN HETEROCYCLIC SYNTHESIS: A NOVEL SYNTHESIS OF 4-AZOLOYL-2-AMINOQUINOLINES*.

(10) Wei, W. J.; Zhong, Y. J.; Feng, Y. F.; Gao, L.; Tang, H. T.; Pan, Y. M.; Ma, X. L.; Mo, Z. Y. Electrochemically Mediated Direct C(Sp3)−H Sulfonylation of Xanthene Derivatives. *Adv Synth Catal* **2022**, *364* (4), 726–731. https://doi.org/10.1002/adsc.202101289.

(11) Cao, H. T.; Wan, J.; Li, B.; Zhang, H.; Xie, L. H.; Sun, C.; Feng, Q. Y.; Yu, W. J.; Huang, W. Highly Efficient Exciplex-Emission from Spiro[Fluorene-9,9′-Xanthene] Derivatives. *Dyes and Pigments* **2021**, *185*. https://doi.org/10.1016/j.dyepig.2020.108894.

(12) Rahnamafar, R.; Moradi, L.; Khoobi, M. Synthesis of Benzo[b]Xanthene-Triones and Tetrahydrochromeno[2,3-b]Xanthene Tetraones via Three- or Pseudo–Five-Component Reactions Using Fe3O4@SiO2/PEtOx as a Novel, Magnetically Recyclable, and Eco-Friendly Nanocatalyst. *J Heterocycl Chem* **2020**, *57* (4), 1825–1837. https://doi.org/10.1002/jhet.3911.

(13) Lee, D. Y.; Sivakumar, G.; Manju; Misra, R.; Seok, S. il. Carbazole-Based Spiro[Fluorene-9,9′-Xanthene] as an Efficient Hole-Transporting Material for Perovskite Solar Cells. *ACS Appl Mater Interfaces* **2020**, *12* (25), 28246–28252. https://doi.org/10.1021/acsami.0c06318.

(14) Xu, B.; Bi, D.; Hua, Y.; Liu, P.; Cheng, M.; Grätzel, M.; Kloo, L.; Hagfeldt, A.; Sun, L. A Low-Cost Spiro[Fluorene-9,9′-Xanthene]-Based Hole Transport Material for Highly Efficient Solid-State Dye-Sensitized Solar Cells and Perovskite Solar Cells. *Energy Environ Sci* **2016**, *9* (3), 873–877. https://doi.org/10.1039/c6ee00056h.

(15) Chen, Q.; Yu, G.; Wang, X.; Ou, Y.; Huo, Y. Catalyst-Free Direct C(Sp3)-H Sulfenylation of Xanthene Derivatives Using Air as the Oxidant. *Green Chemistry* **2019**, *21* (4), 798–802. https://doi.org/10.1039/c8gc03898h.

(16) *Third International Scientific Conference NEW DIRECTIONS IN THE CHEMISTRY OF HETEROCYCLIC COMPOUNDS (NDCHC-2013).*

(17) Callan, J. F.; de Silva, A. P.; Magri, D. C. Luminescent Sensors and Switches in the Early 21st Century. *Tetrahedron*. Elsevier Ltd September 5, 2005, pp 8551–8588. https://doi.org/10.1016/j.tet.2005.05.043.

(18) Yang, Y. Z.; Song, R. J.; Li, J. H. Intermolecular Anodic Oxidative Cross-Dehydrogenative C(Sp 3)-N Bond-Coupling Reactions of Xanthenes with Azoles. *Org Lett* **2019**, *21* (9), 3228–3231. https://doi.org/10.1021/acs.orglett.9b00947.

(19) Barrett, S.; O'brien, P.; Steffens, H. C.; Towers, T. D.; Voith, M. *New Route to 4-Aminocyclopent-2-En-1-Ols: Synthesis and Enantioselective Rearrangement of 4-Amino-Substituted Cyclopentene Oxides*.

(20) Ilangovan, A.; Malayappasamy, S.; Muralidharan, S.; Maruthamuthu, S. A Highly Efficient Green Synthesis of 1, 8-Dioxo-Octahydroxanthenes. *Chem Cent J* **2011**, *5* (1). https://doi.org/10.1186/1752-153X-5-81.

(21) Ghafuri, H.; Ganjali, F.; Hanifehnejad, P. Cu.BTC MOF as a Novel and Efficient Catalyst for the Synthesis of 1,8-Dioxo-Octa-Hydro Xanthene. In *Chemistry Proceedings*; MDPI AG, 2021; p 2. https://doi.org/10.3390/ecsoc-24-08359.

(22) Jas, G.; Kirschning, A. Continuous Flow Techniques in Organic Synthesis. *Chemistry - A European Journal* **2003**, *9* (23), 5708–5723. https://doi.org/10.1002/chem.200305212.

(23) Akwi, F. M.; Watts, P. Continuous Flow Chemistry: Where Are We Now? Recent Applications, Challenges and Limitations. *Chemical Communications* **2018**, *54* (99), 13894–13928. https://doi.org/10.1039/c8cc07427e.

(24) Tanimu, A.; Jaenicke, S.; Alhooshani, K. Heterogeneous Catalysis in Continuous Flow Microreactors: A Review of Methods and Applications. *Chemical Engineering Journal* **2017**, *327*, 792–821. https://doi.org/10.1016/j.cej.2017.06.161.

(25) Gutmann, B.; Kappe, C. O. Forbidden Chemistries — Paths to a Sustainable Future Engaging Continuous Processing. *J Flow Chem* **2017**, *7* (3–4), 65–71. https://doi.org/10.1556/1846.2017.00009.

(26) Tanimu, A.; Jaenicke, S.; Alhooshani, K. Heterogeneous Catalysis in Continuous Flow Microreactors: A Review of Methods and Applications. *Chemical Engineering Journal* **2017**, *327*, 792–821. https://doi.org/10.1016/j.cej.2017.06.161.

(27) Munirathinam, R.; Huskens, J.; Verboom, W. Supported Catalysis in Continuous-Flow Microreactors. *Adv Synth Catal* **2015**, *357* (6), 1093–1123. https://doi.org/10.1002/adsc.201401081.

(28) Paunovic, V.; Schouten, J. C.; Nijhuis, T. A. Direct Synthesis of Hydrogen Peroxide in a Wall-Coated Microchannel Reactor over Au-Pd Catalyst: A Performance Study. *Catal Today* **2015**, *248*, 160–168. https://doi.org/10.1016/j.cattod.2014.04.007.

(29) Sachse, A.; Ameloot, R.; Coq, B.; Fajula, F.; Coasne, B.; de Vos, D.; Galarneau, A. In Situ Synthesis of Cu-BTC (HKUST-1) in Macro-/Mesoporous Silica Monoliths for Continuous Flow Catalysis. *Chemical Communications* **2012**, *48* (39), 4749–4751. https://doi.org/10.1039/c2cc17190b.

(30) Zhang, J.; Chen, J.; Peng, S.; Peng, S.; Zhang, Z.; Tong, Y.; Miller, P. W.; Yan, X. P. Emerging Porous Materials in Confined Spaces: From Chromatographic Applications to Flow Chemistry. *Chem Soc Rev* **2019**, *48* (9), 2566–2595. https://doi.org/10.1039/c8cs00657a.

(31) Len, C.; Bruniaux, S.; Delbecq, F.; Parmar, V. Palladium-Catalyzed Suzuki–Miyaura Cross-Coupling in Continuous Flow. *Catalysts* **2017**, *7* (5), 146. https://doi.org/10.3390/catal7050146.

(32) Hartman, R. L.; McMullen, J. P.; Jensen, K. F. Deciding Whether to Go with the Flow: Evaluating the Merits of Flow Reactors for Synthesis. *Angewandte Chemie - International Edition* **2011**, *50* (33), 7502–7519. https://doi.org/10.1002/anie.201004637.

(33) Bobbitt, N. S.; Mendonca, M. L.; Howarth, A. J.; Islamoglu, T.; Hupp, J. T.; Farha, O. K.; Snurr, R. Q. Metal-Organic Frameworks for the Removal of Toxic Industrial Chemicals

and Chemical Warfare Agents. *Chemical Society Reviews*. 2017. https://doi.org/10.1039/c7cs00108h.

(34) McKinstry, C.; Cussen, E. J.; Fletcher, A. J.; Patwardhan, S. v.; Sefcik, J. Scalable Continuous Production of High Quality HKUST-1 via Conventional and Microwave Heating. *Chemical Engineering Journal* **2017**, *326*, 570–577. https://doi.org/10.1016/j.cej.2017.05.169.

(35) Corella-Ochoa, M. N.; Tapia, J. B.; Rubin, H. N.; Lillo, V.; Gonzalez-Cobos, J.; Núñez Rico, J. L.; Balestra, S. R. G.; Almora-Barrios, N.; Lledos, M.; Guell-Bara, A.; Cabezas-Giménez, J.; Escudero-Adán, E. C.; Vidal-Ferran, A.; Calero, S.; Reynolds, M. M.; Marti-Gastaldo, C.; Galan-Mascaros, J. R. Homochiral Metal-Organic Frameworks for Enantioselective Separations in Liquid Chromatography. *J Am Chem Soc* **2019**, jacs.9b06500. https://doi.org/10.1021/jacs.9b06500.

(36) Corella-Ochoa, M. N.; Tapia, J. B.; Rubin, H. N.; Lillo, V.; González-Cobos, J.; Núñez-Rico, J. L.; Balestra, S. R. G.; Almora-Barrios, N.; Lledós, M.; Guëll-Bara, A.; Cabezas-Giménez, J.; Escudero-Adán, E. C.; Vidal-Ferran, A.; Calero, S.; Reynolds, M.; Martí-Gastaldo, C.; Galán-Mascarós, J. R. Homochiral Metal-Organic Frameworks for Enantioselective Separations in Liquid Chromatography. *J Am Chem Soc* **2019**, *141* (36), 14306–14316. https://doi.org/10.1021/jacs.9b06500.

(37) Groom, C. R.; Bruno, I. J.; Lightfoot, M. P.; Ward, S. C. The Cambridge Structural Database. *Acta Crystallogr B Struct Sci Cryst Eng Mater* **2016**, *72* (2), 171–179. https://doi.org/10.1107/S2052520616003954.

(38) Connelly, N. G.; Hartshorn, R. M.; Damhus, T.; Hutton, A. T. *Nomenclature of Inorganic Chemistry IUPAC Recommendations 2005 IUPAC Periodic Table of the Elements Fm No*; 2005; Vol. 128.

(39) Tranchemontagne, D. J.; Mendoza-Cortés, J. L.; O'Keeffe, M.; Yaghi, O. M. Secondary Building Units, Nets and Bonding in the Chemistry of Metal-Organic Frameworks. *Chem Soc Rev* **2009**, *38* (5), 1257–1283. https://doi.org/10.1039/b817735j.

(40) Liu, D.; Gu, W.; Zhou, L.; Wang, L.; Zhang, J.; Liu, Y.; Lei, J. Recent Advances in MOF-Derived Carbon-Based Nanomaterials for Environmental Applications in Adsorption and Catalytic Degradation. *Chemical Engineering Journal*. Elsevier B.V. January 1, 2022. https://doi.org/10.1016/j.cej.2021.131503.

(41) Gandhi, A.; Hasan, M. M. F. Machine Learning for the Design and Discovery of Zeolites and Porous Crystalline Materials. *Current Opinion in Chemical Engineering*. Elsevier Ltd March 1, 2022. https://doi.org/10.1016/j.coche.2021.100739.

(42) Jarosz, R.; Szerement, J.; Gondek, K.; Mierzwa-Hersztek, M. The Use of Zeolites as an Addition to Fertilisers – A Review. *Catena*. Elsevier B.V. June 1, 2022. https://doi.org/10.1016/j.catena.2022.106125.

(43) Ma, S.; Liu, Z. P. The Role of Zeolite Framework in Zeolite Stability and Catalysis from Recent Atomic Simulation. *Top Catal* **2022**, *65* (1–4), 59–68. https://doi.org/10.1007/s11244-021-01473-6.

(44) Cheng, N.; Ren, L.; Xu, X.; Du, Y.; Dou, S. X. Recent Development of Zeolitic Imidazolate Frameworks (ZIFs) Derived Porous Carbon Based Materials as

Electrocatalysts. *Adv Energy Mater* **2018**, *8* (25). https://doi.org/10.1002/aenm.201801257.

(45) Opanasenko, M.; Dhakshinamoorthy, A.; Shamzhy, M.; Nachtigall, P.; Horáček, M.; Garcia, H.; Čejka, J. Comparison of the Catalytic Activity of MOFs and Zeolites in Knoevenagel Condensation. *Catal Sci Technol* **2013**, *3* (2), 500–507. https://doi.org/10.1039/c2cy20586f.

(46) Venkatesan, K.; Pujari, S. S.; Lahoti, R. J.; Srinivasan, K. v. An Efficient Synthesis of 1,8-Dioxo-Octahydro-Xanthene Derivatives Promoted by a Room Temperature Ionic Liquid at Ambient Conditions under Ultrasound Irradiation. *Ultrason Sonochem* **2008**, *15* (4), 548–553. https://doi.org/10.1016/j.ultsonch.2007.06.001.

(47) Nguyen, L. T. L.; Nguyen, T. T.; Nguyen, K. D.; Phan, N. T. S. Metal-Organic Framework MOF-199 as an Efficient Heterogeneous Catalyst for the Aza-Michael Reaction. *Appl Catal A Gen* **2012**, *425–426*, 44–52. https://doi.org/10.1016/j.apcata.2012.02.045.

(48) Peterson, G. W.; Au, K.; Tovar, T. M.; Epps, T. H. Multivariate Cubtc Metal-Organic Framework with Enhanced Selectivity, Stability, Compatibility, and Processability. *Chemistry of Materials* **2019**, *31* (20), 8459–8465. https://doi.org/10.1021/acs.chemmater.9b02756.

(49) Thai, J. E.; Tuttle, R. R.; Deroo, J.; Cuchiaro, J.; Reynolds, M. M. Cu-Based Metal-Organic Framework Nanosheets Synthesized via a Three-Layer Bottom-Up Method for the Catalytic Conversion of S-Nitrosoglutathione to Nitric Oxide. *ACS Appl Nano Mater* **2021**. https://doi.org/10.1021/acsanm.1c03313.

(50) Kuo, 2012 - Synthesis and Characterization of Porous HKUST-1 Metal Organic Frameworks for Hydrogen Storage.

(51) Liu, Y.; Zhang, J.; Song, L.; Xu, W.; Guo, Z.; Yang, X.; Wu, X.; Chen, X. Au-HKUST-1 Composite Nanocapsules: Synthesis with a Coordination Replication Strategy and Catalysis on CO Oxidation. *ACS Appl Mater Interfaces* **2016**, *8* (35), 22745–22750. https://doi.org/10.1021/acsami.6b06209.

CHAPTER 6

SUMMARY OF CONCLUSIONS AND FUTURE DIRECTIONS

6.1 Summary of Conclusions

This dissertation has made significant contributions across the field towards the use of metal-organic frameworks (MOFs) for applications in heterogeneous catalysis. Through the chapters, the work discussed in this dissertation has made strides towards better understanding Cu-based MOF catalysis, synthesizing Cu-based MOFs with more a more optimal morphology for heterogeneous catalysis, and has shown the possibility to use Cu-based MOFs for heterogeneous catalysis under continuous flow conditions. Chapter 2 is a peer reviewed publication primarily written by Jonathan Thai. Chapters 3-5 are written with the intent of submission to a peer-reviewed journal once all of the experiments required to answer key lingering questions have been completed. The main findings of each chapter and future experiments to be done are discussed in this chapter.

First, a water-stable, copper-based MOF, CuBDTri (where H_2BDTri = 1,4-1*H*-1,2,3-triazol-5-yl)benzene) has been successfully synthesized using a three-layer bottom-up method to create MOF nanosheet (MOFN) particles and using solvothermal methods to create MOF with three-dimensional morphologies for the first time. As a new MOF, the CuBDTri was analyzed using powdered x-ray diffraction (pXRD), SEM, acid digestion followed by mass spectrometry, and elemental analysis to confirm its identity as a MOF. The CuBDTri MOFNs synthesized were also shown to be more catalytically active for the generation of nitric oxide (NO) from *S*-

nitrosoglutathione (GSNO) in water than CuBTTri (where H_3BTTri = 1,3,5-tris(1*H*-1,2,3-triazol-5-yl)benzene) on a per-total-Cu-atom basis.

The synthetic groundwork towards optimizing the synthesis of CuBDTri has also been completed to create thinner MOFN particles. This would allow for the CuBDTri to minimize internal volume while maximizing external surface area so substrates in heterogeneous catalytic processes are not diffusion-limited and thus, are efficient as possible. Furthermore, by obtaining CuBDTri MOFN particles of different average thicknesses, it can be tested to see whether the increased density of easily accessible active sites is a factor in the observed increased in efficiency relative to CuBTTri MOF octahedra.

Towards that end, a method was experimentally developed for atomic force microscopy (AFM) to be able to accurately and efficiently measure the thickness of the CuBDTri MOFN particles so that the data can be used to computationally determine the ideal synthetic conditions to create the thinnest MOFN particles. The development of this AFM method was key as none are clearly reported in the literature. Furthermore, the method developed in this dissertation provides clear images and measurements of several CuBDTri MOFN particles per image, allowing the images to provide larger sample sizes more easily and efficiently.

It was determined that CuBTC (where BTC = benzene-1,3,5-tricarboxylate) MOF has been determined to be broken down when used to try and catalyze the Friedländer synthesis based on AFM, time-of-flight mass-spectrometry (TOF-MS), and scanning electron microscopy (SEM) data. This work shows the importance of thoroughly analyzing the MOFs used in heterogeneous catalysis before and after it has been used. The results of this work have also contributed to a better understanding of Cu-based MOF catalyzed Friedländer synthesis, including why CuBTC breaks down under the conditions used to perform the Friedländer synthesis.

The better understanding of CuBTC in the Friedländer synthesis has also led to work to reidentify the catalyst, further increasing the understanding of this system. This work shows the importance of understanding the mechanism of catalysis in systems using MOFs for heterogeneous catalysis and understanding the difference between MOFs as heterogeneous and homogeneous catalysts.

A continuous flow method has been successfully created to catalyze condensation reactions to create xanthene derivatives without breaking down the CuBTC MOF used as the catalyst after several equivalents of the reaction have been performed. This work shows that CuBTC is indeed capable of catalyzing a condensation reaction under continuous flow conditions, opening the possibility to more easily scale up and automate these reaction processes for chemical manufacturing.

Furthermore, this work with the continuous flow condensations to create xanthene derivatives showed that the instability of the CuBTC in the Friedländer synthesis system is not due to anything inherent with condensation reactions or performing reactions under continuous flow conditions as the CuBTC only broke down under the conditions used for the Friedländer synthesis and not for the condensation to create xanthene derivatives. This provides some key insights to understanding for the use of continuous flow processes of organic transformations and can hopefully help streamline the process of changing more reactions over from the benchtop to automated continuous flow reactors.

6.2 Future Directions

The scientific discoveries reported in this dissertation have led to additional questions. Those questions and some experiments that could help address those questions are included and discussed in this section.

6.2.1 Future Directions for Designing and Synthesizing Cu-Based Metal-Organic Framework Nanosheets for Greater Catalytic Efficiency

While Chapter 2 reported the synthesis of CuBDTri and that it is more catalytically efficient for the generation of NO from GSNO in water than CuBTTri, there still remains the question, why? Based on what is known, it can only be said that there is in increase in catalytic efficiency on a per-total-Cu-atom basis, but it is unknown whether it is due to:

I. The increased density of active sites versus CuBTTri octahedra due to the greater relative external surface area of CuBDTri that result in a greater proportion of readily accessible Cu
II. Th Cu sites on the surface of CuBDTri are kinetically different from CuBTTri and thus catalyze the generation of NO from GSNO at a greater rate than the Cu sites in CuBTTri

To test the first hypothesis, CuBDTri nanosheets of varying thicknesses and even CuBDTri MOF synthesized using solvothermal methods could be used to catalyze the generation of NO from GSNO. This would help determine whether or not this is strictly due to having a greater proportion of readily accessible copper sites. For the second hypothesis would also be important to determine the molecular structure, especially on the surface of the CuBDTri MOF so that experiments like catalyst poisoning can be performed to better understand the kinetics of the catalytic process. To

determine the structure of CuBDTri, experiments such as neutron diffraction, high-res p-XRD, and transmission electron microscopy can be used in combination to try and piece together the structure.

6.2.2 Future Directions in Optimizing the Three-Layer Bottom-Up Synthetic Method for Making CuBDTri MOFNs

Using the foundation created by the work completed and discussed in Chapter 3 of this dissertation, there is still a lot of work to be done before the goal of creating the thinnest CuBDTri MOFN particles as possible can be realized. While all of the initial syntheses have been completed and an AFM method has been developed to measure the thicknesses of the MOFNs produced from each of those syntheses, all of that data needs to be collected. Ideally, we would be able to use this to obtain large sample sizes of nanosheet thicknesses from each of the syntheses and would likely need at least 3 clear AFM images from each synthetic condition used.

Once all of that data has been collected and an average thickness has been determined from each of the syntheses, we can then input that data to create a heatmap that will then predict the ideal set of conditions (temperature, middle-layer buffer thickness, and metal to ligand ratio) to use to synthesize nanosheets that are as this as possible based on those parameters. Those parameters can then be tested experimentally to see how accurate the heatmap is and if it is inaccurate, the data can then be input into the heatmap to repeat this process until the heatmap has enough data to consistently predict conditions for a specific thickness of the MOFNs accurately.

6.2.3 Future Directions to Better the Understanding of the Breakdown of CuBTC MOF by Friedländer Synthesis and to Reidentify the Catalyst

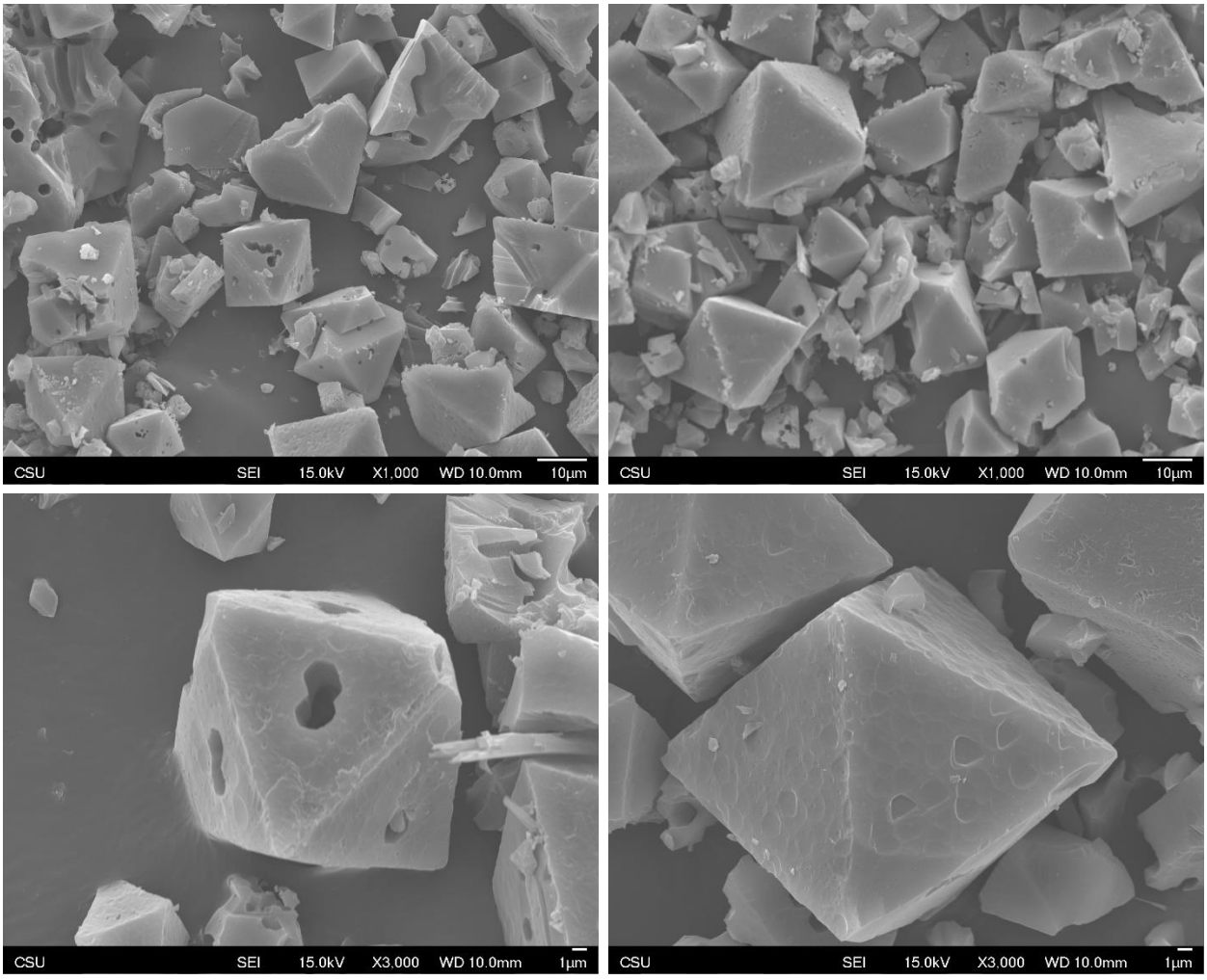

Figure 6.1. This figure is reproduced from Chapter 4 (Figure 4.6). SEM images showing the scaling and hexagonal holes on CuBTC MOF particles after they were used for one equivalent of the Friedländer synthesis under continuous flow conditions.

The work in Chapter 4 had originally aimed to transfer the Friedländer synthesis from batch conditions to continuous flow, but due to data indicating the breakdown of CuBTC, the goal of the project was redirected. Based on the SEM data (Figure 1) and the presence of a compound containing copper in the TOF-MS, it can be said that the CuBTC is indeed being broken down and reforming into a blue solid “mystery crystal”. Because CuBTC is being broken down and not part

of the catalytic cycle itself, it is hypothesized that it is acting as a pre-catalyst instead and that something that it breaks down into is the true catalyst in this system.

Moving forward, the significant remaining question is, what is the actual catalyst of this system. There are several experiments one could run to take steps towards answering that question, such as:

VI. Running a control to determine if any of the reagent is causing the breakdown of the CuBTC
    a. Using the reaction conditions for the Friedländer synthesis with just CuBTC and DMF and then use SEM, pXRD, and TOF-MS to determine if the CuBTC is damaged
    b. Use the reaction conditions for the Friedländer synthesis with CuBTC in DMF and 2-aminobenzophenone and then use SEM, pXRD, and TOF-MS to determine if the CuBTC is damaged
    c. Use the reaction conditions for the Friedländer synthesis with CuBTC in DMF and acetylacetone and then use SEM, pXRD, and TOF-MS to determine if the CuBTC is damaged

VII. Use Cu(I) and Cu(II) specific chelating agents in the supernatant that was eluted from the continuous flow column used for the Friedländer synthesis to determine whether the copper-containing compound hypothesized to catalyze the reaction contains either Cu(I) or Cu(II)

VIII. Since both CuBTC and the eluted supernatant seem to be capable of catalyzing the Friedländer synthesis, perform and compare the reaction rates of the Friedländer synthesis when each of them are used to catalyze the reaction

IX. Measuring the amount of CuBTC left in the column after CuBTC has been broken down and leaves the column to determine the rate of loss of CuBTC from the column and comparing that to the amount of copper present in the collected eluent to see where exactly all of that lost copper is (what compounds it might be attached to and/or how much of it might be free-floating in the supernatant).

X. Analyzing the green fractions collected from the continuous flow system to determine whether copper is present already in those fractions and to try and confirm whether or not it is responsible for the green color of the fraction using UV-Vis

Definitively identifying that this blue solid "mystery crystal" could also be of help in answering the above questions. To do so however, it would need to be analyzed by more techniques, which could potentially be nuclear magnetic resonance (NMR) and infrared spectroscopy (IR). Furthermore,

6.2.4 Future Directions for Developing CuBTC MOFs to Catalyze the Condensation Between Dimedone and Benzaldehyde to Form 3,3,6,6-Tetramethyl-9-phenyl-3,4,5,6,7,9-hexahydro-1*H*-xanthene-1,8(2*H*)-dione Under Continuous Flow Conditions

While the work in Chapter 5 has preliminary was able to complete preliminary experiments that showed proof of concept for the transfer of the condensation between dimedone and benzaldehyde under continuous flow conditions, there are still more experiments that need to be performed. They major point to be taken from the data obtained from Chapter 5, is that the yield from the continuous flow conditions of the reaction is likely to be lower. More experiments would need to be done under continuous flow conditions to determine what the yield from each of the

reaction conditions are and then optimization of the continuous flow system can be done to try and increase the product yield. Some variables to test would include:

I. Decreasing flow rate – while this would slow down the rate of production, it would give more contact time between the reagents the catalyst, potentially increasing yields

II. Increasing temperatures – due to high flow rates, the reaction might not actually be reaching 80°C under continuous flow conditions so increasing the temperature the column is sitting at might be able to help increase the temperature of the reaction faster to ensure it reaches 80°C

III. Increasing length of catalytic column – this would make the reaction take a little longer to elute out of the reactor and require a larger amount of MOF to be packed into the column, but would allow for the reaction to have longer contact time with catalytic MOF which can potentially increase yields

IV. Increasing concentration of the reactants – can increase the concentrations of the reactants to help push the rate of the reaction higher so that it can proceed more quickly under continuous flow

It would also be good to show longevity of the column, running multiple equivalents of the reaction through the column to show that there is no decrease in yield over time, or that if there is a decrease in yield, that there is a solution to such a problem such as just rinsing out the column well with a solvent, such as ethanol. This experiment could be done by running 10 equivalents (or more) equivalents through the column and tracking the yield between each of the equivalents. This would also show whether or not the CuBTC packed in the column is still fully intact after this many

equivalents of the reaction, confirming the conclusions drawn from the experiments that have already been completed.

Future experiments should also conduct a more thorough analysis of the product to ensure the results from the preliminary experiments were indeed successful. By using NMR and IR to characterize the products, the structure and purity of the products can be confirmed. Thin-layer chromatography (TLC) and melting-point experiments can also be done to help confirm the purity of the obtained product. Furthermore, performing TOF-MS in negative mode on the obtained products could help identify potential by-products that could not be seen under positive-mode, to help identify byproducts if any are present. The use of elemental analysis of the product collected when performed under continuous flow conditions could also ensure there is no copper present, which would provide further confirmation and data that there is no breakdown of the CuBTC being used to catalyze the reaction.

Furthermore, experiments can be done to try and scale up the reaction so that it can more closely resemble setups in the chemical manufacturing industry. This can be done by using larger columns so that more reaction mixture can be pumped through more quickly. It can also be tested to see if a full continuous flow setup can be achieved by just pumping a large amount of reaction mixture (>100 mL) continuously through the system and seeing if this can be done as efficiently as possible while maintaining as high of a yield as possible.

6.3 Impacts on Future Research

With the work completed and discussed in this dissertation, new directions in the synthesis and application of MOFs for heterogeneous catalysis have been opened. Ultimately, the work discussed in this dissertation provides a foundation towards the development of MOFs in the field

of heterogeneous catalysis by increasing the efficiency of MOFs as heterogeneous catalysis, providing a standardized way to understand MOF stability when used in catalytic systems, and showing that MOFs can be used to catalyze organic reactions under continuous flow so that they can be used efficiently in the manufacturing of organic compounds.

6.3.1 Impacts of Chapter 2

The CuBDTri MOFNs created in this chapter help create a second generation of Cu-based MOFs that are stable in water, thus allowing it to be safely used in medical devices. From the development of the CuBDTri MOFNs discussed in Chapter 2 of this dissertation, it has been shown that:

I. The three-layer method used to create MOFNs can be applied to a larger scope of MOFs than was previously thought.

II. The use of the CuBDTri MOFN to catalyze the release of NO from GSNO showed that it was likely to be more catalytically efficient than its three-dimensional counterpart, CuBTTri. This pushes researchers to create MOFNs of other MOFs of interest for use in heterogeneous catalysis to increase catalytic efficiency for reactions that use substrates that would be too large to easily diffuse through the pores of the MOF.

Moving forward, this work promotes the use of MOFNs as heterogeneous catalysts, helping push MOFs as a more viable and efficient catalytic material as it eliminates the need for substrates to diffuse through the MOF particle to access the majority of the active catalytic sites of the MOF, and still allow chemists to take advantage of the other properties unique to MOFs.

This work provides key evidence that the modifying the morphology of MOFs may be one of the best ways to increase catalytic efficiency in systems where the substrates being used cannot easily diffuse through the pores of the MOF. In doing so, this work enables the development of new MOF catalysts with higher catalytic efficiencies by modifying the particle morphology of the MOF. Ultimately, the creation of CuBDTri MOFNs provide a new Cu-based MOF that can be used to safely catalyze reactions in medical devices more efficiently that what can be currently achieved using CuBTTri MOF octahedra.

6.3.2 Impacts of Chapter 3

While the work in Chapter 3 of this dissertation is yet to be fully completed, the work that has already been completed can be used to shape the future of materials development. This work has shown:

I. Using a "design of experiments" approach to optimize the synthetic conditions used to create MOFNs. The "design of experiments" approach described here can be used for the optimization of several synthetic processes in both small molecule and materials synthesis, streamlining the process and decreasing the number of experiments needed to optimize the synthetic conditions. This is not an approach that is commonly seen currently in academia and this work provides an example of how moving forward, synthetic chemists can use this approach to help them optimize synthetic methods and conditions they are developing.

II. A standard method of sample prep and set of conditions to analyze MOFNs using AFM has been established within this work where no standard has been shown in the literature before. Most AFM images of MOF and MOFNs are typically low quality and only provide parts of the images whereas the method developed in this

work has been shown to be capable of producing consistent and high-quality images for CuBDTri MOFNs.

While this process has yet to be shown to be applicable for more than just CuBDTri MOFNs, the experimental methods described can be used to help develop methods that can work for other materials to be analyzed by AFM. This is key in determining the thickness of materials such as MOFNs as the thickness of these particles are hypothesized to be instrumental in maximizing the catalytic efficiency of MOFs.

This work helps provide ways to maximize the catalytic efficiency of MOFNs by creating MOFN particles that are as thin as possible, maximizing external surface area and minimizing internal volume. The optimization of MOFN particles in this way will be instrumental in reaching the limits of catalytic efficiency on MOFNs. Ultimately, the work completed in this chapter will enable others to more easily synthesize and optimize new MOFN by providing a "design of experiments" approach that will streamline the process of testing various conditions and by providing a set method for the AFM to thoroughly analyze the resulting MOFN particles.

6.3.3 Impacts of Chapter 4

The work in Chapter 4 of this dissertation calls attention to proper analysis of MOFs being used in heterogeneous catalytic systems. In particular, this work shows that chemists working with MOFs as heterogeneous catalysts need to provide a more thorough analysis of the MOFs being used before and after catalysis. Currently, most of the literature only analyzes MOFs using pXRD, however, the data from this work has shown that it is necessary to show SEM data before and after as well as pXRD could not detect the breakdown of the CuBTC caused by the Friedländer synthesis. Overall, this work will enable a better understanding of MOF stability by looking at the

stability of CuBTC under the conditions used to perform the Friedländer synthesis and examining the potential causes that led to the breakdown of CuBTC in this system.

6.3.4 Impacts of Chapter 5

The work completed in Chapter 5 of this dissertation shows that the continuous flow system created and discussed in Chapters 4 and of 5 of this dissertation can be used to catalyze organic transformations. Specifically, CuBTC can be used as a heterogeneous catalysis to create xanthene derivatives in a continuous flow system that is more efficient than performing the reaction using batch conditions. Furthermore, this work shows the potential for several kinds of organic reactions to be transferred from a batch process to continuous flow process, allowing them to be produced more efficiently. This work shows the viability of MOFs in continuous flow processes, allowing future chemists to use MOFs as designer catalysts for a larger variety of reactions to efficiently produce compounds of interest for use in areas such as pharmaceuticals and materials. Ultimately, this work shows the possibility of catalyzing organic transformations under continuous flow using MOFs, providing a more efficient way to perform these organic transformations by showing that it is possible with the xanthene condensation discussed in Chapter 5.

APPENDIX A

Supporting Information for Chapter 2

Table A1.1. Elemental analysis results from Huffman for the CuBDTri MOF nanosheets (MOFNs). The signal for chlorine was not discernable from noise but was included in this table so that all data obtained could be presented. Mass % is based on how much of the sample is comprised of that specific element and does not add up to 100% as this does not account for any element that was not analyzed for.

	Carbon	**Hydrogen**	**Nitrogen**	**Copper**	**Chlorine**
Mass %	41.82%	4.58%	26.36%	14.7%	0.08%
Ratio	30.10	39.29	16.27	2	0.02

Table A1.2. Elemental analysis results from EDS mapping for the CuBDTri MOFNs. Based on the EDS maps obtained, it can be confirmed that carbon, nitrogen, copper, and oxygen are all present within he CuBDTri MOFNs. Oxygen is hypothesized to be present due to water acting as a capping ligand to the Cu sites. Mass % here is based solely on the elements that were analyzed for so does not account for any elements that were not analyzed for.

	Carbon	**Nitrogen**	**Copper**	**Oxygen**
Mass %	51%	38%	8%	3%
Atomic %	58%	37%	2%	3%

Table A1.3. This table provides some experimental data and information to confirm the water stability of the CuBDTri MOF synthesized via three-layer bottom-up methods. The amount of copper per L of water was obtained by multiplying the amount of CuBDTri MOFNs per L of water by 0.147 as it was found that the sample was 14.7% copper from the elemental analysis. The "Factor Difference" compares the amount of copper that was originally put into the water solution against the amount of copper that was found in the water after the CuBDTri MOFNs were allowed to soak after 24 hours.

	Sample 1	**Sample 2**	**Sample 3**
Mass of CuBDTri MOF nanosheet (mg)	22	23.1	23.1
Volume of Water (mL)	10	10	10
Amount of CuBDTri MOFNs per L of water (mg/L)	2200	2310	2310
Amount of copper per L of water (mg/L)	323.4	339.57	339.57
Factor Difference	660.0	1061.2	970.2
AVERAGE FACTOR DIFFERENCE	897.119		

Equation A1.1.

$$\text{Amount of copper per L of water} = \frac{\text{Amount of CuBDTri MOFNs per L of water } \left(\frac{\text{mg}}{\text{L}}\right)}{0.147}$$

Equation A1.2.

$$\text{Factor Difference} = \frac{\text{Amount of copper put in per L of water } \left(\frac{\text{mg}}{\text{L}}\right)}{\text{Amount of copper leached into the water } \left(\frac{\text{mg}}{\text{L}}\right)}$$

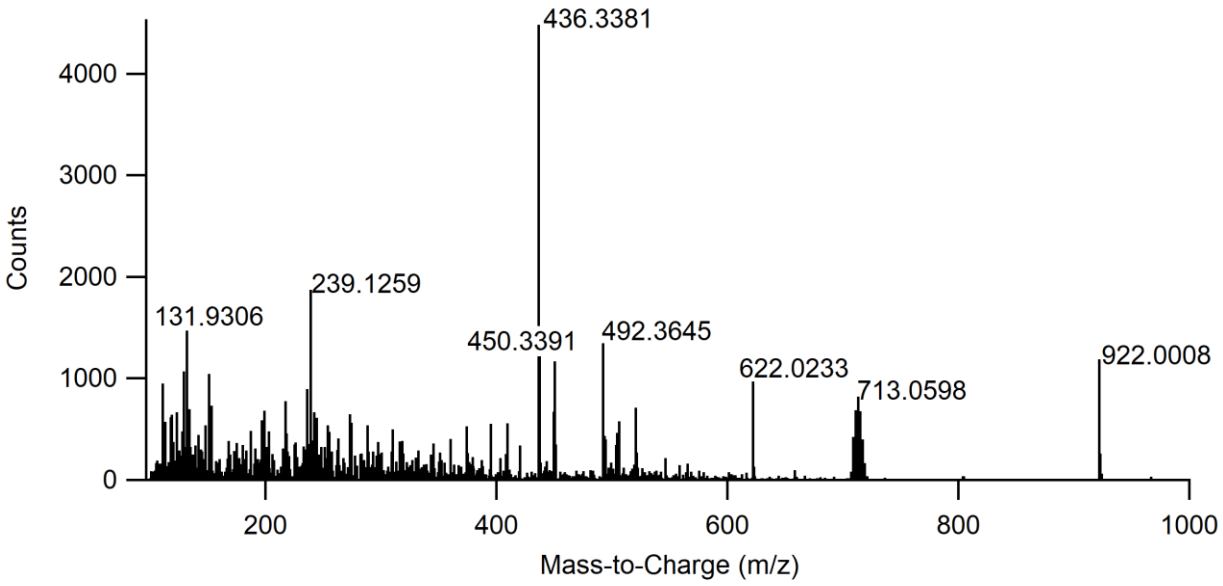

Figure A1.1. Mass spectrum of only the 6M HCl used to digest the CuBDTri MOFNs. This spectrum shows that the signal at 436 *m/z*, also seen in the spectrum after it digested the CuBDTri MOFNs, is a signal that produced from the 6M HCl. This spectrum also confirms that the 213 *m/z* peak is indeed a product of the CuBDTri MOF nanosheet after it was digested by the 6M HCl for 24 hours.

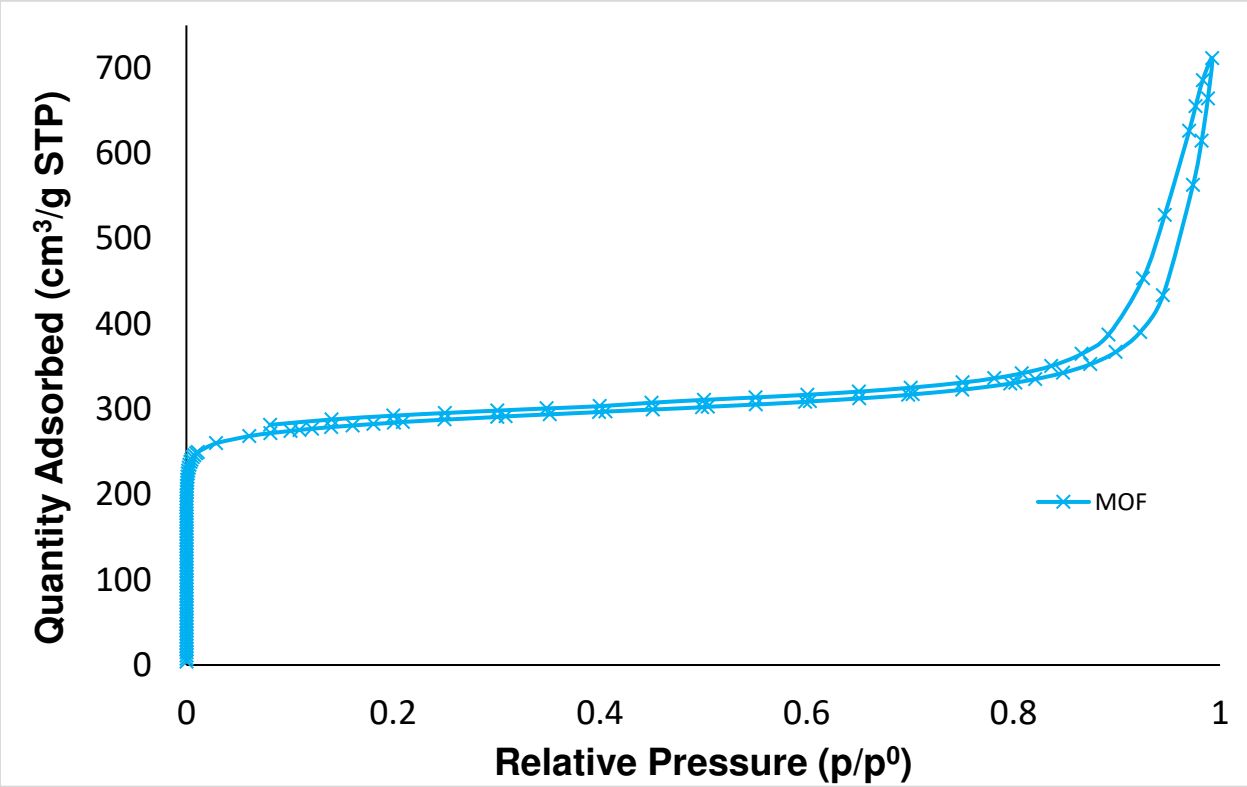

Figure A1.2. BET analysis of a MIL-53 (Al) standard. This control shows that there were no errors with the instrumentation and that the two-step isotherm observed for CuBDTri is not a result of instrumental error and is indeed associated with the CuBDTri MOF itself. The sample prep for MIL-53 (Al) was identical to that of the CuBDTri MOF.

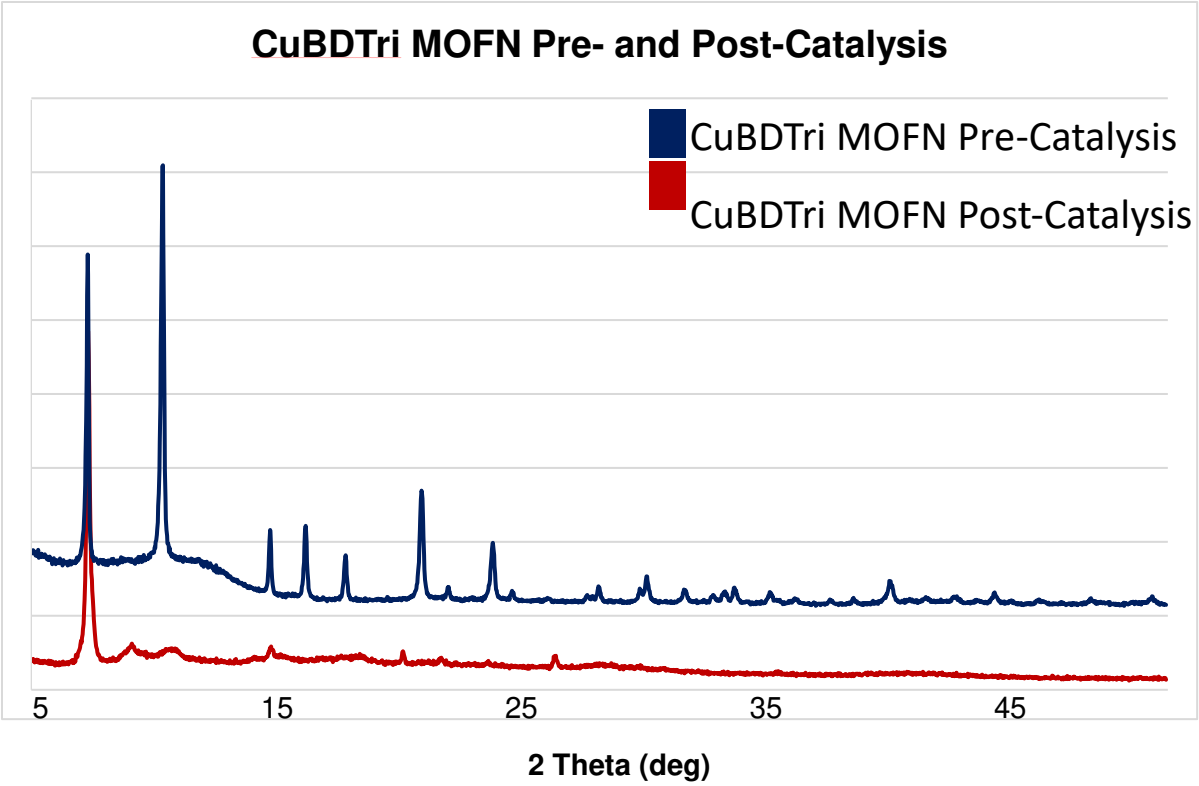

Figure A1.3. pXRD of i.) CuBDTri MOFN before it was used to catalyze the generation of NO from GSNO (in blue, top) and ii.) CuBDTri MOFN after it was used to catalyze the generation of NO from GNSO (in red, bottom). The peak at 7θ is retained in the diffraction pattern, but the intensity of the other peaks is reduced, or they are not present. The retention of the peak at 7 2θ after catalysis indicates that the crystal structure of CuBDTri is not destroyed during catalysis, a result in good agreement with the water stability of CuBDTri established herein. However, the loss of intensity or disappearance of other peaks in the diffraction pattern indicates that some of the previously observed diffraction events for bare CuBDTri nanosheets are not present after catalysis. The CuBDTri nanosheets are extremely thin materials (~50 nm thick on average), and therefore we hypothesize that any species present on the surfaces of the nanosheets after catalysis should have a significant impact on the observed diffraction pattern. We hypothesize that the change in diffraction pattern is caused by the adsorption of some combination of GSNO, GSH, and/or GSSG from the reaction onto the surface of CuBDTri. Future experimental work will test our hypothesis of reactant/product adsorption as the source of the change in the diffraction pattern observed in this figure. However, the key result currently is that the conditions used for NO release catalysis herein do not destroy the CuBDTri nanosheets, which would result in a complete loss of crystallinity (as opposed to a retention of crystallinity but a change in diffraction pattern as observed).

Synthesis of H_3BTTri (1,3,5-tris(1*H*1,2,3,-triazol-5-yl)benzene). To synthesize the H_3BTTri ligand, copper(I) iodide (1.011 g, 5.308 mmol) and 1,3,5-triethynylbenzene (35.291 mmol, 1 equiv.) were combined in a two-necked 500 mL round-bottomed flask. DMF (180 mL) and methanol (20 mL) were then used to suspend the solid reagents. A reflux condenser was then set up with the vertical neck while a rubber septum was used to seal the other. The system was then purged with nitrogen. Trimethylsilylazide (20 ml, 5 equiv) was then injected through the rubber septum, into the reaction. The dark brown mixture was then stirred at 300 rpm at 100°C for 48 hours. The reaction was then filtered hot through a course glass filter frit, collecting a green solid, and golden/brown liquid. The collected liquid filtrate was then concentrated under reduced pressure until only about 10-20 mL was left. Then, deionized water (250 mL) was added to the concentrated filtrate, producing a light green precipitate. The solid mixture was then filtered through a fine glass filter frit. The collected solid was then washed with deionized water (6 x 250 mL) and diethyl ether (6 x 250 mL). The resulting solid was then dried under reduced pressure overnight.